National Library
of Canada

Acquisitions and
Bibliographic Services Branch

395 Wellington Street
Ottawa, Ontario
K1A 0N4

Bibliothèque nationale
du Canada

Direction des acquisitions et
des services bibliographiques

395, rue Wellington
Ottawa (Ontario)
K1A 0N4

Your file Votre référence

Our file Notre référence

NOTICE

The quality of this microform is heavily dependent upon the quality of the original thesis submitted for microfilming. Every effort has been made to ensure the highest quality of reproduction possible.

If pages are missing, contact the university which granted the degree.

Some pages may have indistinct print especially if the original pages were typed with a poor typewriter ribbon or if the university sent us an inferior photocopy.

Reproduction in full or in part of this microform is governed by the Canadian Copyright Act, R.S.C. 1970, c. C-30, and subsequent amendments.

AVIS

La qualité de cette microforme dépend grandement de la qualité de la thèse soumise au microfilmage. Nous avons tout fait pour assurer une qualité supérieure de reproduction.

S'il manque des pages, veuillez communiquer avec l'université qui a conféré le grade.

La qualité d'impression de certaines pages peut laisser à désirer, surtout si les pages originales ont été dactylographiées à l'aide d'un ruban usé ou si l'université nous a fait parvenir une photocopie de qualité inférieure.

La reproduction, même partielle, de cette microforme est soumise à la Loi canadienne sur le droit d'auteur, SRC 1970, c. C-30, et ses amendements subséquents.

Canada

Optical Depth Profiling of Thin Polymer Films and Diffusion in Membranes by Photothermal Deflection or "Mirage Effect" Spectroscopy

by

Melodie A. Schweitzer

A thesis submitted to the Faculty of Graduate Studies and Research
in partial fulfilment of the requirements for the degree of PhD.

April 1995
Department of Chemistry
McGill University
Montreal, Quebec, Canada

National Library of Canada

Acquisitions and Bibliographic Services Branch

395 Wellington Street
Ottawa, Ontario
K1A 0N4

Bibliothèque nationale du Canada

Direction des acquisitions et des services bibliographiques

395, rue Wellington
Ottawa (Ontario)
K1A 0N4

Your file Votre référence

Our file Notre référence

The author has granted an irrevocable non-exclusive licence allowing the National Library of Canada to reproduce, loan, distribute or sell copies of his/her thesis by any means and in any form or format, making this thesis available to interested persons.

L'auteur a accordé une licence irrévocable et non exclusive permettant à la Bibliothèque nationale du Canada de reproduire, prêter, distribuer ou vendre des copies de sa thèse de quelque manière et sous quelque forme que ce soit pour mettre des exemplaires de cette thèse à la disposition des personnes intéressées.

The author retains ownership of the copyright in his/her thesis. Neither the thesis nor substantial extracts from it may be printed or otherwise reproduced without his/her permission.

L'auteur conserve la propriété du droit d'auteur qui protège sa thèse. Ni la thèse ni des extraits substantiels de celle-ci ne doivent être imprimés ou autrement reproduits sans son autorisation.

ISBN 0-612-08155-9

Canada

ABSTRACT

Photothermal deflection or 'mirage effect' spectroscopy was applied to the quantitative profiling of the optical absorbers in thin polymer films with depth dependent absorption coefficients. In addition, the mirage effect system instrumentation was designed and constructed. Improvements to the precision and accuracy of the instrumentation were implemented, which allowed for quantitative measurements of optical depth dependent layers to be profiled in samples consisting of thin polymer multilayered films. A theoretical model based on one-dimensional heat conduction was developed and used to analyze the experimental results. Further improvements were made to the model by applying diffraction theory to recover heat flux profiles. This added precision for the analysis was required for use in the inverse problem theory. The results from using this theoretical model were interpreted. The mirage effect technique was applied to the dynamic diffusion of solutions containing ionic species through a perfluorosulphonated ionomer membrane. The recovery of the heat flux profiles (solved using inverse problem theory) enabled the recovery of optical absorption profiles, and therefore, concentration profiles. A diffusion model (also developed in this work), enabled the diffusion coefficients of these species to be determined from the concentration profiles. By these means, the diffusion processes of species into the membrane were examined.

RÉSUMÉ

La spectroscopie de déflexions photothermales ou à effet de mirage fut appliquée pour l'étude quantitative des profils d'absorbeurs optiques dans des films polymérisés minces ayant des coefficients d'absorption dépendants de la profondeurs. De plus, le système spectroscopique à effet de mirage a été conçu et construit. Des améliorations quant à l'exactitude et la précision de l'instrument furent ajoutés. Ces dernières ont permis d'obtenir, quantitativement, une vue d'ensemble des couches dépendantes de la profondeur optique dans des échantillons consistant en plusieurs minces films polymérisés superposés. Un modèle théorique basé sur la conduction unidimensionnelle de chaleur a été développé et utilisé pour fins d'analyse des résultats. Des améliorations additionnelles furent apportées au modèle par l'application de la théorie de diffraction, afin de récupérer des profiles de flux de chaleur. Cet ajout au modèle s'avérait requis pour l'utilisation de la théorie de problème inverse. Les résultats obtenus à partir de ce modèle théorique ont été interprétés. La technique à effet de mirage fut appliquée à la diffusion dynamique de solutions ioniques à travers une membrane ionomérique perfluorosulphonatée. La récupération des profils de flux de chaleurs (résolue à l'aide de la théorie de problème inverse), a permis de récupérer les profils d'absorption optiques et donc, les profils de concentrations. Un modèle de diffusion (aussi développé dans cet ouvrage) a rendu possible la détermination des coefficients de diffusion et ce, à partir des profils de concentrations. Avec ses moyens, les procédés de diffusion d'espèces à l'intérieur de membranes ont été examinés.

For my parents, Arthur and Carol, and my sister, Virginia,

for all their love and support throughout my education.

ACKNOWLEDGMENTS

I would like to thank my supervisor, Prof. J. Power, for her guidance and support over the course of this thesis. I would like to express my gratitude to Profs. B. Lennox, A. Eisenberg, and R. Brown, for their insights into the scientific process, and in particular, on the properties of membrane materials.

I would like to acknowledge:

Drs. S. Brienne, M. Prystay, and R. Markwell for proofreading my thesis and providing valuable comments on style and content.

Mr. D. Lesage for translating the abstract into French.

Ms. L. Lipowski for all her help in formatting the thesis and typing some of the long equations.

Messrs. F. Kluck and W. Bastian from the machine shop in the Chemistry department for their excellent work, especially in the construction of my diffusion cell.

Messrs. R. Gaulin and R. Rossi from the electronics shop in the Chemistry department for all their technical assistance.

I would to thank in particular:

Marc Prystay, Steve Barnett, Andrew Vreugdenhil, Ross Markwell, Robin Rattray, Michael Quigley, Veronica Calderhead, and all the graduate students of the Analytical division, and a special thanks to Stéphane Brienne, for all their valuable discussions, their friendship, and for making my years at McGill University memorable.

Finally, I would like to express my deepest gratitude to my parents, my sister, my boyfriend, Doug, and my close friends. They have always supported me and encouraged me through the course of this thesis. Furthermore, they have instilled in me the desire to strive to attain my goals.

I would like to thank the Natural Sciences and Engineering Research Council of Canada (NSERC) for the award of a postgraduate scholarship, and les Fonds pour la Formation de Chercheurs et l'Aide à la Recherche (FCAR) for the award of a postgraduate scholarship, for funding my graduate work. The final stages of the project were generously funded by Prof. J. Power.

TABLE OF CONTENTS

CHAPTER 1 INTRODUCTION

CHAPTER 2 MIRAGE EFFECT INSTRUMENTATION

CHAPTER 3 A THEORETICAL MODEL FOR THE INTERPRETATION OF OPTICAL DEPTH PROFILING OF THIN FILMS USING MIRAGE EFFECT SPECTROSCOPY

CHAPTER 4 OPTICAL DEPTH PROFILING OF DISCRETE AND CONTINUOUS ABSORBERS USING MIRAGE EFFECT SPECTROSCOPY

CHAPTER 5 DIFFRACTION MODEL AND ITS IMPLEMENTATION IN INVERSE PROBLEM THEORY FOR MIRAGE EFFECT DEPTH PROFILING

CHAPTER 6 DIFFUSION OF COLOURED SPECIES INTO NAFION MEMBRANES

LIST OF FIGURES

CHAPTER 3

CHAPTER 4

CHAPTER 5

CHAPTER 6

LIST OF TABLES

CHAPTER 1 INTRODUCTION

1.1 INTRODUCTION

Non-destructive methods of evaluating the surface and bulk properties of a sample are favoured due to their ability to maintain the integrity of both the properties and structure of the sample for further analysis. Several techniques are available, each having advantages and limitations with respect to the sample properties being examined. These properties, such as the range of the thicknesses which can be probed in a sample, the corresponding depth resolution, types of material which can be examined or the complexity of the instrumentation required, can dictate the method which is applicable to the sample under examination. This thesis focuses on photothermal techniques as a non-destructive method of examining samples with depth dependent optical absorbing layers.

1.2 GENERAL INTRODUCTION TO PHOTOTHERMAL SPECTROSCOPY

Photothermal spectroscopy is an area encompassing a wide variety of techniques, which focus on the excitation of a sample material using electromagnetic radiation, and measuring the spectral response from the thermal response in the material. Photothermal techniques are flexible in that one can choose both the method of heating and the method of detection for the system. Photo-excitation, such as broadband sources in the form of a Xenon arc lamp or as discrete wavelength sources such as a laser, are typically used to profile properties of a material from the UV through to the IR regions of the electromagnetic spectrum. Excitation with electromagnetic radiation will perturb the system from a ground state to an excited state. Relaxation of the system may occur through both radiative and non-radiative de-excitation processes. Radiationless processes will convert the energy to thermal motion or heat. Interpretation of photothermal spectroscopy is dependent on creating an accurate model of the energy dissipation process. For example, if the energy absorbed causes elastic deformation of the material, then both the thermal and elastic properties of the material need to be considered in the model. For the majority of samples there is no significant delay between the photo-excitation of the sample and the onset of heating. The process can then be modeled in terms of the linear properties of heat transfer (1-3). For the purposes of this thesis, samples were chosen which limit any radiative mechanisms, so that the signal can be modeled entirely as a thermal response.

The excitation method which should be chosen is one which accesses optical wavelengths which interact with the sample. In conventional spectroscopy, a direct measurement of the transmitted, reflected or scattered optical radiation occurs. A relationship exists between the quantity measured and the absorption coefficient of the material under investigation. Photothermal techniques are able to recover the absorption coefficient by analysis of the spatial profile resulting from the thermal gradients in the sample caused by light absorption (4-7). The absorption coefficient determines the depth at which the energy can be deposited in the sample by a light source, and is given by

$$\beta = \frac{4\pi k}{\lambda} \tag{1.1}$$

where λ is the wavelength of the incident radiation, k is a propagation factor (with real and imaginary parts), and ß is the absorption coefficient (8).

By tuning to wavelengths where a layer in a multilayered sample absorbs, depth profiling of the layered sample can be performed. At wavelengths where the layer strongly absorbs, the light is attenuated in the sample layer. If this layer is positioned close to the detector, the signal response will be sharp and rapid. For a more weakly absorbed wavelength, less light energy is deposited in the layer and a corresponding delay in the signal response is noted.

Photothermal methods use heat conduction as the main source of thermal and spectroscopic information from the sample. The technique uses the modulation of the excitation beam to apply a transient heating source to the sample. This time dependent heating causes a dynamic temperature response in the material, which is characteristic of the properties of the substance and is also a function of the initial deposition of the heat in the sample (8).

Thermal waves are critically damped, which means that they are attenuated as they propagate through a material; therefore, thermal waves originating deeper in the sample will be more strongly attenuated and take longer to reach surface (9). By varying the modulation frequency of the heating source, the depth of interaction of the thermal waves can be controlled. The modulation frequency, ω, is dependent upon the thermal diffusion length, μ, for the sample. The latter is defined as the distance at which the thermal wave is attenuated to 1/e of its peak amplitude, and is given by the following relationship

$$\mu = \left(\frac{\alpha}{\pi\omega}\right)^{\frac{1}{2}} \tag{1.2}$$

where α is the thermal diffusivity. By adjusting the modulation frequency, the thermal diffusion length will be altered and this will permit depth profiling of the sample. The use of a high modulation frequency will result in the profiling of the surface layers (eg. a modulation frequency of 1 MHz will profile 3 μm of a typical metal), and a lower frequency will probe the layers in the bulk in addition to the surface layers (eg. for a 1 Hz modulation frequency, a sample region located 3 mm from the surface will be sampled for the same metal sample) (10). Photothermal techniques allow for the nondestructive determination of the properties of surface and subsurface layers as well as the distribution of materials in the sample (2, 3, 11, 12). These techniques have been used to study the depth dependence of optical (13-16) or thermal properties (17-19) of thin samples in a wide variety of applications.

1.2.1 Different Modes of Detection for Photothermal Techniques

The variation in the temperature profile within a sample can be detected by several methods. Fig. 1.1 illustrates some of the different detection methods available (20). The mode of detection best suited to determine the temperature profile is dependent upon the geometry of the sample and the properties of the material under investigation.

Infrared radiometry (21) or infrared emission involve the excitation of the sample by electromagnetic radiation and the detection of the infrared radiation either absorbed or emitted by the sample. This radiation is detected by an infrared detector, such as a

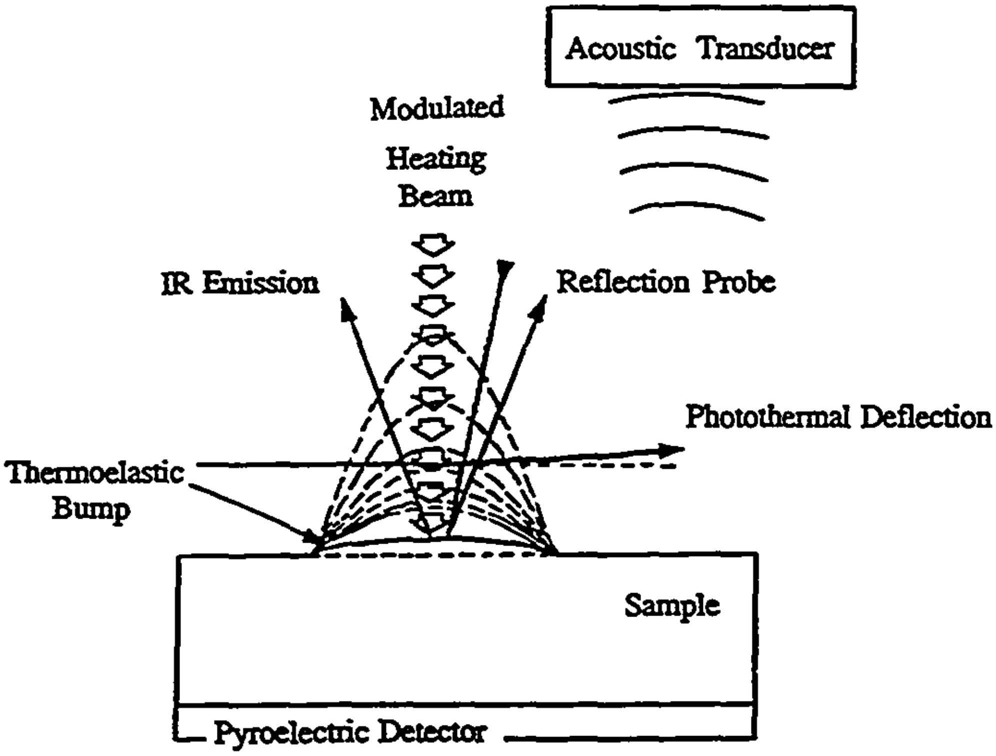

Figure 1.1: Schematic diagram showing several photothermal detection methods.

Golay or pyroelectric detector. Infrared emission detection involves positioning the detector away from the sample. The backscattered radiation off the surface of the sample allows for the depth probing of surface features via a surface temperature (assuming the sample is optically opaque). The transmission method permits depth profile detection primarily via the rear surface temperature. The disadvantage of this method is that samples with low emissivity can exhibit reduced signal sensitivity. Furthermore, the equipment is expensive.

Thermal transmission can also be measured by using a pyroelectric sensor which is thermally connected to the opposite side of the sample to that irradiated by the exciting source. The change in the temperature is detected as a change in polarization of the pyroelectric detector which is proportional to the temperature change. This polarization change is measured as a current or voltage (1, 5, 12, 22). One disadvantage of this method is that it requires an efficient thermal contact between the transducer and the sample. The presence of this interface can result in thermal reflections which can be difficult to model theoretically.

Infrared radiometry has been used to examine film thickness, adhesion, and delamination of composites (23). The technique of time-resolved infrared radiometry has been used to examine microstructure; defects in metals, semiconductors, and ceramics; and coatings. The surface is monitored as a function of time during and after the application of the heating pulse. The variations that occur in the heat flow profile are related to the sample structure (24-26).

An alternative method of detection involves a modulated heating beam striking the surface of the sample, which will change the surface temperature. This heating may result in small variations in the surface reflectivity. These changes are detected by a probe beam which is aligned collinearly with the pump or heating beam, and which is deflected due to the temperature induced reflectivity variations. This technique of photothermal reflectance is only suitable for surfaces with high reflectivity, such as semiconductors; therefore, not all samples are appropriate (1, 5, 27-30).

When the sample surface is heated strongly, a deformation or buckling of the surface is possible. This is referred to as a thermoelastic deformation. A probe beam passing collinearly relative to the pump beam will then be deflected due to the deformation on the surface. This will lead to a spatial variation of the returning probe beam which will provide information about the bulk elastic properties of the material (5, 28, 29). Photoacoustic (PA) detection also involves the modulation of a heating beam incident on a sample, which is sealed in a gas-tight chamber. The gas in the cell is transparent to the incident radiation, and serves as a coupling medium. The thin layer of gas adjacent to the sample surface expands and contracts in response to the heating of the sample causing pressure waves. These waves propagate to the microphone, which acts as the detector, converting the signal to a voltage. The acoustic waves are not significantly attenuated in the frequency range (0.1-20 kHz), and can travel for a longer distance than the thermal waves (1, 31-33).

The main limitation of this method is that it requires the sample to be contained in a cell, in order to trap the propagating acoustic waves. This allows for the accommodation of a limited variety of sizes and shapes of samples. Furthermore, while the microphone detector has a high sensitivity, its response bandwidth is small (2 KHz as compared with 10 KHz for mirage effect spectroscopy), and this limits the degree of depth profiling which can be performed. The main advantage of the PA technique is that spectra can be obtained on a variety of materials existing in different forms, such as solid, semi-solid, crystalline materials, and powders. Only the absorbed light is converted to sound, and produces a signal (34, 35). Photoacoustic spectroscopy has been used to image surface properties (36) and subsurface defects (37-39).

The methods outlined above generally require an experimental arrangement in which the detector is coupled to the sample, or there is contact of the probe beam on the sample surface. However, the optimal arrangement for non-destructive analysis is having the transducer removed from the sample. This arrangement would enable *in situ* analyses and samples which are difficult to access to be examined. Photothermal deflection spectroscopy is applicable to these kinds of measurements and has an additional advantage in that it can be used in both gases and liquids.

1.3 PHOTOTHERMAL DEFLECTION OR "MIRAGE EFFECT" SPECTROSCOPY

A mirage is an optical illusion. They are common in deserts, where conditions are optimal for the intense radiation from the sun to be dissipated from the earth into the air. This results in a fluctuation in the refractive index of the air distributed above the earth's surface. Refracted rays passing through these layers in which the refractive index varies causes distant objects to appear closer to the observer than they are in reality. "Mirage effect" spectroscopy is based on this phenomenon, where a probe ray passing through a volume above the sample surface, in which a refractive index change has been induced, will be deflected.

The technique of mirage effect (ME) or photothermal deflection spectroscopy (PDS) (40-46) of all of the photothermal techniques, provides an optical depth profiling technique which is well adapted to the study of solid/fluid interfaces, and to phenomena occurring in the vicinity of these interfaces. In 1980, Boccarra *et al* described a technique which monitored thermal gradients near a heated sample surface. Boccarra found that the magnitude of the probe beam deflection could be directly related to the absorption coefficient of the material being examined (40). For example, a short impulse of defined wavelength directed at the sample surface, will be attenuated by optical absorbers in the sample, producing a heat flux source in the material which is dependent upon the depth of these absorbers (4).

The temperature profile being created in the fluid medium above the sample surface by irradiation is determined by the material's optical absorption and thermal diffusion properties. As the sample surface is heated by an irradiated pulse, this temperature gradient in the fluid produces a change in the index of refraction of the medium above the sample. A laser probe beam aligned parallel with the surface, will be deflected in this region of altered refractive index. The deflection can be shown to be proportional, in the case of one dimensional heat conduction, to the gradient temperature profile produced in the fluid medium above the sample surface, and is sensitive to small variations in temperature.

The fluid phase may be either a gas or a liquid, provided that the medium is sufficiently optically transparent at the probe wavelength. Because, the mirage effect's time and/or frequency dependence is determined by the heat flux profile in the sample (induced by the absorption of light), this dependence is governed more strongly by the presence of true molecular absorption than reflectance measurements, which record the intensity of the reflected beam. Therefore, the mirage signal, being of photothermal origin, generally will be less affected by the presence of extraneous light scattering from the sample, and subsurface refractive index gradients than reflectance based techniques (31). However, this breaks down in heavily scattering matrices, where light scattering processes dominate the depth dependence of the light deposition profile in the sample (47, 48).

The popular orientations for photothermal deflection spectroscopy are that of the transverse deflection and normal deflection. Fig. 1.2 illustrates these geometries. The following two expressions describe the two deflection angles

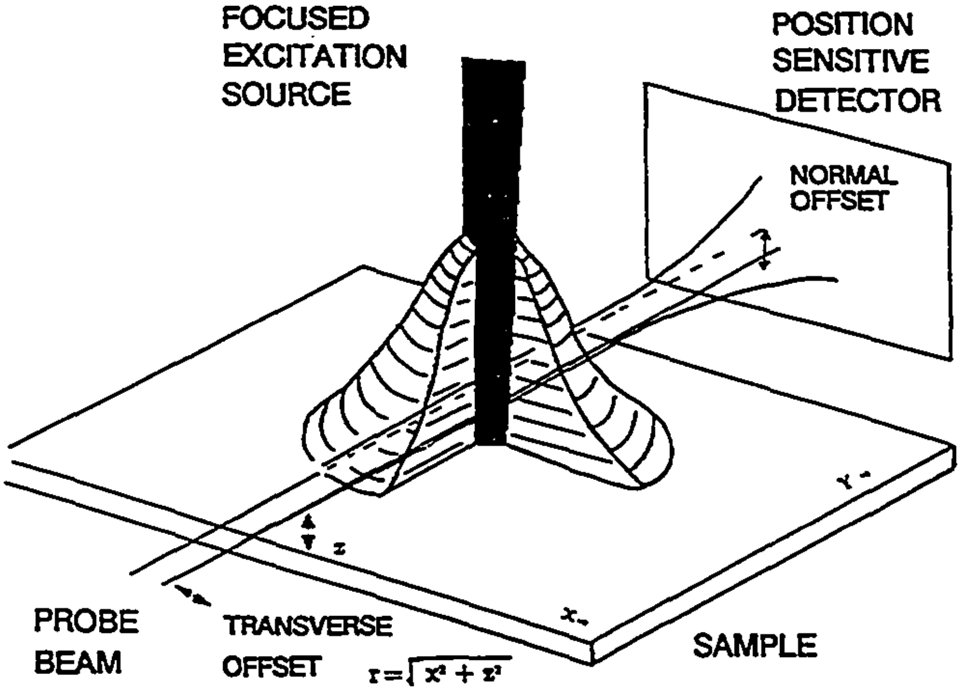

Figure 1.2: Schematic diagram of the mirage effect showing both the normal and the transverse beam deflection components.

$$\theta_n = -\frac{1}{n}\cdot\frac{dn}{dT}\cdot\frac{d\bar{T}}{dz} \tag{1.3}$$

$$\theta_t = \frac{1}{n}\cdot\frac{dn}{dT}\cdot\frac{d\bar{T}}{dx} \tag{1.4}$$

where z is the normal direction of the probe beam offset and x is the transverse direction (8). For the transverse deflection, the probe beam lies offset and perpendicular to the original probe beam path. The deflection occurs parallel to the sample surface and allows differences in the spatial heating profile due to anisotropy in the sample (such as in the detection of vertical cracks) to be monitored (49-51).

In order to perform depth profiling of absorbers located in a sample, the probe beam must lie in the normal configuration, which means that the deflection will occur perpendicular to the sample surface. For our experiments, depth profiling of the sample is performed; therefore, the normal orientation is used. The heating beam has broad dimensions, greater than the depth of the features to be profiled, and the probe beam is tightly focused; this ensures one-dimensional heat conduction, and that contributions from the transverse effect are minimised (52).

Depth profiling of subsurface layers of the sample is achieved by monitoring the time or frequency dependence of the probe beam deflection signal (8, 31). The time dependence of the transient response of the probe beam deflection will be affected by the depth of the heat flux source. This depth dependence is caused by differences in the transit time for heat conduction from the buried subsurface absorbers to the offset position of the probe beam above the sample surface. The signal is dominated by an absorbing layer located closer to the sample surface since the thermal conduction times are short. An absorber distributed more deeply in the sample will have a delayed response time.

Mirage effect spectroscopy has been used in past work for a variety of applications in thin film technology, including the examination of thin surface coatings (53), the detection of subsurface thermal features in opaque materials (51, 54), the detection of optical absorption in homogeneous thin films (55-60), absorption losses in thin films and optical coatings (56, 61), and the measurement of film thickness (62, 63). The mirage effect has also been used in the examination of delamination, defects and cracks in polymer materials (64-67), and subsurface features (51, 68). The analysis of semiconductor surfaces is very popular using photothermal techniques (69, 70). The mirage effect can also be used to determine the thermal diffusivity of solids (71-75).

1.4 OPTICAL DEPTH PROFILING USING PHOTOTHERMAL SPECTROSCOPY

Few spectroscopic techniques are capable of resolving the optical absorption spectra of samples both *in situ* and in a non-destructive manner. An added advantage is that these absorption spectra may be obtained as a function of subsurface depth. Of all the photothermal methods, the mirage effect is probably the best suited for the study of liquid/solid interfaces. Many solvents absorb strongly in the MID-IR so that infrared photothermal radiometry is not adaptable for measurements *in situ*. Gas microphone photoacoustic spectrometry is not expected to perform well in interfacial (solid/liquid) measurements. This is because heat transfer from the heated solid to the liquid may occur efficiently, but there is a relatively poor matching in acoustic impedance at the interface between the liquid and the gas phase necessary for detection. The limited modulation bandwidth of the gas microphone technique also limits the depth resolution in the layers studied. Piezoelectric photoacoustic detection is usually narrowband, and suffers from the problem of multiple acoustic reflections off cell walls and other obstructions, resulting in a signal which is dependent on geometry and not readily theoretically interpretable (76). Methods such as photopyroelectric effect spectrometry (77) have been used for optical absorptivity profiling (4, 14, 15) but they must place a calorimetric sensor below the surface, away from the solid/liquid interface.

Examining the optical absorption of the chromophores in the sample will lead to information about the absorbing layer's position as well as the thickness. Multilayered samples are used in a wide range of applications and have been investigated using different techniques, including mirage effect spectroscopy. Photoacoustic spectroscopy has been used to examine and depth profile chromophores in multilayered samples (9, 11, 13, 16, 78, 79) as well as monitoring the distribution of chromophores in time (80-82). Biological samples have also been studied using photoacoustic spectroscopy (80, 83-86) and photothermal deflection spectroscopy (87, 88).

Recent techniques such as confocal microscopy (89, 90) and coherent Raman effect imaging (91) are able to recover the depth dependent optical images of materials, while the use of optical waveguides (92) appears to be promising in obtaining depth sensitive infrared and Raman signals in adjacent phases exhibiting variable indices of refraction. Confocal microscopy has been shown to be capable of non-destructively recovering depth dependent images of materials. However, the confocal microscopic technique as well as reflectance spectrometry are sensitive to local gradients of refractive index of a material, and the image quality may degrade dramatically in the presence of small to moderate amounts of light scattering. The depth dependence of confocal microscopy images may be strongly influenced by refractive index gradients and also depth dependent Fresnel losses (93). Confocal microscopy has been used to monitor the distribution of chemical species throughout a fibre, for dye and colour-fastness, which will affect the durability of the fibre (90, 94).

Methods based on classical reflectance spectroscopy (95) are highly susceptible to scattering and to optical artifacts which may be caused by local gradients in the index of refraction of the sample, resulting from inhomogeneities in the material. Attenuated total reflectance infrared spectroscopy (ATR-IR) is capable of achieving depth resolved infrared spectral information through variation of the launch angle of an infrared beam into a planar waveguide, which is placed in contact with the sample surface (96-98). The beam is internally reflected at the contact surface with a portion of the light penetrating into the sample, and undergoing an attenuation, dependent on the optical properties of the material. The method requires an intimate mechanical contact of the waveguide to the sample surface. For samples with textured surfaces or for fibres, it may be difficult to obtain a reproducible contact with the waveguide (3). Also, the method is sensitive to the same optical artifacts that plague reflectance methods. The depth range which is accessible by the ATR-IR method, is usually restricted to within about 10 μm below the sample surface. It is well suited for studying materials with low absorption coefficient (96, 99).

In summary the mirage effect method shows unique advantages and has been used as a powerful tool for the non-destructive evaluation of solids, and for the evaluation of the thermo-physical and optical properties of a variety of substrates.

1.5 AIMS AND OBJECTIVES

In the processing of thin films, laminates and coatings, a variety of processes exist which produce spatial and depth dependent inhomogeneities. Gradients of optical absorption may result from many different processes, including the diffusion of penetrants through a thin film sample (80, 81, 100), the degradation of paint films caused by weathering (3), extrusion processes used to form laminates of varying composition, and in biological samples, where the morphology of plant or human tissues varies (86, 101-103).

The purpose of this thesis was to apply the technique of mirage effect spectroscopy to depth profile optical absorbers embedded in a thin film matrix. The development and optimization of the instrumentation was discussed in chapter 2 of this thesis to allow for semi-quantitative depth profiling. In chapter 4, the mirage effect technique was used to examine multilayered composites exhibiting either a continuously varying optical absorbance or discrete optical absorbing layers in the surrounding matrix. The samples provide insight into the capabilities of the technique and the resolution obtained in samples containing more than one absorbing layer. Chapter 3 outlines the one dimensional heat conduction theoretical model developed to understand and explain the experimental results. Good semi-quantitative agreement was found between experiment and the theoretical simulations from the model. Inverse problem theory was applied to the experimental results to further quantify the depth profiling capabilities of the mirage effect technique. This is discussed in chapter 5. Finally, in chapter 6, the dynamic diffusion of chemical species into an ion exchange polymer membrane material was examined using mirage effect spectroscopy. The corresponding diffusion model accommodating the ion exchange properties of the membrane was developed. The experimental results were also explained in this chapter. By this investigation, the application of mirage effect spectroscopy to real samples, as well as an understanding of the results obtained from the theoretical analysis of the experimental data is demonstrated.

REFERENCES

---

1. R.A. Palmer, *Physical Methods of Chemistry*, 2nd Ed., Vol. VIII, Chapter 2, B.W. Rossiter, and R.C. Baetzold, Ed., (John Wiley & Sons, Inc., Toronto, 1993) 61-108.
2. F.A. McDonald, and G.C. Wetsel, Jr., *Physical Acoustics: Principles and Methods*, Vol. XVIII, W.P. Mason, Ed. (Academic Press, Inc., Toronto, 1988) 167-277.
3. R.M. Miller, SPIE **1320** Infrared Technology and Applications, 50 (1990).
4. J.F. Power, Appl. Spectrosc. **45**, 1240 (1991).
5. J.F. Power, Prog. Anal. Spectrosc. **12**, 453 (1989).
6. H. Coufal, Fresenius J. Anal. Chem. **337**, 835 (1990).
7. A.C. Tam, SPIE **1435** Optical Methods for Ultrasensitive Detection and Analysis: Techniques and Applications, 114 (1991).
8. J.W. Maclachlan. *Contrast Mechanisms in Thermal Wave Imaging*. PhD. thesis U.M.I. (1987).
9. G.F. Kirkbright, M. Liezers, R.M. Miller, and Y. Sugitani, Analyst **109**, 465 (1984).
10. J.W. Maclachlan, L.C. Aamodt, and J.C. Murphy, Ceram. Eng. Sci. Proc. **9**, 1181 (1988).

11. G.F. Kirkbright, R.M. Miller, D.E.M. Spillane, and I.P. Vickery, J. Phys. Colloq. (France) 44, C6-243 (1983).

12. R.L. Thomas, L.D. Favro, and P.K. Kuo, Can. J. Phys. **64**, 1234 (1986).

13. G.F. Kirkbright, R.M. Miller, D.E.M. Spillane, and Y. Sugitani, Anal. Chem. **56**, 2043 (1984).

14. J.F. Power, Appl. Spectrosc. **45**, 1252 (1991).

15. M.C. Prystay and J.F. Power, Polym. Engin. Sci. **33**, 43 (1993).

16. A. Harata and T. Sawada, *Photoacoustic and Photothermal Phenomena II*, J.C. Murphy, J.W. Maclachlan-Spicer, L. Aamodt, and B.S.H. Royce, Ed. (Springer-Verlag Berlin, Heidelberg, 1990) 64-66.

17. P. Cielo, J. Appl. Phys. **56**, 230 (1984).

18. G. Busse, B. Rief and P. Eyerer, Polym. Compos. **8**, 283 (1987).

19. C. Glorieux, J. Fivez, and J. Thoen, J. Appl. Phys. **73**, 684 (1993).

20. J.C. Murphy, and G.C. Wetsel, Mater. Eval. **44**, 1224 (1986).

21. S.O. Kanstad, and P.-E. Nordal, Can. J. Phys. **64**, 1155 (1986).

22. H. Coufal, Polym. Eng. Sci. **31**, 92 (1991).

23. A.C. Tam, W.P. Leung, and H. Sontag, *Photoacoustic and Photothermal Phenomena III*, D. Bicanic (Springer-Verlag Berlin, Heidelberg, 1992), 672-678.

24. J.W. Maclachlan Spicer, L.C. Aamodt, and J.C. Murphy, Johns Hopkins APL Tech. Dig. **II**, 175 (1990).

25. L.C. Aamodt, J.W. Maclachlan Spicer, and J.C. Murphy, J. Appl. Phys. **68**, 6087 (1990).

26. J.W. Maclachlan Spicer, W.D. Kerns, L.C. Aamodt, and J.C. Murphy, J. Nondestr. Eval. **8**, 107 (1989).

27. A. Mandelis, *Photoacoustic, Photothermal and Photochemical Processes at Surfaces and in Thin Films*, P. Hess, Ed. (Springer-Verlag Berlin, Heidelberg, 1989), 211-250.

28. A. Mandelis, and J.F. Power, Appl. Opt. **27**, 3397 (1988).

29. J.P. Power, and A. Mandelis, Appl. Opt. **27**, 3408 (1988).

30. A. Rosencwaig, J. Opsal, and D.L. Willenborg, Appl. Phys. Lett. **46**, 1013 (1985).

31. A. Rosencwaig, *Photoacoustics and Photoacoustic Spectroscopy*, (John Wiley & Sons, New York, 1980) Chapt. 3, 9, 21.

32. H. Coufal, and J.F. McClelland, J. Mol. Struct. **173**, 129 (1988).

33. J.F. McClelland, S. Luo, R.W. Jones, and L.M. Seaverson, *Photoacoustic and Photothermal Phenomena III*, D. Bicanic (Springer-Verlag Berlin, Heidelberg, 1992), 113-124.

34. J.F. McClelland, Anal. Chem. **55**, 89A (1983).

35. A. Rosencwaig, and A. Gersho, J. Appl. Phys. **47**, 64 (1976).

36. R.O. Carter III, M.C. Paputa Peck, and D.R. Bauer, Polym. Degrad. Stab. **23**, 121 (1989).

37. R.M. Miller, SPIE **685** Infrared Technology XII, 16 (1986).

38. G.F. Kirkbright, R.M. Miller, and A. Rzadkiewicz, J. Phys. E: Sci. Instrum. **17**, 526 (1984).

39. G. Busse, and A. Rosencwaig, Appl. Phys. Lett. **36**, 815 (1980).

40. A.C. Boccara, D. Fournier, and J. Badoz, Appl. Phys. Lett. **36**, 130 (1980).

41. M.J. Smith, and R.A. Palmer, Appl. Spectrosc. **41**, 1106 (1987).

42. W.B. Jackson, N.M. Amer, A.C. Boccara and D. Fournier, Appl. Opt. **20**, 1333 (1981).

43. L.C. Aamodt, and J.C. Murphy, J. Appl. Phys. **52**, 4903 (1981).

44. R.A. Palmer, and M.J. Smith, Can. J. Phys. **64**, 1086 (1986).

45. L.C. Aamodt and J.C. Murphy, J. Appl. Phys. **54**, 581 (1983).

46. J.C. Murphy, and L.C. Aamodt, J. Appl. Phys. **51**, 4580 (1980).

47. P. Helander, I. Lundström, and D. McQueen, J. Appl. Phys. **51**, 3841 (1980).

48. J.-P. Monchalin, L. Bertrand, G. Rousset, and F. Lepoutre, J. Appl. Phys. **56**, 190 (1984).

49. L.J. Inglehart, *Photoacoustic and Photothermal Phenomena II*, J.C. Murphy, J.W. Maclachlan-Spicer, L. Aamodt, and B.S.H. Royce, Ed. (Springer-Verlag Berlin, Heidelberg, 1990), 40-43.

50. F. A. McDonald, G.C. Wetsel, Jr., and G.E. Jamieson, Can. J. Phys. **64**, 1265 (1986).

51. G.C. Wetsel, Jr., J.B. Spicer, J.W. Maclachlan, and J.C. Murphy, IEEE Ultrasonics Symposium 443 (1985).

52. M.A. Schweitzer, and J.F. Power, Appl. Spectrosc. **48**, 1054 (1994).

53. T. Hata, T. Hatsuda, and T. Komatsu, Jap. J. of Appl. Phys. **24**, 1463 (1985).

54. J.C. Murphy, L.C. Aamodt, and J.W. Maclachlan, SPIE **897** Scanning Microscopy Technology and Applications, 135 (1988).

55. H. Xuebo, C. Wenbin, and C. Jian, SPIE **1230** International Conference on Optoelectronic Science and Engineering, 379 (1990).

56. M. Commandré, P. Roche, G. Albrand, and E. Pelletier, SPIE **1270** Optical Thin Films and Applications, 82 (1990).

57. M. Montecchi, E. Masetti, and G. Emiliani, SPIE **1270** Optical Thin Films and Applications, 116 (1990).

58. H. Xue-bo, and C. Wen-bin, *Photoacoustic and Photothermal Phenomena II*, J.C. Murphy, J.W. Maclachlan-Spicer, L. Aamodt, and B.S.H. Royce, Ed. (Springer-Verlag Berlin, Heidelberg, 1990), 133-137.

59. Y.-X. Nie, and L. Bertrand, J. Appl. Phys. **65**, 438 (1989).

60. Z.L. Wu, P.K. Kuo, Lanhua Wei, S.L. Gu, and R.L. Thomas, Thin Solid Films **236**, 191 (1993).

61. M. Commandré, L. Bertrand, G. Albrand, and E. Pelletier, SPIE **805**, Optical Components and Systems 128 (1987).

62. H. Fujimori, Y. Asakura, K. Suzuki, and S. Uchida, Jap. J. of Appl. Phys. **26**, 1759 (1987).

63. A. Rosencwaig, J. Opsal, and D.L. Willenborg, J. Phys. Colloq. (France) **44**, C6-483 (1983).

64. L.J. Inglehart, F. Lepoutre, and F. Charbonnier, J. Appl. Phys. **59**, 234 (1986).

65. K.R. Grice, L.J. Inglehart, L.D. Favro, P.K. Kuo, and R.L. Thomas, J. Phys. Colloq. (France) **44**, C6-519 (1983).

66. K.R. Grice, L.J. Inglehart, L.D. Favro, P.K. Kuo, and R.L. Thomas, J. Appl. Phys. **54**, 6245 (1983).

67. J.A. Sell, M.S. Meyer, and J.V. Mantese, *Photoacoustic and Photothermal Phenomena II*, J.C. Murphy, J.W. Maclachlan-Spicer, L. Aamodt, and B.S.H. Royce, Ed. (Springer-Verlag Berlin, Heidelberg, 1990), 191-193.

68. F. Lepoutre, D. Fournier, and A.C. Boccara, J. Appl. Phys. **57**, 1009 (1985).

69. D. Fournier, C. Boccara, A. Skumanich, and N.M. Amer, J. Appl. Phys. **59**, 787 (1986).

70. U. Zammit, F. Gasparrini, M. Marinelli, R. Pizzoferrato, F. Scudieri, and S. Martellucci, J. Appl. Phys. **69**, 2577 (1991).

71. I. Hatta, Int. J. Thermophys. **II**, 293 (1990).

72. P.K. Kuo, M.J. Lin, C.B. Reyes, L.D. Favro, R.L. Thomas, D.S. Kim, S.-Y. Zhang, L.J. Inglehart, D. Fournier, A.C. Boccara, and N. Yacoubi, Can. J. Phys. **64**, 1165 (1986).

73. M. Bertolotti, L. Fabbri, C. Sibilia, A. Ferrari, N. Sparvieri, G. Suber, J. Phys. D: Appl. Phys. **21**, S14 (1988).

74. G. Suber, M. Bertolotti, C. Sibilia, and A. Ferrari, Appl. Opt. **27**, 1807 (1988).

75. J.P. Roger, F. Lepoutre, D. Fournier, and A.C. Boccara, Thin Solid Films **155**, 165 (1987).

76. A.C. Tam, and C.K.N. Patel, Appl. Opt. **18**, 3348 (1979).

77. H. Coufal, IEEE Trans. Ultrasonics, Ferroelectrics, and Frequency Control, **UFFC-33**, 507 (1986).

78. G.F. Kirkbright, and R.M. Miller, Analyst **107**, 798 (1982).

79. R.M. Dittmar, J.L. Chao, and A. Palmer, *Photoacoustic and Photothermal Phenomena III*, D. Bicanic, Ed. (Springer-Verlag, Berlin, 1992) 492.

80. R.M. Miller, Spectrochim. Acta **43B**, 687 (1988).

81. R.M. Miller; G.R. Surtees, and C.T. Tye, Analyst **114**, 547 (1989).

82. R.M. Miller, G.R. Surtees, C.T. Tye, and I.P. Vickery, Can. J. Phys. **64**, 1146 (1986).

83. K. Veeranjaneyulu, and V.S.R. Das, J. Phys. Colloq. (France) **44**, C6-367 (1983).

84. J.W. Nery, O. Pessoa, Jr., and H. Vargas; F. de A.M. Reis; A.C. Gabrielli; L.C.M. Miranda; C.A. Vinha, Analyst **112**, 1487 (1987).

85. P. Poulet, and J. Chambron, J. Phys. Colloq. (France) **44**, C6-413 (1983).

86. G.F. Kirkbright, R.M. Miller, D.E.M. Spillane, and I.P. Vickery, Analyst **109**, 1443 (1984).

87. L. Lorrain, M. Havaux, A. Tessier, and R.M. Leblanc, Photochem. Photobiol. **51**, 491 (1990).

88. M. Havaux, L. Lorrain, and R.M. Leblanc, FEBS Lett. **250**, 395 (1989).

89. A. Boyde, Science **230**, 1270 (1985).

90. M.C. Moss, J.A. Veiro, S. Singleton, D.P. Gregory, J.J. Birmingham, C.L. Jones, P.G. Cummins, D. Cummins, R.M. Miller, R.C. Sheppard, V.C. Howard, and N. Bhaskar, Analyst **118**, 1 (1993).

91. M.D. Duncan, J. Reintjes, and T. Manuccia, Opt. Lett. 350 (1982).

92. D.R. Miller and P.W. Bohn, Anal. Chem. **60**, 407 (1988).

93. D.K. Hamilton, T. Wilson, and C.J.R. Sheppard, Opt. Lett. **6**, 625 (1981).

94. R.M. Miller, J.J. Birmingham, P.G. Cummins, and S. Singleton, SPIE **1439** International Conference on Scientific Optical Imaging, 66 (1990).

95. K. Ohta, and H. Ishida, Appl. Opt. **29**, 1952 (1990).

96. R.T. Holm, and E.D. Palik, Appl. Opt. **17**, 394 (1978).

97. G. Müller, K. Abraham, and M. Schaldach, Appl. Opt. **20**, 1182 (1981).

98. J.A. Gardella Jr., G.L. Grobe III, W.L. Hopson, and E. M. Eyring, Anal. Chem. **56**, 1169 (1984).

99. K. Ohta, and R. Iwamoto, Anal. Chem. **57**, 2491 (1985).

100. R.A. Palmer, and R.M. Dittmar, Thin Solid Films **223**, 31 (1993).

101. M. Havaux, L. Lorrain, and R.M. Leblanc, Photosynth. Res. **24**, 63 (1990).

102. F.H. Long, and T.F. Deutsch, IEEE J. Quantum Elec. **QE-23**, 1821 (1987).

103. S.A. Prahl, I.A. Vitkin, U. Bruggemann, B.C. Wilson, and R.R. Anderson, Phys. Med. Biol. **37**, 1203 (1992).

CHAPTER 2 MIRAGE EFFECT INSTRUMENTATION

2.1 INTRODUCTION

In this chapter, the instrumentation for mirage effect spectroscopy, which was designed and constructed, is described. Several experimental parameters were modified and adjusted, in order to provide quantitative measurements of depth profiles in samples.

2.2 EXPERIMENTAL APPARATUS

Experimental measurements were performed using the instrumentation diagrammed in Figure 2.1. The excitation source used was either an argon-ion laser (Coherent Innova 70-6) using the 514 nm excitation wavelength, or a tunable dye laser (Coherent Model 599-01) pumped by the argon ion laser in the all-line mode. The dye laser was operated using Rhodamine 6G as the gain medium, yielding irradiation wavelengths between 570 nm and 640 nm. The wavelength of excitation source chosen is dependent upon the optical absorption characteristics of the layer to be profiled in the sample. The excitation beam was intensity modulated using an acousto-optic modulator (AOM) (Isomet 201E). This intensity is time varied by the drive signals which are supplied by the synthesizer to the AOM video input. This is described in more detail in section 2.3. For this system the drive waveform is an amplitude modulated frequency sweep (1).

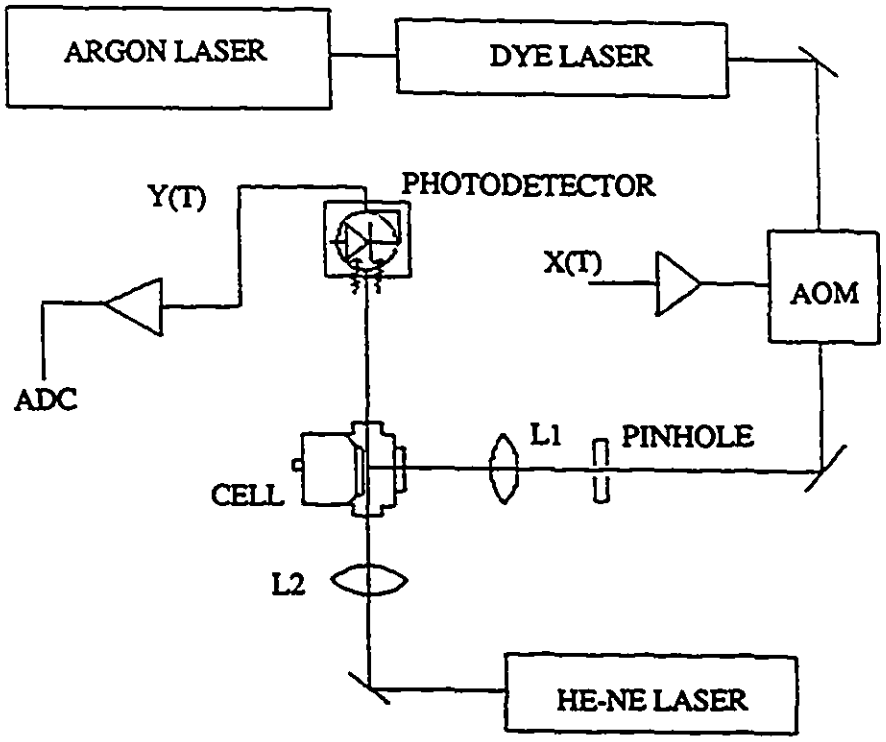

Figure 2.1: Schematic of the 'mirage effect' instrumental apparatus used in these experiments.

The first order output of the modulator, with ca. 50% depth of modulation (peak to peak), was isolated using an aperture and then directed through lenses, which permits the adjustment of the pump beam radius. This dimension determines the type of heat conduction present in the system. In order to maintain one-dimensional heat conduction, the beam diameter striking the sample surface must be much greater than the sum of the offset distance of the helium-neon probe beam from the sample surface plus the maximum absorber depth to be resolved in the sample. A pump beam of 2 mm is sufficient to ensure one dimensional heat conduction at all observation times in the experiment. Neutral density filters were used for adjustment of the light intensity from the first order, to compensate for power variations occurring with wavelength over the gain bandwidth of the dye laser.

A helium-neon laser (He-Ne) (Uniphase 1125P) with an output wavelength of 632.8 nm, was used as the probe beam. The beam was directed through a lens with a focal length of 10 cm, and intersected perpendicular to the pump beam at the centre of the irradiated spot. The deflection was recorded by a position sensor, which detects the integrated probe beam light intensity over the light sensitive area of the detector. The position sensor consisted of a photodiode (Hamamatsu detector s1226-44Kb), fitted with a pinhole of diameter 200 μm, the latter being concentrically positioned in front of the photodiode. The output from the photodetector was coupled to a wide bandwidth preamplifier (Tektronix AM502) equipped with an input bandpass filter (6db/octave rolloff). The filter's low pass frequency cutoff was set near the maximum frequency in the sweep, while the filter's high pass frequency cutoff was set slightly above the minimum resolvable frequency, in most cases this being 0.1 Hz. The preamplifier output was digitized by a 12-bit analog-to-digital converter (Labmaster DT 5712, Scientific Solutions, Solon, OH) and logged onto an IBM compatible PC-XT computer. The drive waveform, x(t), and response waveform, y(t), are processed according to the algorithm derived in the next section, in order to obtain the impulse and frequency response information of the system.

2.3 SIGNAL PROCESSING

For all photothermal systems, a modulated source is employed, either as discrete pulses or the modulation of a continuous wave source. The response of the system to this modulated source is measured. There are two general methods used to recover the frequency response or the time domain response from a linear photothermal system. The frequency domain method uses a narrow-band harmonic measurement with the system excited at a steady-state. The response of the system is obtained one frequency at a time using a lock-in amplifier and the system must reach harmonic steady state before a measurement reading can be taken. This approach is advantageous because it can resolve weak signals in the presence of high levels of noise and multifrequency interferences; however, very long times are required to obtain high resolution. The sinusoidal signal from the photothermal system is characterized by a magnitude and a phase. The phase lag is related to the location of the buried layers relative to the surface (2). The pulsed-excitation method, on the other hand, involves heating the system with a short pulse and recovering the time domain response of the system. The impulse response of a system provides a relationship between a subsurface feature located within the sample and the thermal transit time required for the heat conduction to reach the surface of the sample (3). The thermal transit time is given by

$$\tau = l_o^2/4\alpha \tag{2.1}$$

where l_o is the offset distance. The transit time will increase if the material is a good insulator, the thermal diffusivity, α, is small, or if the distance, l_o, is large. The advantage of this method is that the data acquisition time is short and high resolution is obtained. The dynamic range is lower than that obtained for the frequency domain technique; however, the main disadvantage of this system is that the high power delivered by the short pulse can result in non-linearities in the system or the destruction of the sample. The theory and experiment associated with the frequency domain and the time domain processes have been developed and investigated by several workers (1-9).

In this work, the method for recovering the impulse response of the system utilises amplitude and phase modulation (AM-PM) wide-band time-delay domain photothermal spectrometry (10, 11). The AM-PM technique uses a waveform with a flatband power spectrum, but whose phase varies quadratically. This produces a tailored frequency sweep, which delivers all of the Fourier components of the excitation to the photothermal system out of phase at t=0. The end result of this is the reduction of the peak power of the excitation, and the improvement in the measurement dynamic range (10). Impulse and frequency response information are simultaneously available at high resolution by the method, and can be recovered using standard correlation and spectral analysis procedures (12). The basics of this method will be outlined, with more details being given in references (10) and (11).

The excitation input waveform, x(t), can be written as a cosinusoidal function

$$X(t) = A(t) \cos [\phi_i(t)] \tag{2.2}$$

where A(t) is the amplitude modulation and $\phi_i(t)$ is the instantaneous phase of the input and is defined as

$$\phi_i(t) = (\pi S)t^2 + \omega_c t + \phi_0 \tag{2.3}$$

where ϕ_0 is the initial phase, ω_c is the average carrier frequency and the modulation occurs by a time dependent or instantaneous frequency, f_i, given by St/2, where S is the sweep rate (6, 10).

The requirement of this excitation waveform is for its power spectrum to be flat over the response bandwidth of the system. The Wiener-Khinchin relationships outlined in Table 2.1 (see end of Chapter 2, page 49), show the interrelationship between the correlation functions and their corresponding frequency domain functions the spectral density functions. The autocorrelation function is a measure of the similarity between the input signal, x(t), and a time-delayed version of itself, $x(t+\tau)$.

$$Rxx(\tau) = \lim_{T \to \infty} \frac{1}{T} \int_0^T x(t)x(t+\tau)dt \tag{2.4}$$

where T is the record length and where it is assumed that x(t)=0 for t<0. The cross correlation function is a measure of the similarity between the input waveform and a time-delayed output, $y(t+\tau)$.

$$Rxy(\tau) = \lim_{T \to \infty} \frac{1}{T} \int_0^T x(t)y(t+\tau)dt \tag{2.5}$$

The corresponding relationships in the frequency domain are given by the spectral density functions, which are defined over both the negative and positive frequencies. For display purposes, the one-sided spectral density functions are used. The relationship between them can be illustrated, for example, by the autospectrum,

$$Gxx(\omega) = 2Sxx(\omega) = 2\left[\int_{-\infty}^{\infty} Rxx(\tau)e^{-j\omega\tau}d\tau\right]\cdot U(\omega) \qquad (2.6)$$

where Gxx(ω) is the one-sided function and Sxx(ω), the double-sided function. The quantity, Sxx(ω), provides a measure of the distribution of the signal energy as a function of frequency. The cross spectrum gives the frequency interrelationship between the input signal x(t) and the output signal y(t).

$$Sxy(\omega) = \int_{-\infty}^{\infty} Rxy(\tau)e^{-j\omega\tau}d\tau \qquad (2.7)$$

The input waveform, x(t), is related to its frequency domain quantity, X(ω), by a Fourier transform equation

$$X(\omega) = \int_{-\infty}^{\infty} e^{-j\omega t}x(t)dt \qquad (2.8)$$

The power spectrum, or input autospectral density function, is given by

$$Sxx(\omega) = \lim_{T\to\infty} \frac{1}{T} < X^{*}(\omega,T)\ X(\omega,T) > \qquad (2.9)$$

where * indicates the complex conjugate. This power spectrum is defined, by Bendat and Piersol, as the average square modulus of the magnitude of X(ω) (12).

$$Sxx(\omega) = \lim_{T\to\infty} \frac{1}{T} < |X(\omega,T)|^2 > \qquad (2.10)$$

Figure 2.2 illustrates the one-sided spectrum, Gxx(ω). (The double-sided functions are used in the actual FFT calculations.) No phase information is provided by this function; therefore, by varying the frequency dependence of the phase of X(ω), an optimum excitation waveform can be generated. By applying the Fourier components of the frequency spectrum out of phase, a low peak power of excitation will result, and the response of the system will be more likely to behave in a linear fashion. The AM-PM wide-band time domain signal is attenuated to zero in the regions outside the desired frequency bandwidth limits. Figure 2.3 shows the resulting x(t) waveform, for a 100 Hz frequency sweep.

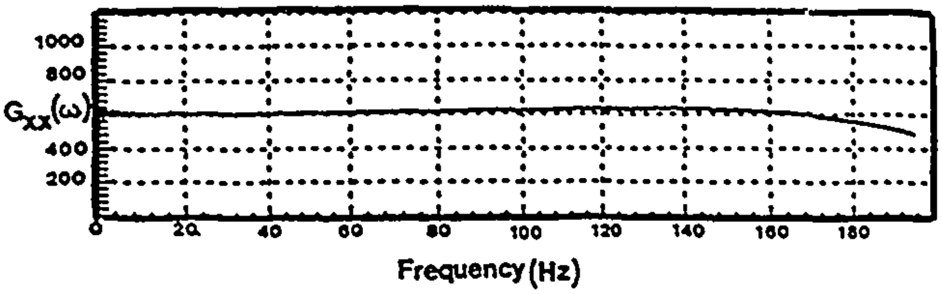

Figure 2.2: A typical power spectrum, Gxx(ω), of an input waveform.

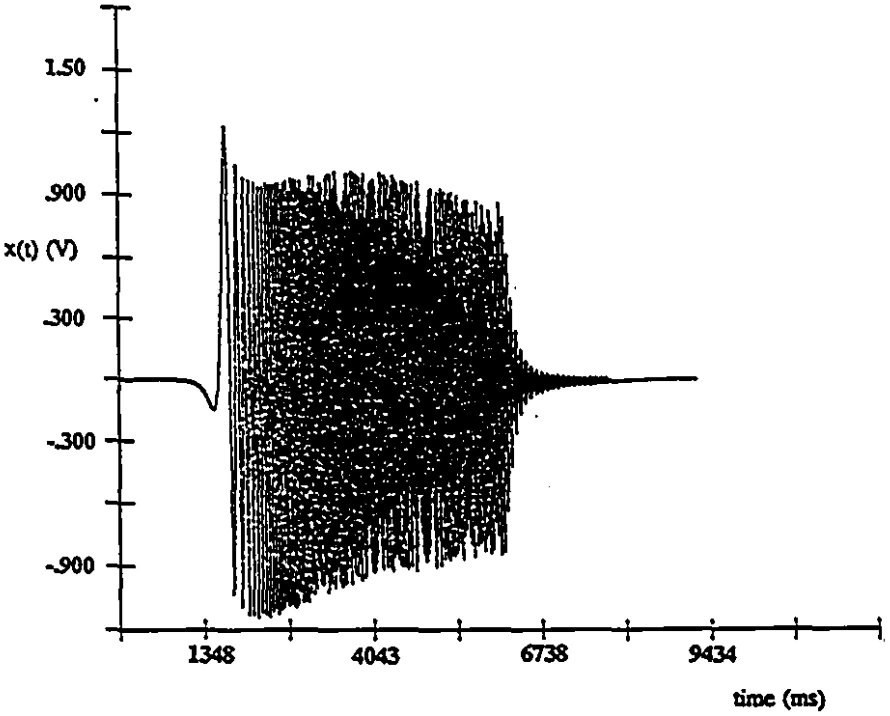

Figure 2.3: Input waveform, x(t), for a 100 Hz. frequency sweep.

The frequency response function, H(ω), is given by the following relationship

$$H(\omega) = \frac{Sxy(\omega)}{Sxx(\omega)} \tag{2.11}$$

By obtaining a power spectrum which is flat over the response bandwidth of the photothermal system, Sxx(ω) = 1. This results in

$$H(\omega) = Sxy(\omega) \tag{2.12}$$

providing a direct relationship of the transfer function of the system to the frequency relationship between the input signal x(t) and the output signal y(t) (1, 10-12).

The frequency response, or transfer function H(ω), is related to the time-domain or impulse response, h(t), by the following Fourier transform relationships:

$$\begin{aligned} H(\omega) &= \int_{-\infty}^{+\infty} h(t)e^{-j\omega t}dt \\ h(t) &= \frac{1}{2\pi}\int_{-\infty}^{+\infty} H(\omega)e^{j\omega t}d\omega \end{aligned} \tag{2.13}$$

(12). The response of the system which is of interest is h(t) (note that h(t)=0 for t<0); therefore solving for the frequency response function, H(ω) in the frequency domain followed by the impulse response, h(t), in the time domain, is required. The response of the photothermal system to a well-defined input waveform can be deduced from the relationships outlined in Table 2.1. However, this is only true for systems behaving in a linear fashion.

Implementation of this signal processing system is described in detail in reference (11). The input waveform, x(t), was computed from theory and converted to a binary data file which was read out of an IBM compatible PC-XT computer data port under software control. This signal is then sent out through an 8-bit digital to analog converter (Analog Devices AD 551). The output from the digital to analog converter is filtered through a variable bandpass filter (Kronhite model 3700), set to the range of frequencies being swept. The studies reported in this thesis use relatively slow frequency sweep ranges from 0.1-50 Hz to 0.1-250 Hz, depending upon the sample thickness studied. Except were indicated, measurements were made with a sweep bandwidth of 0.1-100 Hz. The drive signals are then supplied to the acousto-optic modulator. The x(t) and y(t) channels were swept successively and up to 25 replicate sweeps were averaged in the time domain to improve the signal-to-noise ratio. Since the frequency sweep is time averaged (e.g. over multiple sweeps), the signal-to-noise in x(t) and y(t) increases as $1/\sqrt{N}$, where N is the number of averages. This relationship is true because x(t) and y(t) are deterministic signals (10). Fig. 2.4 illustrates a typical output waveform, y(t), generated from a surface absorber. Data acquisition and data processing routines were written using the ASYST software package (copyright Adaptable Laboratory Software Inc.). The computers communicate with each other through the parallel I/O ports, in order to transmit the timing and waveform information.

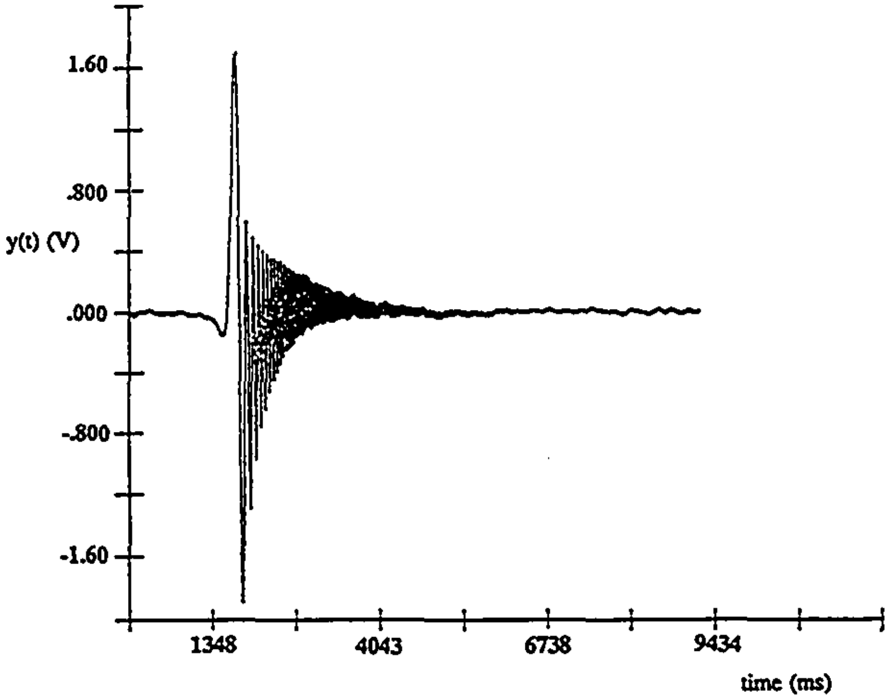

Figure 2.4: A typical output waveform, y(t), generated for a surface absorber.

2.4 CHARACTERIZATION OF THE INSTRUMENTAL RESPONSE

2.4.1 Frequency Response Limitations in the Apparatus

A plot of the photothermal impulse response observed for the mirage effect at a solid/water interface is shown in Fig. 2.5(a). This mirage effect signal is typical of the response observed for a system which is critically damped and where the slowly varying components of the response strongly dominate the signal (13). The measured photothermal transients are coupled through high pass filters, which are present at the input of the measurement amplifier. These high pass filters cause a loss of low frequency information.

The bandpass filter also attenuates the photothermal response on the high frequency end of the scale, affecting the signals measured at short times after excitation (14). This attenuation usually has a smaller effect on the impulse response data recorded in liquids, because the impulse response is relatively slow and dominated by the low frequency information. However, the information encoded in the signal rarely exceeds the band limit on the high frequency end of the measurement.

It is essential though, to compensate for the losses of low frequency information in these measurements if the impulse response is to be quantitatively interpreted. While most of the losses are created by the input filters on the preamplifier, there may also be frequency response variations produced by the photodetector, and these may affect magnitude and phase. The measurement system consists of the photodetector, preamplifier input filters, and the preamplifier stage, in cascade. The impulse response for the detection system is given by:

$$h_c(t) = h_{pd}(t) * h_{pf}(t) * h_{pa}(t) \tag{2.14}$$

where * denotes a convolution operation, and where $h_{pd}(t)$, $h_{pf}(t)$,and $h_{pa}(t)$ correspond to the impulse response of the photodetector, the preamplifier input filter and the preamplifier, respectively. Therefore, the measurement describes the distortion effects produced in all stages of the detection system.

A practical approach for compensating for non-uniformities in the instrument frequency response effect is correction by convolution (15); one measures the impulse response of the detection system in the absence of the mirage effect, and then by digital aperiodic convolution (16), corrects the theoretical impulse response prior to comparison with experiment. The configuration diagrammed in Fig. 2.6 was used to record the instrumental impulse response in the absence of the mirage effect. The He-Ne probe laser was sent directly through the acousto-optic modulator, where the latter is driven by an AM/PM type wideband frequency sweep. The modulator's first order beam strikes the photodetector, where the time dependence of the drive waveform, is recorded to obtain $h_c(t)$. The implementation of the measurement is outlined in Fig. 2.5(a) - Fig. 2.5(d). The experimental impulse response measured for the mirage effect in water with a sample having a surface absorber is given in Fig. 2.5(a), while the impulse response measured for the instrument's detection system is given in Fig. 2.5(c), under the same conditions of bandwidth. The detection system responds rapidly at early times, but settles relatively slowly over the long times, as a consequence of the low frequency filtering effect. The theoretical profile corresponding to this geometry is given in Fig. 2.5(b), and the effect of its aperiodic convolution with the detection system's impulse response is given in Fig. 2.5(d). This correction accounts for a major source of non-ideality in the experiments and should be included in photothermal impulse response measurements, since the latter will be strongly dominated by this low frequency information. In order to quantify results generated by the theory, $h_c(t)$ should be measured and the appropriate correction applied to the theory, for all bandwidth settings used in the experiment.

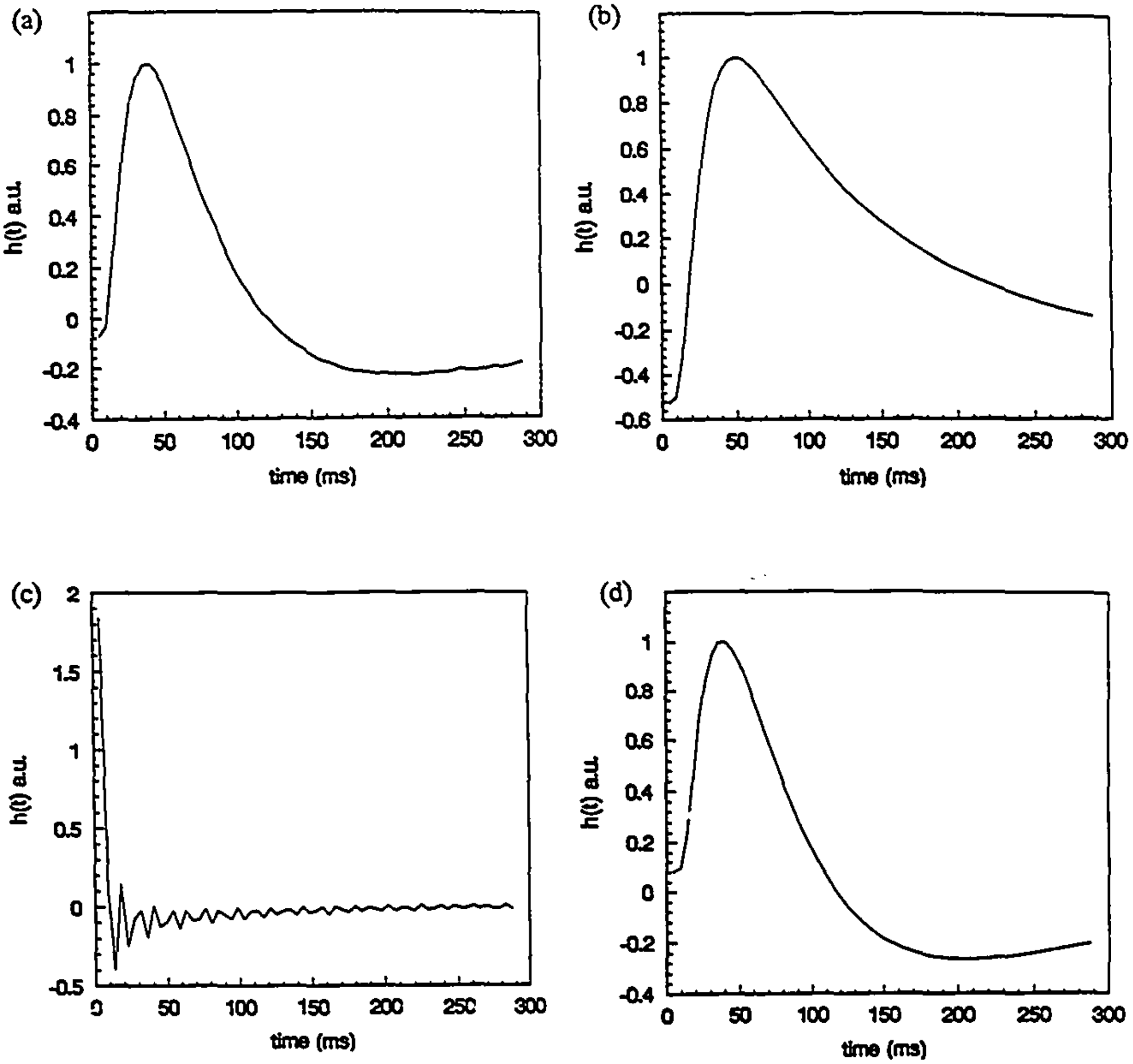

Figure 2.5:

(a) Experimental mirage effect impulse response trace observed at the solid/water interface. Sample is depicted in Fig. 2(a), inspected with a probe beam offset of 205 microns.

(b) Theoretical photothermal impulse response for this sample with variables determined from the experimental conditions.

(c) Impulse response of the electronic detection system measured in the absence of the photothermal signal. All other sweep conditions as in 2.4(a).

(d) Theoretical impulse response recovered by aperiodic convolution of the electrical impulse response of 2.4(c) with the theory of 2.4(b).

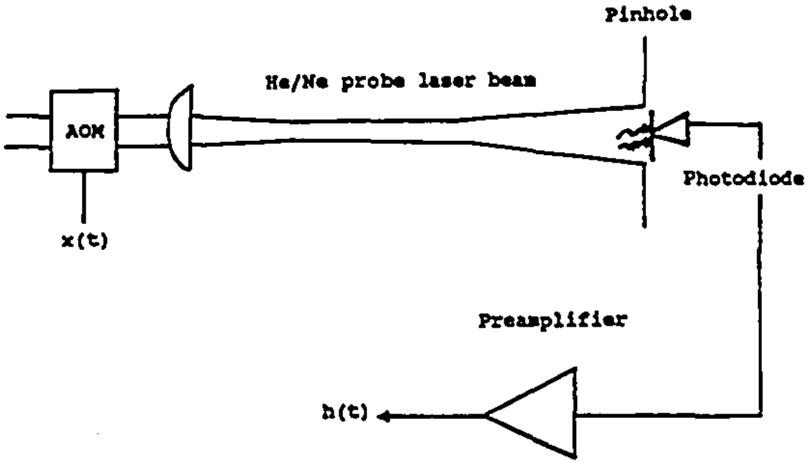

Figure 2.6: Schematic of the instrumental apparatus used for the measurement of the instrumental transfer function of the system.

2.4.2 Linearity of the Photothermal Response

Response linearity is a critical assumption of both the theory and the application of the wideband excitation used for measurement of the impulse response. In mirage spectrometry, two sources of non-linearity are expected: thermal non-linearity and thermo-optical non-linearity. Thermal non-linearity occurs if the sample is heated sufficiently that its thermal properties (conductivity or diffusivity) change with temperature. Since small temperature changes are usually associated with most mirage measurements, thermal non-linearity is not expected. Thermo-optical non-linearity will occur when the beam deflection becomes excessively large. This happens at a lower level of excitation power than the thermal non-linearity mechanism, and will depend on the detection geometry and thermo-optical properties of the solvent, especially the change in the refractive index with temperature. A key assumption of the theoretical model outlined in Chapter 3 is that the mirage signals are small. This assumption may become invalid, even if the measured beam deflection is of the order of a few millidegrees.

The probe beam passing parallel to the sample surface is deflected normal to the surface, as depicted in Fig. 2.7. Large scale movements of the probe beam across the detector/pinhole aperture of the photodiode will result in a non-linear variation of optical intensity with displacement. This effect may be easily simulated by computing h(t) from theory, and computing the projected displacement of the probe beam from its deflected position in the detector plane. The probe beam centre is displaced by a distance $L\tan\theta_N(t)$, and the perturbation of the beam profile is described by

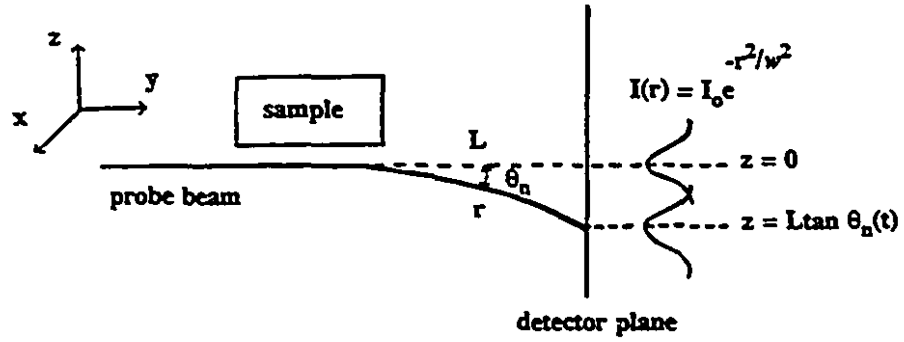

Figure 2.7: Depiction of the geometry used in calculating the probe beam deflection normal to the surface of the sample.

$$h(t) = I(x,z,t) = I_0 e^{\left[\frac{-x^2}{\omega_p^2}\right]} \cdot e^{\left[\frac{-(z-L\tan\theta_N(t))^2}{\omega_p^2}\right]} \tag{2.15}$$

where ω_p is the spot radius of the He-Ne beam at the detector. For very small signal levels, there is almost no variation of the theoretical time dependence of h(t) across the beam profile except for sign differences due to symmetry about the propagation axis. As the deflection becomes larger, the signal I(x,z,t), begins to depend on the offset position, z, of the sensor in the detection plane. The signal becomes sensitive to the non-linearity with distance along the beam profile in the regions far from the inflection points. Fig. 2.8 shows the experimental dependence of the mirage effect impulse response for the variation of the pinhole position, as it is translated across the beam profile in the detection plane. In the vicinity of the inflection points (regions 2 and 6, in Fig. 2.8), linearity is better preserved because the probe beam intensity, I(x,z,t), varies almost linearly with spatial position. To within a good approximation, a small change in the beam centre

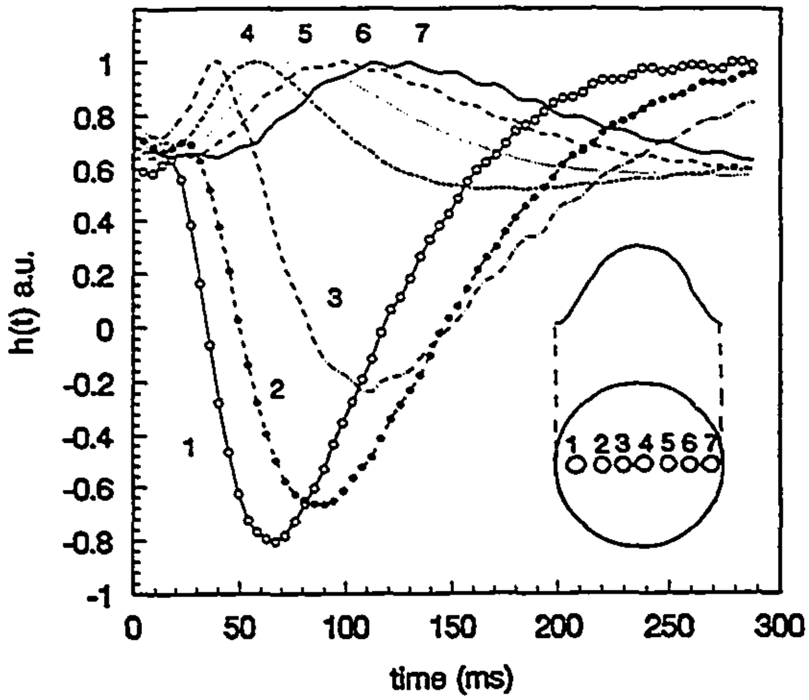

Figure 2.8: Effect of pinhole translation in the detector plane on the time dependence of the experimental impulse response; pinhole is translated in a direction perpendicular to the axis of propagation of the probe beam.

position gives rise to a proportional variation of the beam intensity, and the latter quantity is then linearly proportional to the angular deflection. The measured mirage effect impulse response becomes in this region, $h(t) = I(x,z,t) \propto \theta_N(t)$. Any departure from this approximation can be observed in the experiment by changing the excitation power and observing any changes in the time dependence of the impulse response. In the linear region (low power), this time dependence becomes invariant with the excitation power. Since thermo-optical non-linearity arises due to non-linear variations in $I(x,z,t)$ with respect to z, in the neighbourhood of the detector offset position, it may also be induced by imperfections in the quality of the Gaussian beam profile, due to scattering, reflections, or optical interference. Therefore, a probe beam with good modal quality with respect to the He-Ne beam, is essential to ensure interpretable, linear signals.

2.4.3 Calibration of the Probe Beam Offset Position

An important variable in the mirage effect measurement is the offset position, z, of the probe beam in the fluid medium above the surface of the sample. This distance determines the maximum response speed available from the mirage effect measurement. For minimum risetime, the offset should be made as small as possible, although practically this distance is of the order of 100 μm (8). The close alignment of the probe beam requires a surface with good flatness, and/or high uniformity. A means of calibrating the offset distance with good precision is also essential.

As is seen in Fig. 2.9, He-Ne beam offset differences greatly affect the signal

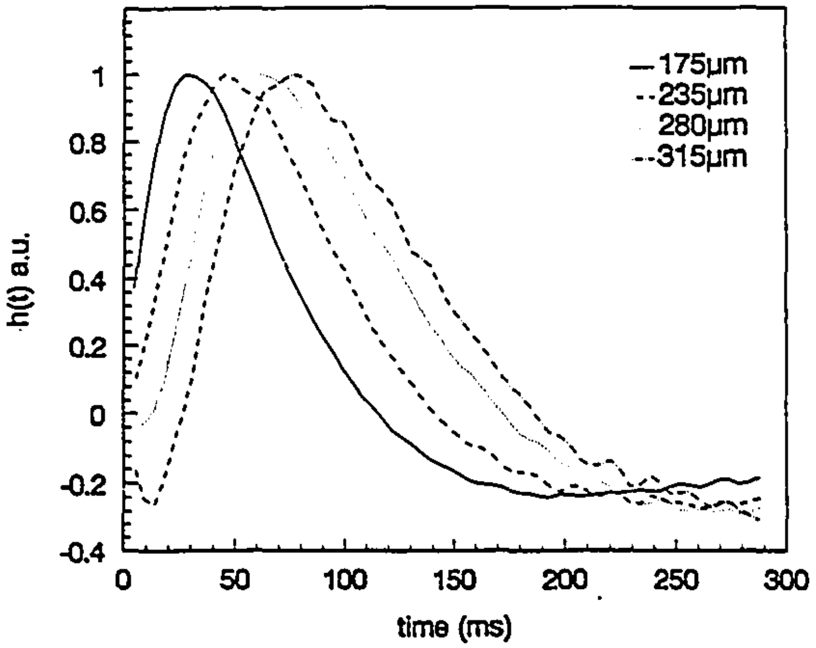

Figure 2.9: Effect of probe beam offset, z, above the surface of the sample, on the experimentally measured impulse response.

response. As the beam is translated further away from the sample surface, there is an associated delay in the position of the impulse response peak, due to the increased thermal transit time from the sample surface. The mirage effect technique is topographically dependent (17); therefore, the need for an 'internal standardization' of the beam height for each sample, on every alignment, is essential.

In the literature, there has been little mention of procedures for determining the precise value of the probe beam offset above the sample surface in the normal plane. A possible technique which may be used is that of striking the sample surface with the probe beam and measuring the angular deflection of the reflected beam. This procedure requires the sample surface to be reflective, and highly opaque and suffers from the disadvantage that the measurement is no longer non-contact. Other workers estimate the offset by aligning the probe beam so that its waist position coincides with the mirage. The probe beam is passed over the sample so that the edge of the probe beam grazes the edges of the sample on the sides incident and opposite to the incoming probe. From a knowledge of the beam waist radius, the offset at the centre of the beam may be inferred (18). In practice this alignment technique is not sufficiently precise for quantitative measurements unless the surface is extremely flat over its entire length. Local topographic variations may limit the closest approach of the probe beam, and small angular tilts in the probe beam relative to the sample surface may not be compensated. If the probe beam grazes the sample surface over a sufficient interaction length, optical interference fringes may be superimposed on the beam profile due to grazing incidence reflections which may occur. These latter effects will introduce artifacts into the measured photothermal deflection signal.

To determine an accurate value of the He-Ne offset, a black absorber was placed on the sample surface, to provide index marks for aligning the probe beam. These marks were made on the surface using water insoluble black ink from a marker pen. The thickness of the ink film is of the order of a few microns, which is very small compared to the minimum offset of 150 μm from the probe beam. Alternatively, one may use sputtering or ion deposition to place small opaque and thermally thin islands of metal on the surface.

The diameter of the black index spots was on the order of 1-2 mm. The spots were chosen to be thermally thin and optically opaque, so that they behave as nearly ideal planar surface sources. Since the diffusivity of the fluid above the surface of the sample is a known quantity, the offset distance of the probe beam, z, may be calibrated by fitting the experimental impulse response of the irradiated black spots to the theoretical mirage effect response calculated with the theory outlined in Chapter 3. In the studies reported below, the fluid medium used was either water with a thermal diffusivity of 1.4×10^{-7} m^2/s, or paraffin oil with an assumed thermal diffusivity of 0.9×10^{-7} m^2/s (19). Some studies were run with air as the detection medium, but the observed photothermal signals were weak in this case, due to poor thermal matching between the solid and gas phases. An air medium, with its large thermal diffusivity, has the effect of reducing the thermal length between the sample surface and the probe beam offset position. This, in turn is equivalent to physically pulling the probe beam closer to the surface, increasing the surface domination of the mirage signals. These results are discussed in further detail in Chapters 3 and 4.

Two index spots are placed on the sample surface along the axis of the probe beam. Once the offset for the black absorbers is obtained, the region in between the absorbers can be depth profiled. The offset for this sample is determined from the known offset measured at the index spots. Should a small tilt be present in the sample surface relative to the probe beam, the tilt angles can be easily determined in the two normal planes from the offset measurements made at each of the spots. The location of the probe beam offset above the region to be depth profiled can be determined to a precision of ca. 5 μm.

Fig. 2.10 illustrates the offset calibration procedure. The first trace (205 μm offset) and second trace (230 μm offset) in Fig. 2.10 give the response from index spots bracketing a sample region of 5.90 mm wide. The delayed trace gives the impulse response obtained from the depth profiled region, lying between the two spots. The offset distance determined for each index position is labelled on the graph. The buried optical feature to be recovered in this example is a thin planar absorber, located at a distance of

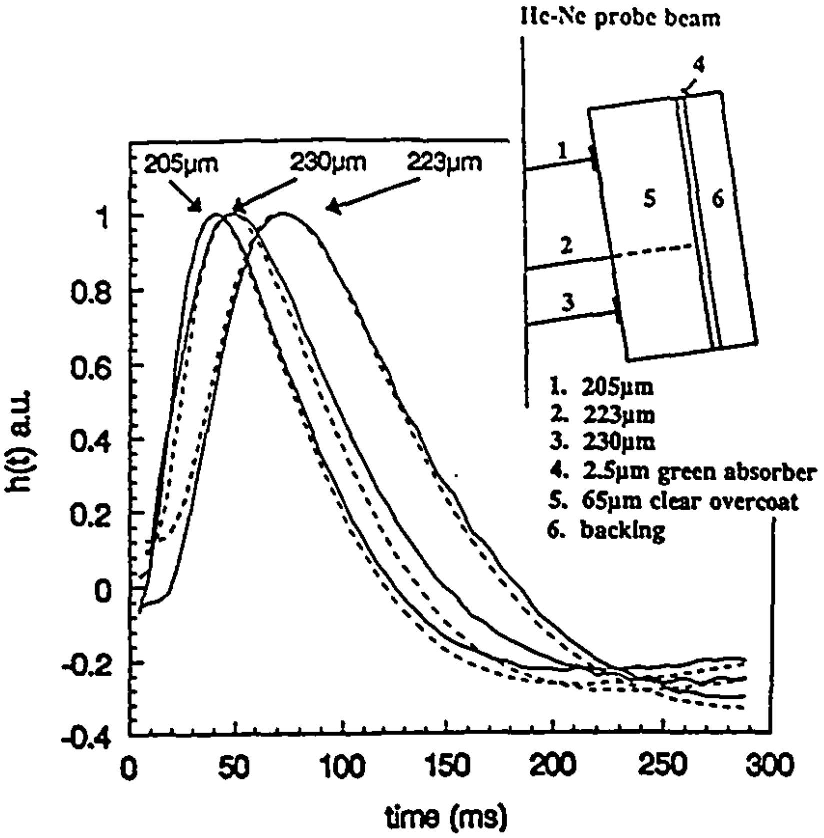

Figure 2.10: Impulse response traces for index spots located at 0.0 mm (205 μm offset), an index spot located 5.90 mm away along the sample surface (230 μm offset) and a sample region located between the index spots (223 μm offset). The corresponding theoretical predictions are also indicated (dotted lines).

65 μm below the surface. Once the probe beam offsets are determined at the two surface spots bracketing the region to be profiled, a simple triangulation method gives an offset of 223 μm for the depth profile position. The theoretical impulse response was computed assuming that the sample had a diffusivity of 1.0 x 10^{-7} m^2/s, and the experimentally measured thickness. As seen in the figure (Fig. 2.10), a good agreement was obtained between the experimental (continuous line) and theoretical (dotted line) traces for the depth profiled region, and for the index spots.

Another factor affecting calibration of the offset position above the sample is the width of the probe beam at the position where it intersects the mirage. As seen in Fig. 2.1, the He-Ne probe beam passes through a lens, and is directed parallel to the sample surface. The lens focuses the probe beam to a measured waist diameter of 80 μm, which is aligned to coincide with the position of the mirage. In the waist region, the optical phase fronts are theoretically flat (20), so that the rays propagate nearly parallel to the sample surface, as assumed in the theoretical derivation. However, the 80 μm diameter of the ray bundle is not negligibly small compared with the offset distance, which varies, on average, from 150 to 350 μm.

In the detection plane, the deflected probe beam is sampled near its inflection points, to ensure the best linearity. However, the probe beam diameter in the waist region is not negligibly small compared to the offset, z. Therefore, in the detection plane, different regions of the probe beam show a variation in the experimental impulse response, which is generally consistent with local variation in z in the mirage region probed (from which the measured deflection originates).

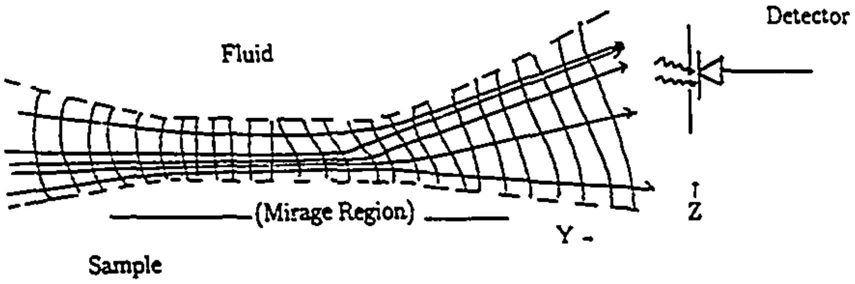

Figure 2.11: Approximate ray trace showing perturbations of the laser probe beam phase fronts and phase front normals when a probe beam of finite dimensions intersects the mirage.

Figure 2.11 gives a simple ray diagram explaining the phenomenon. By using the inflection point located on the side of the probe beam furthest from the sample surface, any relative variations in the local value of z at the greater distance are reduced. The effect of finite beam radius can only be exactly described using diffraction theory (21). However, the results obtained indicate that even without diffraction theory, the forward model derived in Chapter 3 gives a nearly quantitative descriptions of the mirage effect impulse response. Chapter 5 describes the diffraction theory, which was solved in order to improve the accuracy necessary for solving the inverse problem theory. This is also discussed in Chapter 5.

One dimensional heat conduction should be maintained to obtain quantitative agreement between theory and experiment for the most general case. This is easily maintained by keeping the excitation beam diameter large compared with the offset distance from the surface, and the depth of the features probed. This can be easily verified in practice; the time dependence of the impulse response becomes independent of the spot size when the beam diameter is of the order of three to four times the thickness of the features probed. For these studies, the 2 mm pump beam diameter was sufficient to ensure one dimensional heat conduction.

2.5 CONCLUSION

By using the improvements in the instrumental procedure, as outlined in this chapter, quantitative experimental measurements of characteristic and well-defined samples can be made, and thus extended to other samples. In order to interpret these results, a theoretical model must be developed to explain and understand the photothermal deflection phenomenon. The next chapter outlines the forward model derived for one-dimensional heat conduction.

REFERENCES

1. A. Mandelis, *Photoacoustic, Photothermal and Photochemical Processes at Surfaces and in Thin Films*, P. Hess, Ed. (Springer-Verlag Berlin, Heidelberg, 1989), 211-250.
2. J.F. Power, Prog. Anal. Spectrosc. 12, 453 (1989).
3. J.F. Power, Appl. Spectrosc. 45, 1240 (1991).
4. A. Mandelis, and J.F. Power, Appl. Opt. 27, 3397 (1988).
5. J.P. Power, and A. Mandelis, Appl. Opt. 27, 3408 (1988).
6. A. Mandelis, Rev. Sci. Instrum. 57, 617 (1986).
7. A. Mandelis, IEEE Trans. Ultrasonics, Ferroelectrics, and Frequency Control UFFC-33, 590 (1986).

8. A. Mandelis, L.M.L. Borm, and J. Tiessinga, Rev. Sci. Instrum. **57**, 622 (1986).

9. A. Mandelis, L.M.L. Borm, and J. Tiessinga, Rev. Sci. Instrum. **57**, 630 (1986).

10. J.F. Power, Rev. Sci. Instrum. **61**, 90 (1990).

11. J.F. Power, Rev. Sci. Instrum. **61**, 101 (1990).

12. J.S. Bendat, and A.G. Piersol, *Engineering Applications of Correlation and Spectral Analysis* (John Wiley & Sons, Toronto, 1980) Chapt. 1-5.

13. A. Rosencwaig, *Photoacoustics and Photoacoustic Spectroscopy*, (John Wiley & Sons, Toronto, 1980) Chapt. 3, 9, 21.

14. J.F. Power, Appl. Spectrosc. **45**, 1252 (1991).

15. H. Coufal, and P. Hefferle, Can. J. Phys. **64**, 1200 (1986).

16. S. Stearns, *Digital Signal Analysis* (Hayden Book Company, Rochelle Park, New Jersey, 1975).

17. R.L. Thomas, L.D. Favro, and P.K. Kuo, Can. J. Phys. **64**, 1234 (1986).

18. M.J. Smith, and R.A. Palmer, Appl. Spectrosc. **41**, 1106 (1987).

19. J.W. Maclachlan Spicer, W.D. Kerns, L.C. Aamodt, and J.C. Murphy, J. Nondestr. Eval. **8**, 107 (1989).

20. H. Xue-bo, and C. Wen-bin, *Photoacoustic and Photothermal Phenomena II*, J.C. Murphy, J.W. Maclachlan-Spicer, L. Aamodt, and B.S.H. Royce, Ed. (Springer-Verlag, Berlin, 1990), 133-137.

21. A.L. Glazov and K.L. Muratikov, Sov. Phys. Tech. Phys. **36**, 1302 (1991).

TABLE 2.1 SIGNAL RECOVERY
WEINER-KHINCHIN RELATIONS

Spectral Density Functions

input autospectrum: $S_{xx}(\omega) = \lim_{T\to\infty} \frac{1}{T} < (X^{*}(\omega) X(\omega)) >$

output autospectrum: $S_{yy}(\omega) = \lim_{T\to\infty} \frac{1}{T} < (Y^{*}(\omega) Y(\omega)) >$

cross spectrum: $S_{xy}(\omega) = \lim_{T\to\infty} \frac{1}{T} < (X^{*}(\omega) Y(\omega)) >$

Correlation Functions

input autocorrelation function: $R_{xx}(\tau) = \frac{1}{2\pi}\left[\int_{-\infty}^{\infty} e^{2\pi jf\tau}\, S_{xx}(\omega)\, d\omega \right]$

output autocorrelation function: $R_{yy}(\tau) = \frac{1}{2\pi}\left[\int_{-\infty}^{\infty} e^{2\pi jf\tau}\, S_{yy}(\omega)\, d\omega \right]$

cross correlation function: $R_{xy}(\tau) = \frac{1}{2\pi}\left[\int_{-\infty}^{\infty} e^{2\pi jf\tau}\, S_{xy}(\omega)\, d\omega \right]$

CHAPTER 3 A THEORETICAL MODEL FOR THE INTERPRETATION OF OPTICAL DEPTH PROFILING OF THIN FILMS USING MIRAGE EFFECT SPECTROSCOPY

3.1 INTRODUCTION

In this chapter, a theory is presented which describes the detection of the mirage effect signal in a sample excited by an optical impulse. The sample's thermal properties are assumed to be homogeneous, but the optical properties vary with depth in a series of discrete layers. This theory can also be extended to apply to the case of a quasi-continuous sample. The theory yields a relatively simple analytical solution accommodating one, two and three dimensional heat conduction processes, under certain commonly used experimental conditions.

Previous work on the mirage effect has been focused on optically and thermally homogeneous samples (1-5) and on explaining the dependence of the mirage effect (ME) signal on the sample properties and experimental geometry in the frequency domain. No previous theoretical treatments of the mirage effect have been reported for the impulse measurements performed in optically inhomogeneous media. More recently, Aamodt, Murphy and Maclachlan-Spicer derived a general time domain theory describing thermal wave propagation in thermally and optically layered materials (6) although their theory was applied to detection using photothermal radiometry. This theory gave the temperature field as a superposition of characteristic layer responses and included the effect of arbitrary thermal reflections between layers. The general theory required simplifications to special cases for interpretation, and consideration of the mirage geometry for an optically inhomogeneous sample was not covered. The following theory describes a simpler approach to characterize the temperature profiles observed in materials which contain varying depth dependent absorptivity, and use the resulting theoretical expressions to calculate the mirage effect impulse response. The theory can be extended to three-dimensional cases (7).

3.2 THEORETICAL MODEL

3.2.1 Equations of Refractive Bending

The derivation of the mirage effect starts from the equation of refractive bending of a ray by a gradient of refractive index, n, in an optically inhomogeneous medium. The ray position, $\vec{r}$, varies along the direction of propagation, s, according to (8):

$$\frac{d}{ds}\left(n\,\frac{d\vec{r}}{ds}\right) = \nabla n \qquad (3.1)$$

The deflection angle, $\vec{\theta}$, in the medium, $\vec{\theta} = d\vec{r}/ds$, may be obtained by integration of this gradient along the axis of propagation:

$$\vec{\theta} = \int_s \frac{\nabla n}{n} \times ds \qquad (3.2)$$

where x indicates the vector cross product. The refractive index is temperature dependent and may be expanded in a Taylor's series in increasing powers of the change in temperature, ΔT, about the index of refraction at the ambient temperature, n_0:

$$n = n_0 + \frac{\partial n}{\partial T}\,\Delta T + \ldots \tag{3.3}$$

For small changes in temperature, only the first two terms in the expression are retained, and ∇n may be expressed as:

$$\nabla n = \left(\frac{\partial n}{\partial T}\right)\,\nabla(\Delta T) \tag{3.4}$$

Substitution into equation (3.2) gives:

$$\vec{\theta} = \int_s \frac{1}{n}\,\left(\frac{\partial n}{\partial T}\right)\,\nabla(\Delta T)\times ds \tag{3.5}$$

If temperature changes are small through the heated zone, and if the probe beam follows a nearly straight line, which is true if deflections are small, then ds ≈ dy and the beam deflection is approximated by:

$$\vec{\theta} = \frac{1}{n}\,\frac{\partial n}{\partial T}\int_0^y \nabla(\Delta T)\times \hat{j}\,dy \tag{3.6}$$

where $\hat{j}$ is the unit vector lying along the y axis direction. A diagram of the ray propagation geometry is shown in Fig. 3.1.

Finally, if the deflection medium is thermally matched to the heated sample, the probe beam may be seen to encounter an average gradient along y (9), resulting in:

$$\bar{T}(x,z) = \int_{-\infty}^{+\infty} \Delta T(x,y,z)\,dy \tag{3.7}$$

and equation (3.6) becomes:

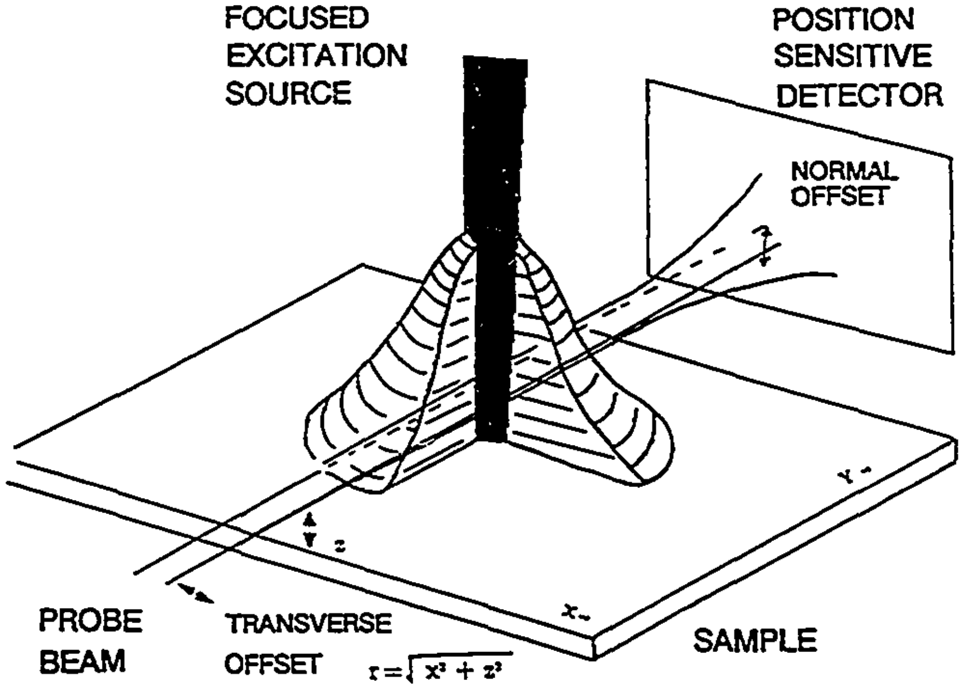

Figure 3.1: Schematic diagram of the mirage effect measurement and geometry used in these experiments.

$$\begin{aligned}\theta &= \frac{1}{n}\left(\frac{\partial n}{\partial T}\right)\nabla\bar{T}\times\hat{j} \\ &= \frac{1}{n}\left(\frac{\partial n}{\partial T}\right)\left[-\hat{i}\,\overline{\frac{\partial T}{\partial z}}+\hat{k}\,\overline{\frac{\partial T}{\partial x}}\right]\end{aligned} \tag{3.8}$$

where the unit vectors $\hat{\imath}$ and $\hat{k}$ are interpreted as axes of rotation lying in the x and z directions, respectively (2). The first term corresponds to the deflection normal to the surface,

$$\theta_n = \frac{-1}{n}\left(\frac{\partial n}{\partial T}\right)\left(\frac{\partial\bar{T}}{\partial z}\right) \tag{3.9}$$

and the second term to the transverse displacement,

$$\theta_t = \frac{1}{n}\left(\frac{\partial n}{\partial T}\right)\left(\frac{\partial\bar{T}}{\partial x}\right) \tag{3.10}$$

For depth profiling, the deflection in the normal direction is the quantity to be determined.

3.2.2 Temperature Profile Accompanying Heat Conduction in an Infinite Medium

The next step is the evaluation of the temperature profile $\Delta T(x,y,z,t)$ produced above the surface of the heated sample. The sample is assumed to be heated by a laser pulse with a TEM (0,0) intensity profile given by:

$$I(r,t) = I_0\, e^{-r^2/\omega^2}\, \delta t_p \,/\, \pi\omega^2 \tag{3.11}$$

where ω is the spot size, $r = \sqrt{x^2 + y^2}$, and δt_p is the laser pulse duration (Fig. 3.1) (10). The intensity may be considered to be approximately invariant over the pulse duration provided that δt_p is small compared to all thermal response times.

The optical profile in the sample is assumed to be composed of the contributions of N discrete layers, where each layer obeys Beer's law individually. Fig. 3.2 shows the sample geometry and the defined layer thicknesses, while Fig. 3.3 shows the form of the

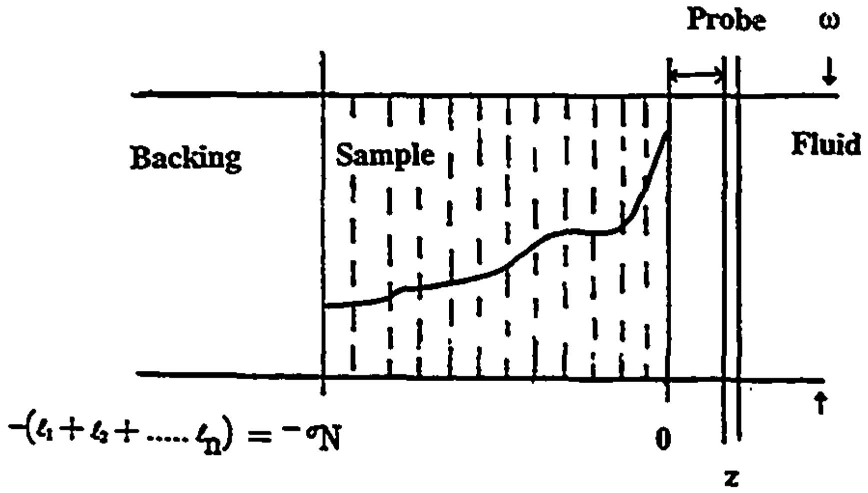

Figure 3.2: Schematic diagram of the heat flux source profile established below the surface of an optically multilayered sample, of total thickness σ_N.

heat flux profile observed in a single layer. Each layer is assumed to have its top surface at position $-\sigma_{i-1}$ and its bottom $-\sigma_i$, where the individual layer's thickness is given by l_i. The total thickness of a sample composed of N layers is given by σ_N.

The sample is considered as an assemblage of thin layers, each of arbitrary thickness, l_i, and optical absorption coefficient β_i. If the excitation beam has the form of an ideal impulse, applied at time t=0, a heat flux profile of the following dependence is generated below the sample surface in the ith layer (see Fig. 3.2 and 3.3):

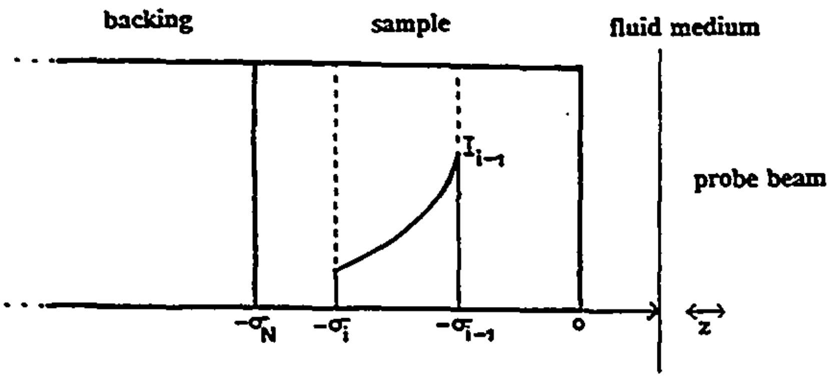

Figure 3.3: Schematic diagram showing the geometry of the heat flux term induced in the ith layer by irradiation.

$$\dot{q}_i(x,y,z,t) = \frac{\eta_i \beta_i \, I_{i-1} \, \delta t_p \, e^{-(x^2+y^2)/\omega^2}}{\pi \omega^2 \kappa_2} \cdot e^{\beta(z+\sigma_{i-1})} \cdot [U(-(z+\sigma_{i-1})) - U(-(z+\sigma_i))] \, \delta(t) \tag{3.12}$$

where U(z) is the unit step function, κ_2 is the thermal conductivity of the sample layer, $\delta(t)$ is the Dirac delta function, η_i is the non-radiative conversion efficiency for each layer, and I_{i-1} is the light intensity reaching the ith buried layer, through i-1 layers of arbitrary thickness and optical absorption coefficient:

$$I_{i-1} = I_0\, e^{-\sum^{i-1} \beta_i l_i} \tag{3.13}$$

The total heat flux profile observed in the sample consists of the summation of the individual terms of equation (3.12) for i=1 to N.

In the absence of boundary effects of thermal reflection or absorption, the temperature change in the sample is given by the convolution of the Green's function for heat conduction in an infinite medium, g(x,y,z) with the heat flux source in the sample, $q^{*}(x,y,z)$ as given in equation (3.12). This integral is expressed as:

$$\Delta T = \int_0^{t^{*}} \int \int \int_{-\infty}^{+\infty} g(x-x_0,y-y_0,z-z_0,t-t_0)\; q^{*}\,(x_0,y_0,z_0,t_0)\; dt_0\, dx_0\, dy_0\, dz_0 \tag{3.14}$$

where the Green's function for three dimensional heat conduction in an infinite medium is given by (11):

$$g(x-x_0,y-y_0,z-z_0) = (4\alpha_2/\sqrt{\pi}) \left[\frac{1}{\sqrt{4\alpha_2(t-t_0)}}\right]^3 \cdot \; e^{-[(x-x_0)^2 + (y-y_0)^2 + (z-z_0)^2]/4\alpha_2(t-t_0)} \tag{3.15}$$

where α_2 is the thermal diffusivity of the sample medium, (for the moment assumed to be matched to that of the fluid layer, $\alpha_2 = \alpha_1$), and the weighting factor A_0 will be equal to $4\alpha_2/\sqrt{\pi}$.

In a multilayered sample, the heat profile will consist of the summation of N terms of the form given by equation (3.12). The convolution operation defined by equation (3.14) is linear. Therefore, the temperature profile is recovered by the summation of the individual terms of the form of equation (3.12), and is consistent with the superposition principle (12). The temperature change in response to heating of the i^{th} layer by a source of the form given in equation (3.12) is obtained from integration of equation (3.14):

$$\Delta T(x,y,z,t)=\frac{A_0\ \partial t_p}{\pi\ \omega^2\ \kappa_2}\ (\eta_i \beta_i I_{i-1})\ (4\alpha t)^{-3/2}\ \cdot$$
$$\int_{-\sigma_i}^{-\sigma_{i-1}} e^{\beta_i(z_0+\sigma_{i-1})}\ e^{-(z-z_0)^2/4\alpha_2 t}\ dz_0\ \cdot \tag{3.16}$$
$$\int \int_{-\infty}^{\infty} e^{-[(y-y_0)^2+(x-x_0)^2]/4\alpha_2 t}\ e^{-(x_0^2+y_0^2)/\omega^2}\ dx_0\ dy_0$$

In order to solve each of the integrals in equation (3.16), a completion of the square in each variable is made in the exponential expressions. Then the final integral is solved in terms of the complementary error function, erfc(x) (13), resulting in the following two expressions:

$$\Delta T_z=e^{\beta_i(z+\sigma_{i-1})}\ e^{\beta_i^2\alpha_2 t}\ \sqrt{4\alpha_2 t}\ \cdot$$
$$\left[erfc\ \left[\ \frac{(z+\sigma_{i-1})}{\sqrt{4\alpha_2 t}}+\beta_i\sqrt{\alpha_2 t}\right]\ -erfc\ \left[\ \frac{(z+\sigma_i)}{\sqrt{4\alpha_2 t}}+\beta_i\sqrt{\alpha_2 t}\right]\right] \tag{3.17}$$

$$\Delta T_{rad}=\frac{4\pi\ \ (4\alpha_2 t\omega^2)}{\omega_c^2}\ \ e^{-(x^2+y^2)/\omega_c^2} \tag{3.18}$$

where $\omega_c^2 = (\omega^2+4\alpha_2 t)$. The quantity ω_c measures the radial distance travelled in the sample by a cylindrical thermal wave away from the initial irradiation spot of radius ω, in a given time t. It is assumed in the above derivation that the sample layer is thermally matched to the surroundings, e.g. that the heat conduction occurs into an infinite medium. The imposition of thermal discontinuities at the gas/fluid interface will be examined in section 3.2.3.

A combination of the results obtained in equations (3.17) and (3.18) gives the following expression (equation 3.19) for the induced temperature change in the sample due to the heat source in the ith layer:

$$\Delta T_i(x,y,z,t) = \left(\frac{4A_0\ \partial t_p}{\kappa_2}\right)\left[\frac{e^{-(x^2+y^2)/\omega_c^2}}{\omega_c^2}\right](\eta_i\beta_i I_{i-1})\cdot \left[e^{\beta_i(z+\sigma_{i-1})}\,e^{\beta_i^2\alpha_2 t}\cdot\left[\operatorname{erfc}\left[\frac{(z+\sigma_{i-1})}{\sqrt{4\alpha_2 t}}+\beta_i\sqrt{\alpha_2 t}\right]-\operatorname{erfc}\left[\frac{(z+\sigma_i)}{\sqrt{4\alpha_2 t}}+\beta_i\sqrt{\alpha_2 t}\right]\right]\right] \tag{3.19}$$

where the first term in parentheses represents factors which are independent of time, radial distance, subsurface depth, and layer weighting. This term is always normalised out of the calculation. The second term in parentheses ([e$^{-(x^2+y^2)/\omega c^2}$ ...]) is dependent on the radial distance from the axis of the heating beam (see Fig. 3.1 for geometry). In one dimensional problems it approaches a value of $1/\omega^2$, and is the factor responsible for the transverse deflection signals. The remaining factors in parentheses are dependent on the contribution of light absorption and heat generation in each layer, and are of key importance to the calculation since they determine the relative contribution of each layer's response to the observed signal. The last factor in large square brackets ([erfc ...]) is the contribution to the temperature profile in the sample layer, and is sensitive to the light profile dependence in each individual layer.

Because of the linearity of the convolution operations inherent in equation (3.14), the temperature response in the N layered sample is given by:

$$\Delta T_i(x,y,z,t) = \left(\frac{4A_0\ \partial t_p}{\kappa_2}\right)\left[\frac{e^{-(x^2+y^2)/\omega_c^2}}{\omega_c^2}\right] \cdot \sum_{i=1}^{N} (\eta_i \beta_i I_{i-1}) \cdot e^{\beta_i(z+\sigma_{i-1})}\, e^{\beta_i^2 \alpha_2 t} \cdot \left[erfc\left[\frac{(z+\sigma_{i-1})}{\sqrt{4\alpha_2 t}} + \beta_i\sqrt{\alpha_2 t}\right] - erfc\left[\frac{(z+\sigma_i)}{\sqrt{4\alpha_2 t}} + \beta_i\sqrt{\alpha_2 t}\right] \right] \tag{3.20}$$

This equation only applies for the 'infinite medium case', which is valid when sample, backing and fluid layers have matched thermo-physical properties. In practice, this thermal matching condition may be approximately arranged by choosing the appropriate backing and fluid layers. The heat flux source producing the temperature change lies between the boundaries z=0 and $z=-\sigma_N$, as diagrammed in Fig. 3.2, but for z > 0 the temperature change predicted by equation (3.20) applies to the fluid layer, likewise, equation (3.20) for $z < -\sigma_N$ applies to the backing.

With the assumption that z > 0, the theoretical deflection arising from the ME deflection may then be computed. In order to compute the mirage deflection, the temperature profile is integrated along the y direction as dictated by equation (3.7). Integration of each term in equation (3.20) along the y coordinate gives the ith term of the form:

$$\bar{T}_i = \frac{4A_0\ \delta t_p}{\kappa_2}\ \frac{\sqrt{2\pi}}{\omega_c}\ e^{-x^2/\omega_c^2}\ (\eta_i \beta_i I_{i-1}) \cdot e^{\beta_i(z+\sigma_{i-1})}\, e^{\beta_i^2 \alpha_2 t} \cdot \left[erfc\left[\frac{(z+\sigma_{i-1})}{\sqrt{4\alpha_2 t}} + \beta_i\sqrt{\alpha_2 t}\right] - erfc\left[\frac{(z+\sigma_i)}{\sqrt{4\alpha_2 t}} + \beta_i\sqrt{\alpha_2 t}\right] \right] \tag{3.21}$$

In order to evaluate the normal component of the deflection as in equation (3.9), the derivative of T_i with respect to z is solved. The Leibnitz theorem (13) must be used for differentiation of the error function. The resulting expression for the normal deflection case is given by:

$$\begin{aligned}\theta_n = -\frac{1}{n}\left(\frac{\partial n}{\partial T}\right)\left(\frac{4A_0\,\delta t_p}{\kappa_2}\right)\left(\frac{\sqrt{2\pi}}{\omega_c}e^{-x^2/\omega_c^2}\right)\cdot \\ \sum_{i=1}^{N}(\eta_i\beta_i I_{i-1})\cdot\Bigg[\beta_i\, e^{\beta_i(z+\sigma_{i-1})}\, e^{\beta_i^2\alpha_2 t}\,\cdot \\ \left[erfc\left[\frac{(z+\sigma_{i-1})}{\sqrt{4\alpha_2 t}}+\beta_i\sqrt{\alpha_2 t}\right]-erfc\left[\frac{(z+\sigma_i)}{\sqrt{4\alpha_2 t}}+\beta_i\sqrt{\alpha_2 t}\right]\right]+ \\ \frac{1}{\sqrt{\pi\alpha_2 t}}\left[e^{-\beta_i l_i}\, e^{-(z+\sigma_i)^2/4\alpha_2 t}-e^{-(z+\sigma_{i-1})^2/4\alpha_2 t}\right]\Bigg]\end{aligned} \tag{3.22}$$

The factors of the form $\tau_i=(z+\sigma_i)^2/4\alpha_2$ are the characteristic thermal transit times for heat conduction from an offset position at $z=-\sigma_i$ in the sample, to the probe offset position at $z=z$. The expression $\tau_{0i}=1/\beta_i^2\alpha_2$ is a thermo-optical transit time for heat conduction across an optical absorption length given by $l_{0i}=1/\beta_i$.

The theoretical model is then extended to specific cases, generated to explain experimental results obtained. The next section deals with a specific case of heat conduction in thermally discontinuous systems.

3.2.3 Temperature Profiles Resulting from Heat Conduction in Thermally Discontinuous Systems

In this section, the case in which a distributed subsurface heat source is present, is considered. The sample is assumed to be irradiated with a distributed heat flux source of the form given by (3.12), with the sample assumed to be contacted to layers of fluid and backing as in Fig. 3.2, but where there is a discontinuity in thermal effusivity at the sample surface. The heat conduction equations for the problem are written (15):

$$\nabla^2 T_1 - \frac{1}{\alpha_1}\frac{\partial T_1}{\partial t} = 0 \qquad \text{fluid (3.23)}$$

$$\nabla^2 T_2 - \frac{1}{\alpha_2}\frac{\partial T_2}{\partial t} = -q^{\cdot}\,(x,y,z,t)/\kappa_2 \qquad \text{sample (3.24)}$$

$$\nabla^2 T_3 - \frac{1}{\alpha_3}\frac{\partial T_3}{\partial t} = 0 \qquad \text{backing (3.25)}$$

Evaluation of the impulse response in the fluid layer is made by means of the Laplace transform method (13). The Laplace transforms in (3.23, 3.24, 3.25) are written for the homogeneous equations of the form:

$$\nabla^2 T_i(x,y,z,s) - q_i^2\, T_i(x,y,z,s) = 0 \qquad (3.26)$$

where $q_i = \sqrt{s/\alpha_i}$ and s is the Laplace domain variable.

In the sample region, the presence of the source contributes an inhomogeneous (particular) solution in addition to the homogeneous solution. The particular solution is given by equation (3.20). Application of boundary conditions of temperature and heat flux continuity is made at all interfaces in the model and yields the following set of linear equations in the boundary coefficients, A_i:

$$A_1(k,s) - A_2(k,s) - A_3(k,s) = S_0(k,s) = \Delta T_{2i}\ (z=0,k,s) \tag{3.27}$$

(temperature continuity at sample/fluid boundary)

$$b_{12}A_1(k,s) - A_2(k,s) + A_3(k,s) = S_1(k,s) = \frac{-1}{q_2}\,\frac{\partial \Delta \hat{T}_2{}^{I}}{\partial z}\ (z,k,s)\ \Bigg|_{z=0} \tag{3.28}$$

(heat flux continuity at sample/fluid boundary)

$$\begin{gathered} A_2(k,s)\ e^{q_2\sigma_N} + A_3(k,s)\ e^{-q_2\sigma_N} - A_4(k,s) = S_2(k,s) = \\ -\Delta T_2^{I}(z=-\sigma_N,k,s) \end{gathered} \tag{3.29}$$

(temperature continuity at sample/backing boundary)

$$\begin{gathered} A_2(k,s)\ e^{q_2\sigma_N} - A_3(k,s)\ e^{-q_2\sigma_N} + b_{32}\ A_4(k,s) = S_3(k,s) \\ = \frac{1}{q_2}\,\frac{\partial \Delta T_2^{I}}{\partial z}(z,k,s)\ \Bigg|_{z=-\sigma_N} \end{gathered} \tag{3.30}$$

(heat flux continuity at sample/backing boundary)

The parameters b_{ij} in equations (3.28) and (3.30) are interfacial thermal effusivity ratios between adjacent layers in the model:

$$b_{ij} = (\kappa_i\ q_i / \kappa_j\ q_j) \tag{3.31}$$

where k is the radial wavenumber and q is the wavenumber for a cylindrical thermal wave. This ratio critically controls the extent to which a thermal wave is damped or reflected at a thermal interface in a material (14).

Evaluation of the coefficient $A_1(k,s)$ gives the transform of the temperature profile in the fluid phase above the sample as desired:

$$\Delta T_1(z,s,k) = \left[\frac{-2\,e^{q_2\sigma_N}(b_{32}+1)S_0 - 2\,S_2(b_{32}-1)}{e^{-q_2\sigma_N}(b_{32}-1)(b_{12}-1) - e^{q_2\sigma_N}(b_{32}+1)(b_{12}+1)} \right] e^{-q_1 z} \qquad (3.32)$$

where S_0 and S_2 are defined in equations (3.27) and (3.29). For certain special cases which are of experimental interest, this expression is inverted in order to obtain the time domain response. The first approximation which may be made in many cases is to choose a backing material which is thermo-physically similar to the sample. In this case $b_{32} \approx 1$ and there is a negligible contribution of thermal reflection or absorption to the temperature profile in the fluid medium. Subject to this simplification, equation (3.32) becomes:

$$\Delta T_1(z,s,k) = \left[\frac{2\,S_0}{(b_{12}+1)} \right] e^{-q_1 z} \qquad (3.33)$$

The approximations to equation (3.20) in this case are maintained with many polymers having a conductivity in the range k = 0.1-0.4 W/m°K and α in the range 0.8-1.2 x 10^{-7} m^2/s, while for water, k = 1.2 W/m°K and $\alpha \approx 1.4$ x 10^{-7} m^2/s (15).

For the case of one dimensional heat conduction, the pump beam radius is much larger than both the depth of the features to be probed and the radial heat diffusion length, $\omega >> (z+\sigma_i)$, and, in the time domain, $\omega^2 >> 4\alpha_2 t$. Correspondingly, in the Laplace domain, $s/\alpha_i >> k$ or $q_i \approx \sqrt{s/\alpha_i}$ (e.g. q_i becomes independent of k). Heat conduction becomes one dimensional, $\Delta\hat{T}(k,s,z) \approx \Delta T(s,z)$, resulting in the following equation in the limit of one dimensional heat conduction applied to equation 3.22:

$$\theta_n^{(1D)} = -\frac{1}{n}\left(\frac{\partial n}{\partial T}\right)\left(\frac{4A_0\ \delta t_p}{\kappa_2}\right)\left(\frac{\sqrt{2\pi}}{\omega}\right)\cdot \sum_{i=1}^{N}(\eta_i\beta_i I_{i-1})\cdot\Bigg[\beta_i\ e^{\beta_i(z+\sigma_{i-1})}\ e^{\beta_i^2\alpha_2 t}\ . \left[\mathit{erfc}\left[\frac{(z+\sigma_{i-1})}{\sqrt{4\alpha_2 t}}+\beta_i\sqrt{\alpha_2 t}\right]-\mathit{erfc}\left[\frac{(z+\sigma_i)}{\sqrt{4\alpha_2 t}}+\beta_i\sqrt{\alpha_2 t}\right]\right]+ \frac{1}{\sqrt{\pi\alpha_2 t}}\cdot e^{-\beta_i l_i}\ e^{-(z+\sigma_i)^2/4\alpha_2 t}-e^{-(z+\sigma_{i-1})^2/4\alpha_2 t}\Bigg] \tag{3.34}$$

In all the situations discussed below, the assumption of one dimensional heat conduction applies.

A case which is of interest to the analysis of solids occurs when the fluid layer is a gas, so that the interfacial thermal effusivity, b_{12}, at the sample surface, is nearly zero, $b_{12} << 1$. If one dimensional heat conduction is maintained, equation (3.33) then becomes:

$$\Delta T_1(s,z) = \frac{8A_0\ \delta t_p}{\kappa_2\ \alpha_2}\sum_{i=1}^{N}\frac{\eta_i\beta_i I_{i-1}}{q_2(\beta_i+q_2)}\ \cdot \left[\ e^{-q_2\sigma_{i-1}}-e^{-\beta_i l_i}e^{-q_2\sigma_i}\right]\ e^{-q_1 z} \tag{3.35}$$

This expression, upon inversion of the Laplace transform gives a temperature profile of the form:

$$\Delta T_1(z,t) = \frac{8A_0\ \delta t_p}{\kappa_2}\sum_{i=1}^{N}\eta_i\beta_i I_{i-1}\ e^{\beta_i^2\alpha_2 t}\ e^{\beta_i(z\sqrt{\alpha_2/\alpha_1}+\sigma_{i-1})}\cdot \left[\mathit{erfc}\left[\frac{(z\sqrt{\alpha_2/\alpha_1}+\sigma_{i-1})}{\sqrt{4\alpha_2 t}}+\beta_i\sqrt{\alpha_2 t}\right] -\mathit{erfc}\left[\frac{(z\sqrt{\alpha_2/\alpha_1}+\sigma_i)}{\sqrt{4\alpha_2 t}}+\beta_i\sqrt{\alpha_2 t}\right]\right] \tag{3.36}$$

It can be shown that equation (3.20) and equations (3.34) and (3.36) are of the same form (to within a multiplicative constant factor) under the assumptions that $\omega >> 4\alpha_2 t$ and $\alpha_1 = \alpha_2$.

If the other extreme, $b_{12} >> 1$ is encountered, then equation (3.33) results in the following:

$$\begin{aligned} \Delta T_1(z,s,k) &= \frac{2}{b_{12}} S_0\, e^{-q_1 z} \\ &= \frac{\delta A_0\, \delta t_p}{\kappa_2\, \alpha_2\, b_{12}} \sum_{i=1}^{n} \frac{\eta_i \beta_i I_{i-1}}{q_2(\beta_i + q_2)} \left[e^{-q_2 \sigma_{i-1}} - e^{-\beta_i l_i}\, e^{-q_2 \sigma_i} \right] \cdot e^{-q_1 z} \end{aligned} \tag{3.37}$$

This equation, upon inversion of the Laplace transform gives:

$$\begin{aligned} \Delta T_1(z,t) = \frac{\delta A_0\, \delta t_p}{\kappa_2\, b_{12}} \sum_{i=1}^{N} \eta_i \beta_i I_{i-1}\, e^{\beta_i^2 \alpha_2 t}\, e^{\beta_i (z\sqrt{\alpha_2/\alpha_1} + \sigma_{i-1})} \cdot \\ \left[erfc\left[\frac{(z\sqrt{\alpha_2/\alpha_1} + \sigma_{i-1})}{\sqrt{4\alpha_2 t}} + \beta_i \sqrt{\alpha_2 t} \right] \right. \\ \left. - erfc\left[\frac{(z\sqrt{\alpha_2/\alpha_1} + \sigma_i)}{\sqrt{4\alpha_2 t}} + \beta_i \sqrt{\alpha_2 t} \right] \right] \end{aligned} \tag{3.38}$$

which, to within a multiplicative constant of $(2/b_{12})$ has the same form as equation (3.20) with $\omega \to \infty$ and $\alpha_1 = \alpha_2$. In the case of equations (3.37) and (3.38), the condition $\alpha_1 \neq \alpha_2$ may be encountered. If we write $z_e = z\sqrt{\alpha_2/\alpha_1}$, then equations (3.34), (3.36) and (3.38) may be seen to be of the same form with respect to the substitution $z = z_e$.

3.3 DISCUSSION OF RESULTS OF THEORETICAL SIMULATIONS

In order to understand the principal contrast mechanisms that give rise to variations in ME depth profiling, the most important factors in the theory must be identified and their effects on the impulse response understood. The theory, outlined above, is developed using a model consisting of a sample with an arbitrary absorption profile. It is assumed that by incorporating enough closely spaced layers, the sample's properties may be simulated. This general theory reduces to all of the standard cases previously discussed. Additionally equation (3.22) and its related forms, show the correct asymptotic behaviour with respect to parameters such as ß. Finally, the special cases permit one to examine the resolving power of the mirage effect one variable at a time, before proceeding to more complicated sample types.

The normal deflection, θ_n, is the signal component considered in this section, for depth profiling purposes (all computations of θ_n were made in this work, by means of equation (3.34)). For the case $\alpha_1 \neq \alpha_2$, the substitution $z_e = z\sqrt{\alpha_2/\alpha_1}$ was made in the equation. All of the constants appearing as multiplying factors preceding the summation sign in equation (3.34), which were either space (r or x), time or layer index (i) independent, were normalised out of the calculations. The calculations were made using the ASYST language (copyright Adaptable Laboratory Software Inc.).

3.3.1 Effect of Probe Beam Offset Position on ME Depth Profiling

One of the most important parameters in ME experiments is the offset distance of the probe beam from the sample surface, z, since this factor affects both the speed of the mirage response and the resolution of the depth profile. In normal deflection mode, as the offset z above the surface increases, there is a delay in the peak value of the impulse response which results from an increase in the thermal transit time from the surface to the offset position. Fig. 3.4 shows the variation of the theoretical normalised ME impulse

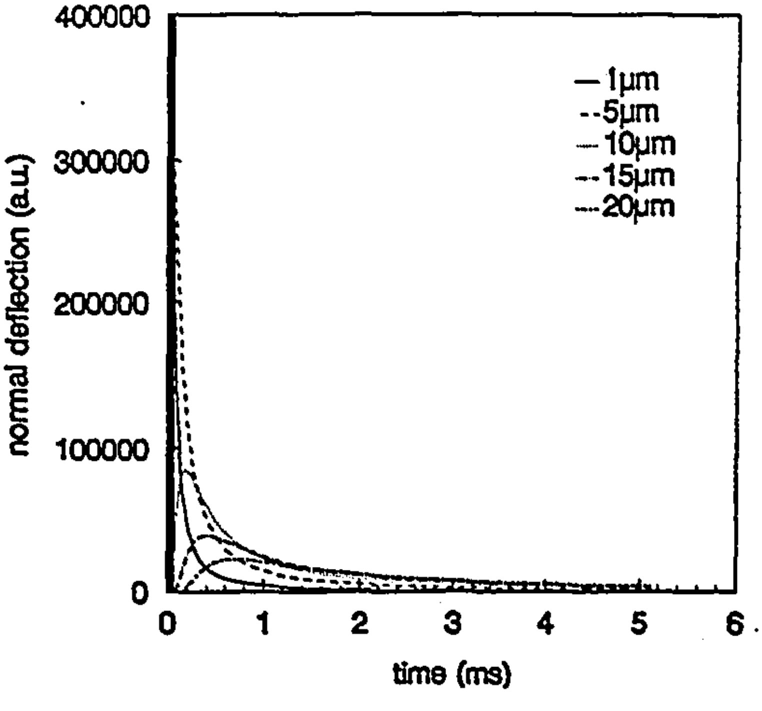

Figure 3.4: Variation of the theoretical impulse response function (from equation 3.22) plotted as a function of various values of the normal offset, z, as indicated in the legend.

response with z for the case of irradiation of the sample in a thin planar surface region where all of the absorbed energy is concentrated in this surface region. The computed mirage deflection shows increased broadening of the impulse transient which is consistent with the increased thermal transit time, as observed by others (4).

The ME deflection is proportional to the spatial derivative of temperature rather than the temperature itself. If the temperature gradient, in this situation is considered to be an expanding Gaussian profile whose half width increases with time (as sketched in Fig 3.5) then, at early times, the temperature gradient is large, but concentrated close to the heated surface, so that the probe beam samples only the tail of the temperature profile, where the local gradient is relatively small. Sufficient time is required to move a significant component of the temperature profile into the fluid region intersected by the probe beam. On the other hand, the temperature gradient collapses at very long times past

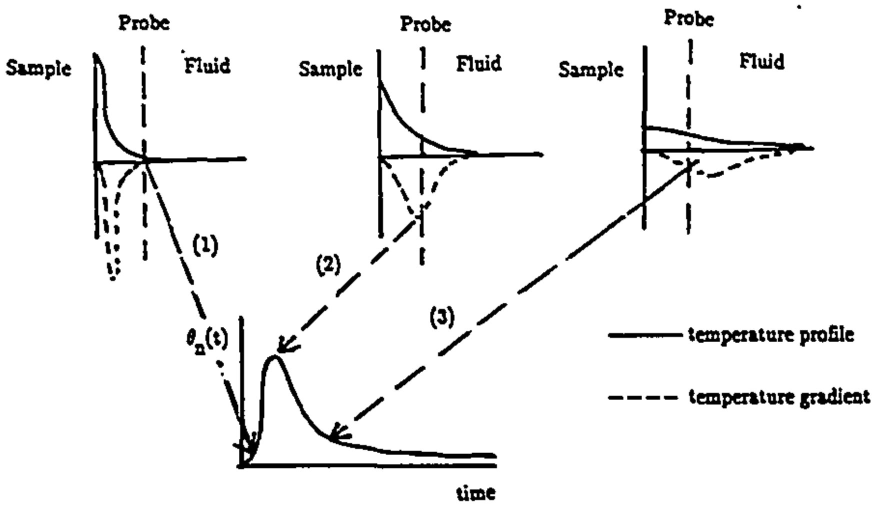

Figure 3.5: Schematic diagram illustrating the probe beam offset dependence, for various values of z, on local fluid temperature gradient. The sample modelled contained a surface absorber with ß → ∞.

excitation. The position in time of the peak maximum, therefore, represents a compromise between these two competing effects. It can be shown that the peak value of the spatial derivative of the temperature is damped with distance, scaling as $\{k^3ze^{-kz^2}\}$, where k is a spatially independent arbitrary constant. The peak signal speed and peak signal response magnitude both decrease significantly with increasing offset, z. This key parameter has a dramatic effect on the depth resolving power of the ME technique.

3.3.2 Effect of the Optical Absorption Coefficient on ME Depth Profiling in Thermally Matched and Thermally Mismatched Fluids

Since mirage effect detection and photothermal methods, in general, are frequently used as methods of spectroscopy, it is worthwhile to consider first the measurements on homogeneous absorbing layers. Unlike conventional absorption spectrophotometry, which relies on measurements of transmitted light levels for recovery of the optical absorption coefficient, photothermal methods measure ß through the spatial dependence of the heat flux profile deposited below the sample surface by light absorption. In principle, there is no reason to prefer an exponential (spatial) light deposition profile as the basis for measurement, unlike spectrophotometric methods which critically rely on such a dependence (through Beer's law) for measurement. As far as the photothermal method is concerned, the exponential profile is only one of an infinite variety of possible optical profiles giving rise to a signal dependence which can be approximated in equations (3.22) and/or (3.34).

The ME normal deflection signal dependence expected for the irradiation of a single layer sample whose absorbance varies from nearly zero to a value approaching 30 a.u. can be seen in Figures 3.6 and 3.7. At a fixed offset, z, as the value of ß increases from 1.0×10^3 m^{-1} to 1.0×10^4 m^{-1}, in Fig. 3.6 and from 1.0×10^4 m^{-1} to 7.5×10^5 m^{-1} in Fig. 3.7, more and more of the heat flux deposited in the sample at t=0 is confined to a near surface region, corresponding to rapid spatial decay of the light field with depth into the sample. As more of this initial heating occurs close to the surface, both the peak delay and the peak width of the impulse response diminish. On the other hand, as ß decreases in value, there is significantly more light deposited at a greater initial depth from the surface, and both the peak width and position of the impulse response both increase.

The impulse ME technique gives very good contrast for samples exhibiting moderate to strong optical absorptivity. For example, an absorbance of 20 a.u. can just be distinguished from an absorbance of 30 a.u., whereas such a contrast would not be easily obtainable on a conventional absorption spectrophotometer. Tests run on samples of very low ß approached the optically thin limit, but in no case was any feature of the above thermal impulse response found to be attributable to the limitations imposed by the thickness of the sample. However, the resolution of small values of ß, corresponding in this case to absorbance values in the range less than 0.050 a.u. is poor if the impulse response variation is used to infer ß.

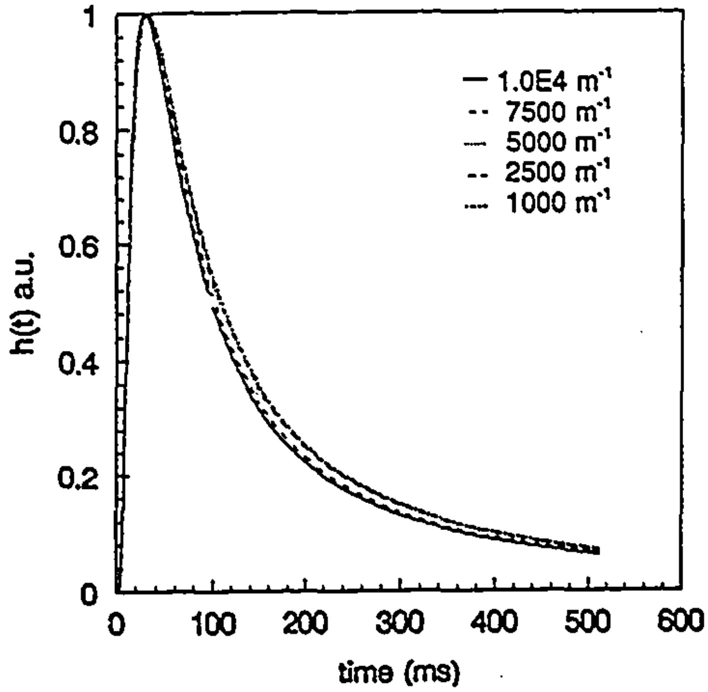

Figure 3.6: Effect of optical absorption coefficient on the normalised impulse response observed for a single, optically homogeneous layer with small to moderate values of ß (1.0×10^3 m^{-1} < ß < 1.0×10^4 m^{-1}). Sample thickness was 100 μm, heating spot 1000 μm, probe beam offset was 100 μm, $b_{12} = 1$.

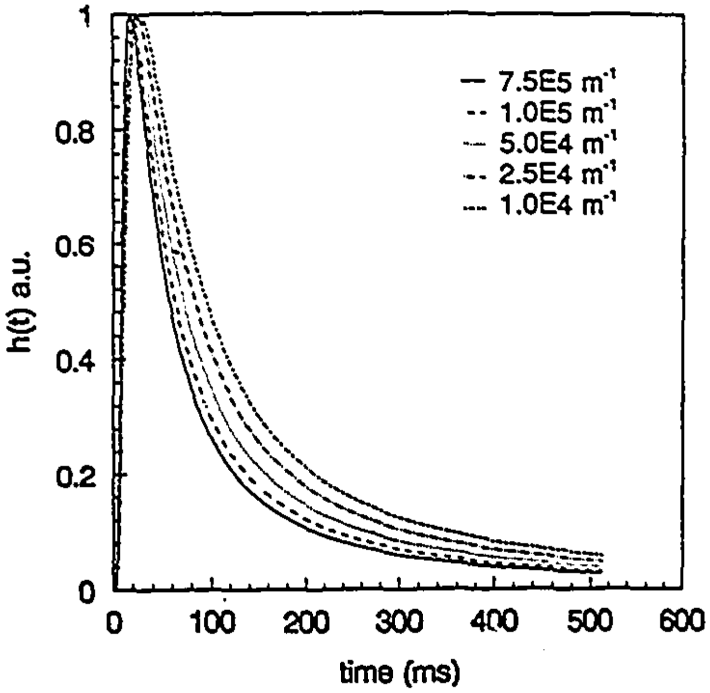

Figure 3.7: Effect of optical absorption coefficient on the normalised impulse response observed for a single, optically homogeneous layer with large values of ß (1.0×10^4 m^{-1} < ß < 7.5×10^5 m^{-1}). Sample thickness was 100 μm, heating spot 1000 μm, probe beam offset was 100 μm, $b_{12} = 1$.

If the fluid layer above the sample surface is changed so that the thermal properties are those of air, the thermal effusivity at the front surface becomes nearly zero due to a decrease in the thermal conductivity of the air layer ($k \approx 0.001$ W/m°K and $\alpha = 2.5 \times 10^{-5}$ m^2/s). Only a small component of the temperature field in the sample diffuses across the interface that the thermal wave propagating in the air layer. It has a time dependence governed strongly by the temperature at the sample surface. Equivalently, the thermal wave propagating in the sample is negligibly affected by losses to the gas layer.

By changing from a low diffusivity fluid to air as the medium above the sample surface, the thermal diffusivity increases from a value of ca. $1. \times 10^{-7}$ m^2/s to a value of 2.5×10^{-5} m^2/s, and this change reduces the thermal transit times in the model given by equation (3.34). In the case where $b_{12} >> 1$ or $b_{12} = 1$ and where $\alpha_1 \neq \alpha_2$, the general form of the thermal time constants are given by:

$$\tau_i = \left(\frac{\sigma_i}{\sqrt{2\alpha_2}} + \frac{z}{\sqrt{2\alpha_1}}\right)^2 = \left(\frac{\sigma_i}{\sqrt{2\alpha_2}} + \frac{z_e}{\sqrt{2\alpha_2}}\right)^2 \qquad (3.39)$$

where $z_e = z\sqrt{\alpha_2/\alpha_1}$. The factor $\sigma_i^2/4\alpha_1$ measures heat flow from buried subsurface features to the sample/gas interface, and the factor $z^2/4\alpha_1$ measures the thermal transit time from the surface of the sample to the probe beam offset position. If $\alpha_1 \neq \alpha_2$, the change in the thermal time constant may be seen as a modification of the offset length from z to $z_e = z\sqrt{\alpha_2/\alpha_1}$. Therefore, increasing α_1 has the same effect as contracting the physical offset, z, by a factor $\sqrt{\alpha_2/\alpha_1}$. The predicted response for the effect of an air layer above the sample surface (e.g. with a probe beam offset z of $1. \times 10^{-4}$ m) is seen to be equivalent to the response obtained when the probe beam is aligned at an offset $z_e = 6\,\mu m$ in a medium with the same diffusivity as the sample. This has the same effect on the ME impulse response as positioning the probe beam closer to the sample surface in a medium of diffusivity matched to that of the sample.

The effect of detecting the ME impulse response in air is an improved resolution for the small values of ß as shown in Fig. 3.8. The enhanced resolution at low ß may be

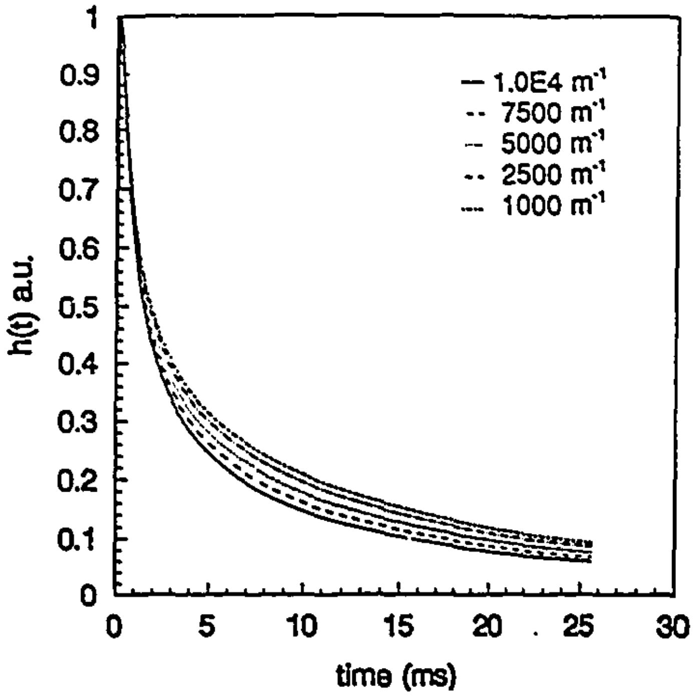

Figure 3.8: Effect of detecting mirage effect impulse response in air (as opposed to a thermally matched fluid) with $b_{12} \approx 0$ and $\alpha_1 = 2.5 \times 10^{-5}$ m²/s. All other conditions are the same as in Fig. 3.6 and Fig. 3.7.

due to an increased sensitivity of the measurement to the value of the initial slope in the optical and the heat flux profile, as it attenuates away from the surface. For this case, $b_{12} \approx 0$ and results in nearly zero heat flow into the fluid layer. The normalised traces used for the calculations presented here obscure the fact that the signal to noise ratio drops by nearly an order of magnitude relative to the condition $b_{12} \approx 1$.

From the impulse response profiles shown in Figs. 3.6 - 3.8, a saturation effect is observed when large β values are approached; all of the light is deposited within a thin zone near the surface so that the time required for heat conduction through this zone is small relative to the time required for heat conduction to occur from the surface to the probe offset position. In full saturation, the ME impulse signal becomes completely invariant with β. The asymptotic form of $\theta_n(t)$ expected when $\beta \rightarrow \infty$, is derived in detail in Appendix A; however, the form of $\theta_n(t)$ in the saturation limit is shown to approach the following:

$$\theta_n(t) \propto \frac{-z}{4(\sqrt{\alpha_2 t})^3} e^{-z^2/4\alpha_2 t} \tag{3.40}$$

In this regime, $\theta_n(t)$ becomes independent of β as expected. When light attenuates in a sample layer according to Beer's law, the effective depth of optical penetration is given by the optical deposition length $l_{0i} = 1/\beta_i$. The thermal transit time associated with the optical deposition length is given by $\tau_{0i} = l_{0i}^2/\alpha_2 = 1/\beta^2\alpha_2$. Therefore near saturation, the condition $\tau_{0i} << \tau_{i-1}$ is obtained, where $\tau_{i-1} = (z + \sigma_{i-1})^2/4\alpha_2$, the thermal transit time from the sample surface to the probe beam offset position. The following saturation criterion for the optical absorptivity measurement can be proposed:

$$\tau_{i-1} >> \tau_{th} \quad \vee \quad z+\sigma_{i-1} >> 2l_{th} \tag{3.41}$$

To summarise, the result of either reducing z or increasing the diffusivity α_1 has the effect of increasing the value of ß at which saturation occurs.

At the other extreme, i.e. extremely small ß, the light deposition profile in the sample approaches the form of a square spatial pulse. The time dependence of the ME impulse response becomes invariant to values of ß, although the peak value of the response is still proportional to ß, as seen below in equation 3.42:

$$\theta_N \propto \frac{\beta_2}{\sqrt{\pi\alpha_2 t}}\left[e^{-z^2/4\alpha_2 t} - e^{-(z+l)^2/4\alpha_2 t}\right] \tag{3.42}$$

This partial saturation effect encountered with optically thin absorbers gives a simple test for determining whether they account for the sample response. For a photothermally thin layer, a variation in the peak value of the ME impulse response occurs with wavelength according to the absorption spectrum of that layer. If no corresponding change in the time dependence of the ME impulse response is observed (e.g. after peak normalisation), then the sample may be seen to be composed of only a thin planar absorber.

3.3.3 Use of ME Depth Profiling to Examine Samples with Unknown Properties

In addition to the cases discussed above, equation (3.34) can be used to predict the ME impulse response of samples whose optical absorption profiles are unknown with subsurface depth. This may be done by assuming the sample is composed of a sufficient number of closely spaced thin layers within which the heat flux profile is approximately constant. This will be true if each layer, as well as the sample as a whole, is assumed to be optically thin (i.e. $\beta_i l_i << 1$). In order to simulate the effect of a varying depth dependent profile, each thin section is multiplied with a weighting factor, ξ_i, which varies with depth and whose height approximates the optical absorption profile encountered in each layer in the sample. These operations are summarised in the sketch shown in Fig. 3.9. The reliability of the profile simulations by comparing the results for a single homogeneous layer in equation (3.34) with known β, has been verified in practice against the results of a simulation which used a discretized approximation to the same profile. The error introduced into the impulse response by the discretization was less than 1% (full scale) for a range of values and the detection geometry given in Fig. 3.9.

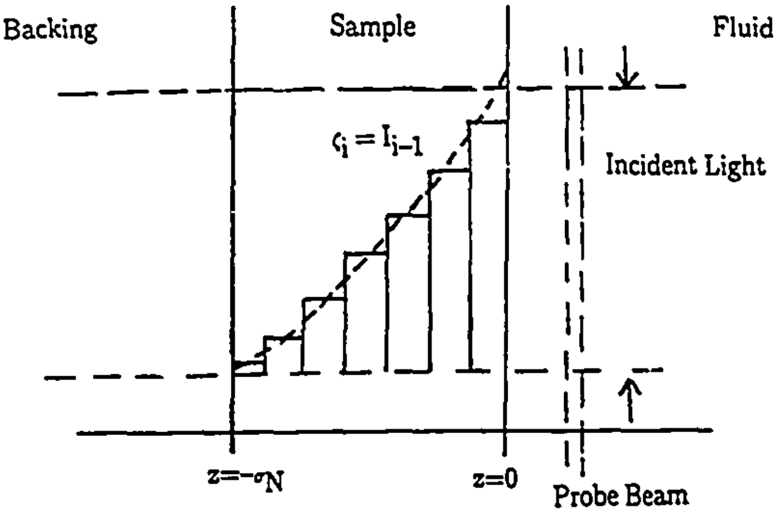

Figure 3.9: A schematic of the ME geometry with illustration of detection of the absorption coefficient in a single layer, showing attenuation factors for light propagation in a discretized layered model which approximates a continuous structure.

Mirage spectrometry may also be used to depth profile the optical absorptivity of samples where the absorbers are present as discrete thin layers at or below the surface. This type of structuring is very common in manufactured products, especially for the many types of laminated thin films used in packaging. In the discussion below, the conditions required to just resolve the contributions from two thin absorbers, where one of the absorbers is displaced at varying depths below the surface is considered. The experimental measurements are discussed in Chapter 4.

The dependence of the ME impulse response can be greatly simplified if very thin absorber layers are present as sources. Equation (3.22) becomes, to a good approximation:

$$\theta_N \propto \eta_i I_{i-1} \frac{(1-e^{-\beta_i l_i})}{(\sqrt{\pi\alpha_2 t}\,)^3}(-(z+\sigma_i))e^{-(z+\sigma_i)^2/4\alpha_2 t} \tag{3.43}$$

This equation can easily explain the dependence of the mirage signal with distance from a surface or displaced subsurface absorber. The peak time delay τ_d, in the ME impulse response for a displaced absorber is obtained by differentiation of equation (3.43) and equating the derivative to zero:

$$\tau_d = (z+\sigma_i)^2/6\alpha_2 \tag{3.44}$$

The relative weighting of the peak value in response to a displaced layer at distance σ_i is given by:

$$\theta_{n,j}(z,t=\tau_d) \propto A_0 \beta_i I_{i-1}(1-e^{-\beta_i l_i})\frac{e^{-(1/2)}}{\sqrt{2}\,(z+\sigma_i)^2}\;[e^{-6/4}\,6^{3/2}/2\sqrt{\pi}] \tag{3.45}$$

The first study presented (Fig. 3.10) shows the effect on the ME impulse response

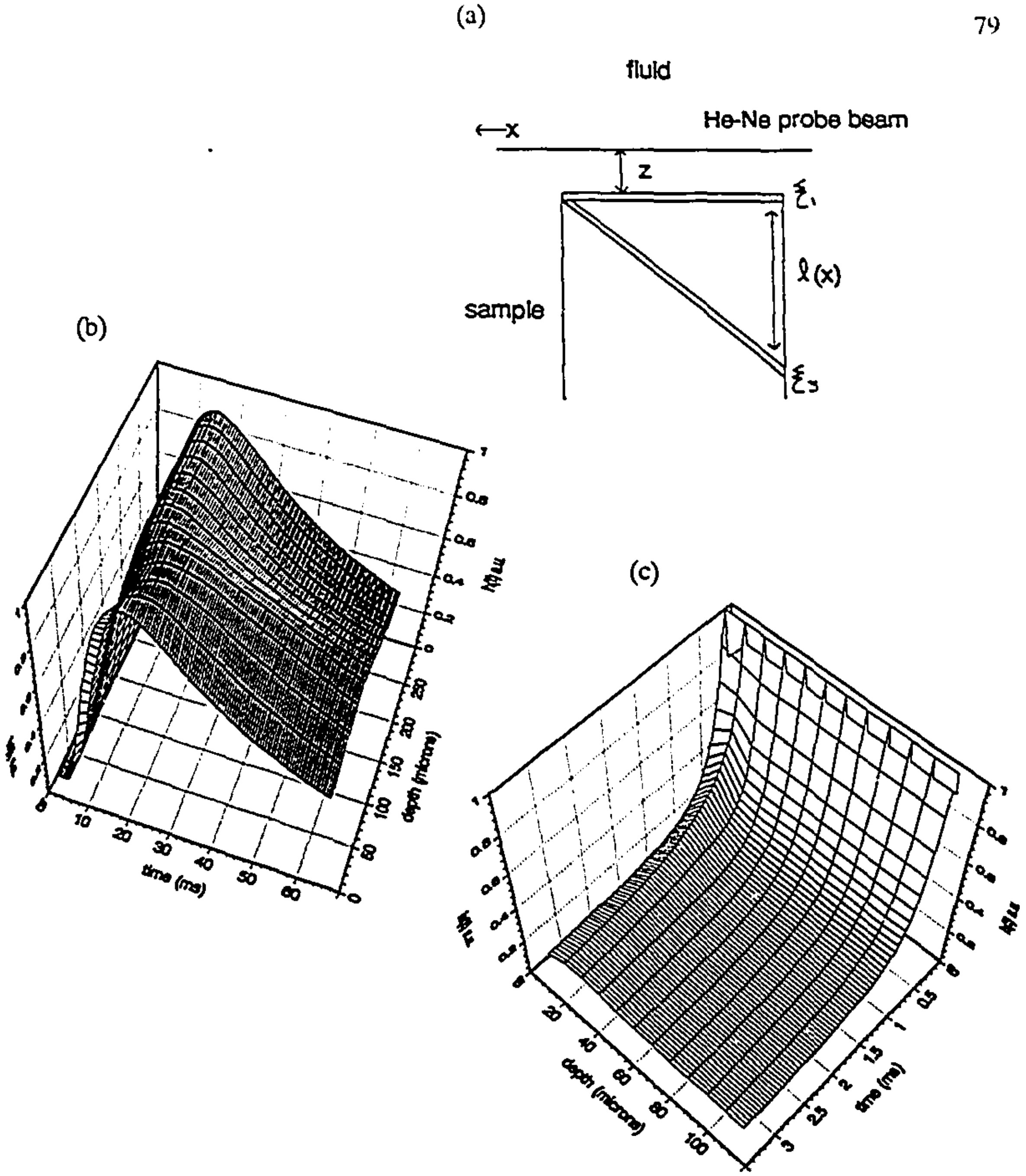

Figure 3.10: Resolution of thin absorber layers by the normalised mirage effect impulse response where two layers of equal optical absorption ($\xi_1 = \xi_3 = 1$), are separated by a variable spacer layer composed of transparent, thermally matched material (a) schematic diagram showing the spatial position of the thin layer absorber structures along an arbitrary coordinate, x; (b) response surface observed with $b_{12} = 1$ and thermally matched fluid; (c) detection in air with $b_{12} \approx 0$ and $\alpha_1 = 2.5 \times 10^{-5}$ m^2/s.

of varying the spacing between two equally weighted thin optical absorbers (Fig. 3.10(a)), separated by a transparent spacer of variable thickness. The data of Fig. 3.10(b) show the calculated ME impulse response for the case where $b_{12} = 1$ (detection in a thermally matched fluid layer) where the probe beam is displaced at an offset distance of 100 μm from the surface. At separations less than 50 μm, a difference is just detectable in θ_n, while at a 100 μm separation between the optically absorbing layers, a significant broadening of the normalised peak impulse response traces is obvious, due to the underlayer's photothermal contribution. If air is substituted as the fluid medium, as was assumed in the study of Fig 3.10(c), the effect of the larger diffusivity reduces the equivalent probe beam offset to 6 μm, and the impulse response peaks much more rapidly. In this case, the 5-10 μm spacings are readily resolvable, while the contrast starts to diminish above about 25 μm. By 75 μm depth, contrast for the lower layer is nearly lost. The effect of decreasing the probe beam offset to very small values results in an increased surface weighting of the response.

This behaviour may be readily explained by considering the depth dependent contribution in equation (3.43) for the i^{th} layer, which is weighted by the factor

$$-(z+\sigma_i)\, e^{-(z+\sigma_i^2)/4\alpha_2 t} \tag{3.46}$$

This expression is dominated by the spatial dependence of a Gaussian profile displaced to the left by $z = -\sigma_i$. The extent of surface domination is determined by the value of the depth dependent source at a distance σ_i, relative to the probe offset distance, z. If $\sigma_i \geq z$, a steep drop in the ME response with absorber depth, σ_i, is seen, because the ME impulse response diminishes exponentially as $\exp\{-k(z+\sigma_i)^2\}$ and $z \to 0$. However, if $\sigma_i < z$ then the depth contribution presents a smaller fraction of the total value of the expression and the relative damping of the subsurface contribution to the decay is more gradual with σ_i. The surface weighting phenomenon could be viewed as a form of surface saturation of the signal, where it becomes difficult to see the contributions of layers buried at sufficient depths beneath a surface absorber.

For the case of equally weighted thin layer sources it can be shown that the contribution of a buried absorber attenuates rapidly with depth when $\sigma_i \geq 5z\sqrt{\alpha_2/\alpha_1}$. At the other extreme, if $\sigma_i << z$, then another condition of saturation is approached. In this extreme, the ME impulse response cannot detect a difference between two closely spaced profiles offset at a distance z from the probe beam. The measured ME impulse response then approaches the form expected for $z + \sigma_i \to z$. Consequently, the lower limit of spacing between the sources before saturation occurs is given by $\sigma_i \geq 0.1z\sqrt{\alpha_2/\alpha_1}$.

In order to resolve a subsurface layer in the presence of an equally weighted surface layer by the ME impulse response, the depth of the subsurface layer must lie within the range:

$$0.1\, z \sqrt{\alpha_2/\alpha_1} \;\leq\; \sigma_i \;\leq 5\, z \sqrt{\alpha_2/\alpha_1} \tag{3.47}$$

The relation (3.47) sets the practical limitation concerning the resolution of thin layers by the ME impulse response method. If the contributions of two thin layers at spacing *l* are to be resolved, then the impulse response is capable of resolving the contributions of the two layers only when the thermal separation between them is of the same order of magnitude as z. Fig. 3.11 confirms the strong effect that the surface weighting has on the

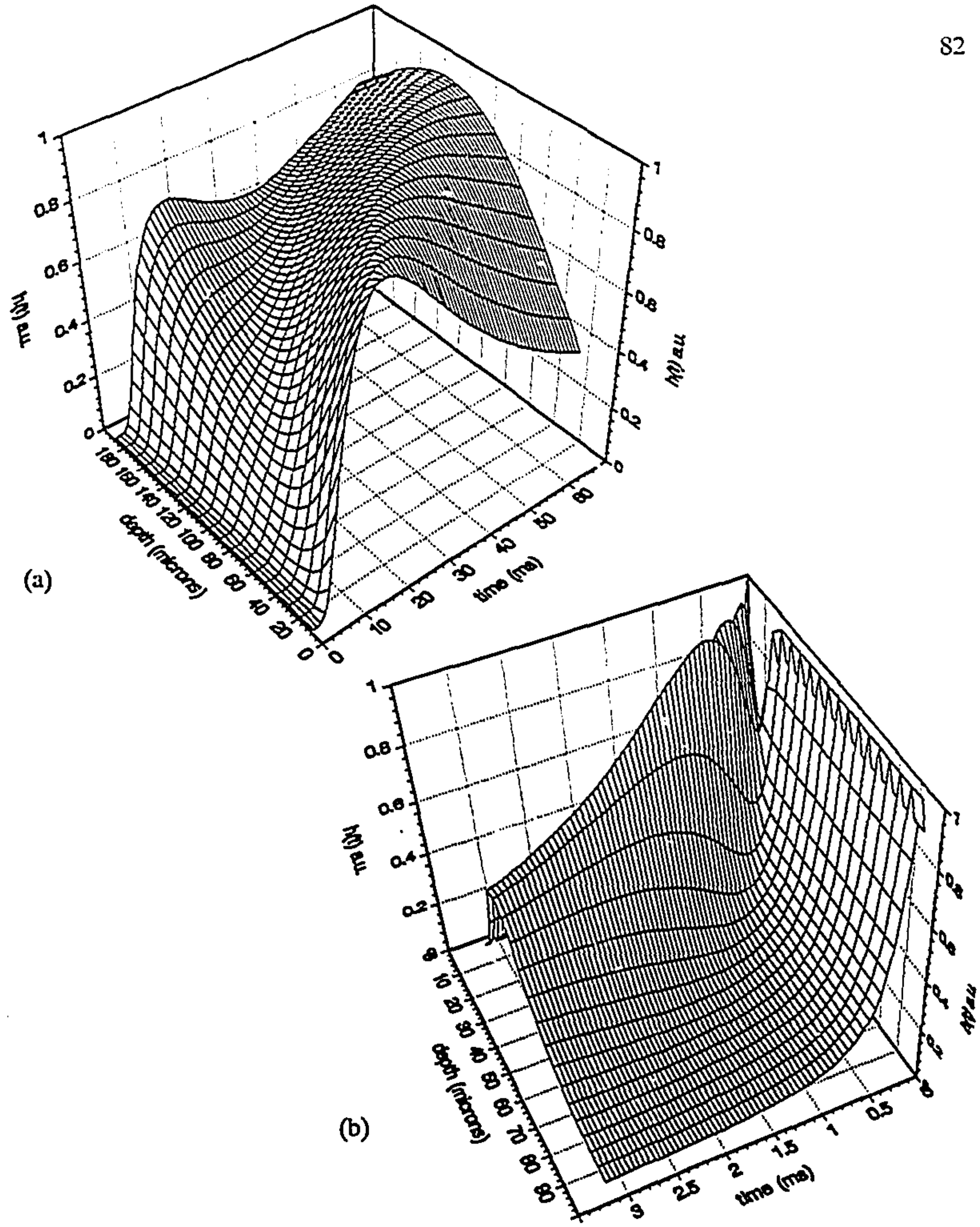

(a)

(b)

Figure 3.11: Resolution of thin absorber layers by the normalised mirage effect impulse response where a subsurface absorber of strong weighting is ($\xi_3 = 0.2\xi_1$; $\xi_1 = 1$), is separated from the surface layer by a variable spacer layer of transparent, thermally matched material (a) response surface observed with $b_{12} = 1$ and thermally matched fluid; (b) detection in air with $b_{12} \approx 0$ and $\alpha_1 = 2.5 \times 10^{-5}$ m^2/s.

mirage effect impulse response. The sample structure studied in Fig. 3.11 was identical to that of Fig. 3.10 except that the weighting of the surface absorber was reduced to 0.2 of that of the underlayer. A dramatically enhanced contrast is seen for the underlayer in both the thermally matched case (Fig. 3.11(a)) and where air was used as the fluid medium (Fig. 3.11(b)).

3.4 CONCLUSION

The model discussed in this chapter, outlines certain unique properties in comparing mirage effect optical depth profiling to other methods. The key feature of the contrast provided by the ME depth profiling is that it is heavily surface dominated; however, this is readily modified by changing the probe beam's offset position, z. In depth profiling, the most important limitation of the impulse mirage effect is the risetime, which is limited by the closeness of the approach of the probe beam to the sample surface.

The impulse mirage effect detection was theoretically explored in this model to be capable of simulating arbitrary depth profiles of optical absorptivity. The mirage effect impulse response is heavily surface weighted, and is capable of resolving very large optical densities. It is necessary, however, to optimize the probe beam offset distance in order to obtain resolvable contrast for buried features. In general, the offset position should be set to approximately the same distance (in a thermally matched fluid) as the features to be resolved. Chapter 4 details some experimental work done in examining the response of discrete and continuous absorbers.

REFERENCES

---

1. W.B. Jackson, N.M. Amer, A.C. Boccara, D. Fournier, Appl. Opt. **20**, 1333 (1981).
2. L.C. Aamodt, and J.C. Murphy, J. Appl. Phys. **52**, 4903 (1981).
3. L.C. Aamodt, and J.C. Murphy, J. Appl. Phys. **54**, 581 (1983).
4. A. Mandelis, L.M.L. Borm, and J. Tiessinga, Rev. Sci. Instrum. **57**, 622 (1986).
5. P.K. Kuo, M.J. Lin, C.B. Reyes, L.D. Favro, R.L. Thomas, D.S. Kim, S.-Y. Zhang, L.J. Inglehart, D. Fournier, A.C. Boccara, and N. Yacoubi, Can. J. Phys. **64**, 1165 (1986).
6. L.C. Aaomdt, J.W. Maclachlan Spicer, and J.C. Murphy, J. Appl. Phys. **68**, 6087 (1990).
7. M.A. Schweitzer, and J.F. Power, Appl. Spectrosc. **48**, 1054 (1994).
8. M. Born, and E. Wolff, *Principles of Optics*, 3rd Ed. (Pergamon Press, New York, 1965).
9. P.K. Kuo, E.D. Sendler, L.D. Favro, and R.L. Thomas, Can J. Phys. **64**, 1168 (1986).
10. A.E. Siegman, *An Introduction to Lasers and Masers* (McGraw-Hill Book Company, New York, 1971).
11. P.M. Morse, and H. Feshbach, *Methods of Theoretical Physics* Vol I (McGraw-Hill Book Company, New York, 1953) Chapt. 7.
12. J.F. Power, Appl. Spectrosc. **45**, 1240 (1991).
13. M. Abramowitz, and I.A. Stegun, Ed., *Handbook of Mathematical Functions*, NBS Mathematics Series 55 (National Bureau of Standards, Washington D.C., 1964).

14. S.O. Kanstad, and P.-E. Nordal, Can. J. Phys. **64**, 1155 (1986).

15. Y. S. Touloukian, *Thermophysical Properties of Matter* (IFI/Plenum, New York, 1979).

CHAPTER 4 OPTICAL DEPTH PROFILING OF DISCRETE AND CONTINUOUS ABSORBERS USING MIRAGE EFFECT SPECTROSCOPY

4.1 INTRODUCTION

Mirage effect spectroscopy was used to depth profile optical absorbers located in multilayered composites. By using the calibration procedure for determining the offset position of the probe beam relative to the sample surface, as described in section 2.4.3, and the theoretical model described in the previous chapter, quantitative depth profiling of the samples is obtained. These results of these experiments are presented in the following sections.

4.2 SAMPLE PREPARATION OF LAMINATES AND WRATTEN GEL COMPOSITES

In order to characterize the response of the system, and to determine the depth profiling capabilities of mirage effect spectroscopy using this geometry, a series of multilayered composites were prepared, whose structures are summarized in Fig. 4.1 (a)-(k). The laminates were of two varieties, samples (a) through (j) consisting of commercially available mylar films composed of a 2.5 μm pigment layer and a transparent mylar backing, of thickness ranging from 9-25 μm. The absorption spectra for the red-pigmented and green-pigmented mylar films can be found in Fig. 4.2. For the dye laser wavelengths of interest (570 nm - 610 nm), the green overcoat of pigment on the mylar absorbs strongly to moderately over the entire region, whereas, the red pigmented coat becomes

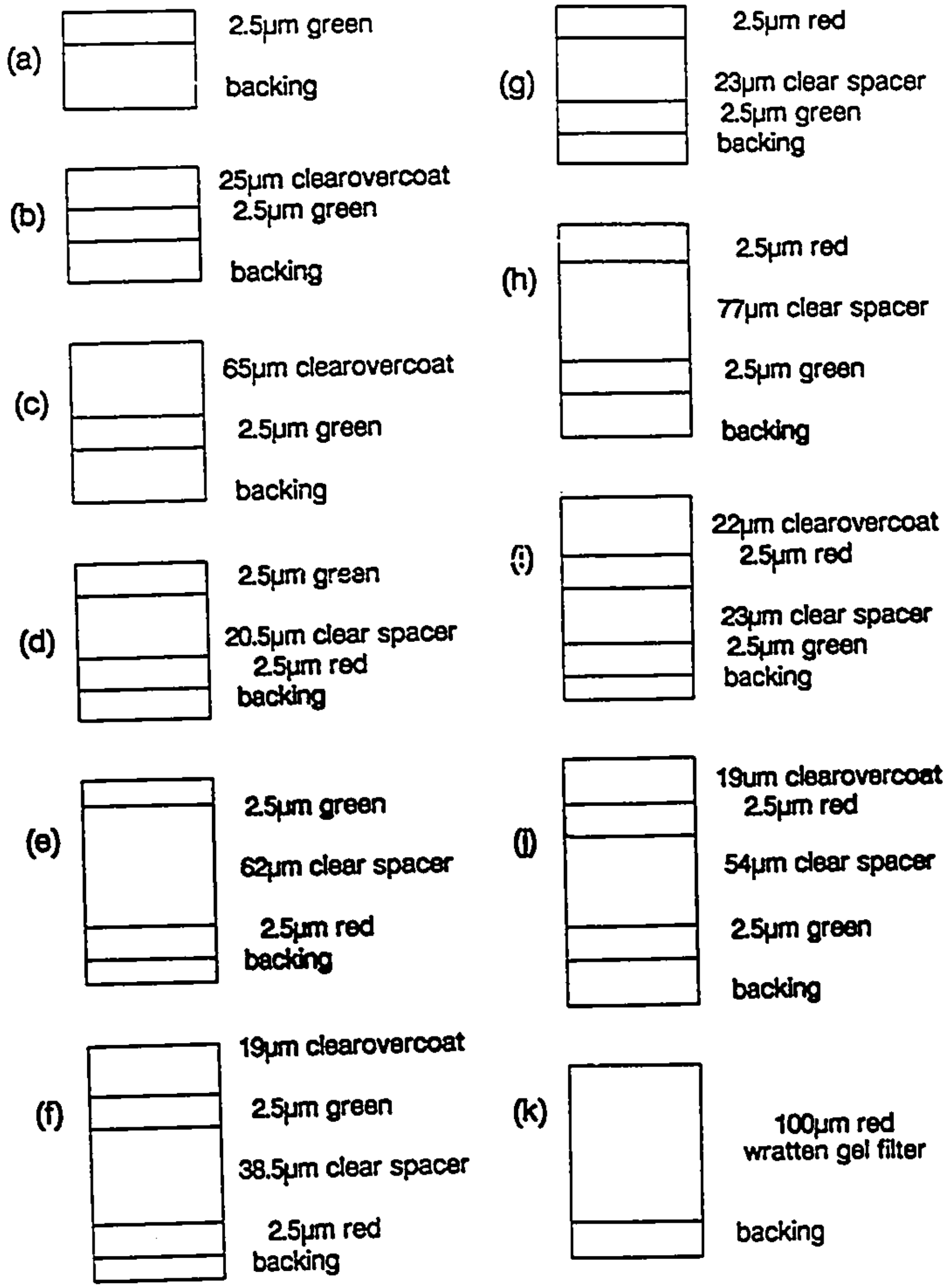

Figure 4.1: Schematic diagram of the sample composites discussed in this chapter (a-k).

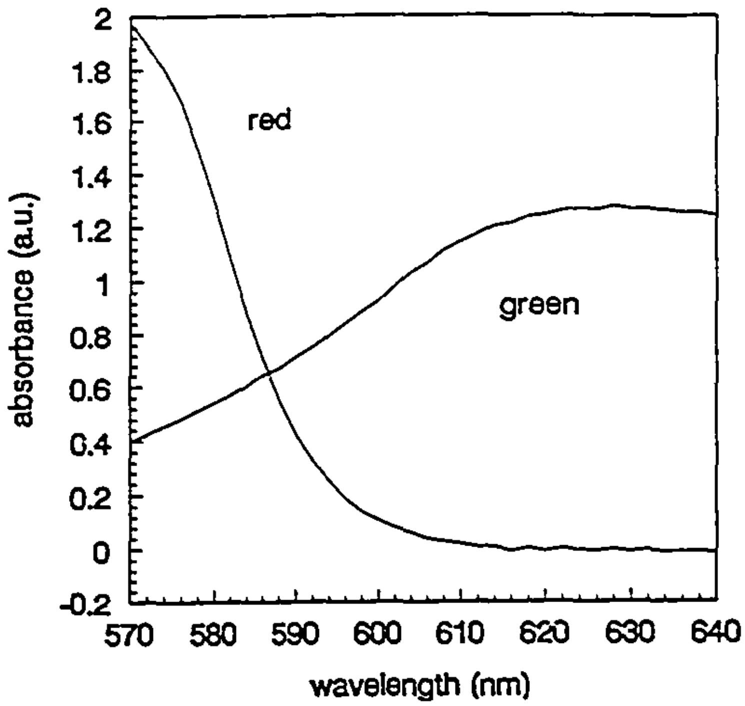

Figure 4.2: Absorption spectra for the red and green mylar films, measured using conventional UV-Visible spectrophotometry.

transparent above 600 nm. The variation of the absorbance of these two pigments over a range of wavelengths, may strongly affect the time dependence of the mirage effect impulse response. The layered composites were generated by pressing several mylar sheets together using optical epoxy glue (Epo-tek) at the interfaces. The thickness range of the application of the glue is in the order of 1-10 μm. The optical epoxy has thermal properties similar to the polymers examined; therefore, the layered composites were nearly thermally continuous. Replicate measurements of the thickness of films were made with a micrometer and average thickness is reported in the diagrams. The uncertainty in the thickness measurements is ca. 3 μm.

The other sample material used, (see Fig. 4.1(k)), is a Kodak™ wratten gel filter, which was found to be optically continuous over its 100 μm thickness, based on inspection by low magnification microscopy. Fig. 4.3 shows the absorption spectrum for a red Kodak™ wratten gel filter. The absorption measurements were made with a UV-Visible photodiode array spectrophotometer (Hewlett Packard 8452A). All samples were mounted with optical epoxy to polymethylmethacrylate (PMMA) disks, which was used to maintain, to a good approximation, a thermally continuous layer at the backing of the samples.

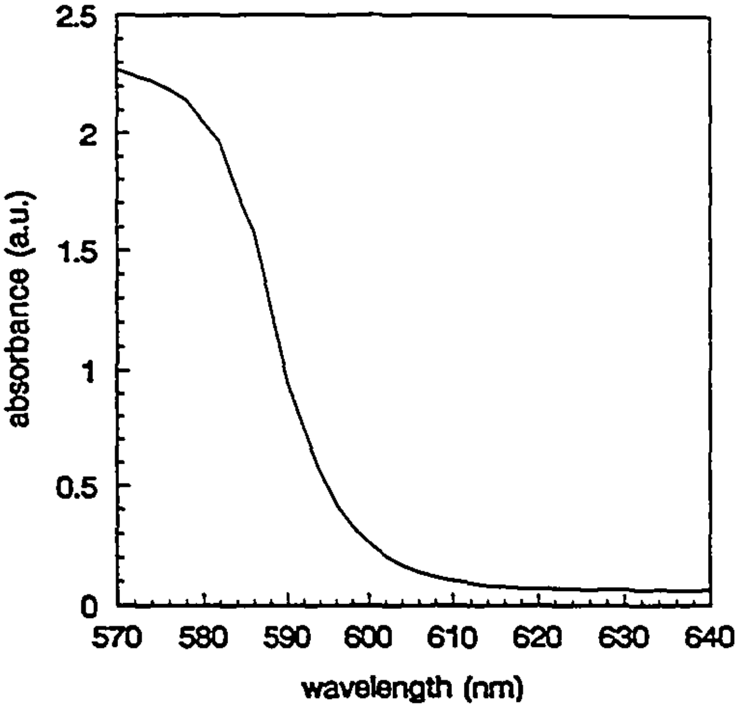

Figure 4.3: Absorption spectrum of Kodak™ wratten gel filter No. 25 measured using UV-Visible conventional spectrophotometry.

4.3 MIRAGE EFFECT DETECTION ON WELL CHARACTERIZED OPTICALLY INHOMOGENEOUS SAMPLES

4.3.1 Multilayered Laminate Composites

Several multilayered composites were prepared by arbitrarily stacking red and green pigmented mylar thin films in order to create samples which were approximately thermally homogeneous and optically heterogeneous. The composites formed by this method varied the position of the centroid of sample's optical absorption with depth, and in some cases, also with wavelength. All of the samples studied in this section were examined with water as the detection fluid.

The light deposition profile in a laminate composed of thin absorbers is approximated by the expression:

$$I(z) = \sum_{i=1}^{N} I_{i-1} \left(1 - e^{-\beta_i l_i}\right) \left[U(-(z+\sigma_{i-1})) - U(-(z+\sigma_i))\right] \tag{4.1}$$

where β_i is the absorption coefficient of the ith layer, U(z) is the unit step function, I_{i-1} is the light intensity incident on each layer

$$I_{i-1} = I_0 e^{-\beta_1 l_1} e^{-\beta_2 l_2} \cdots e^{-\beta_{i-1} l_{i-1}} \tag{4.2}$$

and where the summation is over N layers. Since the absorbing layers are very thin compared to the sample's total thickness, each layer behaves approximately as a thin planar heat source, weighted by a constant factor, which is proportional to the light absorbed in the layer:

$$[\, 1 - e^{-\beta_i l_i} \,] \tag{4.3}$$

It is assumed that the non-radiative conversion efficiency for each absorbing layer is approximately unity. Essentially all of the absorbed energy is converted to heat; no appreciable photoluminescence results and it is assumed that no photochemical reactions occur in the absorber layers.

The first series of composites examined shows the depth dependence of a plane heat source, placed at varying distances below the surface. A mylar film containing a 2.5 μm green pigment layer, was arbitrarily positioned at increasing depths from the sample surface. Fig. 4.1(a), (b), and (c) illustrate the samples prepared. For each sample region profiled, the corresponding He-Ne beam offset was determined as explained in section 2.4.3. Fig. 4.4 illustrates the impulse response traces obtained for a green absorbing layer positioned on the surface (Fig. 4.1(a)), beneath a 25 μm polymer clear overcoat (Fig. 4.1(b)), and beneath a 65 μm polymer clear overcoat (Fig. 4.1(c)) respectively. The corresponding theoretical traces are also shown (dotted lines), where the film thicknesses used to calculate the theoretical profiles, were those measured experimentally. In all cases, a thermal diffusivity of 1.0 x 10^{-7} m^2/s was assumed for this material, which is in agreement with the value determined in earlier work (1). For an absorber positioned near the surface of the sample, the thermal transit time required for heat conduction to the sample/fluid interface is short, giving an impulse response which peaks quickly and decays rapidly, as is seen in the first trace (Fig. 4.4, surface). As the absorber is positioned further away from the sample/fluid interface, there is a corresponding delay in the impulse response.

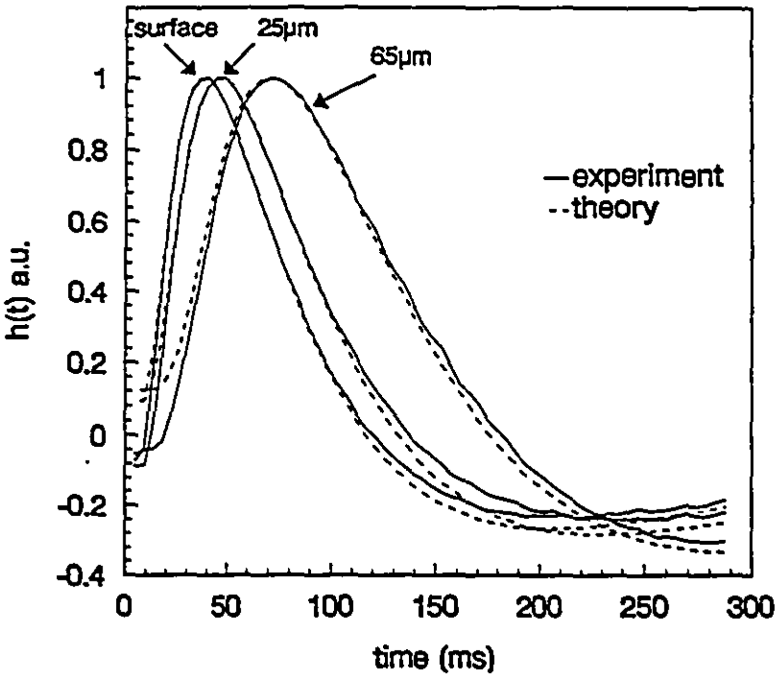

Fig. 4.4: Experimental impulse response traces for green absorber positioned at increasing depths below the surface. The corresponding theoretical curves are also indicated (dotted line). Measured He-Ne beam offset values were, respectively: 205 µm, 200 µm, 223 µm.

The significance of this study was two-fold. The multilayered composites were shown to be effectively thermally continuous throughout the sample, since good agreement between traces (calculated using the measured thicknesses and diffusivity for this material) and the experimental traces obtained using the apparatus, was observed. This indicates that variations in the depth profiling of the sample features are dominated by optical inhomogeneities rather than depth dependent thermal variations in the sample material; there are no significant thermal reflections detected between layers. For all impulse responses, the thermal transit time required for heat conduction to the deflecting beam, is dependent upon the He-Ne beam offset distance and the position of the absorbing layer in the sample. Once the He-Ne beam offset was experimentally determined, the corresponding impulse response was able to be precisely related to the position of the absorber. These experiments indicate that the mirage effect can be quantitatively used to determine the position of such absorbers.

An important limitation of the mirage effect technique in optical depth profiling is the strong surface weighting of the impulse response. The closer the distance at which the probe beam is offset from the surface, the stronger the weighting of any surface contributions to the impulse response. This idea is tested by performing experiments on samples in which the wavelength dependence of an absorbing underlayer was studied in the presence of a surface absorber. The corresponding structures used to obtain the traces in Fig. 4.5 are given in Figs. 4.1(d) and (e). The results from the experiments are presented in Fig. 4.5(a) to (d) respectively. As seen in Fig. 4.2, the surface layer of green pigment has moderate to strong absorption over the range of wavelengths studied. When the underlying red layer is located closer to the surface, at ca. 20 μm (as in Fig. 4.5(a)), the impulse response becomes even less sensitive to the presence of the underlayer. The impulse response obtained by applying the theory, presented in Fig. 4.5(b), shows the same trends. Although the mirage signal is strongly surface dominated in this case, it was shown that the key to enhancing the resolution of a buried feature in the presence of a strong surface absorber, is to ensure that probe beam offset distance from the surface is

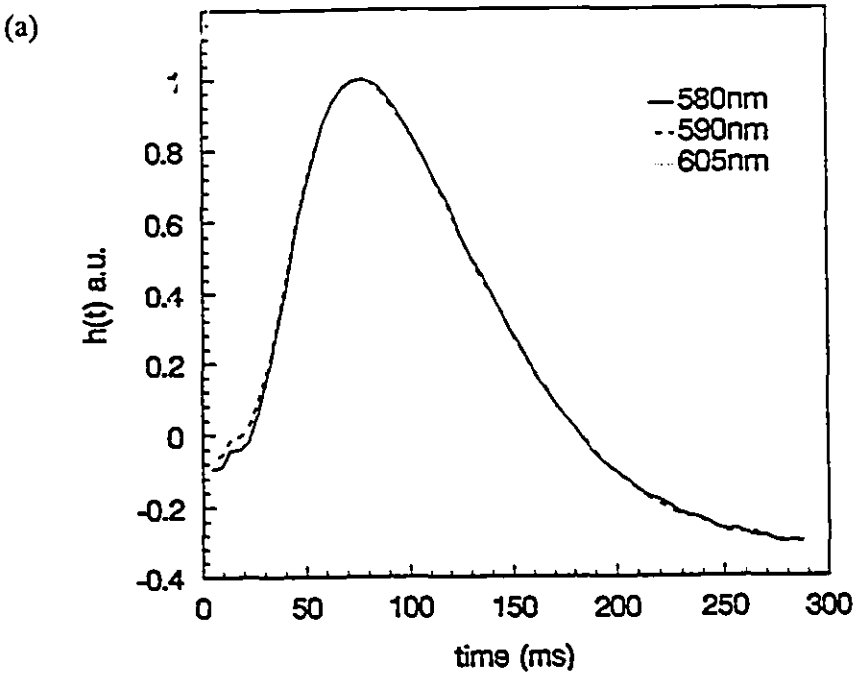

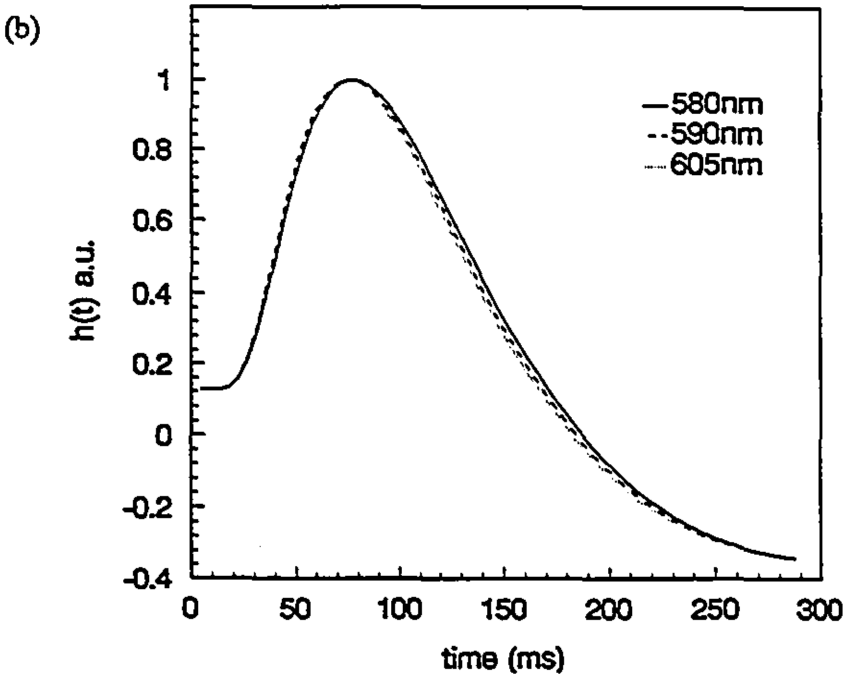

Figure 4.5:
(a) Experimental impulse response traces for sample depicted in Fig. 4.1(d).
(b) Theoretical traces corresponding to 4.5(a).

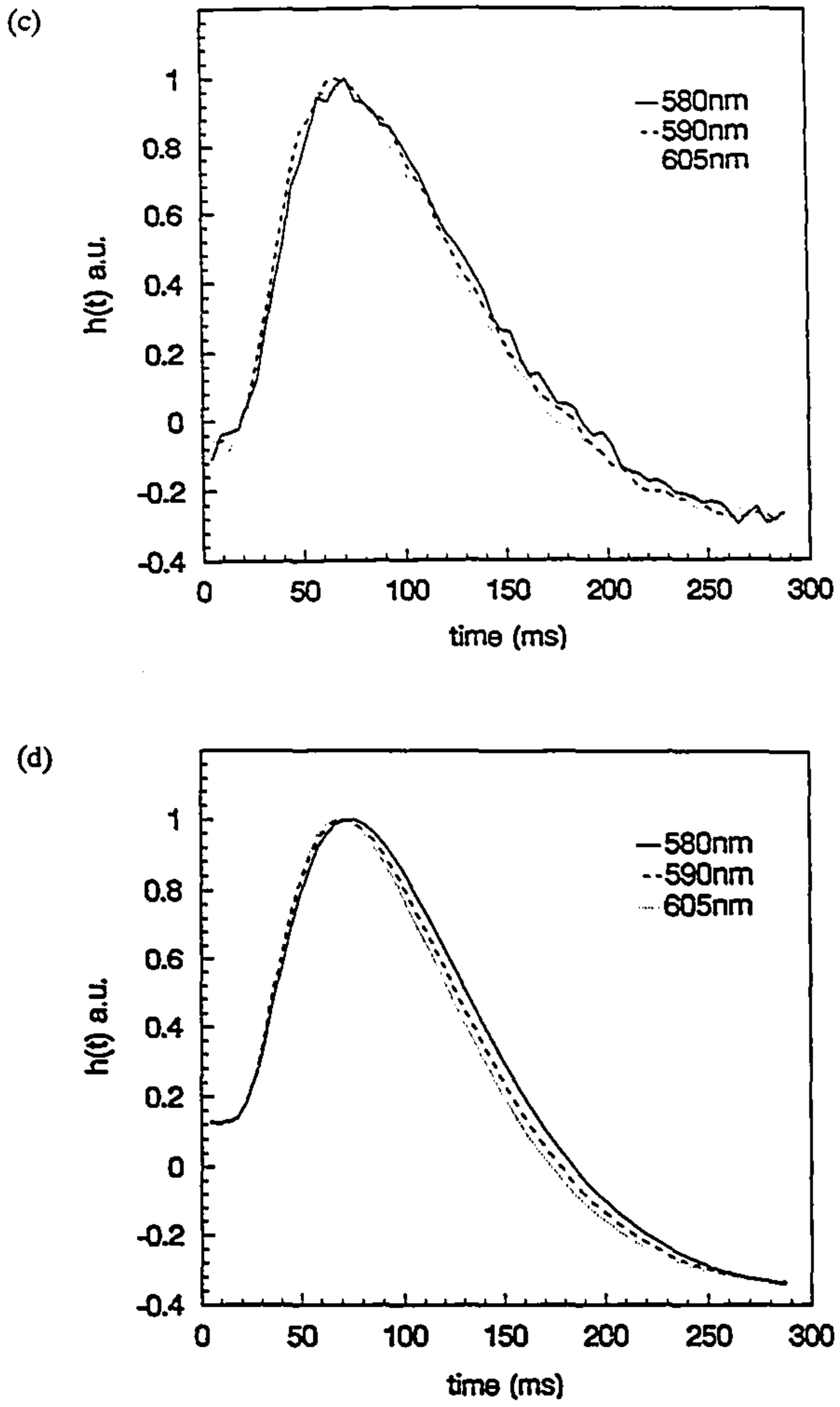

Figure 4.5:
(c) Experimental impulse response traces for sample depicted in Fig. 4.1(e).
(d) Theoretical traces corresponding to 4.5(c).

of the same order of thermal distance as the separation of the layers to be resolved. As the red absorber is displaced at the larger distance of 62 μm from the surface, it is just possible to detect the absorption of the red underlayer, as a broadening of the impulse response at the shorter wavelengths (Fig. 4.5(c) and corresponding theoretical trace in Fig. 4.5(d)). The layer spacing of 62 μm represents a larger fraction of the experimental probe beam offset distance (which is ca. 300 μm), than is the case for the layer placed at a spacing of 20 μm. This suggests that the resolving power for the 62 μm spacing is greater at this offset distance.

The structures studied in Fig. 4.5 give a severe test of the method's resolving power because of the relatively strong optical absorption at the surface. Good contrast for depth profiling of subsurface features is only obtained when the surface absorbing layer becomes sufficiently transparent within a range of wavelengths, to allow subsurface layers to contribute significantly to the signal, and, therefore, to be profiled. The structures given by Fig. 4.1(g) and (h) illustrate the situation which arises when the position of absorbers in the structure are reversed. The red absorbing layer now appears at the surface, with the green subsurface absorber lying under a transparent spacer of variable thickness. The absorption spectrum of Fig. 4.2, shows that the red pigment becomes transparent at wavelengths greater than 600 nm. Depth profiling performed in this range will allow the features of the green subsurface absorber to be visually resolved, including its position in the sample composite. Fig. 4.6(a) and Fig. 4.6(b) illustrate the wavelength dependence of experimental impulse response traces, as the spacer thickness increases from 23 to 77 μm.

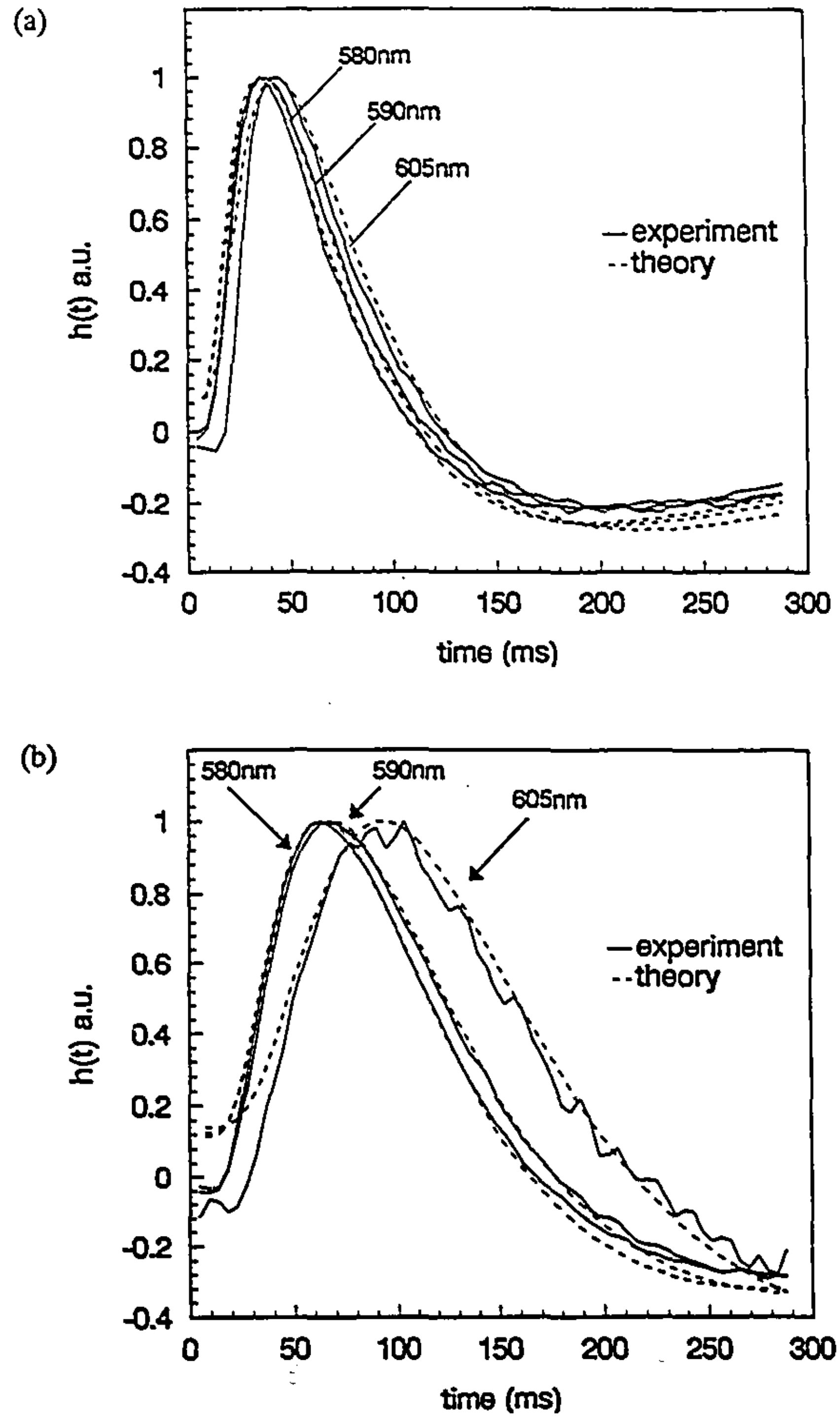

Figure 4.6:

(a) Experimental impulse response traces for sample depicted in Fig. 4.1(g) and the corresponding theoretical traces (dotted lines).

(b) Experimental impulse response traces for sample depicted in Fig. 4.1(h) and the corresponding theoretical traces (dotted lines).

At 580 nm and 590 nm, similar impulse response traces are expected, corresponding to a strong signal dominated mainly by the red absorber, but with a contribution also from the green subsurface layer. At 605 nm, the impulse response traces show mainly the absorption from the green subsurface absorbing layer. As the position of the green absorber is increased from 23 μm (Fig. 4.6(a)) to 77 μm (Fig. 4.6(b)), a corresponding delay is noted in the impulse response, with the visual contrast improving for the deeper layer. It should be noted that the more rapid impulse response observed for the data of Fig. 4.6(a) is due to the substantially smaller probe beam offset that was used for this measurement ($z = 193$ μm) compared to that of Fig. 4.6(b) ($z = 280$ μm). Theoretical predictions obtained for these cases were in good agreement with the experimental results. The axonometric displays of Fig. 4.7(a) and Fig. 4.7(b) compare the wavelength dependence of the experimental and theoretical impulse response data for sample Fig. 4.1(h). The three dimensional response surface shows the increase in the peak delay position of the impulse response with increasing wavelength, corresponding to the depth profiling of the subsurface green absorber as the red surface absorber becomes transparent. Displacing the assembly of absorbers under a spacer layer of 20 μm, (see Fig. 4.1(i), (j)) gave a similar level of visual contrast, and agreement between theory and experiment (Fig. 4.8) and (Fig. 4.9).

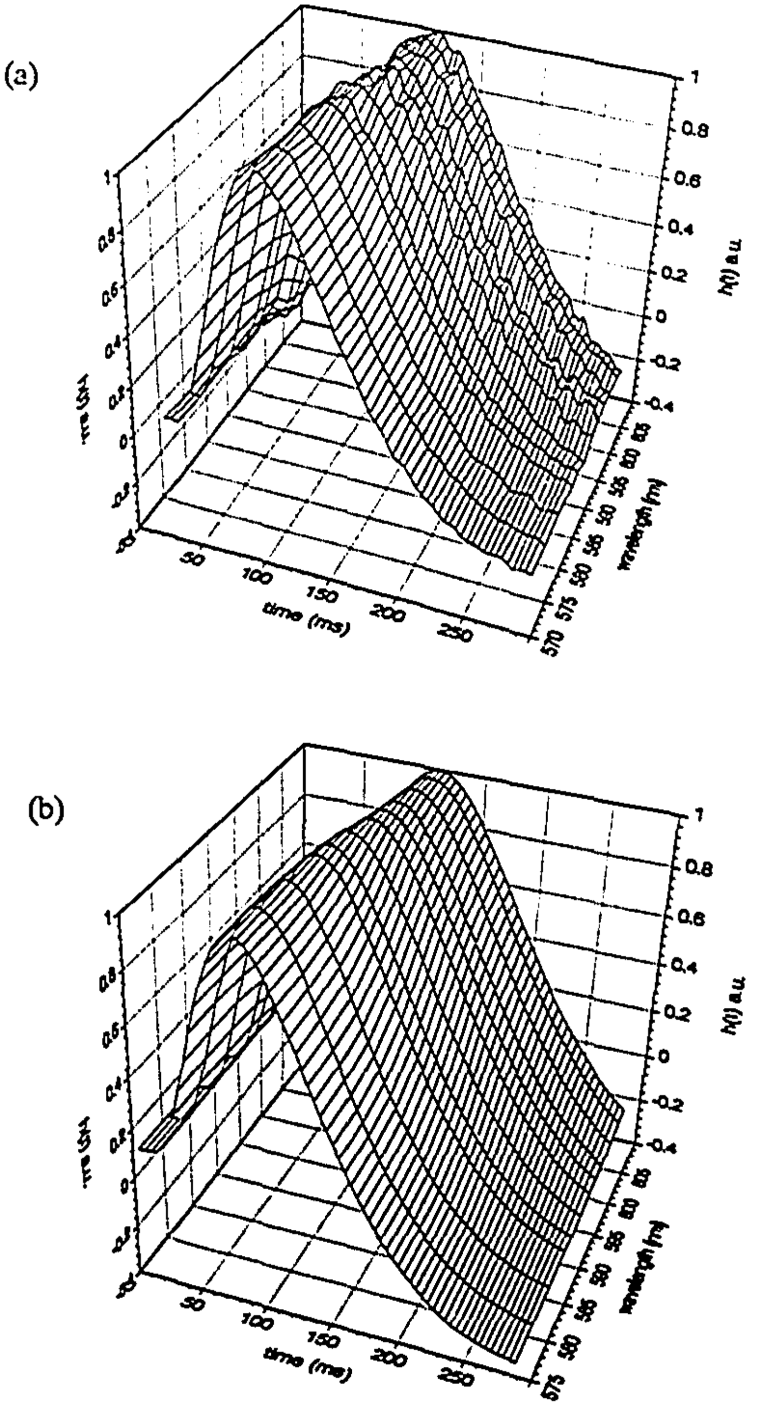

Figure 4.7:

(a) Experimental impulse response traces on variation of the pump beam wavelengths incident on a sample depicted in Fig. 4.1(h).

(b) Corresponding theoretical impulse response traces varying the pump beam wavelengths incident on a sample depicted in Fig. 4.1(h).

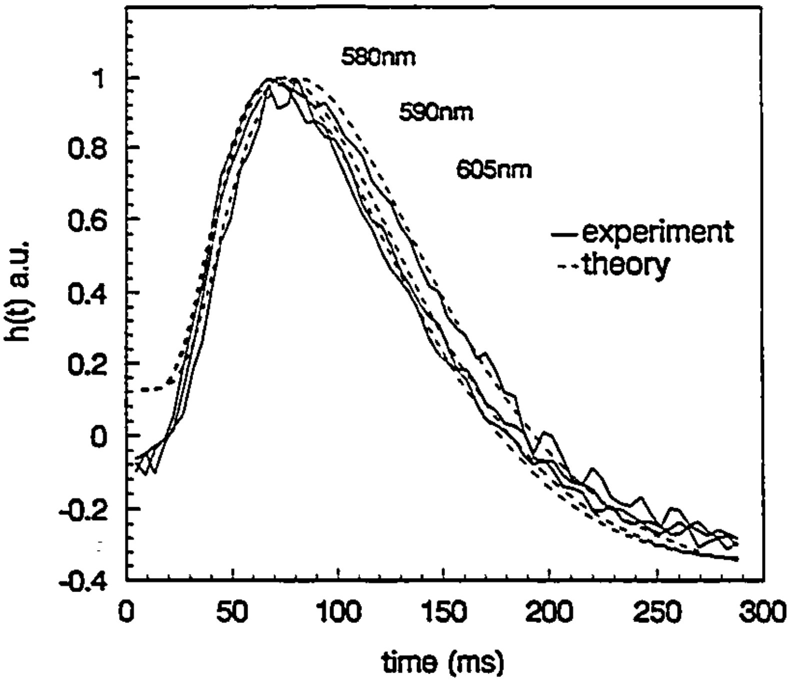

Figure 4.8: Experimental impulse response traces for sample depicted in Fig. 4.1(i) and corresponding theoretical impulse response traces (dotted line).

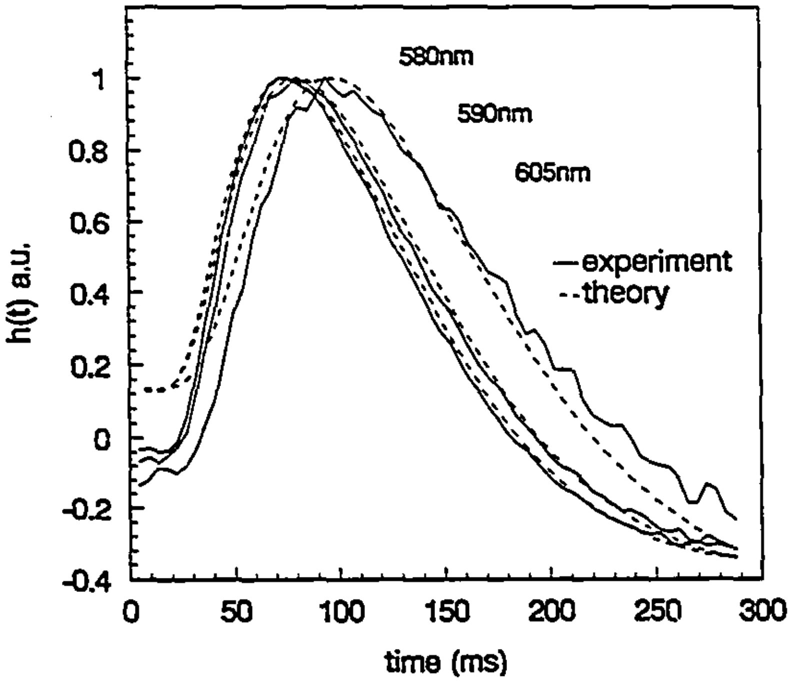

Figure 4.9: Experimental impulse response traces for sample depicted in Fig. 4.1(j) and corresponding theoretical impulse response traces (dotted line).

4.3.2 Samples with Continuous Optical Properties

In this set of studies, the mirage signal was examined in samples having continuous optical properties. These samples consisted of Kodak™ wratten gelatin filters, which are composed of gelatin material doped with a pigment. The distribution of the pigment is verified to be continuous throughout the 100 μm thickness of these filters. Since wratten gel filters are soluble in water, the detection medium was changed to paraffin oil. The latter has a lower thermal diffusivity than water (0.9×10^{-7} m^2/s relative to 1.4×10^{-7} m^2/s). This means that all thermal transit times to the probe beam offset position are increased for the same measured offset distance values. The wratten gel sample is presented in Fig. 4.1(k). The corresponding absorption spectrum can be found in Fig. 4.3. For this sample, the pump wavelength was varied, obtaining impulse response measurements at 1 nm increments from 590 nm to 605 nm. Below 590 nm, there is a saturation of the impulse response signal, with very little variation noted between impulse response traces in this range. Fig. 4.10(a) illustrates one set of experimental data obtained. The corresponding theoretical traces can be found in Fig. 4.10(b). The assumed values of the optical absorption coefficient were obtained directly from Fig. 4.3. For continuous samples the dependence of the photothermal impulse response on the optical absorption coefficient, ß, can be interpreted directly in terms of the optical length obtained in the sample. As the wavelength is increased, the value of ß decreases, according to the absorption spectrum given in Fig. 4.3. The centroid of optical absorption is located more deeply below the sample surface, and the profile of absorbed light becomes more uniform

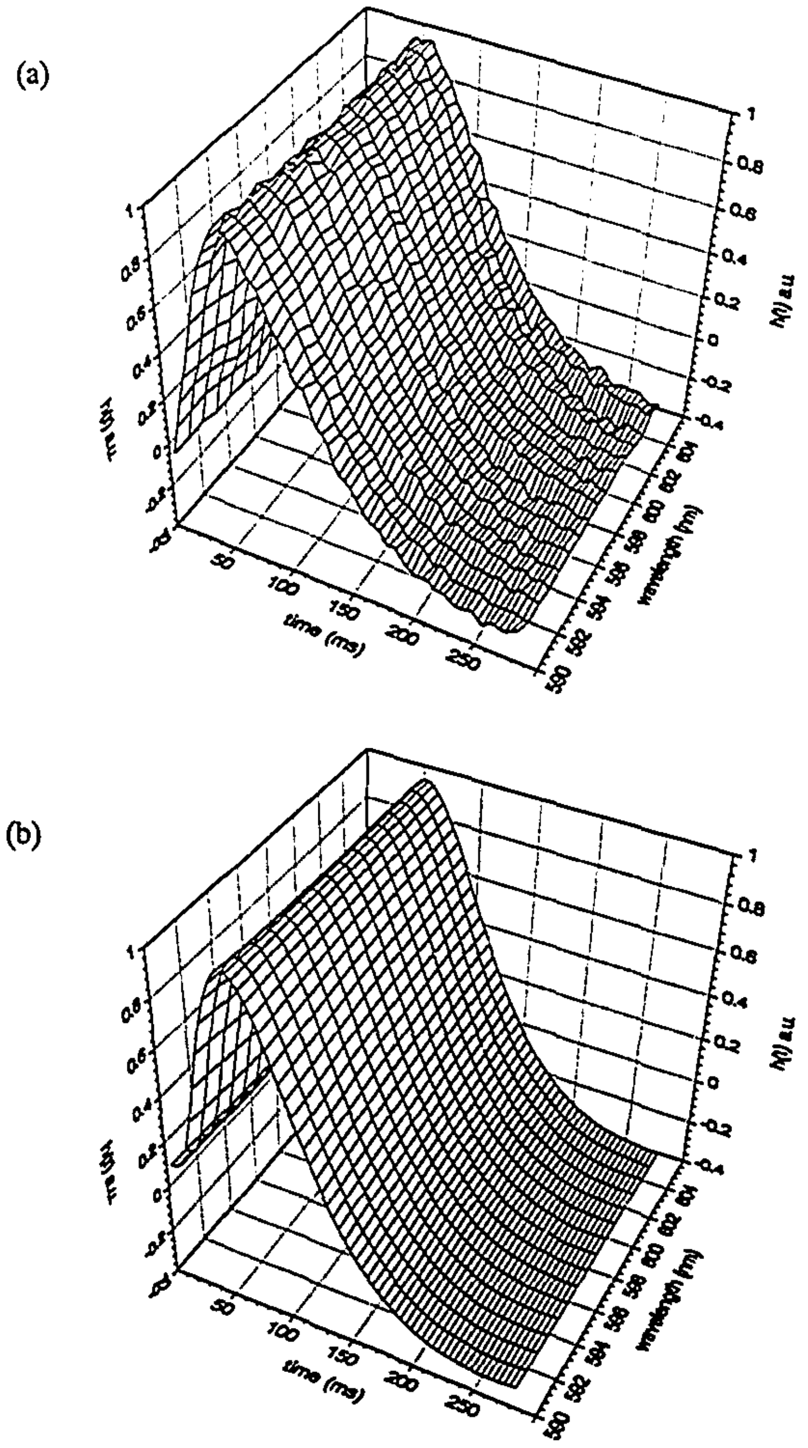

Figure 4.10:

(a) Experimental impulse response traces on variation of the pump beam wavelengths incident on a red wratten gel filter (a continuous absorber), depicted in Fig. 4.1(k).

(b) Corresponding theoretical response traces varying the pump beam wavelengths incident on a red wratten gel filter (a continuous absorber), depicted in Fig. 4.1(k).

with depth. A corresponding delay is observed in the impulse response because more time is required for heat conduction to the sample surface from the lower depths. At shorter wavelengths, where ß is larger, the light attenuation profile is confined closer to the sample surface. A shorter peak delay in the impulse response is observed because the overall thermal transit time to the offset probe beam is now reduced. At the shortest wavelengths, ß becomes large enough that the impulse response starts to become invariant with increased optical absorption, as noted above, with photothermal saturation effectively being attained in this region.

4.4 CONCLUSION

Mirage effect spectroscopy was used for optical depth profiling of discrete and continuous absorbers in multilayered composites. It was shown that the ability to resolve the contributions from individual absorbing layers depends upon the relative weighting of a surface absorber to that of a subsurface feature to be resolved. In addition, it is necessary to have the probe beam offset distance from the surface of the same order of thermal distance as the separation of the layers to be resolved. The ultimate use of this technique would be for the detection of depth dependent absorptivity in a sample of unknown properties. To achieve this goal, the inverse problem theory will be examined in Chapter 5.

REFERENCES

---

1. J.F. Power, Appl. Spectrosc. **45**, 1252 (1991).

CHAPTER 5 DIFFRACTION MODEL AND ITS IMPLEMENTATION IN INVERSE PROBLEM THEORY FOR MIRAGE EFFECT DEPTH PROFILING

5.1 INTRODUCTION

It was shown in Chapter 4 that excellent agreement was obtained between theoretical simulations and experimental results for the impulse mirage effect measurements. The most important systematic errors in the measurement were also identified and compensated. In practice, the He-Ne probe beam dimensions are not infinitesimally small with respect to the He-Ne beam offset from the sample surface. Although the approximations outlined in Chapter 3 give a good general agreement between theory and experiment, a more rigorous theoretical model is needed for highly quantitative modelling. The approach used to enable more quantitative modelling is Fresnel diffraction theory. This theory describes the distributed effects of the refractive index gradient above the sample surface on the beam profile of the probe beam. This model is outlined in this chapter, and is used for the inverse problem theory for the mirage effect phenomenon.

5.2 FRESNEL DIFFRACTION THEORY

5.2.1 Propagation of a wave

A spherical optical wave with a Gaussian variation in its amplitude, can be described as follows:

$$U(x,y) = \sqrt{\frac{2}{\pi}}\,\frac{1}{\omega}\cdot e^{-j\frac{\pi}{\lambda}\frac{(x^2+y^2)}{R}}\cdot e^{-\frac{(x^2+y^2)}{\omega^2}} \tag{5.1}$$

where the first exponential expression describes a spherical wave with radius, R, and the second exponential describes a Gaussian distribution with spot size, ω. By defining a complex radius of curvature, q_r,

$$q_r = z + \frac{j\pi\omega_0^2}{\lambda} \qquad \text{where} \quad R \approx z \quad \text{for} \quad z >> \frac{\pi\omega_0^2}{\lambda} \tag{5.2}$$

equation (5.1) can be rewritten as

$$U(x,y) = \sqrt{\frac{2}{\pi}}\,\frac{1}{\omega}e^{-j\frac{\pi}{\lambda}\frac{(x^2+y^2)}{q_r}} \tag{5.3}$$

This equation may be used to describe the propagation of a Gaussian spherical wave from its initial point, $U_0(x_0,y_0,z_0)$, to a position $z=z_0+L$, as shown in Fig. 5.1. By

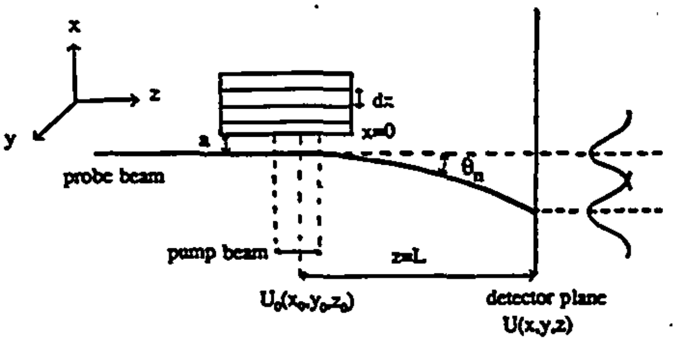

Figure 5.1: A schematic diagram of mirage effect geometry including the propagation of a Gaussian plane wave from its initial point, $U_0(x_0,y_0,z_0)$, to a position z=L. The sample is discretized in x as a series of plane sources, which are spaced at uniform intervals through the sample thickness.

using the relation given in equation (5.3), equation (5.4) describes the Gaussian spherical wave at position $z=z_0+L$:

$$U(x,y) = \sqrt{\frac{2}{\pi}}\,\frac{j}{\omega\lambda}\frac{e^{-jkz}}{z}\int_{-\infty}^{+\infty} e^{-j\frac{k}{2z}[(x-x_0)^2+(y-y_0)^2]}\cdot e^{[-j\frac{k}{2q_r}(x_0^2+y_0^2)]}dx_0dy_0 \tag{5.4}$$

where all variables with subscript 0 indicate the coordinates in the input plane, and $k = 2\pi/\lambda$ (1). Table 5.1 (at the end of Chapter 5, page 158) lists the symbols used for this chapter.

5.2.2 Development of the Diffraction model

The development of the diffraction model was made jointly by Power and Schweitzer, and will be outlined in this section. As the probe beam propagates through space, the beam interacts with the medium and undergoes diffraction. Fig. 5.1 illustrates the mirage effect phenomenon with the propagation of the probe beam, as it undergoes diffraction as well as deflection. This introduces an additional factor, $\exp(j\Phi(x_0))$, to account for the contribution of the mirage effect to the signal's phase variation, where:

$$j\phi(x_0) = jkl(\frac{dn}{dT})\Delta T(x_0,t) \tag{5.5}$$

and l is the diameter of the pump beam. This additional factor, $\exp(j\Phi(x_0))$, multiplies with equation (5.4), resulting in:

$$U(x,y) = \frac{j}{\lambda z}\sqrt{\frac{2}{\pi}\,\frac{1}{\omega}}\,e^{-jkz}\int\!\!\int_{-\infty}^{+\infty} e^{\frac{-jk}{2q_r}(x_0^2+y_0^2)}\cdot e^{\frac{-jk}{2z}[(x-x_0)^2+(y-y_0)^2]}\cdot e^{j\phi(x_0)}\,dx_0dy_0 \tag{5.6}$$

For small changes in temperature, as is the case with mirage effect deflections, the following approximation can be made:

$$e^{j\phi(x_0)} \approx 1+j\phi(x_0) \tag{5.7}$$

making this substitution, equation (5.6) becomes:

$$U(x,y) = \sqrt{\frac{2}{\pi}\,\frac{j}{\lambda z\omega}}\,e^{-jkz}\int\!\!\int_{-\infty}^{+\infty} e^{\frac{-jk}{2q_r}(x_0^2+y_0^2)}\cdot e^{\frac{-jk}{2z}[(x-x_0)^2+(y-y_0)^2]}\cdot[1+j\phi(x_0)]\,dx_0dy_0 \tag{5.8}$$

Substitution of equation (5.5) into equation (5.8) results in equation (5.9):

$$U(x,y) = \frac{j}{\lambda z}\sqrt{\frac{2}{\pi}\,\frac{1}{\omega}}\,e^{-jkz}\int\!\!\int_{-\infty}^{+\infty} e^{\frac{-jk}{2q_r}(x_0^2+y_0^2)}\cdot e^{\frac{-jk}{2z}[(x-x_0)^2+(y-y_0)^2]}\cdot\left[1+jkl\frac{dn}{dT}\Delta T(x_0,t)\right]dx_0dy_0 \tag{5.9}$$

Expanding this expression further, gives:

$$U(x,y) = \frac{j}{\lambda z}\sqrt{\frac{2}{\pi}\,\frac{1}{\omega}}\,e^{-jkz}\;\int\!\!\int_{-\infty}^{+\infty} e^{\frac{-jk}{2q_r}(x_0^2+y_0^2)}\cdot e^{\frac{-jk}{2z}[(x-x_0)^2+(y-y_0)^2]}\,dx_0dy_0 \;+\; jkl\frac{dn}{dT}\int\!\!\int_{-\infty}^{+\infty}\frac{A_0}{\sqrt{4\alpha t}}\cdot e^{\frac{-(x_0+a)^2}{4\alpha t}}\cdot e^{\frac{-jk}{2q_r}[(x_0^2+y_0^2)]}\cdot e^{\frac{-jk}{2z}[(x-x_0)^2+(y-y_0)^2]}\,dx_0dy \tag{5.10}$$

where

$$\frac{A_0}{\sqrt{4\alpha t}}\cdot e^{\frac{-(x_0+a)^2}{4\alpha t}} \tag{5.11}$$

is the expression for the change in the temperature due to the mirage effect at time, t, and where (x_0+a) indicates a combined distance, which includes the offset of the probe beam and the spacing into the sample of the region being profiled, relative to the initial position, x_0 (Fig. 5.1).

In order to solve equation (5.10), the expression is broken into three components:

$$K = \frac{j}{\lambda z}\sqrt{\frac{2}{\pi}\,\frac{1}{\omega}}\,e^{-jkz} \tag{5.12}$$

$$\begin{aligned} I = &\int_{-\infty}^{+\infty} e^{\frac{-jk}{2q_r}(y_0^2)}\cdot e^{\frac{-jk}{2z}[(y-y_0)^2]}dy_0\ \cdot \\ &\int_{-\infty}^{+\infty} e^{\frac{-jk}{2q_r}(x_0^2)}\cdot e^{\frac{-jk}{2z}[(x-x_0)^2]}dx_0 \end{aligned} \tag{5.13}$$

$$\begin{aligned} II = jkl\frac{dn}{dT}\frac{A_0}{\sqrt{4\alpha t}}&\int_{-\infty}^{+\infty} e^{\frac{-jk}{2q_r}(y_0^2)}\cdot e^{\frac{-jk}{2z}[(y-y_0)^2]}dy_o \\ &\int_{-\infty}^{+\infty} e^{-\frac{(x_0+a)^2}{4\alpha t}}\cdot e^{\frac{-jk}{2q_r}(x_0^2)}\cdot e^{\frac{-jk}{2z}[(x-x_o)^2]}dx_0 \end{aligned} \tag{5.14}$$

Each of the integrals in these expressions is solved by completing the square in the exponential term, simplifying the resulting expressions, and obtaining a form of the integral which can be solved using mathematical tables (2).

Solving for equation (5.13) using this procedure, results in the following expression:

$$I = \pi \frac{2q_r z}{jk(q_r+z)} \cdot e^{\frac{-jk}{2(q_r+z)}(x^2+y^2)} \tag{5.15}$$

and for equation (5.14), the following:

$$II = jkl \frac{dn}{dT} \frac{A_0}{\sqrt{4\alpha t}} \frac{2}{jk} \left(\frac{q_r z}{q_r+z}\right)^{\frac{1}{2}} q_p^{\frac{1}{2}} \pi \cdot e^{\frac{-jk}{2(q_r+z)}(y^2)} \cdot e^{\frac{-jk}{2z}(x^2)} \cdot e^{\frac{a^2}{4\alpha t}} \cdot e^{\frac{jkq_p}{2}\left[\frac{x}{z}+\frac{ja}{2k\alpha t}\right]} \tag{5.16}$$

where

$$q_p = \frac{q_r z}{q_r+z} + \frac{1}{2jk\alpha t} \tag{5.17}$$

The quantity of interest is the squared magnitude of U(x,y), which is obtained from equation (5.18)

$$|U(x,y)|^2 = K[(I)(II)^* + (I)^*(II)] \tag{5.18}$$

Upon simplification the following equation results:

$$
\begin{aligned}
|U(x,y)|^2 = {} & \left(\frac{4\pi^2}{jk} \frac{dn}{dT} \frac{lA_0}{\sqrt{4\alpha t}} \, e^{\frac{-a^2}{4\alpha t}} \left[\frac{j}{\lambda z w} \sqrt{\frac{2}{\pi}} \, e^{-jkz} \right] \right) \cdot \\
& \left[\left(\frac{q_r z}{q_r + z} \right) \left[\left(\frac{q_r z}{q_r + z} \right)^{1/2} \right]^{*} \left(q_p^{1/2} \right)^{*} \cdot \right. \\
& e^{\frac{-jk}{2(q_r+z)}(x^2+y^2)} \cdot e^{\left[\frac{-jk}{2(q_r+z)}\right]^{*}(y^2)} \cdot e^{\frac{jk}{2z}(x^2)} \cdot \\
& e^{\left[\frac{jkq_p}{2z^2}\right]^{*}(x^2)} \cdot e^{\left[\frac{-aq_p}{2z\alpha t}\right]^{*}(x)} \cdot e^{\left[\frac{-jkq_p a^2}{2(2k\alpha t)^2}\right]^{*}} + \qquad (5.19) \\
& (-1) \left[\left(\frac{q_r z}{q_r + z} \right) \right]^{*} \left(\frac{q_r z}{q_r + z} \right)^{1/2} \left(q_p^{1/2} \right) e^{-\left(\frac{jk}{2z}\right)(x^2)} \cdot e^{\left[\frac{-jk}{2(q_r+z)}\right]^{*}(x^2+y^2)} \cdot \\
& \left. e^{\left[\frac{-jk}{2(q_r+z)}\right](y^2)} \cdot e^{\left[\frac{jkq_p}{2z^2}\right](x^2)} \cdot e^{\left[\frac{-aq_p}{2z\alpha t}\right](x)} \cdot e^{\left[\frac{-jkq_p a^2}{2(2k\alpha t)^2}\right]} \right]
\end{aligned}
$$

where * indicates the complex conjugate (of the expression in brackets). This equation gives the spatial dependence of the diffracted probe beam intensity perturbed by the mirage effect phenomenon at the detector plane. Equation (5.19) is calculated for each individual planar source in the sample. Due to the linearity implicit in the approximation in equation (5.7), and the fact the change in temperature is very small, the response of an array of discrete layers should yield the sum of the individual responses predicted in equation (5.19).

5.2.3 Addition of Bicell Photodetector to Instrumentation

A modification to the instrumentation was made in the form of replacing the pinhole/photodiode detector with a bicell position sensor (Hamamatsu S2721-02). As was outlined in section 2.4.2, only a small region of the probe beam was integrated with the photodiode/pinhole arrangement. As a result, small imperfections in the modal quality of the He-Ne beam may be detected, and one must ensure that the region of the Gaussian beam around either inflection point is sampled in the detector plane. The two inflection points will give different probe beam offset dimensions, and as the diameter of the He-Ne beam is 80 μm, this means that the inflection point closer to the sample surface will give a different offset to that of the inflection point which is further away from the sample surface. Therefore, the transverse sampling region of the Gaussian profile at the detector plane must ideally be constant at all times during the experiment.

As explained previously, the mirage effect technique uses a modulated heating source to obtain the impulse response. This requires measurement in the frequency domain, which results in a signal response consisting of an inherent d.c. level about which an a.c. signal oscillates (the a.c. component being the signal due to the mirage effect deflection). The Gaussian beam striking the detector contains two regions about the inflection points about which the nonlinearity in the intensity variation is minimal (the response detected within these regions is essentially linear). In this configuration, the measured wideband a.c. response recovers the impulse response of the beam deflection in the neighbourhood of the inflection position of the Gaussian beam. Should a large static deflection of the probe beam occur (which is apparent using oil as the deflecting medium, as was described in section 4.3.2), the position of the monitored inflection point may shift, requiring the manual translation of the photodiode/pinhole apparatus to re-establish the linear Gaussian region of the beam.

To overcome these effects, a position sensor consisting of a bicell was implemented (Fig. 5.2). By setting up the appropriate electronic circuitry, the sensor can operate in two modes. If the sensor is set in the summing mode, the total voltage from both sections of the bicell is received as the signal. If the sensor is set in difference mode, the voltage output is the difference of the voltages from each section of the bicell. The difference voltage will be zero, should the beam be positioned exactly symmetrically with respect to the midline of the bicell.

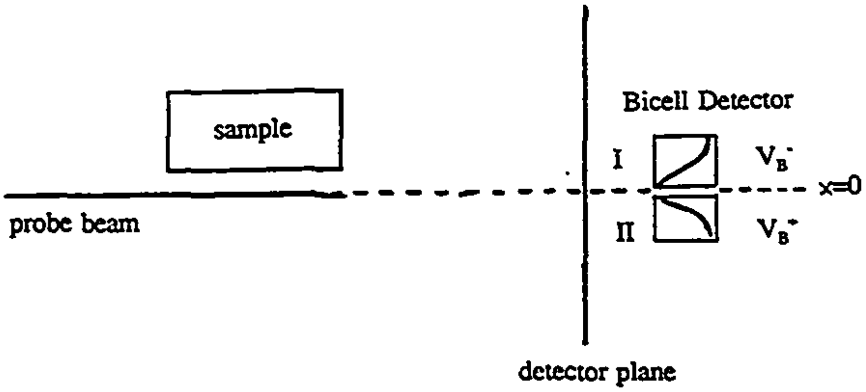

Figure 5.2: A schematic diagram showing the two light sensing regions of the bicell detector, and the Gaussian distribution of the probe beam striking the detector, centred symmetrically about the midline.

The waist position of the He-Ne probe beam and the beam spot size at that position was found using the following procedure. At several positions along the optical axis, a knife edge was scanned across the probe beam diameter. At each position of the knife edge, the total light intensity reaching the detector, in summing mode, was recorded by noting the voltage. The voltage obtained is plotted versus the translation of the knife edge, to reconstruct the integral of the Gaussian light profile at each position of the knife edge. From this integral relationship, the beam spot size at a specific position on the optical axis (z axis) may be determined. The spot size is then plotted versus the various measurement positions taken along the optical axis. The following relationship gives the dimensions of the spot size at a position, z, on the optical axis:

$$\omega(z) = \omega_0 \sqrt{1+\left[\frac{\lambda z}{\pi\omega_0^2}\right]^2} \approx \omega_0 \frac{z}{z_c} \tag{5.20}$$

where this approximation is valid in the far field. By plotting the spot size dimension, $\omega(z)$, versus the position, z, on the optical axis, a linear extrapolation of the curve will give the z intercept, at $z=z_0$, which is the precise position of the waist. The slope of the line will give the beam dimension (radius) at the waist position, w_0. The length of the confocal region will then have a value of $2z_c$ (a length of z_c on either side of the probe waist), where $z_c = \lambda/(\pi\omega_0^2)$ (1).

In the mirage effect experiments, the bicell detector is used in difference mode, since the deflection due to the mirage effect will cause movement of the beam and, therefore, a variation in the light intensity striking each section of the bicell detector (Fig. 5.2). However, the integral intensity will remain the same, as long as the beam remains aligned on the bicell. The summing position is used to ensure that the light intensity is constant over all measurements taken with the sample. The wideband signal consists of an a.c. response superimposed on a d.c. level. Therefore, even if a large d.c. deflection were to occur, the summing mode signal will confirm that the entire beam remains positioned on the detector. The overall difference signal remains linear under these conditions. If the beam physically moves off the detector (which can result from very intense d.c. heating of the sample surface and/or fluid medium), the reference position can be re-established by displacing the detector and monitoring the summing mode signal until it is restored to the maximum level.

5.2.4 Theoretical Bicell Signal

In order to properly compute the diffraction signal, equation (5.19) must be integrated over each of the light sensing sections of the bicell, and the difference between them taken as the signal response:

$$\Delta V_B = V_B^+ - V_B^- \tag{5.21}$$

where the positive and negative regions are indicated in Fig. 5.2. V_B^+ and V_B^- in equation (5.21) are given by:

$$\begin{aligned} V_B^+ &= \int_{-\infty}^{+\infty}\int_{-\delta}^{+\infty} I_t(x,y)\,dx\,dy \\ V_B^- &= \int_{-\infty}^{+\infty}\int_{-\infty}^{+\delta} I_t(x,y)\,dx\,dy \end{aligned} \tag{5.22}$$

Again, the integrals are solved using the completion of squares, resulting in the following expression for the bicell difference signal:

$$
\begin{aligned}
\Delta V_B = \Bigg[& \left[\frac{4\pi^3}{jk}\frac{dn}{dT}\frac{lA_0}{\sqrt{4\alpha t}}\; e^{-a^2/4\alpha t}\left[\frac{j}{\lambda z w}\sqrt{\frac{2}{\pi}}\; e^{-jkz}\right]\left[\frac{[(R+z)\pi\omega^2]^2+[R\lambda z]^2}{k[R\lambda\pi\omega^2(R+z)-R\lambda z\pi\omega^2]}\right]^{1/2}\right]\cdot \\
& \left[\left(\frac{q_r z}{q_r+z}\right)\left[\left(\frac{q_r z}{q_r+z}\right)^{1/2}\right]^{*}\right]\left(q_p^{1/2}\right) e^{\left[\frac{-jkq_p a^2}{2(2\alpha k t)^2}\right]^{*}}\left(\frac{e^{-n_1\beta_1^2}}{jn_1^{1/2}}\right)\left[-erf(jn_1^{1/2}(\delta^{+}-\beta_1))\right] - \\
& \left[\left(\frac{q_r z}{q_r+z}\right)^{*}\right]\left(\frac{q_r z}{q_r+z}\right)^{1/2}\left(q_p^{1/2}\right) e^{\left[\frac{-jkq_p a^2}{2(2\alpha k t)^2}\right]}\left(\frac{e^{n_2\beta_2^2}}{n_2^{1/2}}\right)\left[-erf(n_2^{1/2}(n_2^{1/2}(\ddot{o}^{+}-\beta_2)))\right] - \\
& \left(\frac{q_r z}{q_r+z}\right)\left[\left(\frac{q_r z}{q_r+z}\right)^{1/2}\right]^{*}\left(q_p^{1/2}\right)^{*} e^{\left[\frac{-jkq_p a^2}{2(2\alpha k t)^2}\right]^{*}}\left(\frac{e^{-n_1\beta_1^2}}{jn_1^{1/2}}\right)\left[erf(-jn_1^{1/2}(\delta^{-}-\beta_1))\right] + \\
& \left[\left(\frac{q_r z}{q_r+z}\right)\right]^{*}\left(\frac{q_r z}{q_r+z}\right)^{1/2}\left(q_p^{1/2}\right) e^{\left[\frac{-jkq_p a^2}{2(2\alpha k t)^2}\right]}\left(\frac{e^{n_2\beta_2^2}}{n_2^{1/2}}\right)\left[erf(n_2^{1/2}(\delta^{-}-\beta_2))\right]\Bigg]
\end{aligned}
$$

where

$$
n_1 = \left[\frac{-jk}{(2(q_r+z))}+\frac{jk}{2z}+\left(\frac{jkq_p}{2z^2}\right)^{*}\right] \qquad \beta_1 = \frac{\left[\left(\frac{-aq_p}{2z\alpha t}\right)^{*}\right]}{2n_1}
$$

$$
n_2 = \left[\frac{jk}{2z}-\frac{jkq_p}{2z^2}-\left[\frac{-jk}{2(q_r+z)}\right]^{*}\right] \qquad \beta_2 = \frac{\left(\frac{aq_p}{2z\alpha t}\right)}{2n_2}
$$

(5.23)

Equation (5.23) was computed for various conditions of the experimental geometry, using routines written in MATLAB software (TM The Math Works, Natick, Mass).

The following fixed geometrical parameters were obtained by experimental measurement (Fig. 5.1). The radius of the probe beam at z=0, w_c, was 4.0 x 10^{-5} m. The probe beam waist position was determined, as described in section 5.2.3, and the mirage effect was positioned to occur within the confocal region, a distance of approximately, 9.0 x 10^{-3} m. The wave fronts are approximately planar through this region (Fig. 2.11), and no significant divergence due to the spatial beam expansion is expected over the confocal region. The mirage effect is positioned in this region, and occurs 2.0 x 10^{-3} m from the waist position. The distance from the mirage effect region to the detector plane was also determined (9.5 x 10^{-2} m). The probe beam was aligned to strike the bicell detector centred about the midline, so the position shift for each light sensing region resulted in a voltage which was close to zero. Additional parameters required by the model include the thermal diffusivity of the sample, the wavelength of the probe beam (6.23 x 10^{-7} m), and the pump beam diameter (2.0 x 10^{-3} m). The sampling interval was 4.49 x 10^{-3} s, with a time series length of 128 points. All of these parameters remain constant, since the geometry was fixed for the experiments. Other dimensions which are included in the model are the He-Ne probe beam offset distance from the sample surface, a, and the thickness of the sample, *l*. These quantities vary with each sample/alignment, and are programmed in accordingly. In the next section, the diffraction model will be used in conjunction with inverse problem theory, in order to interpret mirage effect experimental results arising from the mirage effect.

5.3 INVERSE PROBLEM THEORY APPLIED TO THE MIRAGE EFFECT

5.3.1 Introduction

It is possible to derive more specific criteria for the resolving power of mirage effect depth profiling, using inverse methods of signal recovery (3), as opposed to forward methods. A forward theoretical model uses various parameters supplied by the operator, to generate a simulated theoretical response. An inverse theoretical model uses the experimental results to reconstruct the possible origin of the experimental response which was obtained. The inversion of the photothermal response of a sample with arbitrary properties is extremely difficult, since each layer of the sample is characterized by several parameters, such as the thermal diffusivity, the absorption coefficient, the thermal conductivity, and the thickness. However, a number of strategies exist for simplifying the inversion problem. If the sample is irradiated at a wavelength where it is optically opaque (or if it can be over-coated with an opaque, thermally matched, thin layer), then the photothermal response becomes dependent on the thermal effusivity depth profile (4, 5). In optically opaque materials, thermal wave depth profiling can yield a depth profile of the thermal effusivity alone, if one inverts the photothermal frequency response (6).

The main limitation to the impulse response undergoing inversion for the present model, is that the physical thicknesses of individual layers cannot be resolved independently of the thermal diffusivity (the opposite is also true). While many inverse methods of detection have been derived in the photothermal literature (6), most of these methods are extremely sensitive to noise, and potentially highly sensitive to systematic errors. Most of the previously developed methods are applicable only to samples with slowly varying optical profiles. In these cases, several strategies exist for recovering heat flux and diffusivity profiles from photothermal measurements (7, 8, 9).

Recently, a new method of inverse recovery was developed by Power and Prystay (4, 5). This inverse method made use of an algorithm which combined a Monte Carlo simulation with a multilinear least squares minimization, in fitting a theoretical model of the sample properties to the experiment. The model was able to yield robust estimates of the best fit of a set of theoretical thermal Green's functions to photothermal impulse response data, even in the presence of high levels of random noise in the data. Meaningful profiles could be recovered even in the presence of moderate levels of systematic errors (≤ 5%) in the data. Unlike previous theories, the method was capable of reconstructing a heat flux profile for a sample with arbitrary depth dependence, including profiles containing sharp discontinuities. This algorithm is applicable in principle, to any linear heat conduction measurement (5). The main principles of this theory, as applied to the mirage effect diffraction model, will be outlined in the next section.

5.3.2 Theory of the Inverse Model

As was discussed in section 5.2.4, equation (5.23) gives the solution for the change in temperature using the diffraction model. This change in the temperature for a photothermal system can also be described by the following general equation

$$\Delta T(x,t) = \int_{0}^{t^*} dt_0 \int_{-\infty}^{+\infty} g(x-x_0, t-t_0) \cdot q(x_0) dx_0 \tag{5.24}$$

where $g(x-x_0, t-t_0)$ is the Green's function for one dimensional heat conduction in an infinite medium, and $q(x_0)$ is the source heat flux expression (as described previously in section 3.2.2). If the sample is discretized both in x and in t, equation (5.24) becomes

$$\Delta T(x,t_j) = \delta x \sum_{i=1}^{N} g(x-i\delta x, j\delta t) \cdot q_i(i\delta x) \tag{5.25}$$

The discretization in x is performed assuming the sample consists of a series of plane sources, that are spaced at uniform intervals through the sample thickness (Fig. 5.1) (5).

Each term of this discretized Green's function corresponds to the temperature response expected from a plane heat flux source, displaced a distance dx from the detection surface. The temperature, T, and the heat flux profile, q, can be described as column vectors, and the discretized Green's function, G, as a (MxN) matrix, giving the following relationship:

$$T = Gq \tag{5.26}$$

where G can be expressed as a series of column vectors:

$$G = [g_1, g_2, \ldots, g_N] \tag{5.27}$$

and where

$$g_i = g(x-idx, t_j) \quad for \quad j = 1,2..M \tag{5.28}$$

The column vectors in G form the basis for the mathematical solution. Inversion of the appropriate Green's function operator allows the reconstruction of the depth profile of the sample's thermo-physical and optical properties. This is based on expressing the temperature profile as the summation of a series of weighted source responses (5).

The basis function is created by applying the linear diffraction operator, L, (as defined in equations (5.8) to (5.23)) to each plane source separated by dx in the model of the sample (Fig. 5.1). This results in a modified thermal Green's function, as given by the following relationship $L\{T\} = L\{G\} \cdot q(x)$. As was explained in section 5.2, the diffraction operator is determined by the parameters of fixed geometry, i.e. the probe beam offset, a, and the thickness of the sample, *l*. It is also necessary to specify the number of discrete source planes, equally spaced through the thickness of the sample, used to create the desired basis set. This value is usually chosen to be 32 or 64 (any number can be used; it is dependent upon the time available for recovery, and how many sources one wishes the model to fit). The columns of the basis set generated for the (MxN) G matrix then undergo individual convolutions with the electrical transfer function of the instrumental system (see section 2.4.1). Once the basis set is created, it is then used with the observed temperature impulse response to obtain the heat flux source profile.

5.3.3 Recovery of the Heat Flux Source Profile

The algorithm for the solution to the inverse problem theory uses a well-known constrained non-negative least squares minimization, which is described in detail in reference (5). An outline of the main points in the theory will be discussed here. The solution of the source heat flux profile is the projection of the observed temperature vector onto the basis set G's column space. The least squares fit of the function can be given by

$$S^2 = \frac{1}{M}\sum_{j=i}^{M}(T_j-(Gq)_j)^2 \qquad (5.29)$$

where one wishes to select values of q_i which minimize S^2.

Photothermal systems are ill conditioned problems; this means that they are sensitive to small changes, or errors, in matrix G and in T, and that more than one solution may fit the data within the numerical precision of the calculation (5). Each of the column vectors in the G matrix is, in principle, linearly independent; however, this linear independence is very small, and this leads to instability in the calculation (5, 10, 11). By seeding the G matrix with noise, which has a Gaussian distribution, the linear dependency between the columns is removed. The distribution of well characterized noise, may be used to achieve a stable recovery of the inverse solution, and if one takes enough averages, the noise in the solution, q(x), will be averaged out (5, 9). The percentage of noise applied to the basis set is dependent upon the noise present in the experimental data and will be discussed in more detail in section 5.4.

5.3.4 Recovery of the Optical Absorption Profile

Once the heat flux responses are recovered for a sample, the optical absorption profile can then be obtained. As described previously in section 3.2, the sample can be described as a series of discrete layers, where the absorption of light in each i^th^ layer contributes to the solution of the heat flux response, by the following relationship:

$$q_i = \eta_i\beta_i I_{i-1}e^{\beta_i(x+\sigma_{i-1})} \qquad (x<0) \qquad (5.30)$$

where η_i is the non-radiative conversion factor (assumed to be unity), I_{i-1} is the light intensity passing through to the i-1 layer, β_i is the absorption coefficient in the ith layer, and σ_{i-1} is the depth position for the surface of the ith layer.

The total amount of light absorbed by the sample is a function of the initial intensity of light incident on the sample, I_0, and the sample's measured optical transmission, T_s. The total heat flux in the sample is proportional to the total amount of light absorbed, i.e. $q(l) \propto I_0(1-T_s)$, where l is the total thickness of the sample. The optical transmission for any particular depth in the sample can be given by

$$T_s(x_i) = 1-\frac{\overline{q(x_i)}}{\overline{q(l)}}(1-T_s) \tag{5.31}$$

where

$$\overline{q(x_i)} = \sum_{j=1}^{i} I_{j-1}\beta_j e^{-\beta_j l_j} dx \tag{5.32}$$

The optical absorptivity can then be described using equation (5.33), for any depth, x_i, in the sample:

$$\beta(x_i) = -\frac{1}{l_i}\ln\left[\frac{T_s(x_i)}{T_s(x_{i-1})}\right] \tag{5.33}$$

Using equation (5.33), the optical profile can be reconstructed for the sample, by computing $\beta(x_i)$ of each layer in the sample, where each $\beta(x_i)$ is dependent upon the absorptivity in the previous layers in the sample (12).

5.4 EXPERIMENTAL RESULTS AND DISCUSSION USING INVERSE PROBLEM THEORY

In previous work in this thesis (Chapter 4), forward models analyzed with samples of known properties were described. This is now extended by taking the data from samples of known properties and studying the conditions for which an inverse model can reliably reconstruct the profiles. Several of the samples containing discrete optical absorbing and continuous optical absorbing layers (Fig. 4.1 (a, c, e, g, h, j, k)) were re-examined using the bicell position sensor. This increased the accuracy of the experimental data to allow for quantitative depth profiling to be used with the inverse model developed. Although several of the samples were examined, for brevity, the remaining discussion focuses on three samples (Fig. 4.1(g),(h),(k)).

Firstly, the functions comprising the basis set which accommodates all possible resolvable heat flux profiles present in the sample must be computed. The sample is discretized into N heat flux planes of spacing dx, and for each position of the source plane, a=idx (where i=0 to N-1), the mirage effect signal is computed, using equation (5.23). The set of all such response functions comprises the basis set. Once the basis set is determined, it is seeded with noise containing a Gaussian distribution (as described in section 5.3.3) and the heat flux source profiles, q(x), are recovered for a given set of experimental data. The percentage of noise added is determined by examining the noise level in the original signal response. Fig. 5.3 shows the Green's function basis set for a sample which is 100 μm thick, with a probe beam offset distance of 210 μm (standard for the samples depicted in Fig. 4.1). In order to determine the resolving capabilities of this

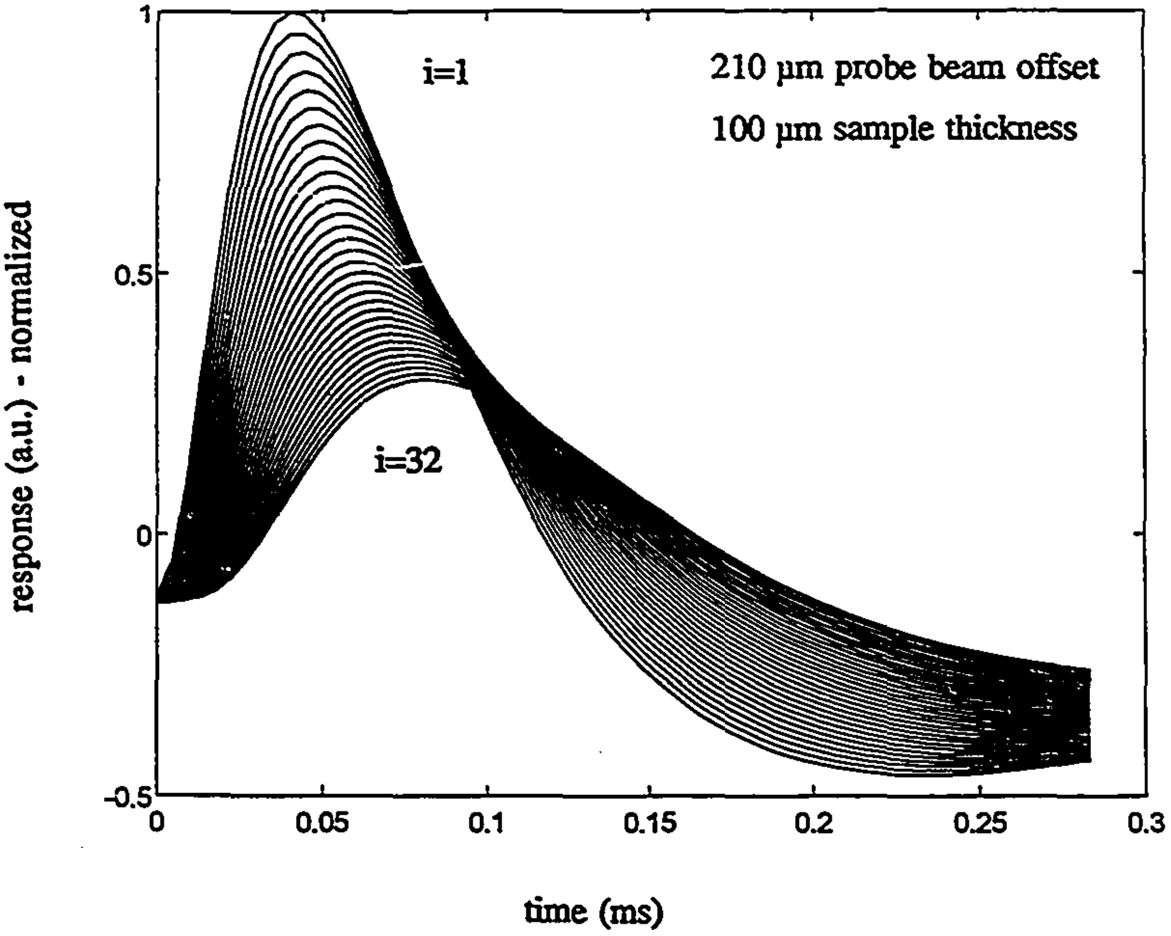

Figure 5.3: The Green's function basis set for a sample which is 100 μm thick (with 32 discrete plane sources), and with a probe beam offset distance of 210 μm.

Green's function basis set (seeded with a given level of noise), a delta function source is positioned at equally spaced depths through the total sample thickness, and a non-negative least squares inversion is recovered from the time domain data at each position, to give the resolving kernel for the analysis. In this case, the sample was divided into 64 source positions (unless otherwise indicated, this is true for all inversions), and was seeded with differing levels (0.1%, 1.0%, and 3.0%) of noise.

Fig. 5.4 (a)-(c) illustrate the resulting resolving kernels for these basis sets. The noise which is added, as explained in section 5.3.3, is averaged out in the solution q(x), by increasing the number of replicates of the heat flux profiles which are inverted. In these figures, there were 100 averages taken. One can see on Fig. 5.4(a) that positions 3 μm away from each other can be easily resolved spatially from each other, whereas, as the noise is increased to 3% (Fig. 5.4(c)), the resolution is not as defined at such small increments, but there is spatial resolution at 10 μm increments.

A 3% noise level was used to recover the heat flux profiles for the experimental data. This level, which tends to be conservative, was chosen in order to obtain a stable recovery. Below this noise level, experimental errors that are systematic or random would become prevalent, and lead to instability when recovering the heat flux profiles. In order to obtain a stable recovery of the heat flux profile, it has been shown that the noise level in the basis set must be greater than the relative noise in the data (5).

The inverse model was then evaluated with respect to its capabilities in recovering discrete and continuous optical absorbers in samples. As was mentioned, for brevity, the results of three samples (Fig. 4.1(g),(h),(k)) using the inverse model will be discussed.

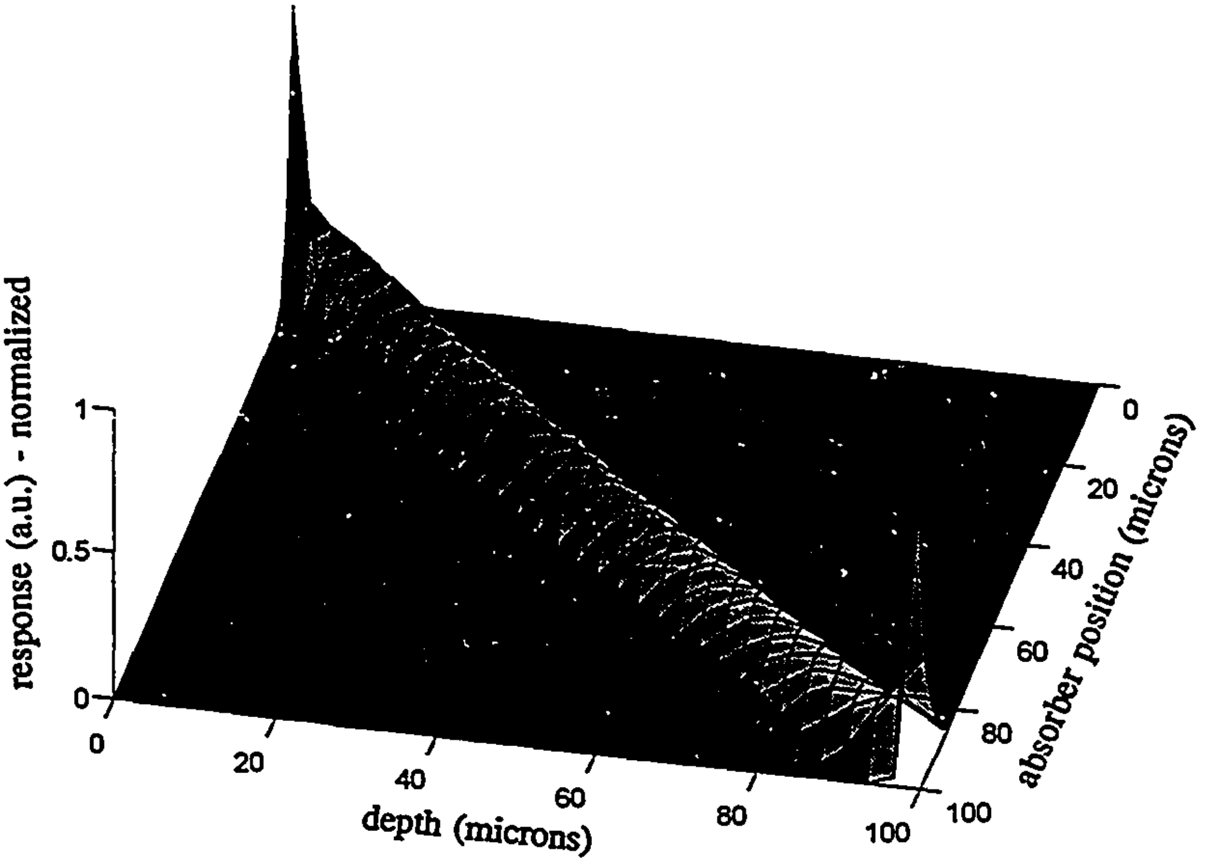

Figure 5.4: (a) The resolving kernel for the Green's function basis set depicted in Fig. 5.3, seeded with 0.1% noise.

The basis set was generated with a sample which was divided into 64 discrete plane source positions. The response is plotted as a function of absorber position within the sample and as a function of depth.

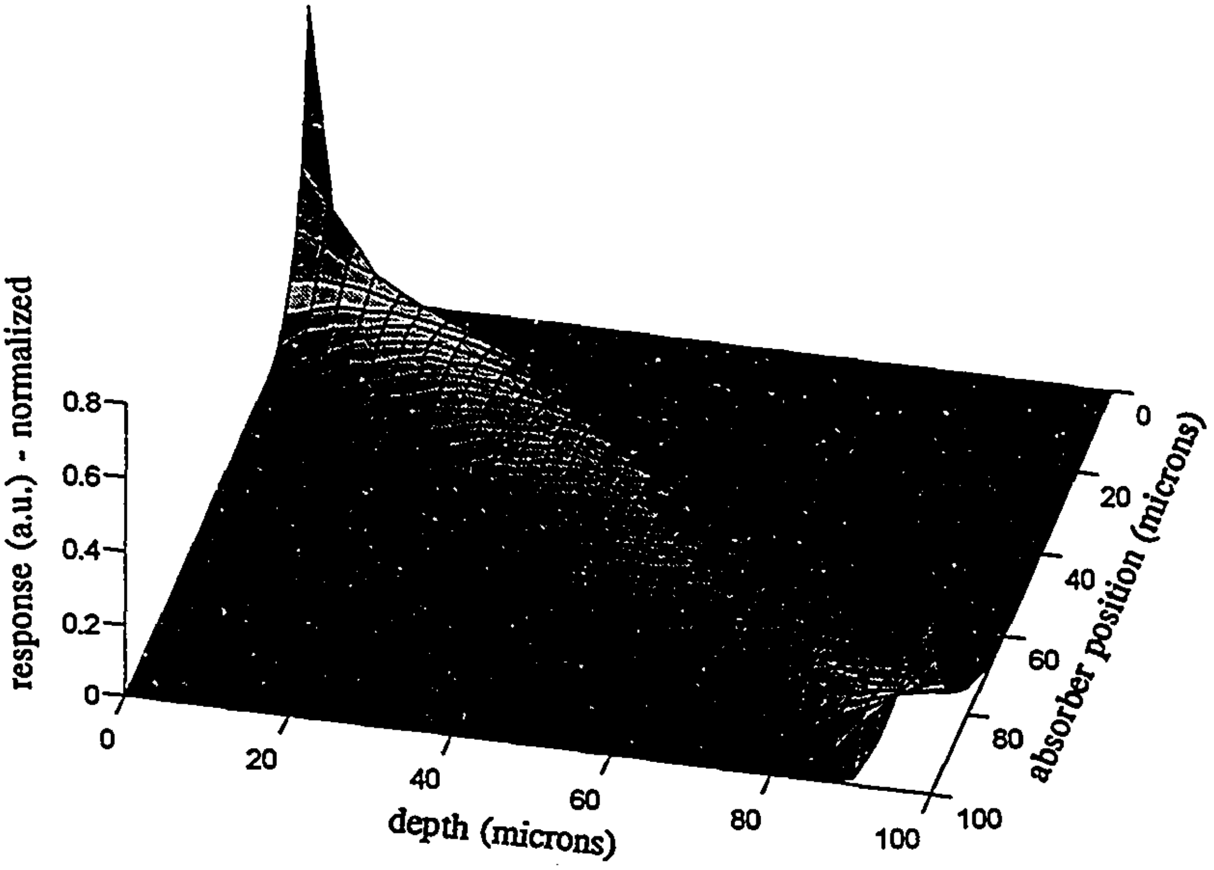

Figure 5.4: (b) The resolving kernel for the Green's function basis set depicted in Fig. 5.3, seeded with 1.0% noise.

The basis set was generated with a sample which was divided into 64 discrete plane source positions. The response is plotted as a function of absorber position within the sample and as a function of depth.

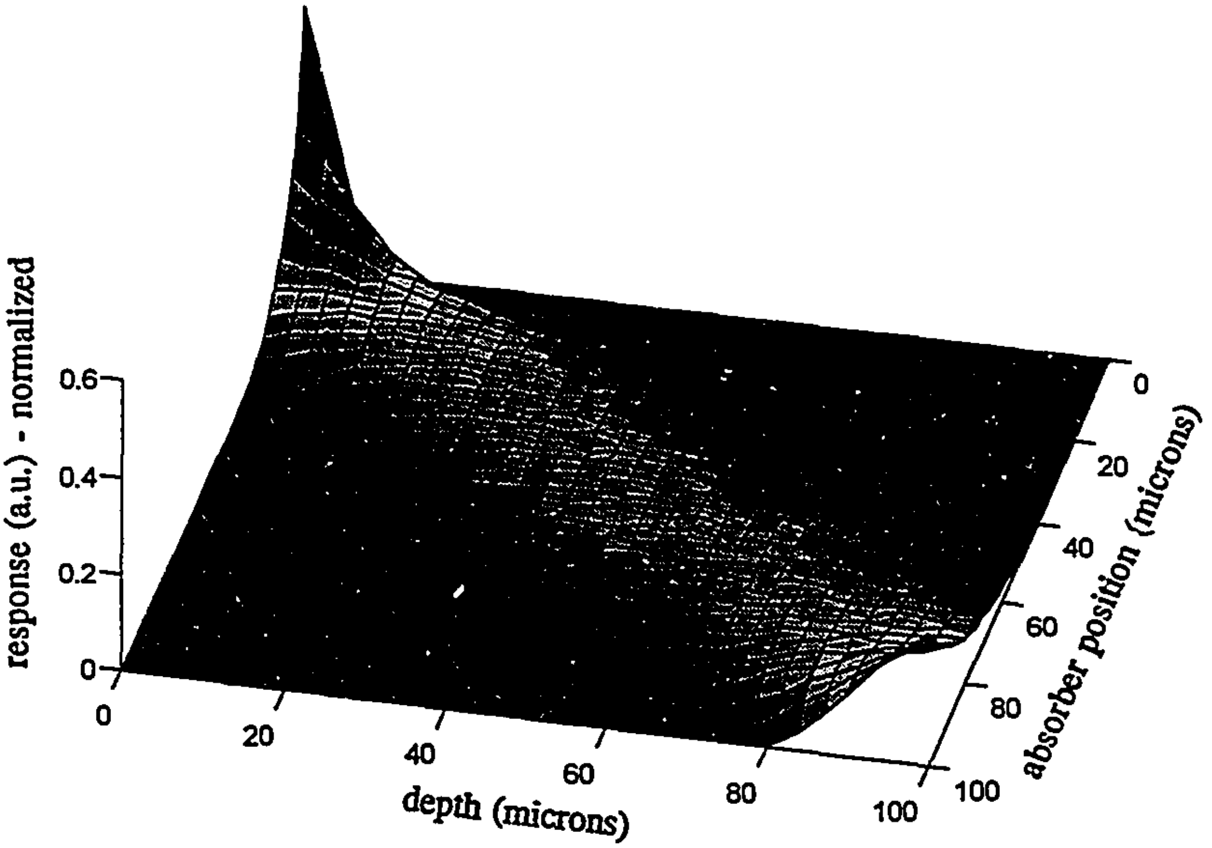

Figure 5.4: (c) The resolving kernel for the Green's function basis set depicted in Fig. 5.3, seeded with 3.0% noise.

The basis set was generated with a sample which was divided into 64 discrete plane source positions. The response is plotted as a function of absorber position within the sample and as a function of depth.

The first sample examined consisted of two discrete absorbers, a red absorber separated from a green absorbing layer by a transparent spacer of 23 μm (Fig. 4.1(g)). The experimental impulse response data obtained from the sample were inverted using the inverse problem theory. As was explained earlier (section 4.3.1), the two absorbing layers are separated by a distance which is smaller than the thermal distance of the probe beam offset to the sample surface. As a result, the mirage effect cannot easily differentiate the contribution of the two individual layers. This is also seen with the heat flux profile reconstructed in Fig. 5.5. The separation between the two absorbing layers lies within the width of the resolving kernel, and the model is therefore unable to resolve the discrete absorbers for this level of noise.

In the next study, the sample depicted in Fig. 4.1(h) with an increased spacing between the discrete absorbers was examined. As the position of the green absorbing layer is increased relative to the red surface absorbing layer, from 23 μm (in the previous example) to 77 μm (in the present case), one can see that the impulse response traces show a substantial increase in the peak delay maximum as the wavelength is increased from 580 nm to 605 nm (see Chapter 4). This delay arises from absorption in the subsurface green layer as the red surface absorber becomes transparent (Fig. 4.2). This improvement in contrast in the impulse response is translated into an improvement in the resolution in the inverse model. Using a basis set similar to that depicted in Fig. 5.4(c), but having a sample thickness of 82 μm and a beam offset of 205 μm, the inverse heat flux profiles were obtained for each data set in the wavelength study (from 580 nm to 610 nm, in increments of 5 nm positions).

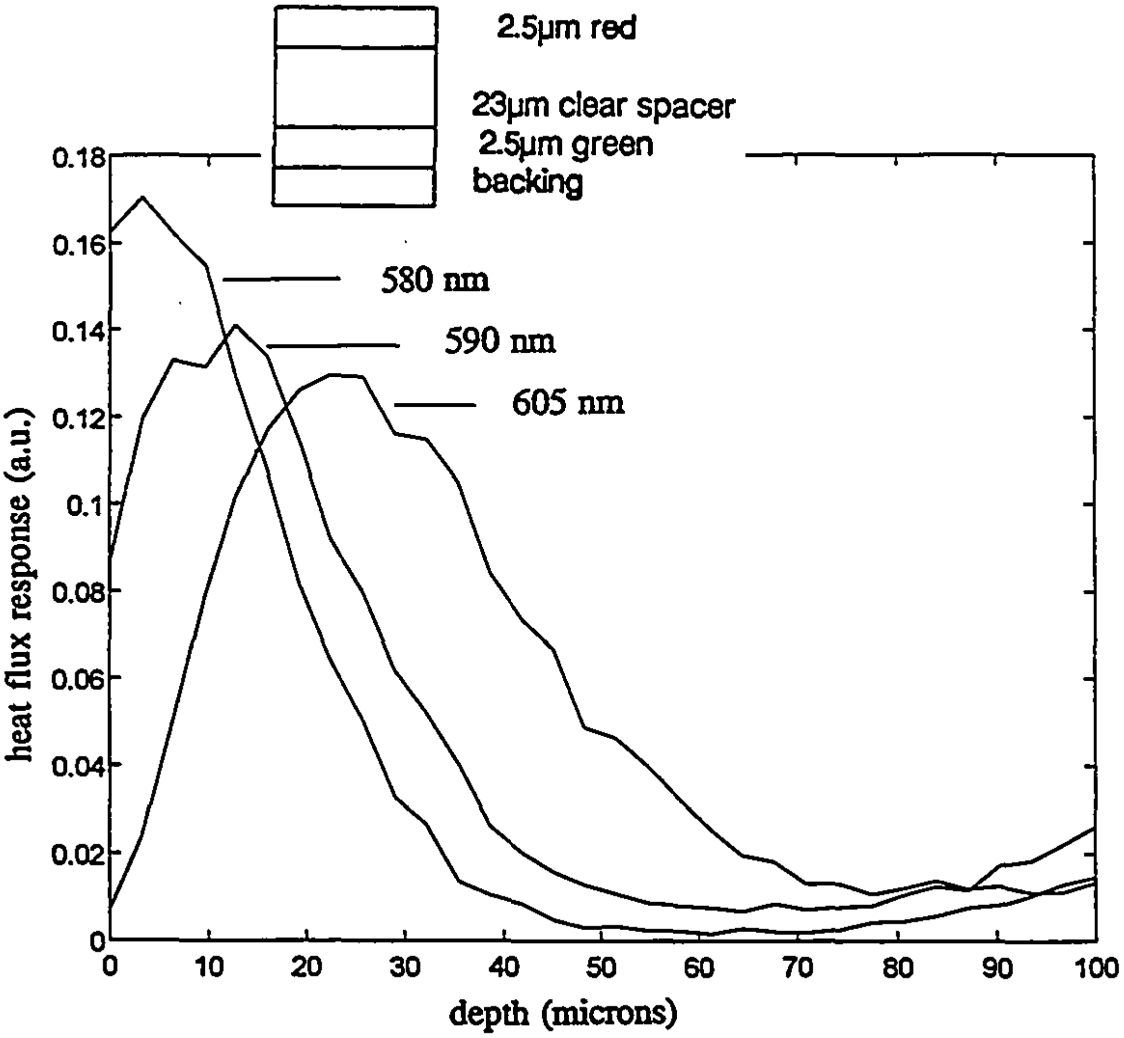

Figure 5.5: Three recovered heat flux traces (at 580 nm, 590 nm, 605 nm) for the sample depicted in Fig. 4.1(g), where a red absorber is separated from a green absorbing layer by a transparent spacer of 23 μm.

Fig. 5.6 shows the heat flux profiles recovered at four different wavelengths: Fig. 5.6(a) at 575 nm, Fig. 5.6(b) at 590 nm, Fig. 5.6(c) at 595 nm, Fig. 5.6(d) at 610 nm. This set of four figures illustrate the variation of the weighting of the red absorbing surface layer to the green absorbing subsurface layer over the wavelength range examined. Fig. 5.6(a) shows a strongly surface dominated absorber. The energy appears to be absorbed in the first 1 μm of the surface layer, and this dimension is less than the resolving ability of the chosen basis set (under these conditions, e.g. level of noise). This results in a recovered heat flux profile which decays rapidly with depth. Fig. 5.7 shows the experimental impulse response data plotted with the corresponding fit to the data from the reconstruction. Individual traces are offset from each other by 0.2 units in the figure in order to better visualize the trend. As is seen in the trace labelled 573 nm, an unbiased match between the traces is not seen. This is due to the poor reconstruction of the heat flux profile for a strongly surface dominated sample, recovered with the resolving power of this basis set. For the traces labelled 580 nm, 590 nm and 595 nm, good agreement between the experimental data and the theoretical curves reconstructed from the heat flux profiles is seen. Fig. 5.6(b) and 5.6(c) also show a close agreement of the heat flux profiles relative to the weighting distribution of the two absorbing layers. The final trace in Fig. 5.7 (labelled 605 nm), does not show an unbiased match of the experimental and the recovered theoretical impulse response traces. This may be due again to the limits in the resolving power of the basis set; the heat flux profile (Fig. 5.6(d)) rises very quickly toward the back of the sample. The model may be unable to resolve accurately the contribution of the absorbing layer at the rear of the sample.

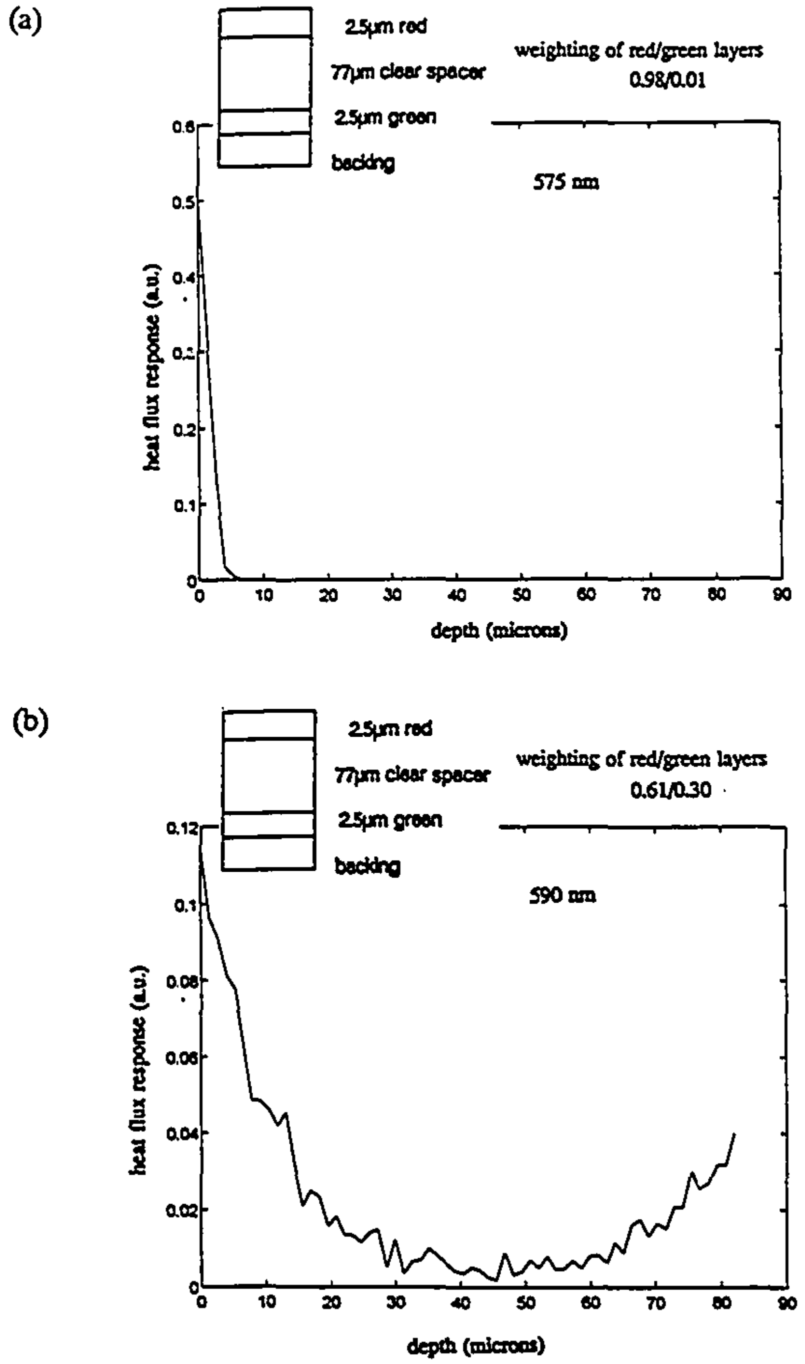

Figure 5.6: Recovered heat flux profiles for the experimental data (measured sample thickness of 82 μm). Recovered profiles for incident pump beam radiation of (a) 575 nm and (b) 590 nm.

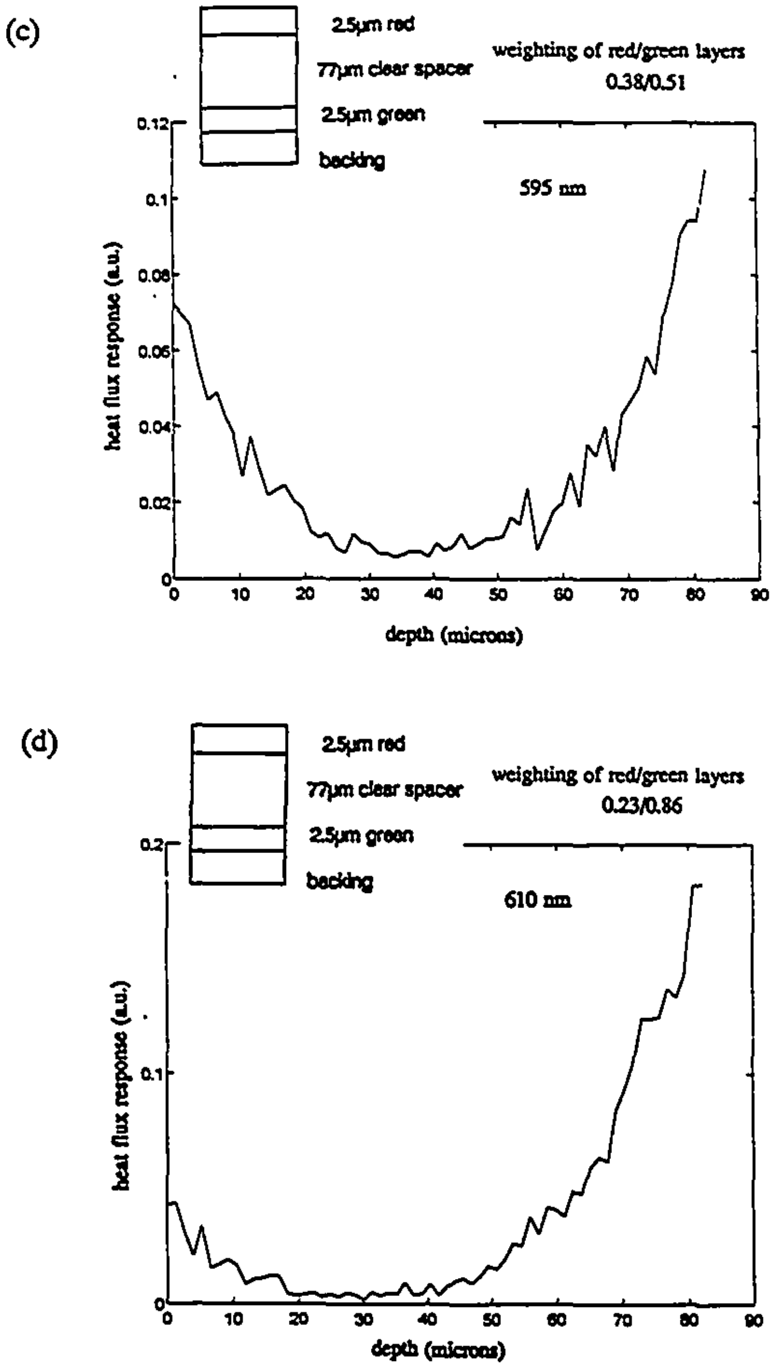

Figure 5.6: Recovered heat flux profiles for the experimental data (measured sample thickness of 82 μm). Recovered profiles for incident pump beam radiation of (c) 595 nm and (d) 610 nm.

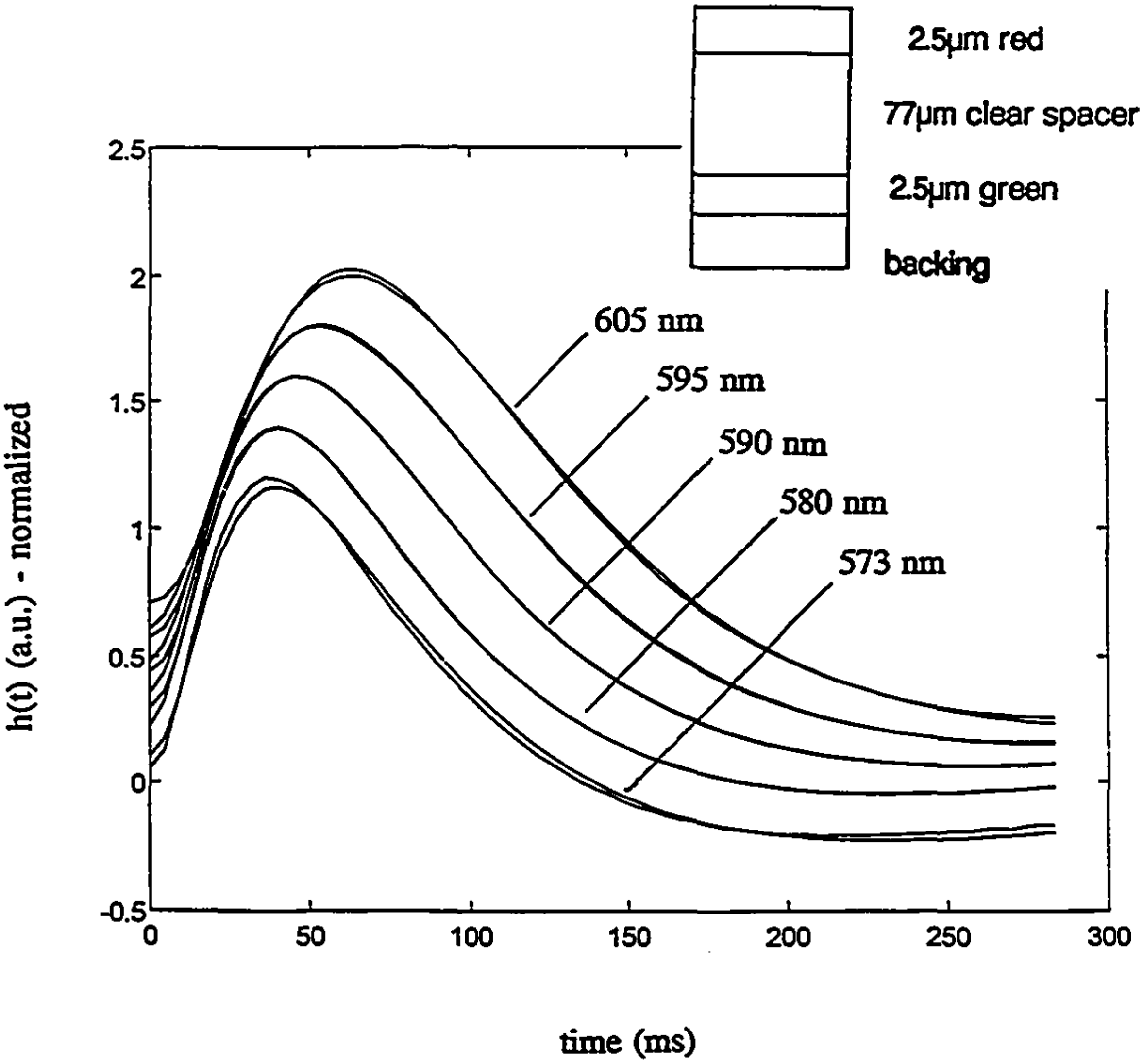

Figure 5.7: Experimental impulse response traces for the sample depicted in Fig. 4.1(h), where a red absorber is separated from a green absorbing layer by a transparent spacer of 77 μm. The traces are offset from each other by 0.2 units. The corresponding fit with the recovered impulse responses are also plotted.

In order to evaluate limitations in the resolving power of the model on the recovery of these heat flux profiles, impulse responses were generated theoretically for the four different wavelengths (575 nm, 590 nm, 595 nm, 610 nm) using delta functions weighted by the measured ratio of the two absorbing layers at each wavelength. The basis set used to recover the experimental heat flux profiles was then applied to generate the theoretical impulse response traces corresponding to these cases. The theoretical impulse response was then inverted assuming the same noise level as was used in the experiments. This evaluates the broadening or bias effects in the recovery of the theoretical heat flux profiles due to the inverse algorithm. Fig. 5.8(a)-(d) show the heat flux profiles recovered from this theoretical data. At 575 nm, the theoretical reconstruction is broader than the recovered heat flux profiles obtained from the experiment. This may be attributed to a systematic error in the experiment which has not been identified, but which is evident in samples which are dominated by surface absorption. However, the bias is less significant when the signal is more strongly dominated by subsurface features.

It was found that the sample thickness must be known to a high precision (< 5%) in order to recover the heat flux profiles with minimal broadening. If the sample thickness assumed by the reconstruction is larger than the physical thickness of the sample, there will be an additional source of broadening of the features located near the back of the sample. This is due to the increase in the degrees of freedom available for locating features of the heat flux. Near the sample boundaries, the model constrains the heat flux to lie at the rear of the sample. To test this effect, a second set of impulse responses was generated theoretically for the experimental wavelengths (as done above),

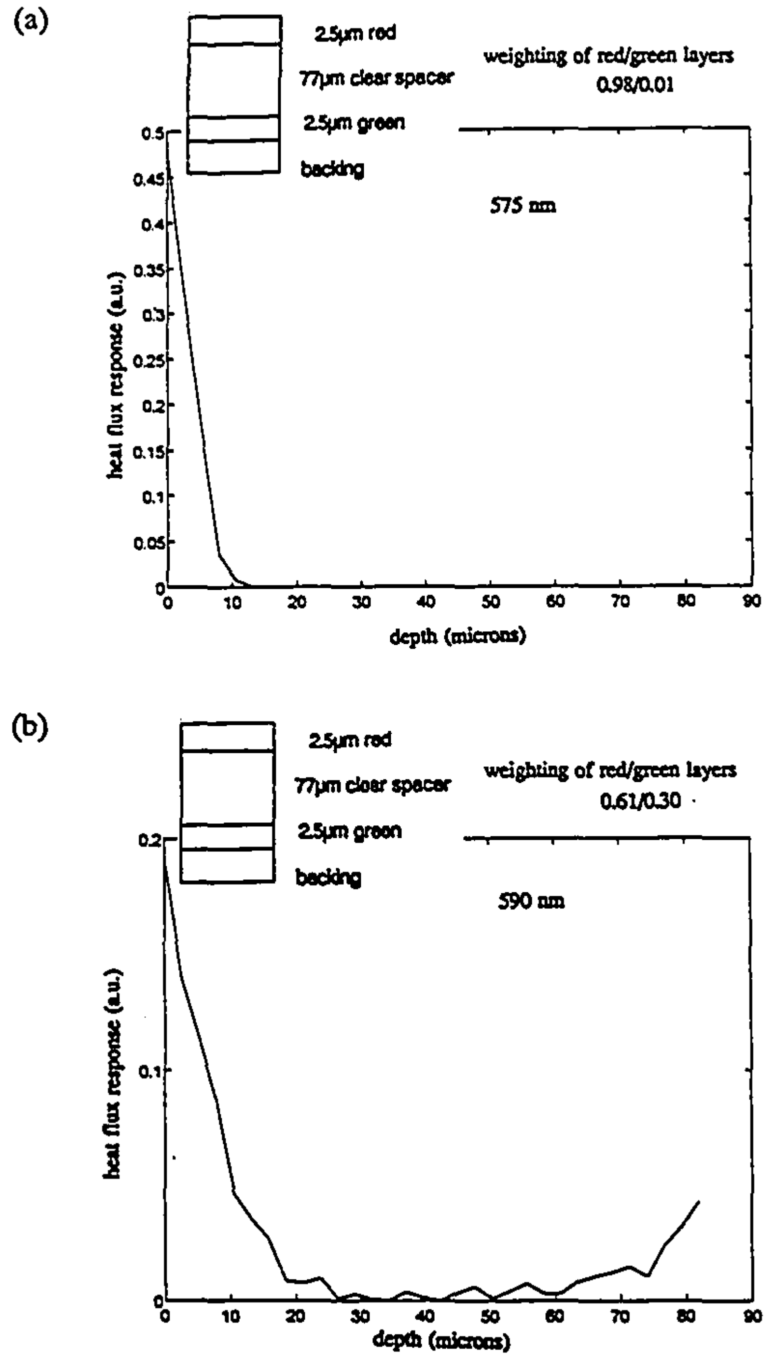

Figure 5.8: Recovered heat flux profiles for the theoretical profiles (with absorbers separated by 77 μm in an 82 μm sample thickness). Recovered profiles for incident pump beam radiation of (a) 575 nm and (b) 590 nm.

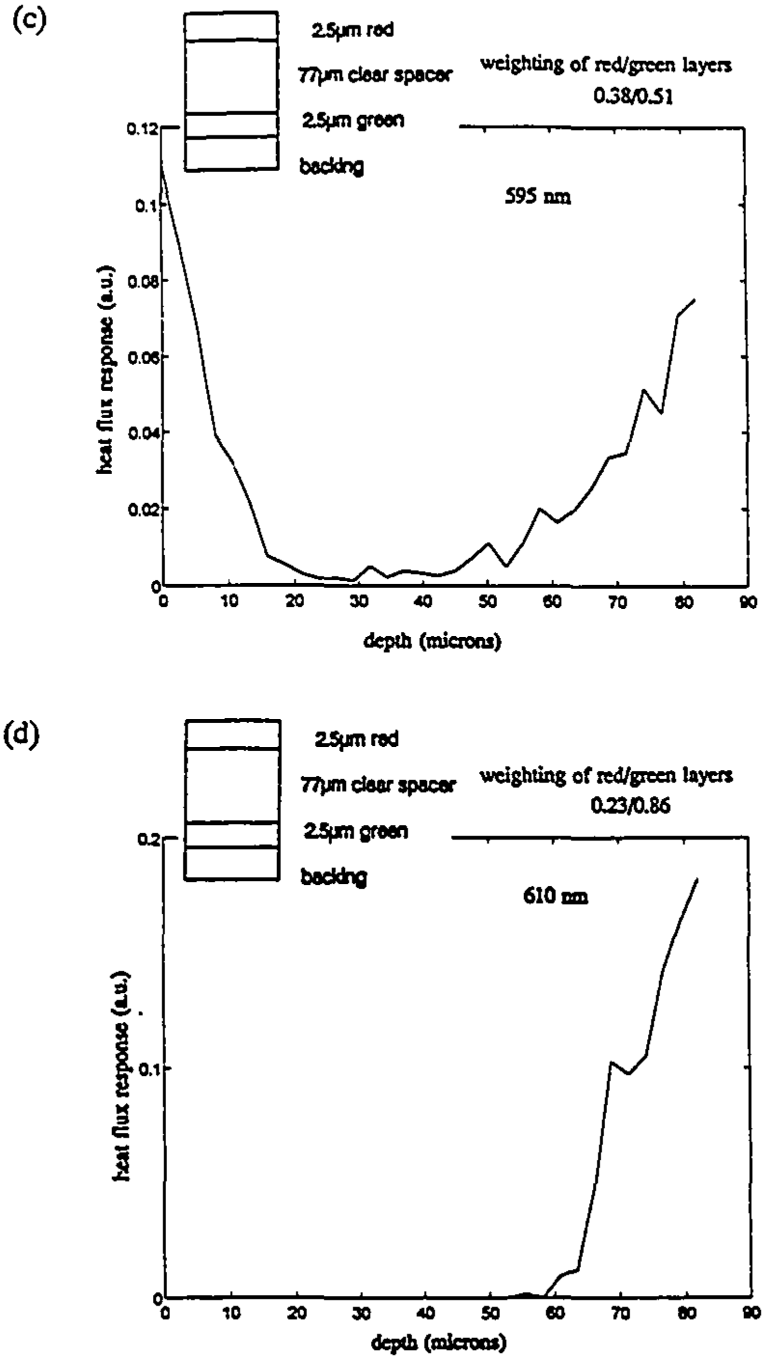

Figure 5.8: Recovered heat flux profiles for the theoretical profiles (with absorbers separated by 77 μm in an 82 μm sample thickness). Recovered profiles for incident pump beam radiation of (c) 595 nm and (d) 610 nm.

using a sample thickness which was slightly greater than that of the sample (84 μm relative to 82 μm). In this model, absorbers were positioned 1 μm in from the top and bottom of the physical sample. Fig. 5.9(a)-(d) show the heat flux profiles which were reconstructed with this new basis set. The broadening seen in the reconstructed theoretical traces with the assumed sample thickness of 84 μm is in better agreement with the experimental reconstruction. Both the theory and experiment indicate that this small difference in the sample thickness assumed by the reconstruction is significant in affecting the resolution of the reconstructions. However, the broadening behaviour of the experiments is explained by theoretical broadening. This suggests that a precise knowledge of the sample's thickness used in the experiment reconstructions is essential to interpret the recovered profile.

The inverse model was next used to evaluate the reconstruction of continuous optical absorption profiles. The sample depicted in Fig. 4.1(k) was used. With reference to Fig. 4.3, one can see that as the wavelength is increased from 580 nm to 620 nm, the centroid of optical absorption is located more deeply below the sample surface, and the profile of absorbed light becomes more uniform with depth. A corresponding delay is observed in the impulse response at the longer wavelengths because more time is required for heat conduction to the sample surface from the lower depths (see Chapter 4).

The basis set was generated where the assumed sample thickness was set at 90 μm and a probe beam offset distance of 210 μm was determined. A 3% noise level was again chosen to recover the heat flux profiles for the experimental impulse response data. The heat flux profiles were recovered and are shown in Fig. 5.11 and Fig. 5.13.

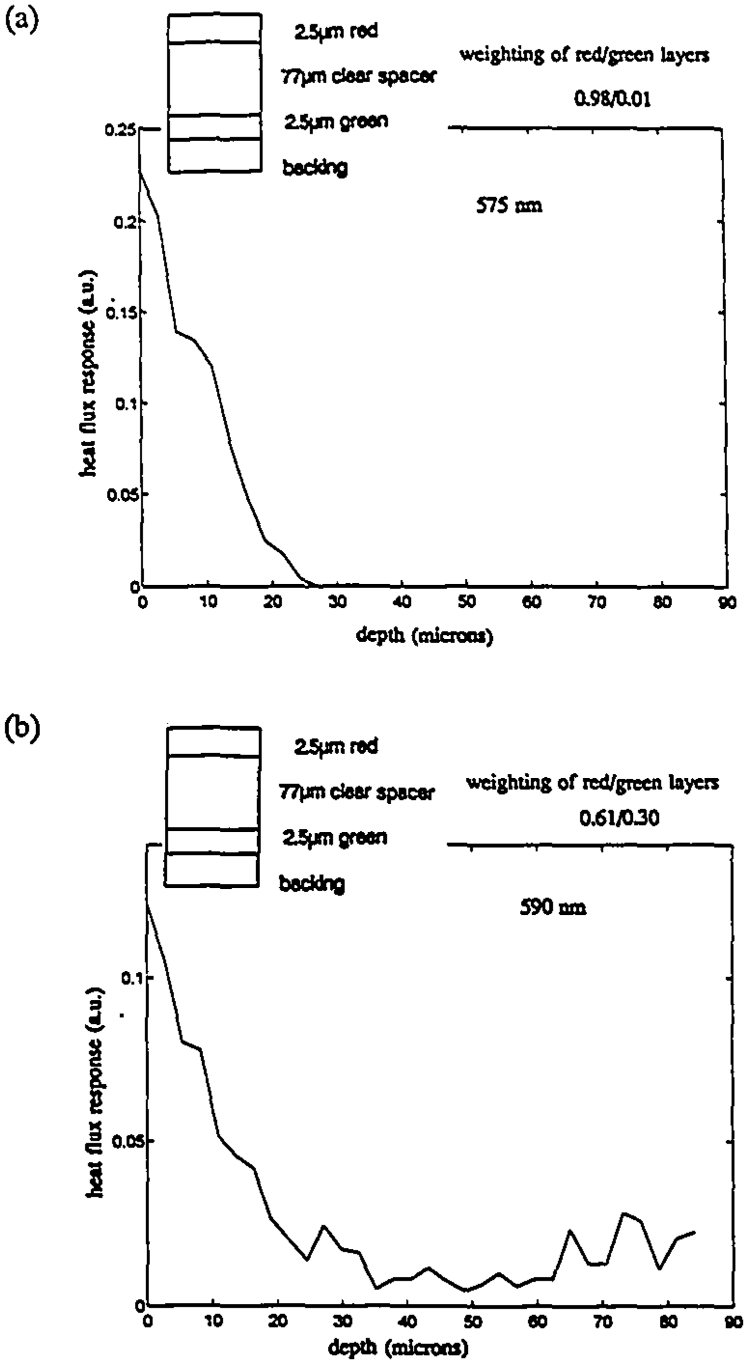

Figure 5.9: Recovered heat flux profiles for the theoretical profiles (with absorbers separated by 77 μm in an 84 μm sample thickness). Recovered profiles for incident pump beam radiation of (a) 575 nm and (b) 590 nm.

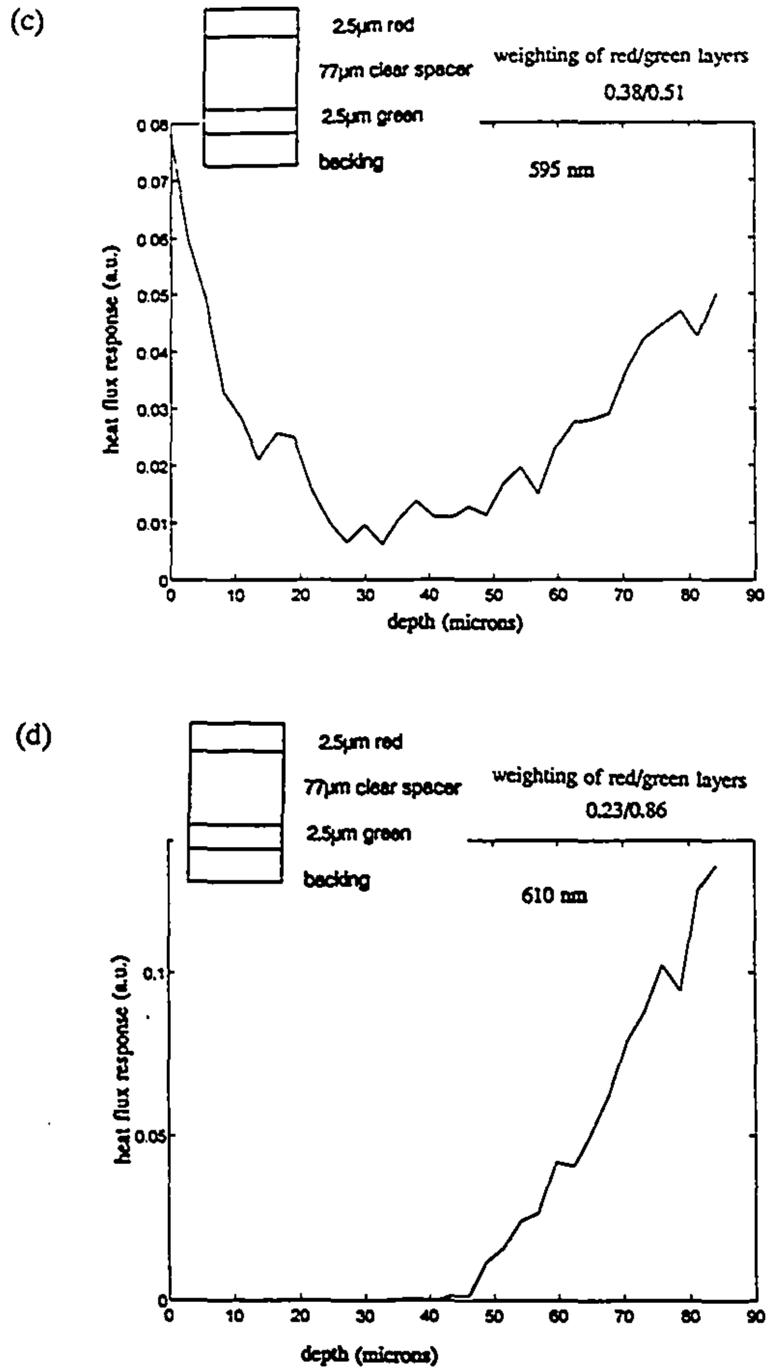

Figure 5.9: Recovered heat flux profiles for the theoretical profiles (with absorbers separated by 77 μm in an 84 μm sample thickness). Recovered profiles for incident pump beam radiation of (c) 595 nm and (d) 610 nm.

Below 590 nm, there is a saturation of the impulse response signal, with very little variation between impulse response traces in this range (Fig. 5.10). This trend is also noted in the reconstructed heat flux profiles, q(x) (Fig. 5.11). In this wavelength range, the light is attenuated very rapidly with depth into the sample (about 30 μm into the sample, as seen in Fig. 5.11), resulting in no significant light penetration below that depth. In recovering the absorption coefficient profiles, the model uses the very low levels of heat flux recovered at depths greater than twice the optical absorption length (1/ß) to reconstruct ß(x) at these depths. This results in an emphasis of errors in the reconstruction of ß(x) with an anomalous "tailing up" of the profile (Fig. 5.12). Here the inverse model attempts to reconstruct the absorption coefficient profile in a region where there is effectively no signal q(x). Therefore, the expected uniformity of the absorption coefficient profile in this wavelength range is not reconstructed in regions where such large absorption is encountered.

At 590 nm, the signal begins to show the expected trend for the optical response present in a continuous absorber. The greatest contrast in the experimental impulse response data occurs between 590 nm and 610 nm. Fig. 5.13 shows the heat flux profiles reconstructed at five representative wavelengths between 590 nm and 610 nm. The optical absorption profiles were reconstructed using the known thickness of the sample, the absorption coefficient for the continuous sample at that wavelength (see Fig. 4.3), and the reconstructed heat flux profiles (see section 5.3.4). These same trends are shown in the optical absorption profiles (Fig. 5.14). The heat flux profile is nearly exponential across the sample thickness, as expected, and this is shows up in the reconstructed optical absorption coefficient profiles being nearly uniform (Fig. 5.14). For the entire wavelength range examined, Fig. 5.15 shows the flat optical absorption coefficient profiles generated using the absorption coefficients obtained using the UV-Visible spectrophotometer (Fig. 4.3). Fig. 5.16 shows the recovered optical absorption profile using the inverse theory, which is in good agreement with the experimental recovery.

The basis set used to recover the heat flux and optical absorption coefficient profiles required the assumption of a thickness of 90 μm, in order to obtain results which were consistent with the sample's optical properties, whereas the measured thickness of the sample was 100 μm. The reason for this discrepancy is most likely due to the presence of a thin layer of non-absorbing lacquer on the wratten gel sample. This can be up to 10% of the total thickness of the sample, leading to a thickness variation of 10 μm (error cited by manufacturer) (13). Inverse studies in previous work using the photopyroelectric effect (12), have detected the presence of the lacquer layer at the rear surface (where the detector is positioned) in these materials. The mirage effect technique is more sensitive to the presence of a lacquer layer at the front surface (indirectly, is also sensitive to the rear surface layer of lacquer). Fig. 5.17 shows a schematic diagram of the sample. The probe beam offset value used in the basis set will take into account the 5 μm lacquer layer at the front surface of the sample, but the amount of lacquer at the rear of the sample needs to be accommodated by the thickness of the sample used in the basis set.

The effect of the variation in the thickness of the sample assumed by the model on the recovery of the heat flux profile is seen by generating a theoretical profile with a continuous optical absorber ($\beta = 2.0 \times 10^4$ m^{-1}), which contains a discontinuity positioned

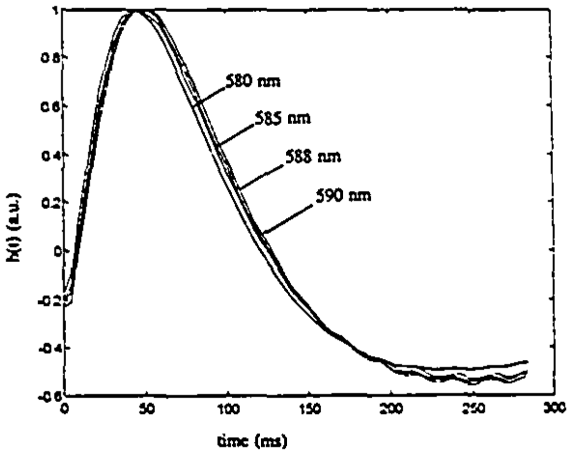

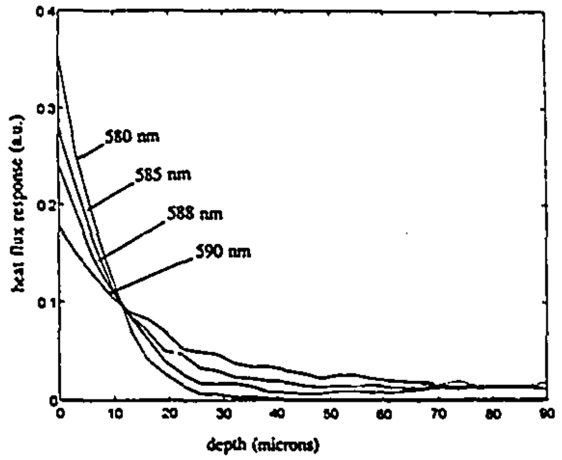

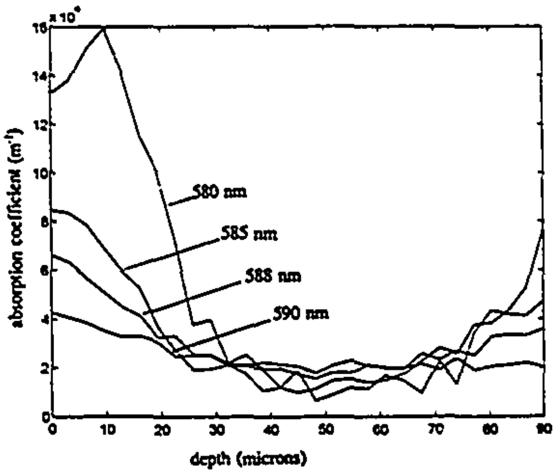

Figure 5.10: The experimental impulse response traces for the sample depicted in Fig. 4.1(k), showing the minor difference in the responses for the region of saturation (580 nm, 585 nm, 588 nm and 590 nm).

Figure 5.11: The recovered heat flux profiles for the data depicted in Fig. 5.10, for the same wavelength range.

Figure 5.12: The recovered optical profiles from the heat flux profiles depicted in Fig. 5.11.

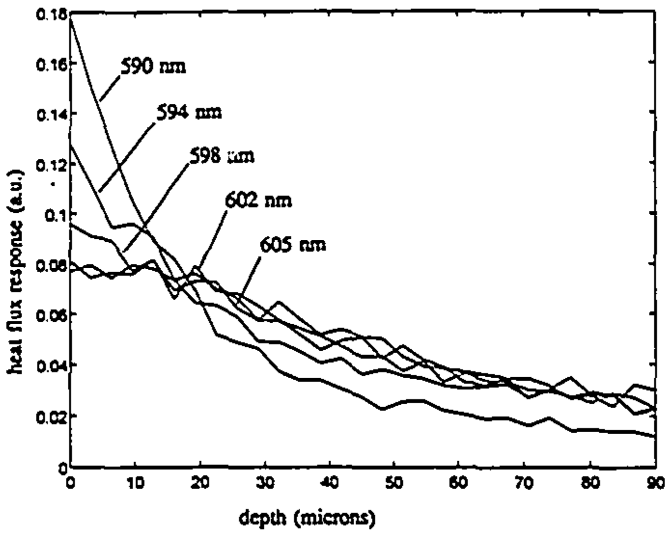

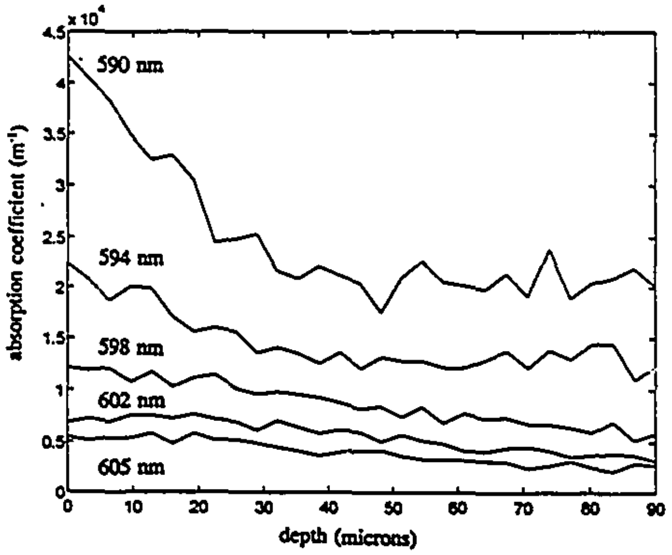

Figure 5.13: Five representative heat flux responses for the sample depicted in Fig. 4.1(k), over the wavelength range (590 nm to 610 nm).

Figure 5.14: The recovered optical profiles corresponding to the heat flux reconstructions in Fig. 5.13.

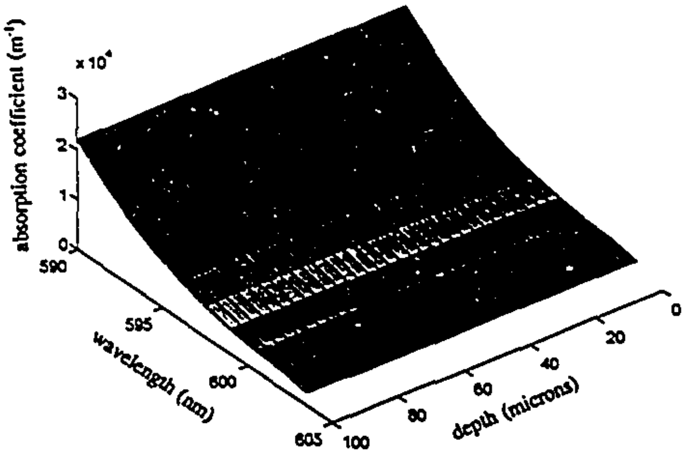

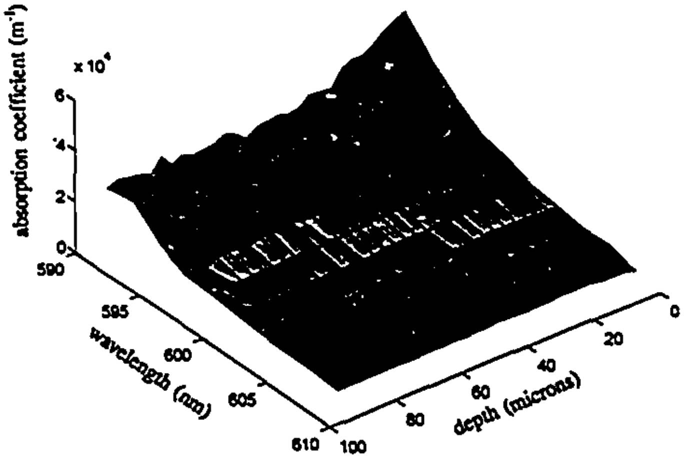

Figure 5.15: The optical absorption profile generated using the actual absorption coefficients obtained using the UV-Visible spectrophotometer for the sample depicted in Fig. 4.1(k), over the wavelength range (590 nm to 610 nm).

Figure 5.16: The reconstructed optical absorption profiles for the experimental data obtained for the sample depicted in Fig. 4.1(k) over the wavelength range (590 nm to 610 nm).

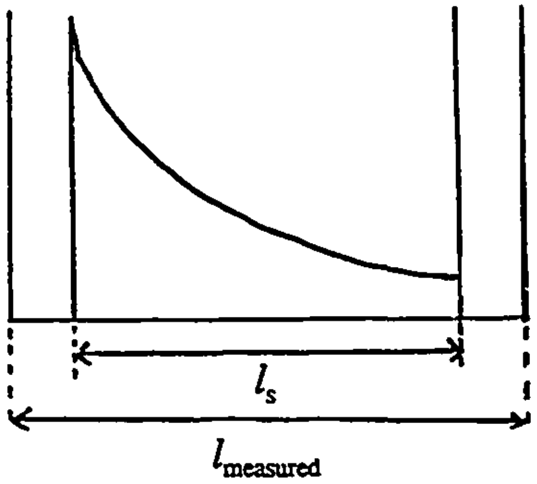

Figure 5.17: Schematic diagram of the optical absorption profile in a continuous sample (Fig 4.1(k)) showing the measured sample thickness, $l_{measured}$, of 100 μm and the actual sample thickness, l_s, which is 90 μm.

90 μm into the sample (trace labelled as 1 in Fig. 5.18 (a), (b), and (c)). The heat flux profiles are then recovered for cases where the assumed sample thickness is made both smaller and larger than the total thickness of 100 μm. Fig. 5.18(a) shows the recovered heat flux profile if the thickness assumed by the basis set is equal to the actual thickness of the sample, 90 μm (trace labelled as 2 in Fig. 5.18(a)). The heat flux profile which decays to the theoretical value at the rear edge of the sample. If the thickness of the layer is decreased to 70 μm in the model, the reconstructed profile tails up toward the rear of the sample. This generally indicates that a greater portion of the heat flux at the rear of the sample (Fig. 5.18(b), trace labelled as 2) must be fitted to account for the experimental response. The inverse model is attempting to account for the most delayed features located behind the rear surface of the sample. This results in the excess heat flux being fitted into a region near the back of the sample, thus creating a build up of the heat flux at this position.

Alternatively, if the reconstruction is performed using a basis set which allows a larger sample thickness of 130 μm to be reconstructed (Fig. 5.18(c), trace labelled as 2), the recovered heat flux profile shows a downward tailing or droop at the rear edge and beyond, indicating a distortion of the recovery. The heat flux profile is attempting to recover the edge located at the back of the sample, but lacks the resolving power (at this noise level in the basis set). The reconstruction of a sharp edge buried this deeply into the sample would require a very low level of noise and experimental error. This may be an unrealistically low level for typical photothermal measurements.

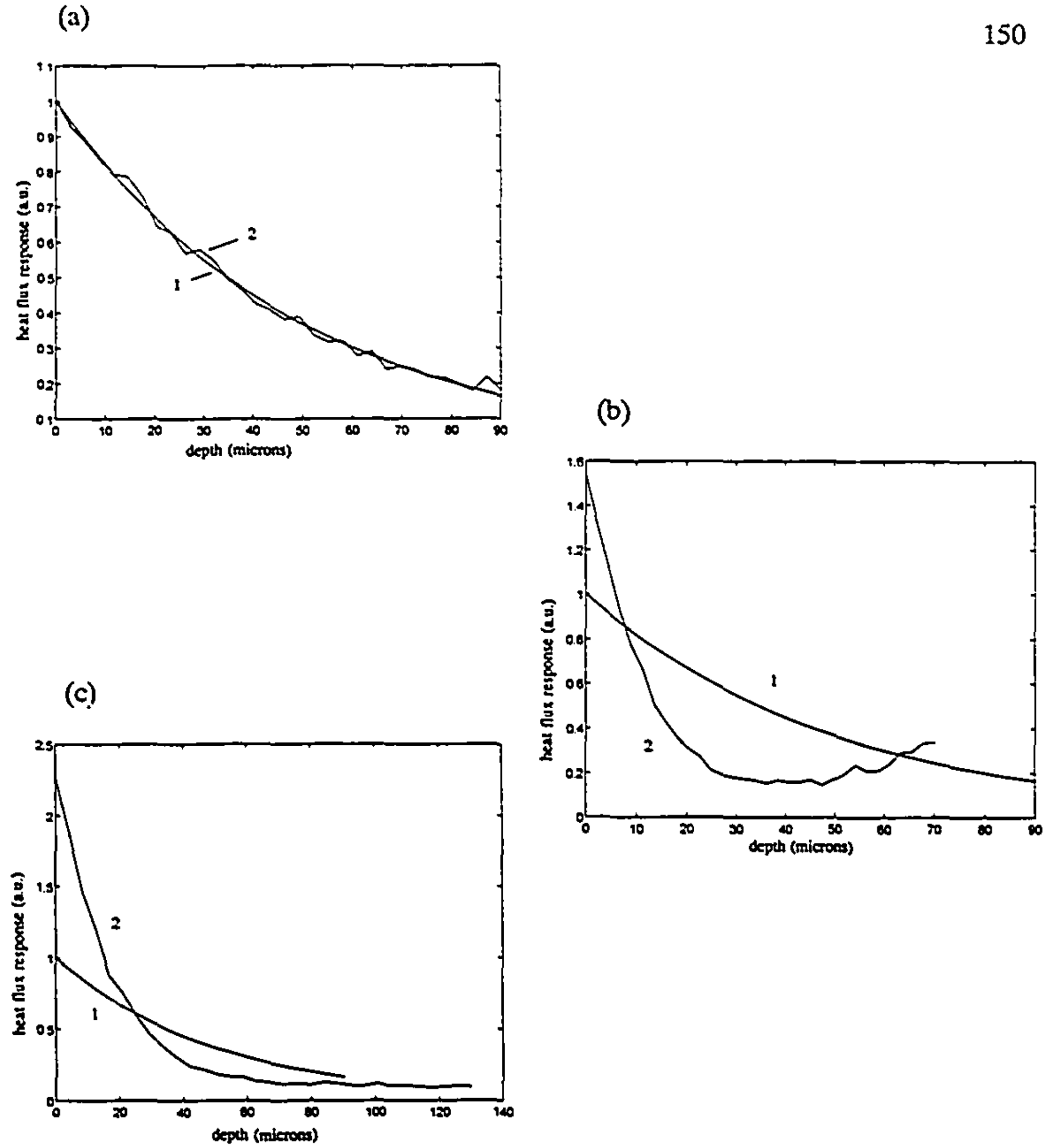

Figure 5.18: Recovered heat flux profiles for a theoretical profile with a continuous optical absorber, which contains a discontinuity introduced at a depth of 90 μm into the sample (trace labelled 1 in the figure). The theoretical heat flux profiles are all recovered using basis sets where the sample thickness is made smaller and larger than the measured thickness. The recovered heat flux profile for a basis set using (a) an actual sample thickness of 90 μm (trace labelled 2 in Fig. 5.18(c)), (b) an assumed sample thickness of 70 μm (trace labelled 2 in Fig. 5.18(b)), (c) an assumed sample thickness of 130 μm (trace labelled 2 in Fig. 5.18(c)).

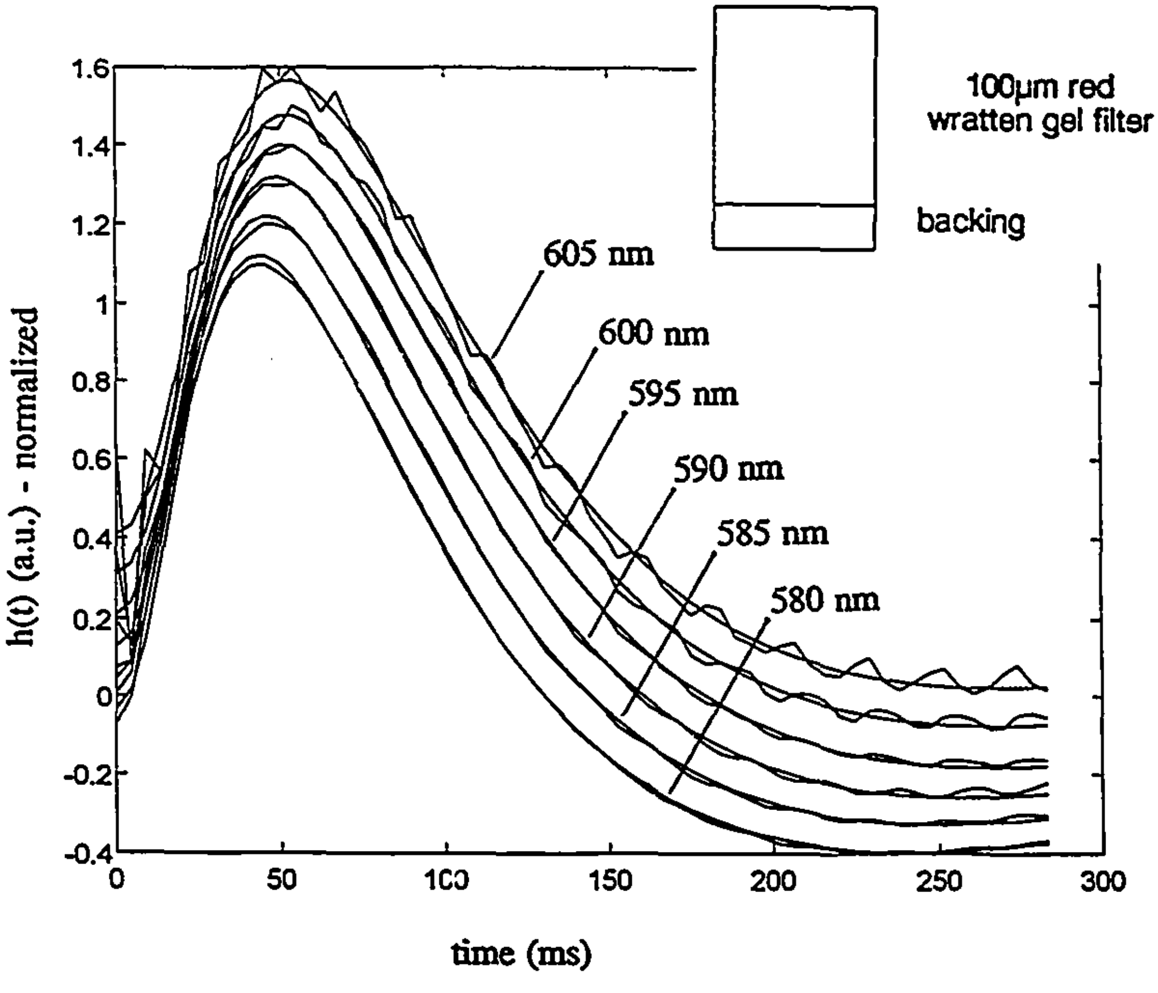

Figure 5.19: Experimental impulse response traces for the sample depicted in Fig. 4.1(k), where the sample consists of a continuous absorbing layer. The traces are offset from each other by 0.1 units. The corresponding fit with the recovered impulse responses are also plotted.

Five representative experimental data sets were plotted with their corresponding fitted impulse responses (Fig. 5.19). These are offset from each other by 0.1 units in the figure (for ease of presentation). A good agreement between the experimental data and the inverse recovery profiles is seen.

5.5 ANALYSIS OF SAMPLES WITH UNKNOWN PROPERTIES USING INVERSE PROBLEM THEORY

The purpose of an inverse model is to be able to determine the heat flux profile, q(x), in a thermally homogeneous sample of unknown q(x). If the profile is to be reconstructed with minimum broadening, a certain amount of *a priori* information must be available. One of these is the probe beam offset position, and the other, the sample thickness (assuming the thermal diffusivity of the sample is known). The probe beam offset position can be determined by supplying a set of experimental data for a surface absorber for the sample being examined. These data are then analyzed with the inverse model in order to determine the probe beam offset position. Different values of the offset position are entered into the basis set, in order to find a basis set which has enough surface region resolution to locate the experimental probe beam position relative to the subsurface. This position must be determined accurately, or the model will see an interface at the front surface which the reconstruction broadens. This is a source of ambiguity in the interpretation of the profile. Once the offset position is determined precisely for this surface absorber, then basis sets can be determined for the other experimental data, by supplying the model with the known thickness or thermal diffusivity of the sample.

If the sample thickness is unknown or poorly characterized, the procedure described below will clarify the interpretation of the reconstructed profiles. Four different situations may be encountered. In the first case, the assumed thickness, l_{assum}, for the reconstruction is the same as the actual thickness of the sample, l_s. This provides a reconstructed heat flux profile which decays to the correct value of l_s (Fig. 5.20). The second case results when the basis set uses l_{assum} greater than l_s. If the heat flux does decay to zero at $x=l_s$ and a discontinuity is present, a "dead zone" will be introduced by the model at the rear of the sample. A sharp discontinuity will appear at $x=l_s$, which will be broadened by the reconstruction. Therefore, the recovered heat flux profile in this case will exhibit a droop in the profile at the rear of the sample (Fig. 5.20).

The third case results when the basis set uses l_{assum} smaller than l_s. The recovered heat flux profile will tail up at the rear surface (Fig. 5.20). In order to determine if this increase in the heat flux profile at the rear surface is real (due to the presence of a source at that location in the sample), l_{assum} must be increased. If the rise in the heat flux profile disappears with increasing l_{assum}, the previous deviation at the rear of the sample was due to a bias in the fit of the basis set. If, in the second case, the profile continues to show a peak located where the previous rise in the profile occurred, followed by a decay of the profile to zero, then one can safely assume that there is indeed a source present at that position. Finally, if l_{assum} is greatly increased beyond l_s, the heat flux profile should decay to zero if l_{assum} is sufficiently large.

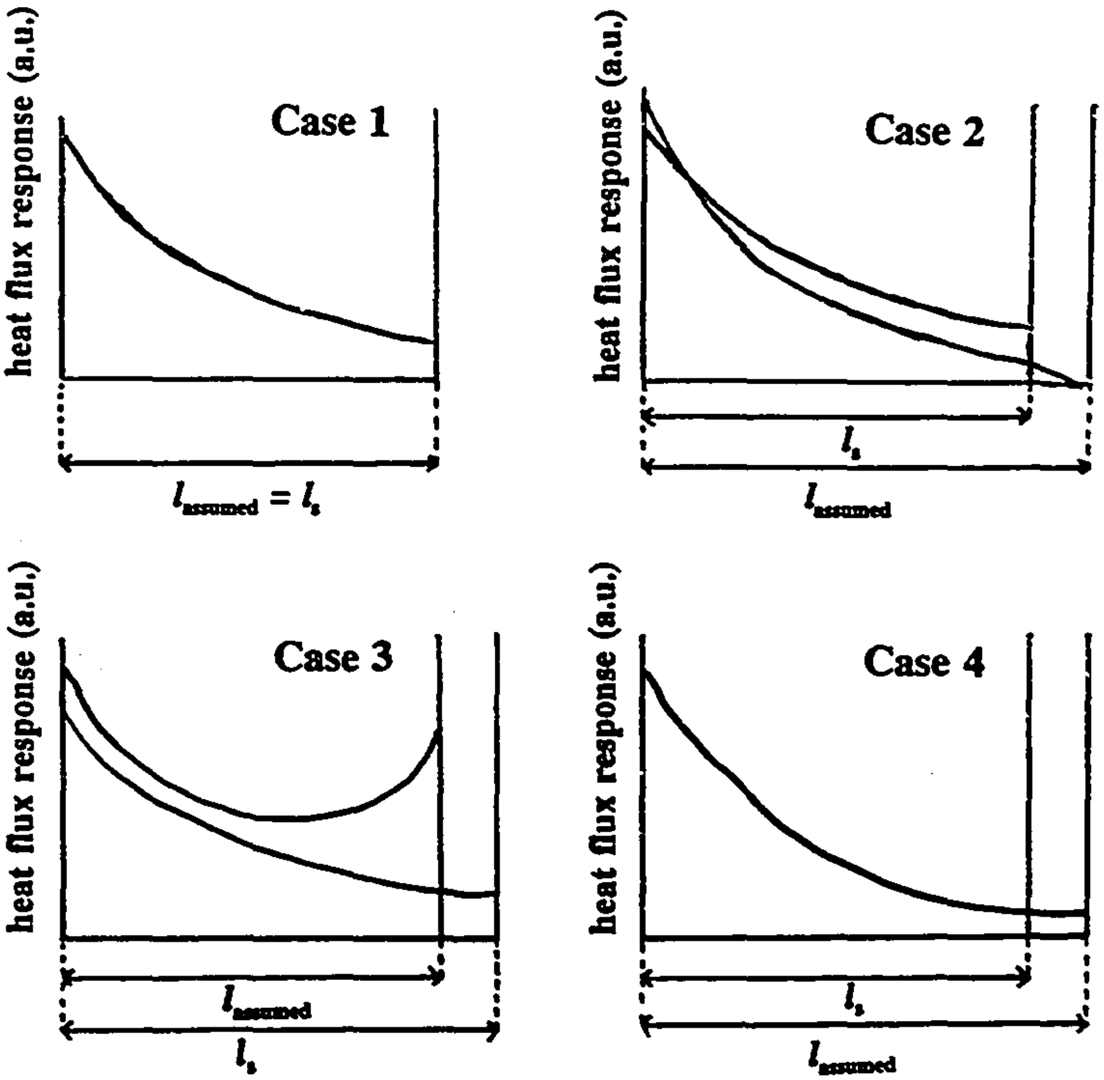

Figure 5.20: Case 1 - $l_{assumed} = l_s$; Case 2 - $l_{assumed} > l_s$; Case 3 - $l_{assumed} < l_s$; Case 4 - $l_{assumed} > l_s$, and heat flux profile does not decay to zero at $x > l_s$.

The final situation which can arise is when l_{assum} is greater than l_s, but the heat flux profile does not decay to zero at $x>l_s$ (Fig. 5.20). This may occur in experiments involving diffusion of optical absorbing species into the rear surface of the film, or in situations where an optically absorbing backing is present. In this case, the thickness used in the model must be increased until the heat flux profile is forced to decay to zero, due to optical absorption. This may require a very large sample thickness, far greater than what is realistic experimentally. In making the sample thickness so large, the resolution of features at smaller depths will be diminished. In such cases, redesigning the experiment is necessary.

The inverse model is able to reconstruct the heat flux profiles semi-quantitatively, for samples which have a continuous (slowly varying optical absorption) layer, at levels of relative random error up to 10%. It is also able to reconstruct the heat flux profiles for two discrete sources for a given level of noise, to within the resolving kernel for the experiment. For several discrete layers in a sample, a lower level of noise is required for accurate reconstruction of the position of these discrete layers. Also, the signal to noise level on the signal response must be high. The resolving kernel for the basis set determined should then be able to differentiate between a sample consisting of several discrete absorbing layers (and their positions in the sample) and a continuous absorbing layer.

5.6 CONCLUSIONS

The inverse model was used to recover the heat flux profiles from the impulse responses generated by examining laminated materials containing discrete and continuous optical absorbing layers. The optical profiles were also reconstructed using the model resulting in the semi-quantitative optical depth profiling of these samples. Using the procedure just outlined for a sample with unknown properties, the heat flux and optical profiles arising from the diffusion of coloured species in membranes is examined in Chapter 6.

REFERENCES

---

1. A.E. Siegman, *An Introduction to Lasers and Masers* (McGraw-Hill Book Company, New York, 1971).

2. M. Abramowitz, and I.A. Stegun, Ed., *Handbook of Mathematical Functions*, NBS Mathematics Series 55 (National Bureau of Standards, Washington D.C., 1964).

3. A. Tarantola, *Inverse Problem Theory: Methods for Data Fitting and Model Parameter Estimation* (Elsevie, New York, 1987).

4. M.C. Prystay, Photothermal Imaging of Optical Polymers, Polymer/Metal Interfaces and the Photodegradation of Poly(vinyl)chloride, Ph.D. Thesis Dissertation, McGill University, Montreal, 1993.

5. J.F. Power, and M.C. Prystay, The Expectation-Minimum (EM): A New Principle for the Solution of Ill Posed Problems in Photothermal Science. In press.

6. J.F. Power, *Microscopic and Spectroscopic Imaging of the Chemical State*, M.D. Morris, Ed. (Marcel Dekker Publishing, New York, 1993) 255-302.

7. A. Harata and T. Sawada, *Photoacoustic and Photothermal Phenomena II*, J.C. Murphy, J.W. MacLachlan-Spicer, L. Aamodt, and B.S.H. Royce, Ed. (Springer-Verlag Berlin, Heidelberg, 1989) 64-66.

8. C. Glorieux, J. Fivez, and J. Thoen, J. Appl. Phys. **73**, 684 (1993).

9. A. Mandelis, S.B. Perralta, and J. Thoen, J. Appl. Phys. **70**, 1761 (1991).

10. B. Noble, *Applied Linear Algebra* (Prentice-Hall, Inc., Englewood Cliffs, New Jersey, 1969).

11. W.H. Press, S.A. Teukolsky, W.T. Vetterling, and B.P. Flannery, **Numerical Recipes in C** (Cambridge University Press, New York, 1992) Chapt. 15, 18.

12. J.F. Power, and M.C. Prystay, Nondestructive Optical Depth Profiling in Thin Films through Robust Inversion of the Laser Photopyroelectric Effect Impulse Response. In press.

13. Ealing Electro-Optics catalogue (Ealing Scientific Ltd., 1988) 238.

TABLE 5.1 DEFINITION OF SYMBOLS USED IN THIS CHAPTER

$U_0(x_0,y_0,z_0)$	complex wave amplitude at initial position (x_0,y_0,z_0)
ω	spot size for the probe beam with a Gaussian distribution
R	radius for a spherical wave
q_r	complex radius of curvature
$U(x,y,z)$	complex wave amplitude at a later output plane (x,y,z), where $z = z_0 + L$
z	distance between the location where the mirage effect occurs and the detector plane
ω_0	spot size for the probe beam at the waist position
$x_0 + a$	position of the He-Ne probe beam, where a = the offset of the probe beam from the sample surface + the distance into the sample of the absorbing layer
k	wavenumber
z_c	waist position of the probe beam on the optical axis
ΔV_B	signal response from the bicell detector, where $V_B = V_B^+ - V_B-$
V_B^+	signal response from the quadrant of the bicell detector, left of the midline
V_B-	signal response from the quadrant of the bicell detector, right of the midline
$g(x-x_0,t-t_0)$	Green's function for one dimensional heat conduction in an infinite medium
$q(x_0)$	heat flux source established in the sample by light absorption
idx	distance of plane heat flux source for the inverse model, in a discretized sample of thickness *l*, where idx = *l*
G	discretized Green's function, (MxN) matrix
S^2	standard deviation for the least square regression

CHAPTER 6 DIFFUSION OF COLOURED SPECIES INTO NAFION MEMBRANES

6.1 INTRODUCTION

The study of transport of materials across a polymeric membrane is important in industrial processes. A measurement technique which could non-destructively examine the concentration profile of species as they diffuse across a membrane would provide a powerful tool for assessing the transport properties of non-homogeneous materials. It would also permit the evaluation of the applicability of these membrane materials in areas such as the barrier properties of packing materials, including those used for protection against hazardous materials, and also a variety of other thin film samples, including coatings and laminates.

Ideally one wishes to examine the time evolution of concentration profiles in materials through which a penetrant diffuses *in situ* with a non-contact, non-destructive method. Mirage effect spectroscopy permits the recovery of absorption coefficients through the spatial profiling of the heat flux in the sample due to light absorption. By the same mechanism, examining the diffusion of a coloured species through the membrane yields the depth dependence of the spatial profile of the concentration. The concentration profile in a thin film, measured as a function of time, contains information relating to the inhomogeneity of the substrate, the concentration dependence of the diffusion coefficient of the substrate material, and the boundary conditions with adjacent layers of solution. Normally such information must be inferred by comparison with a theoretical model of the diffusion process. However, this only applies if the correct model of mass transport in the membrane is assumed. Direct measurements of the depth dependence of the concentration profile may give a better indication of the transport mechanism occurring in a membrane or in a thin film system and would enable the mass transport to be quantitatively evaluated.

6.2 DIFFUSION AND MEMBRANE TRANSPORT

6.2.1 Measurement of Diffusion Coefficients in Membrane Materials

Diffusion is a process in which a species migrating through a solution or substrate becomes spatially dispersed, usually due to the random translational motion of the molecules. The driving force which leads to diffusion is the Gibbs free energy difference between the two regions, one of which has a high solute concentration and the other with a lower value. Under these conditions, the solute will move from a region of high concentration to that of a lower concentration. The diffusion coefficient is a measure of the rate at which the concentration difference between the two regions reduces to zero. It is determined by factors such as the surrounding medium and the thermal mobility of the diffusing particles (1-4).

Diffusion across membrane materials has been examined, previously, in order to characterize the polymer's structure and behaviour. Most methods describe the inter-diffusion of one polymer layer into another or the diffusion of organic solvents into the polymer (2). Fewer methods have been developed to examine the diffusion of water or electrolyte species though a polymer; however, several conventional techniques have been examined for monitoring diffusion and determining diffusion coefficients in polymers.

One method which can be used to study the diffusion of water or other species through a polymer utilizes optical and luminescent indicators. A material which luminesces under ultraviolet radiation, or which changes the luminescence of the material through which it passes, can provide information about the depth of penetration of a diffusant. The penetration of water into a membrane can be examined by adding luminophors to the water and monitoring the integral luminescence with time. If there is any inhomogeneity of the diffusion process with depth, the integral intensity monitored versus time will not be easily interpretable by the theory. Alternatively, if destruction of the sample is permitted, another technique involves taking microtome sections of the material. These sections are examined under UV radiation as a function of the time the polymer has been exposed to a solution containing the diffusant. The disadvantages of this method are that the method is destructive, and the time evolution of the concentration profile of diffusant can only be resolved in the slowest cases (2).

Another means of determining the diffusion coefficient of a substance measures the change in intensity of radiation from a radioactive tracer as the substance diffuses through a membrane into an adjacent solution (5, 6). This experiment may be conducted in an arrangement in which a compartment on one side of the membrane is filled with electrolyte (containing the salt of the ion of interest), doped with a radioactive tracer. On the other side of the membrane, a second compartment contains a solution with the same concentration of the salt. After a time period, an aliquot of the solution in the second compartment is removed and analyzed with a radiation counter. By measuring the change in the radioactivity in the second compartment, the rate of diffusion of the test ion through the membrane can be monitored. A disadvantage with this system is that only diffusants which have a radioactive isotope can be examined (6).

Another method used to determine the diffusion coefficient of species in a membrane is the study of sorption and desorption of gases or the swelling caused by the sorption of liquids. These techniques are outlined in references (2, 7, 8). Eisenberg *et al* examined the sorption of water and electrolytes in Nafion. The procedure involved the immersion of a dry piece of membrane material into a solution containing the diffusant of interest, and the examination of the weight change of the polymer over time. For a plane sheet of a polymer with thickness *l*, where the bulk concentration of the diffusing electrolyte is known, and where the surface concentration of the electrolyte is maintained at a constant level, the apparent diffusion coefficient (after several approximations, including the assumption of very long observation times) is given as

$$D = \frac{0.04919}{(t/l^2)_{1/2}} \tag{6.1}$$

where t is the time when half of the equilibrium concentration of the diffusant has entered the polymer (3, 9). The measurement of water uptake in the membrane was performed by determining the weight change in the membrane from time zero until an equilibrium weight (very small weight change with time) was obtained. The difficulty in using this method is that it requires days for the total weight gain to be obtained (9).

Xu *et al* measured diffusion coefficients of substances penetrating polymers using attenuated total reflectance (ATR) infrared spectroscopy. This technique, unlike most classical measurement methods, offers the possibility of spatially resolving the optical absorption of the diffusant with depth. The intensity variations of the infrared bands were monitored versus time in order to examine the movement of the diffusant into and out of the polymer. The advantage of the technique is that multiple diffusants can be measured, as long as they have different infrared absorption peaks. This same advantage is also one of the limiting features of the technique, since it only applies to infrared absorbing species, and most solvents absorb in wide regions of the infrared spectrum. Another disadvantage of this technique is that the crystal requires a flat surface for adhesion of the sample to the ATR element. Also placement of the crystal adjacent to the diffusing species may result in the perturbation of the surface and the diffusion pattern, requiring modifications of the analytical model used to interpret the data (2, 10).

The diffusion coefficients of electrolytes in a polymer film have been determined using electrical-conductivity measurements, in which assumptions are made to relate the solution conductivity to the diffusion coefficient. The approximations generally assume that a homogeneous polymer is present and that the diffusion coefficient is independent of the electrolyte concentration in the polymer film (11). The measurements using this technique are made using a conductivity bridge, employing a cell consisting of two compartments (each containing an electrode), which are separated by a membrane, which forms a barrier between the two sections of the cell. The equilibrium resistance of the membrane was measured initially, after exposure to the electrolyte solutions for a given time, R(t), as well as once the membrane has reached equilibrium with the electrolyte solution, R(f). A plot of ln(1-[R(f)/R(t)]) versus time can be used to determine the diffusion coefficient if the thickness of the membrane, X, is known (11). The relationship between the resistance and the diffusion coefficient is given by the following equation (assuming that R(f) is known):

$$\ln\left[1-\frac{R(f)}{R(t)}\right] = -\frac{\pi^2 Dt}{X^2}+\ln\frac{8}{\pi^2} \tag{6.2}$$

6.3 USE OF THE MIRAGE EFFECT TO EXAMINE DIFFUSION IN MEMBRANES

Most of the above methods for determining the diffusion coefficients and studying the diffusion process measure an integral concentration, or a slow variation in the mass flux through one surface. The disadvantage with these methods is that they do not directly resolve the spatial concentration profile with time. Interpreting the data requires the selection of a model which correctly identifies the transport mechanism for that system, and the results obtained are dependent on the model chosen. In many cases, the assumed model is simple Fickian diffusion with a concentration independent diffusion coefficient, and often with further simplifying assumptions (eg. one dimensional diffusion, long observation times). Any departures of the experimental behaviour from these restrictive assumptions, will yield misleading or unrealistic results.

Mirage effect spectroscopy is able, in principle, to depth profile the optical absorption coefficient in the membrane directly. The advantage of this technique is that the concentration profile can be resolved as a function of time. Most prior work in this area has been in the direct probing of a concentration gradient above the sample surface where this gradient is established by electrochemical processes in the cell rather than by a photothermal mechanism (12-15). The mirage effect results from a change in the refractive index, which in the case of reactive electrolytic solutions, is comprised of two components. One component originates from the thermal waves caused by absorption of the modulated heating beam, and the other component, from the concentration gradient formed from the diffusion of the electrolyte across the membrane. The experimental conditions that can distinguish the two effects have been previously investigated (15). By altering the position of the probe beam relative to the electrode, the contributions from the thermal diffusivity and the ion diffusivity can be separated and calculated. For example, contributions to the change in the refractive index arising from thermal waves occur on a different timescale to that of ionic waves; however, there is a greater contribution to the refractive index gradient from the mass diffusion of the ion. Ionic and thermal diffusion coefficients were determined and were found to be in good agreement with the literature values (15).

6.4 PROPERTIES OF NAFION MEMBRANES

The study of the transport of ions or neutral species across polymeric ion exchange membranes is of interest in many industrial applications. The use of these membranes is defined by their physical and chemical properties. This chapter will focus on ion transport in a specific membrane, namely Nafion (Nafion is a registered trademark of the E.I. DuPont de Nemours & Co.). Nafion is an ion-exchange membrane consisting of a poly(tetrafluoroethylene) backbone with perfluoroether side chains containing sulphonic acid endgroups. This structure results in a strongly hydrophobic backbone and hydrophillic terminal groups (16). Fig. 6.1 shows the chemical formula for Nafion membranes developed by DuPont (17, 18). Nafion is a high molecular weight polymer,

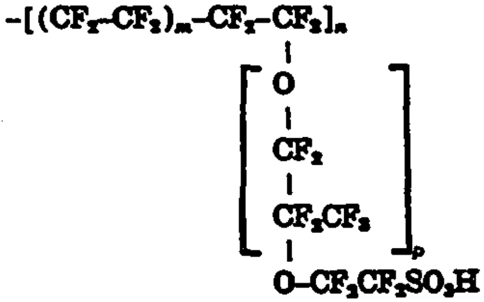

$$-[(\mathrm{CF_2{-}CF_2})_m{-}\mathrm{CF_2}{-}\underset{\underset{\mathrm{O{-}CF_2CF_2SO_3H}}{\left[\begin{array}{c}|\\ \mathrm{O}\\ |\\ \mathrm{CF_2}\\ |\\ \mathrm{CF_2CF_3}\\ |\end{array}\right]_p}}{\mathrm{CF_2}}]_n$$

$(m = 5\text{–}13.5,\ n = \sim 1000,\ p = 1,2,3\ldots)$

Figure 6.1: The chemical formula for Nafion membranes developed by E.I. DuPont de Nemours & Co.

exhibiting an ion-cluster morphology. Fig. 6.2 illustrates this structural model for Nafion.

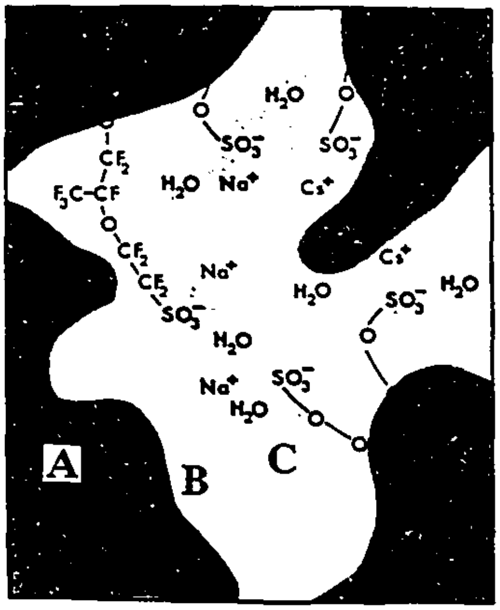

Figure 6.2: Structural model for Nafion membranes. Region A - fluorocarbon; region B - interfacial zone; region C - ion-cluster region (19).

In these ion-clustered polymers, there is no cross-linking and the aggregated ion-clusters are phase-separated from the water and the fluorocarbon material (17). The structure proposed for Nafion consists of three regions: an ion cluster region, an interfacial region, and a fluorocarbon region. These structures appear to be homogeneously distributed over the bulk of the film (19). The presence of these ion clusters result in the unique mechanical and transport properties of the polymer material (20). Sakai *et al* estimated that the clusters located in the membrane had dimensions of approximately 50 x 10^{-10} m, and that these clusters were connected by narrow channels of approximately 10 x 10^{-10} m (21).

Nafion material has been used in many industrial applications due to properties exhibited by the polymer, such as its chemical stability, its permselectivity, and its high conductivity. For example, Nafion has been used in applications such as the chlor-alkali industry (5, 22, 23), fuel cells (24), and coatings for modified electrodes (18, 25-29). The permselectivity of the membrane results from the ability to allow the passage of the cations but not those of anions. Several workers in the field have investigated the permeability and selectivity of this cation-exchange membrane (8, 9, 16, 19, 20, 30-34).

Although Nafion is important in industrial processes, the reason that this membrane material was chosen for this study is due to its well characterized transport properties, and its structural morphology, which exhibits several different diffusion processes depending on the nature of the ionic diffusant (35). The cluster ion regions of Nafion interact with ions having a large charge density resulting in sorption of the ions. The diffusion coefficients were found to be in the range 1.0×10^{-8} m^2/s - 1.0×10^{-10} m^2/s. The interfacial region usually interacts with larger ions, containing hydrophobic functionalities, and leads to a different transport process, ie. one which has a diffusive behaviour. The diffusion coefficients were found to be in the range 1.0×10^{-10} m^2/s - 1.0×10^{-12} m^2/s (35). The diffusion coefficients in the third region, that of the fluorocarbon, are very slow, primarily involving non-ionic diffusants, and were not of interest to this work. The other two diffusion behaviours will be discussed in more detail in section 6.5.

6.4.1 Determination of Diffusion Coefficients in Nafion Membranes

Several workers have examined the transport behaviour of electrolytes across Nafion membranes (5, 6). Wang *et al* used UV-Visible spectrophotometry in a flow through cell to measure the diffusion coefficients of copper, cobalt, and chromium ions into Nafion membranes. The spectral cell consisted of two solution regions, of known thickness, and a Nafion membrane, of known thickness, inserted between the two flow through solution compartments. The solution flow rate was maintained constant on either side of the membrane so that the absorbance would be constant outside the membrane, and any variations in the total cell absorbance would be due to the uptake of cations by the membrane. The differential absorbance was monitored over time until the absorbance in the membrane became constant, indicating that the Nafion was saturated with metal ions. From the time dependence of these absorbance measurements, the apparent diffusion coefficient was determined for the cation species (35).

The theoretical model which was derived to explain the transport of species into the cluster regions of Nafion included the effects of diffusion as well as the reversible coordination of the ions to the sulphonate sites in the ionomer membrane (sorption). This will result in a portion of the diffusant being electrostatically bound to the membrane's ionic clusters, while another component of the species is able to diffuse freely into the interfacial regions of the membrane. The assumptions made by Wang *et al* for their model were as follows: the sorption process was reversible, the diffusion of the metal ions in the solution domains of the Nafion membrane was determined by Fickian diffusion, with a concentration independent diffusion coefficient, no inter-diffusion between bound diffusant and counter ion was assumed to occur. The diffusion coefficient of the exchange counter ion (typically H^+), was assumed to be very large relative to that of the diffusant ion.

If inter-diffusion applies, the chemical interactions between the displaced counter ions and the diffusant ions bound to the ion-exchange sites can be given by the following treatment. The following equilibrium is assumed for the cation in the free (C_f) and bound (C_b) states of the form:

$$C_f \underset{k_b}{\overset{k_f}{\rightleftharpoons}} C_b \tag{6.3}$$

where the rate constants are given by k_b and k_f (35). Samec *et al* used the following modified diffusion equation to describe the inter-diffusion of two exchanged ions, A (H^+ ion for example), and B (the ion of interest), in Nafion:

$$\frac{\partial C_i}{\partial t} = \frac{\partial[D_{AB}(\frac{\partial C_i}{\partial x})]}{\partial x} \tag{6.4}$$

where D_{AB} is the diffusion coefficient for the inter-diffusion of A and B, and is given by:

$$D_{AB} = D_A D_B(z_A^2 C_A + z_B^2 C_B) \, / \, (D_A z_A^2 C_A + D_B z_B^2 C_B) \tag{6.5}$$

where z_i is the charge on the ion and C_i is the ionic concentration.

If the assumptions are made that the diffusion of the H^+ ion is very fast relative to the ion of interest ($D_A z_A^2 C_A >> D_B z_B^2 C_B$), and that the membrane sites are only fractionally occupied by B ($C_B << C_A$), equation (6.5), with division by $D_A z_A^2 C_A$, becomes:

$$D_{AB} \approx D_{B} \tag{6.6}$$

This indicates that the inter-diffusion coefficient is equivalent to the diffusion coefficient of the ion of interest (e.g. the diffusant) (36), and is approximately independent of the counter ion.

6.4.2 Diffusion-Reaction Model

The transport behaviour of ions in Nafion membranes is not well understood (17); however, several workers have used theoretical mass transport models which incorporate Fickian diffusion and sorption (ion exchange) to describe the ion transport in Nafion membranes (35-38). In this section, a one-dimensional transport model incorporating ion exchange interactions between the diffusant and the binding sites is presented. The assumptions made are that the sorption processes (equation (6.3)) occur very rapidly on the time scale of the experiment (whereas the diffusion of the species is much slower), and that the rate constant of the binding of the diffusant species is large relative to the rate constant for dissociation of the diffusant/sulphonate ion pair.

The general equation (in one dimension), for diffusion in which adsorption of the diffusant occurs is:

$$\frac{dC_f}{dt} = D \cdot \frac{d^2C_f}{dx^2} - \frac{dC_b}{dt} \tag{6.7}$$

where D is the diffusion coefficient and C_b is the concentration of the diffusing substance which is immobilized by adsorption into the membrane. The latter is directly related to the concentration of the diffusing species, C_f, by the general relation:

$$C_b = RC_f^{\,n} \tag{6.8}$$

where R is a constant defining the proportion of species which are bound (C_b), versus those which are free to diffuse (C_f) ($R = k_f/k_b$) (37). In the development of this model, the relationship given in equation (6.8) is assumed to be linear (n=1). This results in the following relationship

$$\frac{d^2C_f}{dx^2} = [\frac{R+1}{D}]\frac{dC_f}{dt} \tag{6.9}$$

Fig. 6.3 shows a schematic of the geometry of the system where region 1 and 3 contain a fluid phase and region 2 is the membrane material. The concentration in each of these regions can be given by the following equations

$$\frac{d^2C_1}{dx^2} - \frac{1}{D_1}\frac{dC_1}{dt} = 0 \qquad \text{(Region 1)} \tag{6.10}$$

$$\frac{d^2C_{2f}}{dx^2} - [\frac{R+1}{D_2}]\frac{dC_{2f}}{dt} = 0 \qquad \text{(Region 2)} \tag{6.11}$$

$$\frac{d^2C_3}{dx^2} - \frac{1}{D_3}\frac{dC_3}{dt} = 0 \qquad \text{(Region 3)} \tag{6.12}$$

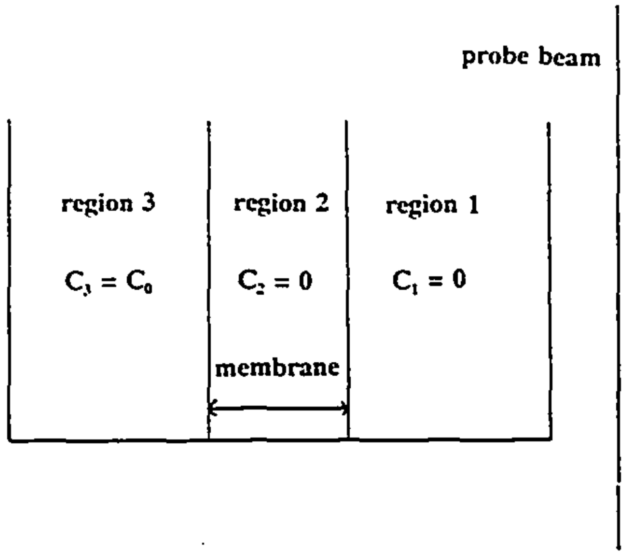

Figure 6.3: Schematic diagram of the system geometry, showing the two regions of solution (region 1 and 3), and that of the membrane (region 2).

where the concentration and diffusion coefficients of the species in regions 1, 2, and 3, are given by C_1, C_2, C_3 and D_1, D_2, D_3, respectively. Evaluation of these expressions is performed by means of the Laplace transform method (39). The Laplace transforms in equations (6.10), (6.11), and (6.12) are written for the homogeneous equations of the form

$$\frac{d^2C(x,s)}{dx^2} - k_c^2 C(x,s) = 0 \qquad \text{where} \quad k_c^2 = \frac{(R+1)s}{D} \tag{6.13}$$

and where s is the Laplace domain variable.

In region 3, there is an additional term introduced, due to the contribution of the initial concentration present in that region ($-\infty<x<-\sigma_N$). This term can be given by equation (6.14):

$$C_3(x,t=0) = C^{INIT} = -\frac{C_0}{D_3}[U(-(x+\sigma_N)) - U(-(x+(\sigma_N+a)))] \qquad \textbf{(6.14)}$$

where 'a' gives the position of the back wall of the rear cell compartment, $[U(-(x+\sigma_N))-U(-(x+(\sigma_N+a)))]$ defines the region where the initial concentration is present, and $q_3 = \sqrt{s}/\sqrt{D_3}$. By integrating this expression within this region, the following expression results for the initial concentration present in region 3

$$\hat{C}_3(x,s)^{initial\ condition} = \frac{C_0}{2s}[2 - e^{q_3(x+\sigma_N)}] \qquad (as \quad a \rightarrow -\infty) \qquad \textbf{(6.15)}$$

The Laplace transforms for the three regions can then be given by the following expressions:

$$C_1(x,s) = A_1 e^{-q_1 x} \qquad \text{(Region 1)} \quad \textbf{(6.16)}$$

$$C_2(x,s) = A_2(s)\, e^{-q_T x} + A_3(s)\, e^{q_T x} \qquad \text{(Region 2)} \quad \textbf{(6.17)}$$

$$C_3(x,s) = A_4(s)\, e^{q_3(x+\sigma_N)} + \frac{C_0}{2s}[2-e^{q_3(x+\sigma_N)}] \qquad \text{(Region 3)} \quad \textbf{(6.18)}$$

where A_i are boundary coefficients, $q_i = \sqrt{s}/\sqrt{D_i}$ is a diffusive mass transport length, and q_T is a mass transport length, given by

$$q_T = \frac{\sqrt{1-R}\,\sqrt{s}}{\sqrt{D_2}} \tag{6.19}$$

Application of concentration and concentration flux continuity boundary conditions at the interfaces, results in the following expressions:

$$at\,x=0 \quad C_1(x,s) = C_2(x,s)$$

$$-D_1\frac{dC_1}{dx}\bigg|_{x=0} = -D_2\frac{dC_2}{dx}\bigg|_{x=0} - h\,\frac{k_f}{k_b}C_2(x,s)\bigg|_{x=0} \tag{6.20}$$

and

$$at\,x=-\sigma_N \qquad C_2(x,s) = C_3(x,s)$$

$$-D_2\frac{dC_2}{dx}\bigg|_{x=-\sigma_N} + h\,\frac{k_f}{k_b}C_2(x,s)\bigg|_{x=-\sigma_N} = -D_3\frac{dC_3}{dx}\bigg|_{x=-\sigma_N} \tag{6.21}$$

where h is the mass transfer coefficient, k_f is the rate constant of the free diffusant binding to the ionic sites, and k_b, that of the release of the bound diffusant.

Application of these boundary conditions results in a set of linear equations in the boundary coefficients, A_i:

$$A_1(s) - A_2(s) - A_3(s) = 0 \tag{6.22}$$

(concentration continuity at x=0 boundary)

$$B_{12}A_1(s) + [\gamma-1]A_2(s) + [\gamma+1]A_3(s) = 0 \tag{6.23}$$

(concentration flux continuity at x=0 boundary)

$$A_2(s)e^{q_T\sigma_N} + A_3(s)e^{-q_T\sigma_N} - A_4(s) = \frac{C_0}{2s} \tag{6.24}$$

(concentration continuity at x=-σ_N boundary)

$$[\gamma+1]A_2(s)e^{q_T\sigma_N} + [\gamma-1]A_3(s)e^{-q_T\sigma_N} + B_{32}A_4(s) = B_{32}\frac{C_0}{2s} \tag{6.25}$$

(concentration flux continuity at x=-σ_N boundary)

The parameters B_{12}, B_{32}, and γ are defined as follows

$$B_{12} = \frac{D_1q_1}{D_2q_T} \qquad B_{32} = \frac{D_3q_3}{D_2q_T}$$
$$\gamma = \frac{h\frac{k_f}{k_r}}{D_2q_T} \tag{6.26}$$

Once the parameters, A_i, are evaluated, then the concentration profile in the membrane, and in region 3 (where the diffusant is initially concentrated), is solved. The effective length over which mass transfer is possible can be given by $h \approx q_T$. The following simplification can then be made to γ:

$$\textit{assume} \qquad s < k_b, k_f$$
$$\wedge \quad h = \frac{\sqrt{D_2}\cdot\sqrt{\frac{k_B}{(k_B+k_F)}}}{\sqrt{s}} \tag{6.27}$$
$$\textit{then} \qquad \gamma = -\frac{k_F}{(k_B+k_F)}$$

The inverse Laplace transform is solved (by means of mathematical tables) (39), resulting in the following expressions for the concentration in regions 2 and 3:

$$C_2(x,t) = \frac{B_{32}}{B_{32}+(\gamma+1)} \cdot erfc[\frac{(x+\sigma_N)}{\sqrt{4D_C t}}] \qquad \textbf{(6.28)}$$

$$where \qquad D_C = D_2(\frac{k_B}{k_B+k_F})$$

and

$$C_3(x,t) = \frac{1}{2}[\frac{(B_{32}-(\gamma+1))}{(B_{32}+(\gamma+1))}-1] \cdot erfc[\frac{(x+\sigma_N)}{\sqrt{4D_3 t}}]+1 \qquad \textbf{(6.29)}$$

These two expressions are then evaluated by calculations using routines written in MATLAB software (TM The Math Works, Natick, Mass).

6.5 EXPERIMENTAL RESULTS AND DISCUSSION

6.5.1 Introduction

The use of the mirage effect as a probe of the diffusion process, by examining the migration of a coloured species as a diffusant in Nafion is examined in this section. The cationic species selected for investigation were chosen according to the following criteria: they exhibited a high absorption coefficient (within the wavelength range of an Argon laser (514 nm) or a dye laser (580 nm - 610 nm)) at low concentration, so that they could be studied; the transport behaviour of the species needed to be well defined or generally predictable; the cationic species had to penetrate the Nafion film (210 μm) in a reasonable amount of time (< 6 hours). The first species chosen was tris(1,10-phenanthroline)iron(II) sulphate which absorbs strongly at 514 nm. In Nafion its diffusion behaviour is similar to that of $Ru(byp)_3^{2+}$ complex (35, 36), which was found to follow a diffusive behaviour due to interaction mainly with the interfacial domains in Nafion. The next test ion examined was tetraamminecopper(II) sulphate, which absorbs strongly at 590 nm, and which is expected to interact mainly with the cluster ion regions of Nafion. The third cation was hexaaquochromium(III) sulphate, known to interact with the cluster ion region. In this latter case, the hexaaquochromium(III) ion was leached from a stained membrane (absorption at 590 nm). The last cationic complexes exhibit reduced ionic radii, compared to the tris(1,10-phenanthroline)iron(II) ion, and are expected to interact mainly with the ion-cluster regions, resulting in a markedly different sorption diffusion behaviour (e.g. rapid sorption) (35).

6.5.2 Preparation of Nafion membranes

Nafion sheets (equivalent weight, EW, of 1100) were purchased from Aldrich Chemical Co., and the thickness of the dry membrane material was measured to be 210 μm (±5 μm). Once exposed to air, the residue on the surface is slowly oxidized forming a yellow discolouration on the material. In order to depth profile the membrane, all residual colour not associated with the species of interest, was eliminated. This discolouration was removed by boiling the membranes in 1.0 M nitric acid (reagent grade) for 2-3 hours, and then the excess acid was removed by boiling the membranes in distilled water for 2-3 hours. The membranes were then stored in deionized water until they were used (40).

6.5.3 Experimental Results and Discussion on Cationic Species Exhibiting Diffusive Behaviour in Nafion Membranes

The mirage effect instrumental apparatus described previously (Chapter 2) was used to study the diffusion in membranes. The schematic of a special cell designed to study diffusion can be found in Fig. 6.4. A Nafion membrane is stretched over the opening (Fig. 6.4, labelled 1 in diagram) of a rear compartment constructed of delrin, and a cap is placed over the membrane, and tightened to keep the membrane taut. This assembly is inserted into the main body of the cell (Fig. 6.4, labelled 4 in diagram). Four index spots are placed on the membrane to allow for precise calibration of alignment of the probe beam above the surface (see section 2.4.3). The membrane is equilibrated in 0.005 M sulphuric acid (ca. 18 hours) and then mounted in the cell. Both front and rear compartments of the cell are filled with 0.005 M sulphuric acid and measurements are taken for the initial alignment of the membrane relative to the He-Ne probe beam. All the impulse response data were recorded with 100 Hz frequency sweep.

At t=0, a 0.01 M solution of tris(1,10-phenanthroline)iron(II) sulphate is injected into the rear compartment, and a complete turnover of the solution in the rear compartment is made to ensure that a constant (known) concentration is present in this

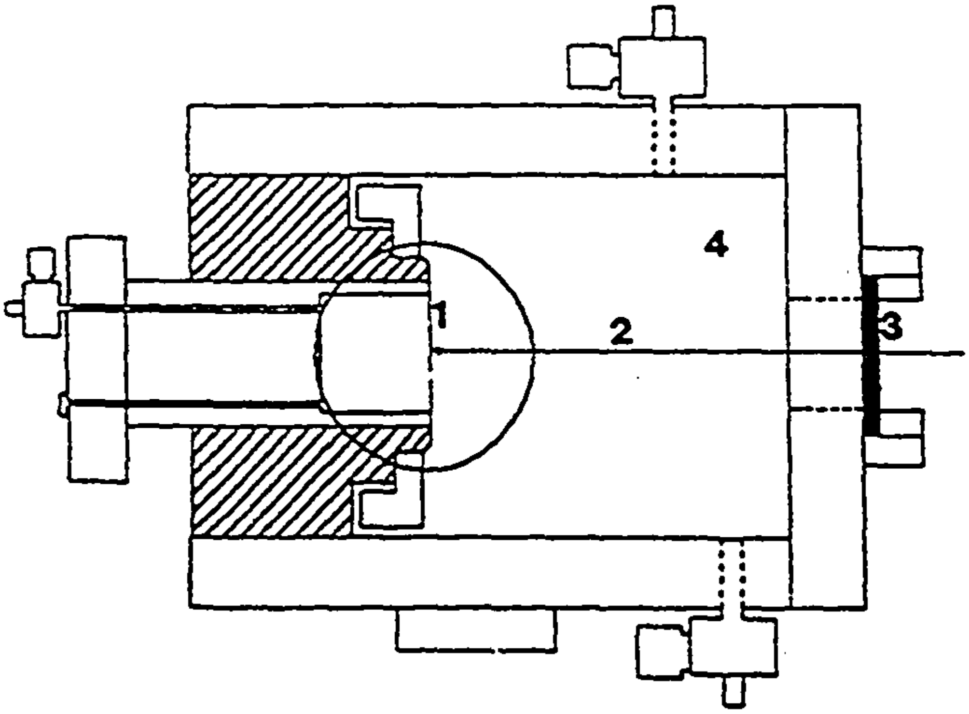

Figure 6.4: Schematic diagram of the cell used to study diffusion in Nafion membranes (1 - membrane surface; 2 - excitation source; 3 - glass window; 4 - front solution compartment).

compartment. An absence of convection cells in the rear compartment was confirmed over time by uniform lateral staining of the membrane. As the cationic species diffuses into the membrane, and undergoes sorption as well as diffusion, which may cause the membrane to expand. In order to avoid large variations in the movement of the membrane, the net differential concentration change of the ions in solution (and the membrane) must be maintained close to zero. This reduces the effect of osmotic pressure and the Donnan potential across the membrane (41).

Impulse response data are taken by alternating the position of the pump beam between an index spot (to locate the surface position at all times during the course of the experiment) and a region of the membrane where the ionic species is diffusing. By monitoring the surface displacement, the expansion of the film due to the sorption process can also be examined. The surface position is required to accurately reference the depth profile of the ionic species as it diffuses into the membrane (see section 2.4.3).

The diffusion of the coloured complex was monitored over a period of about 350 min. The measurement was stopped once the time dependence of the impulse response stopped changing significantly. For the tris(1,10-phenanthroline)iron(II) ion examined in this first study, the optical density in the membrane is confirmed to be several times greater than that in solution. This result is expected since perfluorosulphonated membranes, in general, are known to concentrate ions (28, 35, 36).

Several replicates of the experiment were performed, using a freshly prepared piece of Nafion membrane in each case. In all but one case, the swelling of the membrane due to sorption was very fast, causing the membrane to swell closer to the probe beam passing along the membrane surface. Fig. 6.5 shows the impulse responses of one data set (at representative times) obtained for the sample region (the traces are offset from each other for ease of presentation). The impulse responses show a variation in time, but this is due to a combined effect of swelling of the membrane (which changes the surface position) and the migration of the absorbing ions across the membrane. The swelling behaviour of the membrane seen in these experimental responses can be corrected from the measured variation in the probe beam offset positions in time. In order to monitor the contribution of the optical profile, as the cationic species moves through the membrane, the inverse scattering model of Chapter 5, is used to reconstruct

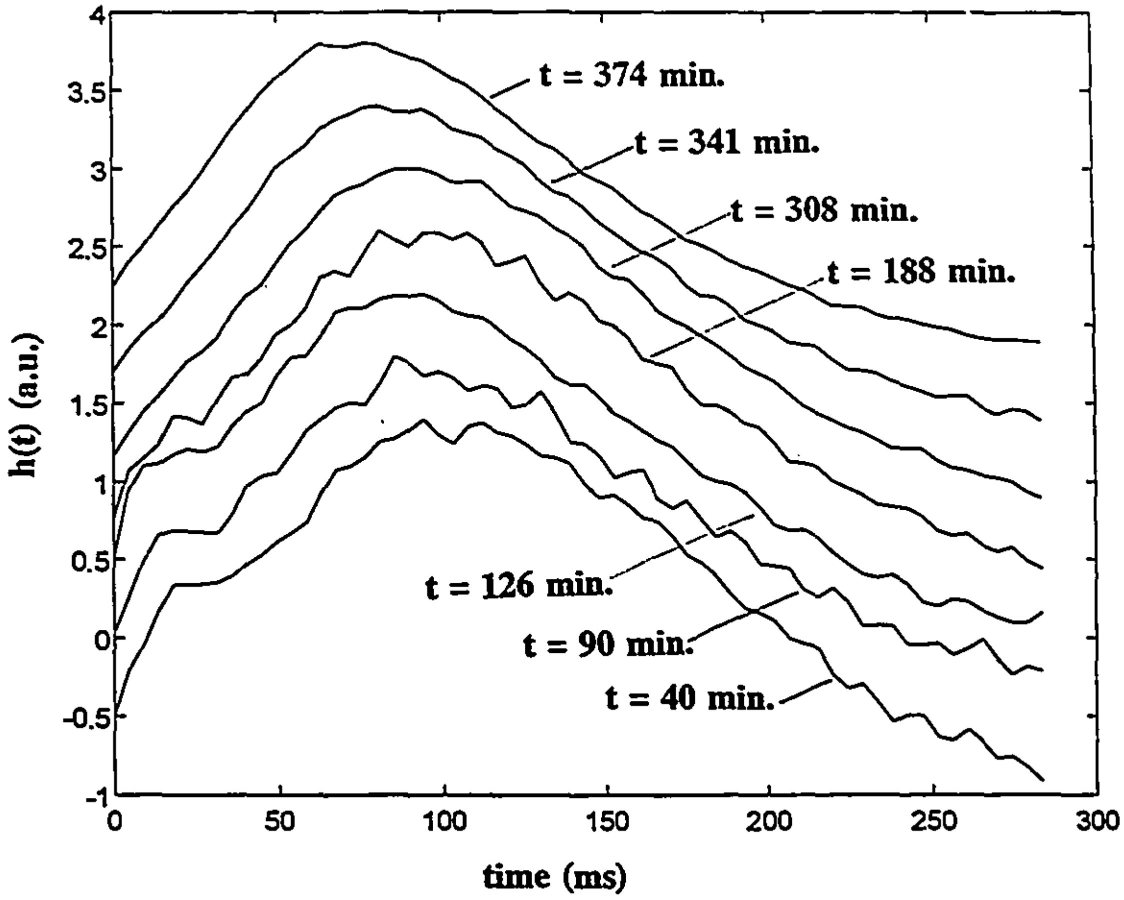

Figure 6.5: The experimental impulse responses data (at representative times) for the sample region. The traces are offset from each other by 0.4 units.

the heat flux profile from the experimental data.

The heat flux reconstructions were made using basis sets with probe beam offset values obtained from the index spot measurements for h(t). A sample thickness of 425 μm was assumed to accommodate any possible contributions of optical absorption from the rear compartment. Fig. 6.6 shows the recovered heat flux profiles for representative times in the experiment.

The heat flux reconstructions are then used to obtain the optical absorption coefficient profiles (as outlined in Chapter 5). To perform the calculation of $\beta(x)$, the membrane thickness was measured and found to be 210 μm (±5 μm). The solution in the rear compartment has a lower absorbance than that present in the membrane (0.373 a.u. versus 2.28 a.u.); therefore, it is not expected to contribute substantially to the optical profile. For this reason the optical absorption coefficient profiles are reconstructed using the actual sample thickness (210 μm) and the optical density of the membrane measured as a function of time. Fig. 6.7 shows the optical absorption coefficient profiles (using the same representative times as indicated in Fig. 6.6).

The absorbance in the membrane was measured as a function of time using a UV-Visible spectrophotometer (under parallel conditions as those in the experiment, except the membrane was removed at various times and the absorbance was recorded). The optical density of the film was found to be invariant with time (after t = 126 min.), which varies from the expected behaviour (an increase in the optical density with time is expected). However, if we consider that a blank piece of Nafion membrane scatters light (at levels as low as 1%), and this level of light scattering is sufficient to produce spectro-

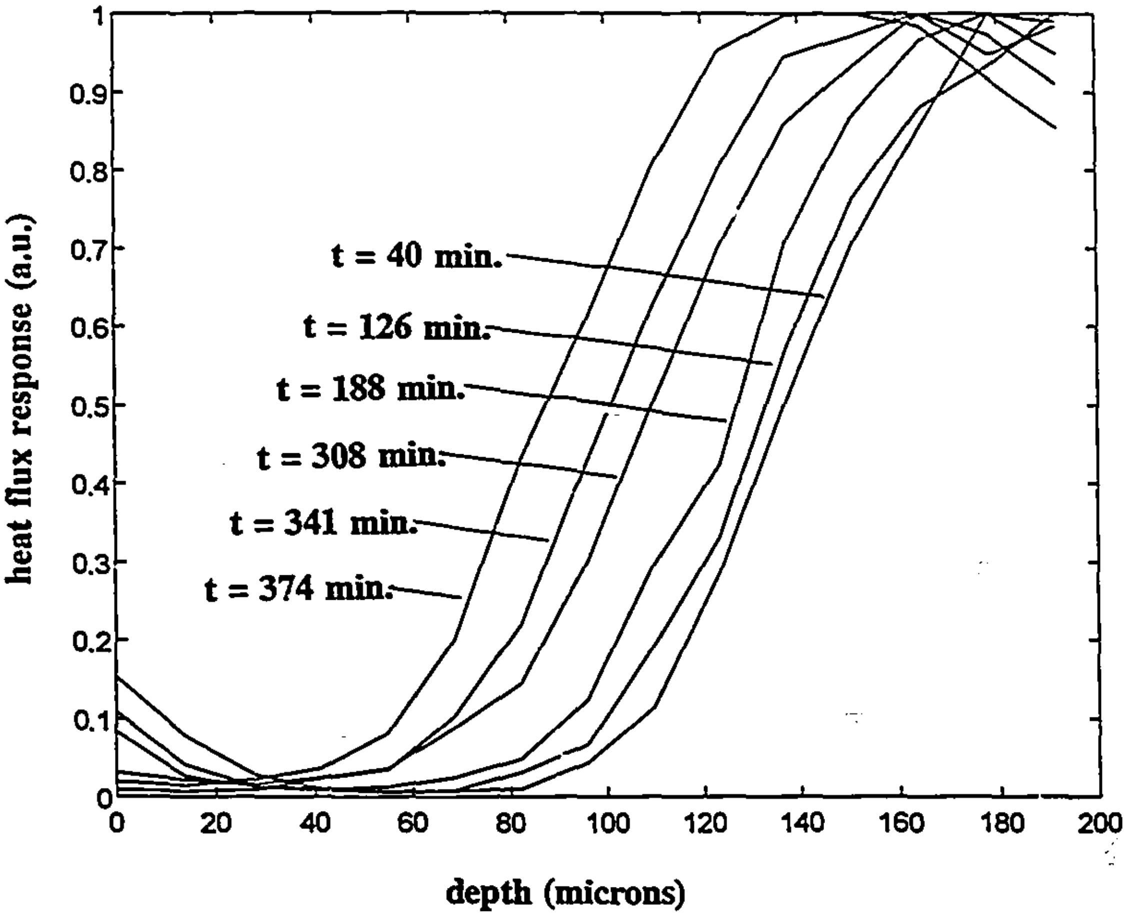

Figure 6.6: Recovered heat flux profiles (at representative times) for the sample region.

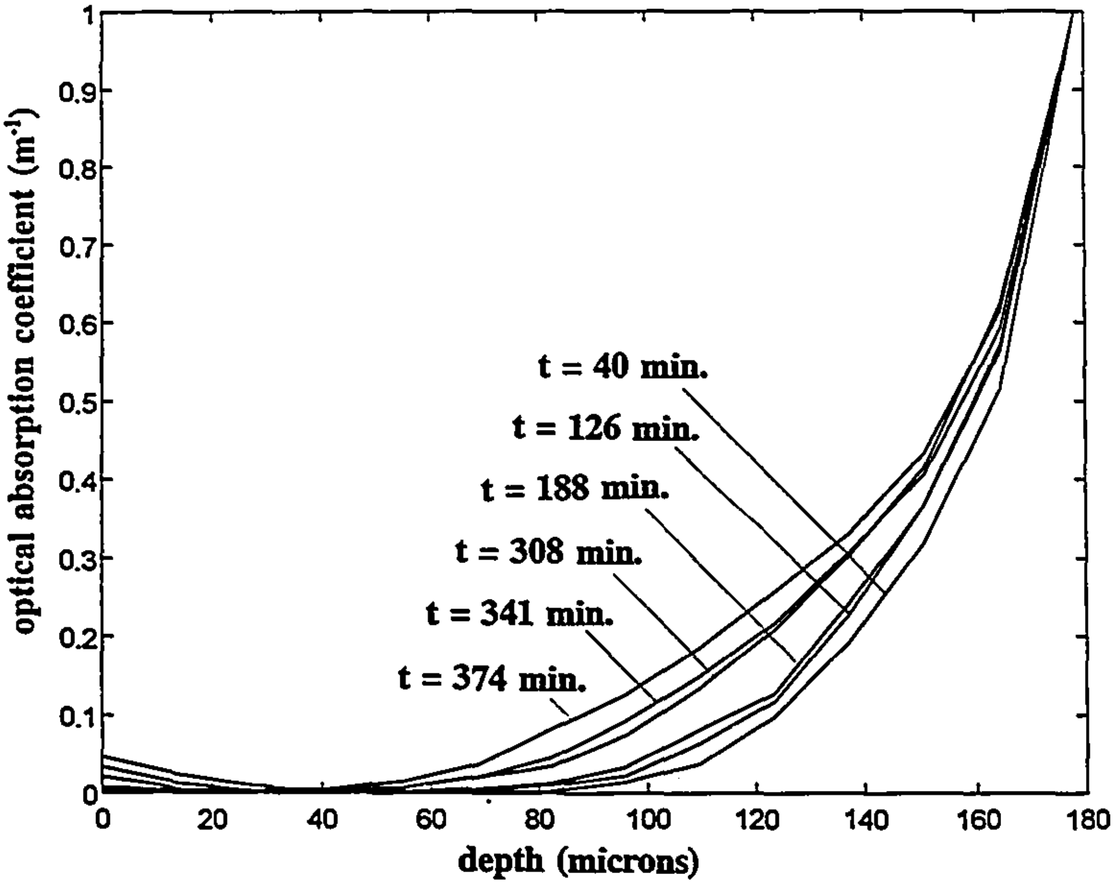

Figure 6.7: Recovered optical absorption coefficient profiles corresponding to the representative times indicated in Fig. 6.6.

photometer saturation above an optical density of 2.0 (42), then it becomes clear that the film is optically saturated under the experimental conditions. Therefore, no effective variation with time is observed, and the recovered ß(x) profiles are only estimates, albeit poor ones, of the film's true optical density.

In order to compare the optical absorption profiles with the concentration profiles predicted from a model, C(x,t) were determined theoretically by using equation (6.28) and (6.29). The parameters required by the model were selected by the following considerations. The initial solution composition in the front and rear compartments, and in the membrane, was predominantly water. A diffusion coefficient of 1.0×10^{-10} m^2/s was chosen for the water (35), which is several orders of magnitude greater than the diffusion coefficient of the complex species. The value estimated for the ionic complex species was 1.0×10^{-12} m^2/s, which is within the range for diffusion coefficients of similar cations (35). The value of R used (see equation (6.28) and (6.29)), defines the ratio of the rates of formation of bound species to that of the dissociation of the complex to the free cation. A 10 fold value was estimated for this parameter from measurements of the optical density of the membrane and a similar thickness (210 μm) of the rear compartment solution, also, $k_b << k_f$. The other parameters entered were the experimental observation times and the spatial resolution. Fig. 6.8 shows the normalized concentration profiles obtained as a function of time.

The experimental ß(x) profiles (Fig. 6.7) show a relatively small variation between the traces, while the theory predicts a large resolvable variation in C(x,t) (Fig. 6.8). The reason for this discrepancy must be explained. The greatest variation can be seen at the earliest times in the experiment (less than 100 min); there is little variation between the experimental ß(x) profiles, while the C(x,t) traces (which are proportional to ß(x)) show a substantially greater variation.

In order to explain this discrepancy, the recovery of ß(x,t) from the theoretical C(x,t) must be made and the pattern of errors in the reconstructions examined. Also, the resolution limit of the inverse reconstruction with a given level of noise (3%) on the basis must be considered. The line spread of the resolving kernel for the basis sets used was determined, by placing a delta function at a depth of 210 μm (corresponding to the back of the film) (see Chapter 5 for more detail), and examining the broadening due to the reconstruction of the heat flux profile at that position. Fig. 6.9 shows the experimental heat flux profiles at early times ($t \leq 100$ min.), and the resolving kernel for this theoretical delta function reconstruction. It is clear that all of the experimental heat flux traces lie within the resolving kernel (for a given level of noise, that of 3%); therefore, these profiles cannot be expected to be resolved.

At later times in the experiment (greater than 100 min), the experimental ß(x) profiles show a greater variation relative to each other, but they continue to differ from the concentration profiles. In order to make a direct comparison between the theoretical concentration profiles and the experimentally reconstructed ß(x), C(x,t) must be subjected to the same analytical treatment as the experimental data. From the measured extinction coefficient for tris(1,10-phenanthroline)iron(II) sulphate, the theoretical profiles of the optical absorption coefficient, ß(x,t), were computed corresponding to C(x,t). These were then used to calculate heat flux profiles from theory, and to predict the expected mirage

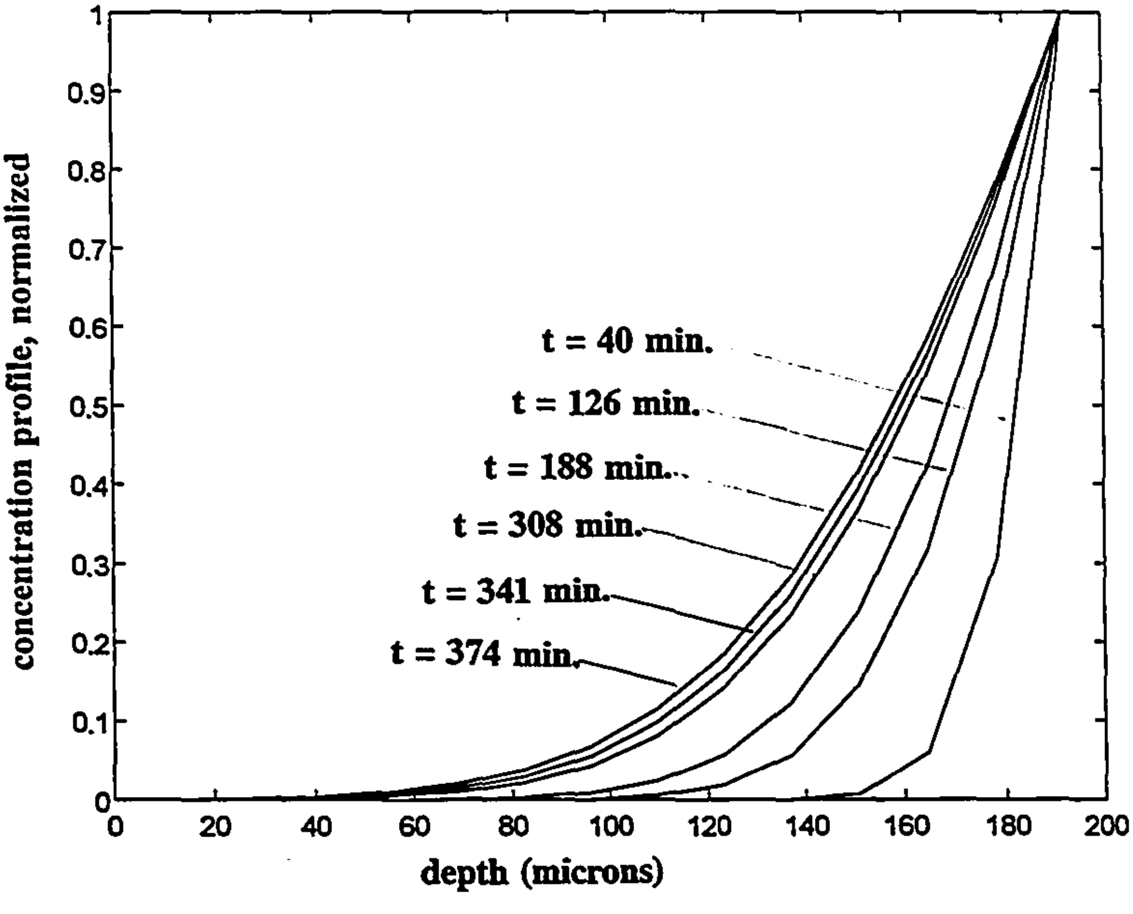

Figure 6.8: Normalized concentration profiles generated from the diffusion model (equation (6.28) and (6.29)).

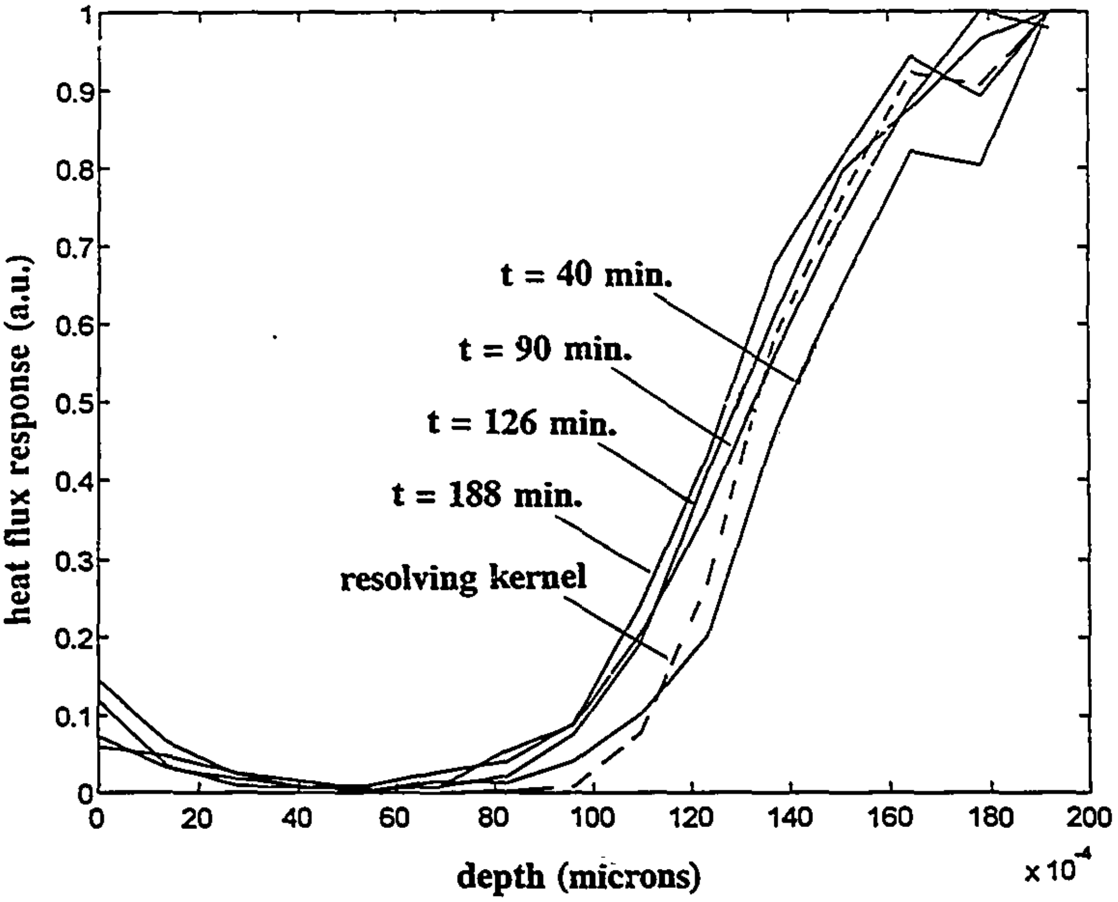

Figure 6.9: The experimental heat flux profiles at early times with the resolving kernel for a theoretical delta function reconstruction (where the delta function is placed at a depth of 210 μm).

effect signal. The resulting theoretical ME impulse responses are then inverted using the inverse model. This allows an evaluation of the influence of the experimental instrument on the reconstruction of the ß(x) profiles from the theoretical data. These recovered heat flux profiles are then compared with the experimental results.

The heat flux profiles reconstructed from theoretical data by the inverse method (Fig. 6.10(a)), show the same pattern of errors in the reconstruction of ß(x) (Fig. 6.10(b)), as the those recovered for the experimental data. These errors are clearly due to the inherent errors associated with the inverse reconstructions and broadening of the heat flux profiles produced at the assumed level of noise on the basis set. Further uncertainty in the apparent diffusion coefficient of the cation in the membrane material, and variation in the membrane thickness (the model uses an assumed thickness of 210 μm) are also possible errors, but these appear to be below the resolving power of the reconstructions.

Fig. 6.11 shows a comparison of the theoretical reconstructed heat flux profiles relative to the experimental heat flux reconstructions. These show a good agreement between the traces. Replicate data sets show a slightly greater variation; this could be associated with the errors mentioned above. It has been shown, that this difference may be due to small errors in the estimate of the peak optical absorption coefficient value of the film or of the film thickness.

The diffusion behaviour and the value of the apparent diffusion coefficient seen for this system, is consistent with the value of D found in the literature for ion complexes diffusing in the interfacial region of the polymer. Variations in the values of the diffusion coefficients can be attributed to differences in the preparation of the Nafion membranes.

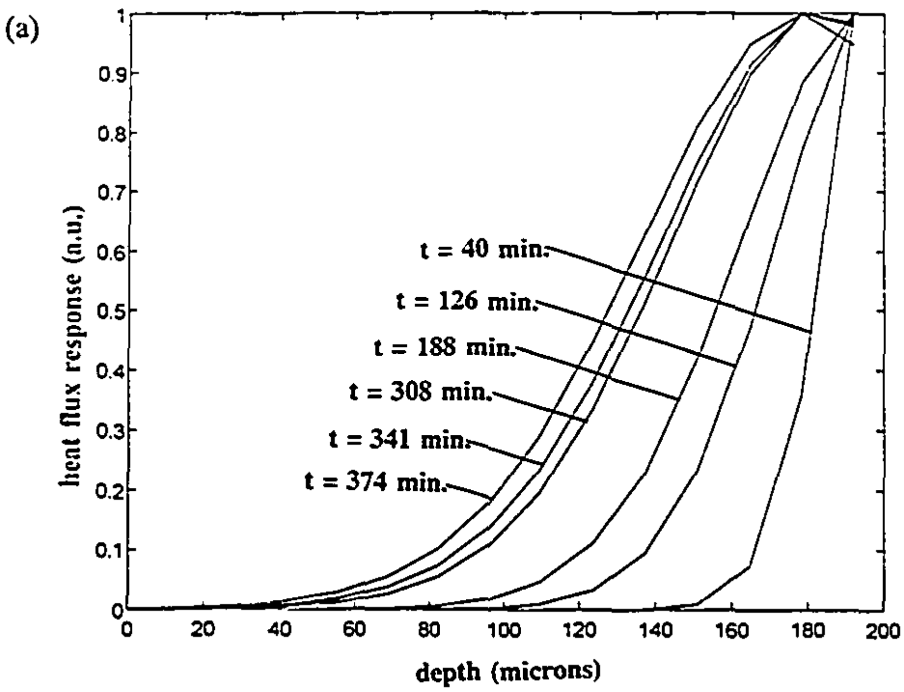

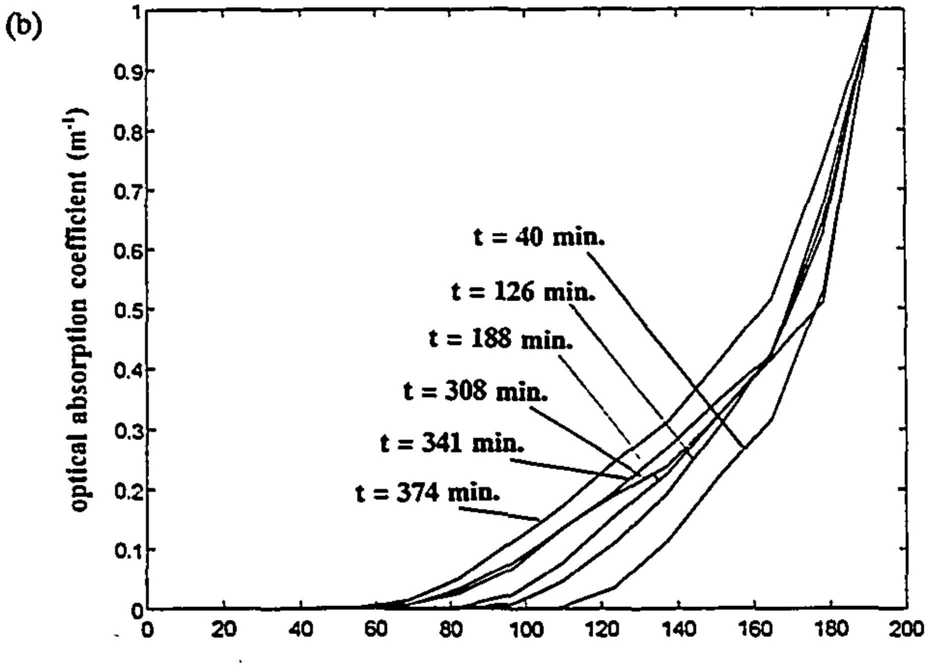

Figure 6.10: (a) The theoretical heat flux profiles.
(b) The reconstructed optical absorption coefficient profiles (theoretical).

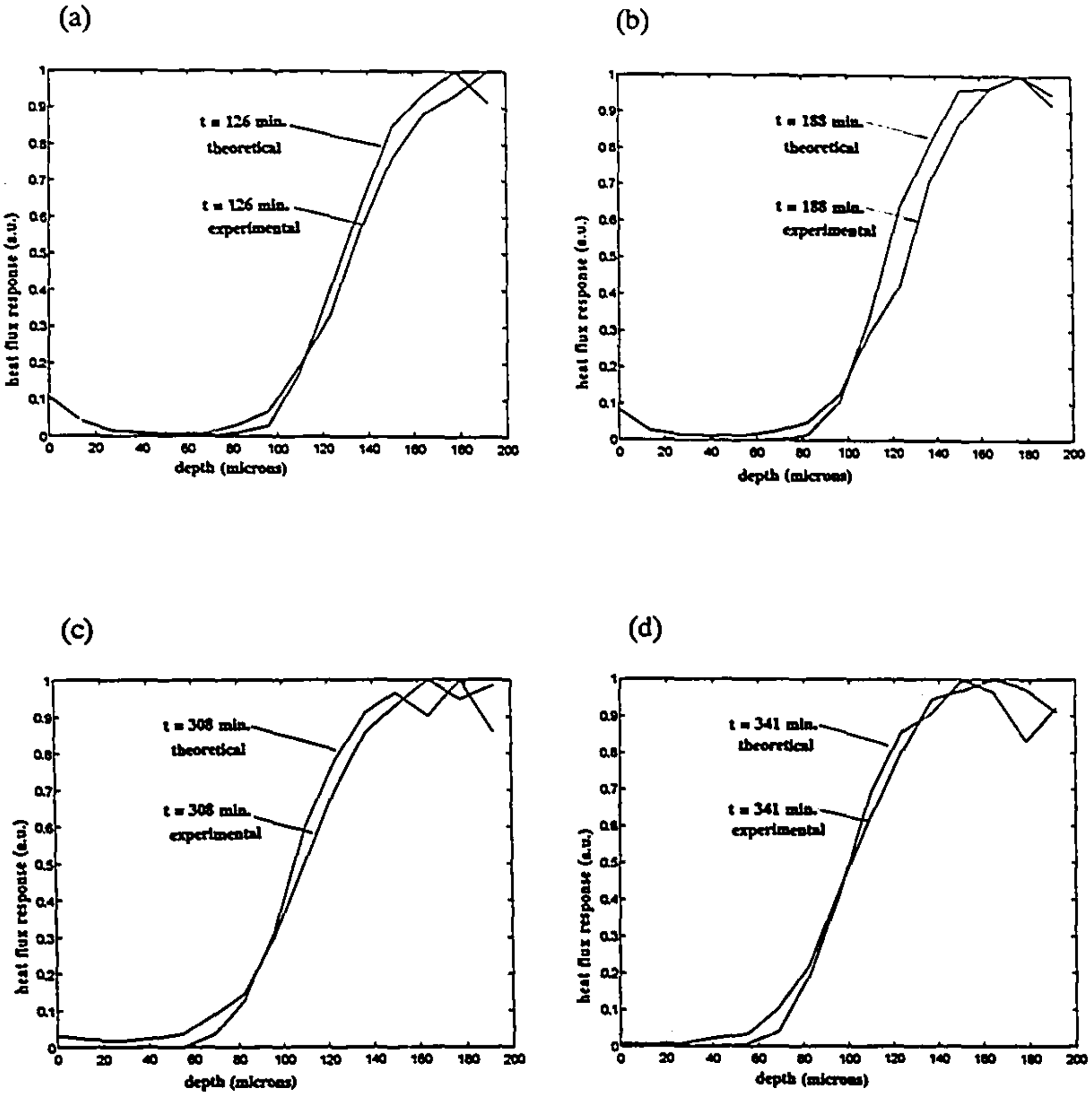

Figure 6.11: Comparison of the theoretical reconstructed heat flux profiles with the experimental heat flux profiles at representative times (a) t = 126 min, (b) t = 188 min, (c) t = 308 min, and (d) t = 341 min.

Samec *et al* show that a change in the water content of the membrane can effect the diffusion coefficient in the polymer. The ion diffusion coefficient will increase with an increase in the water content of the membrane (36). Boiling the Nafion membranes in water (see section 6.5.2), for example, is known to increase the water content capacity, and this can lead to increases in the value of the apparent diffusion coefficient as compared with diffusion coefficients for similar ions mentioned in the literature.

The results obtained are generally consistent with known properties of Nafion and diffusion of this type of probe molecule. The sorption in this film occurs on a time scale of minutes, whereas the diffusive behaviour that of hours. Furthermore, the concentrations are low enough to confirm the absence of inter-diffusion. Based on these assumptions, the derived model is applicable to describe this system. It may be argued that other models may account for the experimental profiles at this level of uncertainty in the reconstruction; however, the results in this study show that the diffusive behaviour is physically reasonable, and generally consistent with known data for Nafion.

6.5.4 Experimental Results and Discussion on Cationic Species Exhibiting Sorption Behaviour in Nafion Membranes

In order to study the effect of another cationic species, the membrane was equilibrated overnight in 0.1 M ammonium hydroxide solution. The membrane was then installed in the cell and both the front and the rear compartments were filled with 0.1 M ammonium hydroxide. Again measurements were taken for the initial alignment of the membrane relative to the He-Ne probe beam.

At t=0, a 0.1 M solution of tetraamminecopper(II) sulphate was injected into the rear compartment, with a complete turnover of the solution in the rear compartment. As outlined in section 6.5.3, the membrane underwent swelling due to sorption as the cationic species diffuses into the membrane. The same procedure as described in the previous section was followed for obtaining the impulse responses. Again the diffusion of the coloured complex was monitored over a period of 350 min, and several replicates of the experiment were performed, using a freshly prepared piece of Nafion membrane in each case.

Fig. 6.12 shows the impulse responses (at representative times) obtained for the sample region (the traces are offset from each other for ease of presentation). In order to determine the effect of the diffusing cationic species on the optical profile as the species moves through the membrane, the inverse scattering model of Chapter 5, was used to reconstruct the heat flux profile from the experimental data.

The heat flux reconstructions were made using basis sets with probe beam offset values corresponding to those obtained for the index spot for each set of experimental data. A sample thickness of 425 μm was assumed for the reconstructions, accounting for the enhanced contribution of the optical absorption in the rear compartment. The optical absorption of the tetraamminecopper(II) ion in the membrane was measured to be 0.68 a.u. (from UV-Visible spectrophotometer measurements).

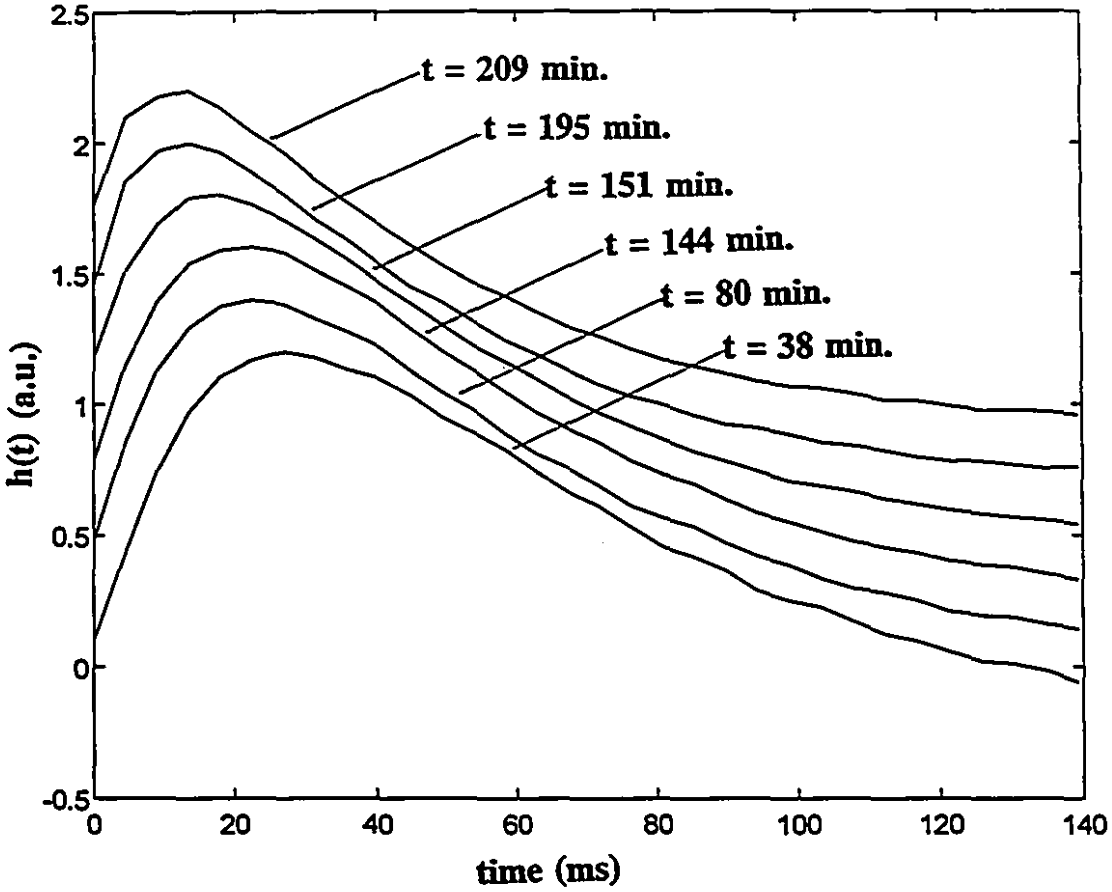

Figure 6.12: The experimental impulse responses data (at representative times) for the sample region. The traces are offset from each other by 0.2 units.

The optical absorption coefficient profiles (at several representative times) are presented in Fig. 6.13. The profiles are essentially identical (from the earliest times to the later times), and this trend was reproduced in all but one of the replicate experimental data sets (sample size of four sets). The recovered profiles showed no sensitivity to errors in measured optical density of the film or film thickness, and could be repeated over multiple replicates of the film. In addition, shifts in the front surface position had no effect on the form of the profile, provided enough back surface space was available for the reconstruction.

It appears that under these conditions, the concentration distribution in the film has reached an effective steady state. A more sophisticated sorption diffusion model is required (at a minimum) to explain these experimental results accommodating sorption processes which occur on a timescale similar to that of diffusion. Diffusion of this complex into the membrane may involve additional complicating processes such as the interaction of the complex ion with the ion-cluster sites, and the dissociation of the complex in the film, resulting in several ionic species being made available to interact with the ion-clusters.

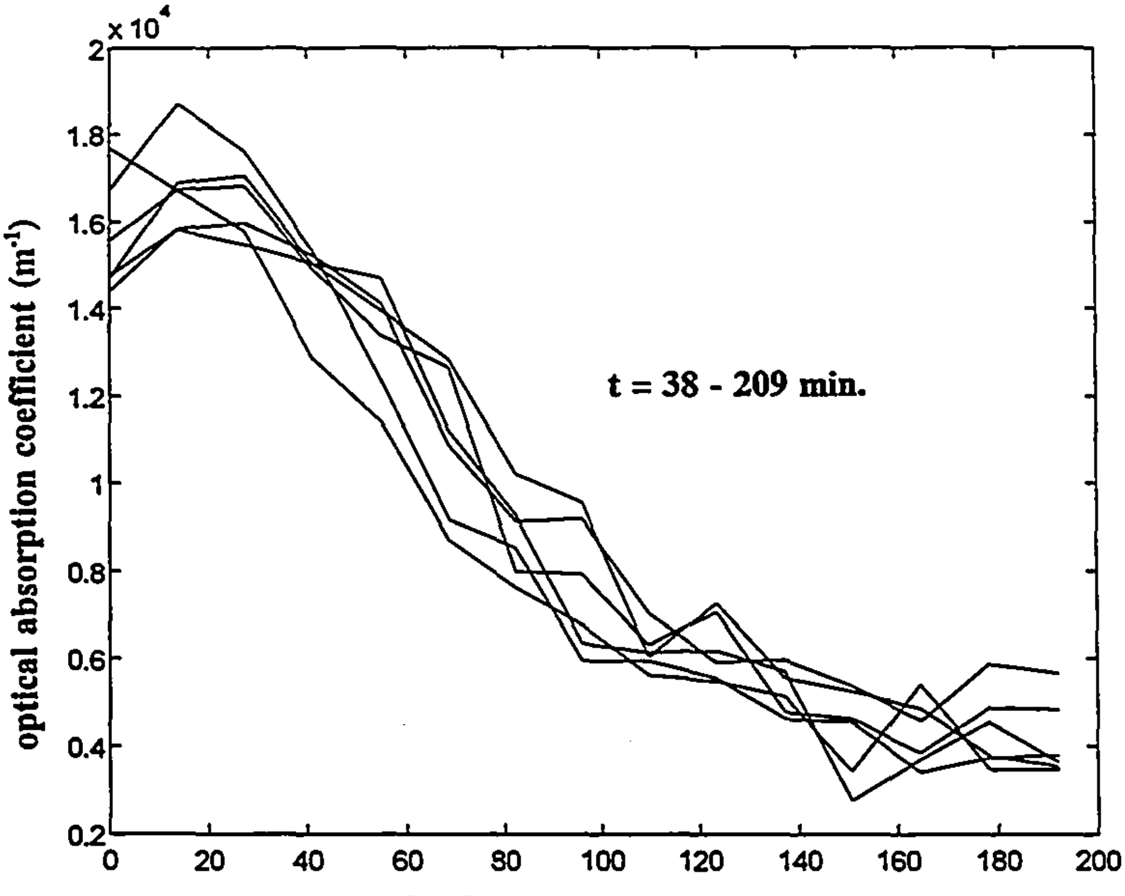

Figure 6.13: Recovered optical absorption coefficient profiles corresponding to the representative times indicated in Fig. 6.12.

6.5.5 Discussion on Cationic Species Exhibiting Extreme Sorption Behaviour in Nafion Membranes

The third process examined was the sorption/diffusion of hexaaquochromium(III) ion in a stained Nafion membrane. The membrane was soaked with 0.25 M chromium sulphate for 18 hours, and then installed in the cell with 0.05 M sulphuric acid. The leaching of the chromium ion in the membrane occurs immediately, but monitoring of the membrane can only be made after 0.5 hours. The reason for this is probably due to the erratic swelling of the membrane at early times due to the fast sorption of the hydrogen ion into the membrane, as the hexaaquochromium(III) ion is displaced. The variation of the optical profile in the membrane was monitored over time. The experimental results indicated that there was significant movement of the membrane occurring over the time scale of the measurement of the photothermal response. This violates the measurement assumptions for the photothermal technique, and interpretation of the experimental results is therefore not possible.

6.5.6 Future Work in Examining Diffusion Processes with Mirage Effect Spectroscopy

This study showed that diffusion processes in real systems can be probed using the optical depth profiling capabilities of mirage effect spectroscopy. Nafion is a complicated membrane material, consisting of three different regions which result in the occurrence of different diffusion processes. The systems examined in this study (see section 6.5.1) provided insight into the transport properties of Nafion membranes by providing a snapshot of the diffusion behaviour in time.

Further examination of diffusion processes of this material could be improved by first using the inverse problem theory to conduct resolution tests on theoretical profiles to provide an insight into the theoretical resolution of the instrument system (under given conditions of alignment, sampling time, bandwidth). Of special concern is the minimum time required to distinguish spatial variations in the concentration profiles at a given resolution, or minimum concentration changes required in order to observe a measurable spatial change at a given probe beam distance. Ultimately a limiting parameter in measurements involving the use of the mirage effect technique will usually be the time required for the heat to diffuse across the sample (of the order of milliseconds) to the probe beam position. In order to examine the rapid diffusion processes across these films, a thinner membrane and a smaller probe beam offset would be required. It is the use of the inverse scattering theory, applied to theoretical test profiles, which will aid in the design and prediction of instrumental configurations with the desired resolution.

6.6 CONCLUSIONS

This chapter discusses the applicability of the mirage effect to probe diffusion in real systems, by examining the migration of coloured species into a membrane material. The observed dependence of the concentration profiles can be accounted for by the resolving power of the inverse reconstructions, over and above a small level of systematic error in the reconstructions. The depth dependence of the concentration profiles recovered by these methods is able to provide insight into the diffusion process, which is not readily achievable with other methods.

REFERENCES

1. K.J. Laidler, and J.H. Meiser, *Physical Chemistry* (The Benjamin/Cummings Publishing Company, Inc., Don Mills, Ontario, 1982) 820-836.
2. A.E. Chalykh, *Experimental Methods of Polymer Physics*, A.Y. Malkin, Ed., G. Leib, Trans. (Prentice-Hall, Inc., New Jersey, 1983) 430-506.
3. J. Crank, and G.S. Park, *Diffusion in Polymers*, J. Crank, and G.S. Park, Ed. (Academic Press, New York, 1968) 1-39.
4. E.L. Cussler, *Diffusion, Mass Transfer in Fluid Systems* (Cambridge University Press, Cambridge, 1984).
5. H.L. Yeager, B. O'Dell, and Z. Twardowski, J. Electrochem. Soc. **129**, 85 (1982).
6. M. Lopez, B. Kipling, and H.L. Yeager, Anal. Chem. **49**, 629 (1977).
7. D.A. Blackadder, and J.S. Keniry, J. Appl. Polym. Sci. **17**, 351 (1973).
8. A. Steck, and H.L. Yeager, Anal. Chem. **52**, 1215 (1980).
9. T. Takamatsu, M. Hashiyama, and A. Eisenberg, J. Appl. Polym. Sci. **24**, 2199 (1979).
10. J.R. Xu, and C.M. Balik, Appl. Spectrosc. **42**, 1543 (1988).
11. C.W. Saltonstall, Jr., W.M. King, and D.L. Hoernschemeyer, Desalination **4**, 309 (1968).
12. F. Decker. R.T. Neuenschwander, C.L. Cesar, and A.F.S. Penna, J. Electroanal. Chem. **228**, 481 (1987).
13. B.S.H. Royce, D. Voss, and A. Bocarsly, J. Phys. Colloq. (France) **44**, C6-325 (1983).

14. J. Pawliszyn, M.F. Weber, M.J. Dignam, A. Mandelis, R.D. Venter, and S.-M. Park, Anal. Chem. **58**, 236 (1986).

15. M. Fracastoro-Decker, and F. Decker, J. Electroanal. Chem. **266**, 215 (1989).

16. T. Takamatsu, and A. Eisenberg, J. Appl. Polym. Sci. **24**, 2221 (1979).

17. T. Xue, R.B. Longwell, and K. Osseo-Asare, J. Membr. Sci. **58**, 175 (1991).

18. L.D. Whiteley, and C.R. Martin, J. Phys. Chem. **93**, 4650 (1989).

19. H.L. Yeager, *Perfluorinated Ionomer Membranes*, A. Eisenberg, and H.L. Yeager, Ed. (Am. Chem. Soc., Washington, D.C., 1982) 41-63.

20. Z. Twardowski, H.L. Yeager, and B. O'Dell, J. Electrochem. Soc. **129**, 328 (1982).

21. T. Sakai, H. Takenaka, and E. Torikai, J. Electrochem. Soc. **133**, 88 (1986).

22. H.L. Yeager, B. Kipling, and R.L. Dotson, J. Electrochem. Soc. **127**, 303 (1980).

23. T.D. Gierke, and W.Y. Hsu, *Perfluorinated Ionomer Membranes*, A. Eisenberg, and H.L. Yeager, Ed. (Am. Chem. Soc., Washington, D.C., 1982) 283-307.

24. P. Bratin, and M. Tomkiewicz, J. Electrochem. Soc. **129**, 2469 (1982).

25. G. Nagy, G.A. Gerhardt, A.F. Oke, M.E. Rice, R.N. Adams, R.B. Moore, III, M.N. Szentirmay, and C.R. Martin, J. Electroanal. Chem. **188**, 85 (1985).

26. R.S. Yeo, J. Electrochem. Soc. **130**, 533 (1983).

27. M.N. Szentirmay, and C.R. Martin, Anal. Chem. **56**, 1898 (1984).

28. L.D. Whiteley, and C.R. Martin, Anal. Chem. **59**, 1746 (1987).

29. W.E. Morf, E. Lindner, and W. Simon, Anal. Chem. **47**, 1596 (1975).

30. H.L. Yeager, and A. Eisenberg, *Perfluorinated Ionomer Membranes*, A. Eisenberg, and H.L. Yeager, Ed. (Am. Chem. Soc., Washington, D.C., 1982) 1-6.

31. H.L. Yeager, and A. Steck, Anal. Chem. **51**, 862 (1979).

32. M. Lopez, B. Kipling, and H.L. Yeager, Anal. Chem. **48**, 1120 (1976).

33. H.L. Yeager, and A. Steck, J. Electrochem. Soc. **128**, 1880 (1981).

34. R.B. Moore, III, and C.R. Martin, Macromolecules **21**, 1334 (1988).

35. C.R.C. Wang, J.W. Strojek, and T. Kuwana, J. Phys. Chem. **91**, 3606 (1987).

36. Z. Samec, A. Trojánek, and E. Samcová, J. Phys. Chem. **98**, 6352 (1994).

37. J. Crank, *The Mathematics of Diffusion*, 2nd Ed. (Clarendon Press, Oxford, 1975) Chapt. 1, 14.

38. Y. He, and E.L. Cussler, J. Membr. Sci. **68**, 43 (1992).

39. M. Abramowitz, and I.A. Stegun, *Handbook of Mathematical Functions*, NBS Mathematics Series 55 (National Bureau of Standards, Washington D.C., 1964).

40. Personal communication with Prof. A. Eisenberg.

41. T.R. Bolam, *The Donnan Equilibra* (G. Bell and Sons Ltd., London, 1932.)

42. J. D. Ingle, and S.R. Crouch, *Spectrochemical Analysis* (Prentice Hall, New Jersey, 1988).

LIST OF CONTRIBUTIONS TO ORIGINAL KNOWLEDGE

1. The development of the instrumentation and methodology to permit accurate quantitative depth profiling of optical absorbers in thin polymer multilayered films. These include considerations such as the accurate determination of the probe beam offset position, and the effect of the pinhole and detector position on the linearity of the photothermal response.

2. A theoretical model of a sample with depth variable optical absorption under the conditions of one-dimensional heat conduction for a thermally homogeneous material. This was applied to the case of optical absorbers embedded in polymer films, and provided nearly quantitative results in the depth profiling capabilities of the mirage effect.

3. Joint development with Prof. Power of a theoretical model using Fresnel diffraction to quantitatively describe the perturbation of the probe beam by a laser induced "mirage".

4. Application of inverse problem theory to the Fresnel diffraction model for quantitative and semi-quantitative modelling of optical absorption coefficient profiles in thermally homogeneous materials.

5. An analytical diffusion model assuming a diffusion-reaction mechanism to account for the uptake of ionic species in a perfluorosulphonated membrane.

6. The use of the mirage effect technique to reconstruct dynamic concentration depth profiles of optically absorbing ionic species in Nafion membranes, and to predict diffusion and sorption coefficient data in such films.

APPENDIX A

SATURATION BEHAVIOUR OF THE SAMPLE SIGNAL ß → ∞

(one dimensional case)

For a single absorbing layer at the sample surface, N=1, $\sigma_{i-1} = 0$ and $\sigma_i = l$ (with l defined as the absorber layer thickness), and an absorption coefficient, ß, the saturation behaviour of the sample signal can be described as follows, with ß → ∞.

The arguments of the error functions in equation (3.22) are defined as

$$u_1 = \frac{z}{\sqrt{4\alpha_2 t}} + \beta\sqrt{\alpha_2 t} \tag{A.1}$$

$$u_2 = \frac{z+l}{\sqrt{4\alpha_2 t}} + \beta\sqrt{\alpha_2 t} \tag{A.2}$$

As $ß \to \infty$, u_1, $u_2 \to \infty$ and the error function may be simplified using the following asymptotic expansion (1, 2):

$$\begin{aligned} erfc(u) &= \frac{e^{-u^2}}{u\sqrt{\pi}}\left[1 + \sum_{m=1}^{\infty} \frac{(-1)^m(1\cdot 3\ldots 2(m-1))}{(2u^2)^m}\right] \\ &= \frac{e^{-u^2}}{u\sqrt{\pi}} \; as \; u \to \infty \end{aligned} \tag{A.3}$$

Applying (A.3) to equation (3.22) (with $\omega^2 >> 4\alpha_2 t$) and grouping all of the factors ahead of the summation sign gives:

$$\theta_n \propto \beta \, \frac{[\beta \, e^{\beta z} e^{\beta^2 \alpha_2 t}]}{\sqrt{\pi}} \; \frac{e^{-(z^2/4\alpha_2 t \, + \, \beta^2 \alpha_2 t \, + \beta z)}}{(\frac{z}{\sqrt{4\alpha_2 t}} + \beta\sqrt{\alpha_2 t})}$$

$$+ \frac{e^{-((z+l)^2/4\alpha_2 t \, + \, \beta^2\alpha_2 t \, + \, \beta(z+l))}}{(\frac{(z+l)}{\sqrt{4\alpha_2 t}} + \beta\sqrt{\alpha_2 t})} \tag{A.4}$$

$$+ \frac{1}{\sqrt{\pi\alpha_2 t}} \left[e^{-\beta l} e^{-(z+l)^2/4\alpha_2 t} - e^{-z^2/4\alpha_2 t} \right]$$

If all terms in $e^{-\alpha l}$ are set to zero in (A.4), the following is obtained

$$\theta_n \propto \beta e^{-z^2/4\alpha_2 t} \left[\frac{\beta}{\sqrt{\pi}} \, \frac{1}{(\frac{z}{\sqrt{4\alpha_2 t}} + \beta\sqrt{\alpha_2 t})} - \frac{1}{\sqrt{\pi\alpha_2 t}} \right] \tag{A.5}$$

Rearrangement of this equation gives:

$$\theta_n \propto \beta \, \frac{e^{-z^2/4\alpha_2 t}}{\sqrt{\pi\alpha_2 t}} \left[\frac{1}{(\frac{z}{2\alpha t \beta} + 1)} - 1 \right] \tag{A.6}$$

The term in the denominator is expanded using the binomial theorem:

$$(1+u)^p = 1 + up + \frac{p(p-1)u^2}{2!} + \dots\dots \tag{A.7}$$

with truncation at the second term, and with p = -1.

Hence:

$$\theta_n \propto \frac{\beta}{\sqrt{\pi\alpha_2 t}}\, e^{-z^2/4\alpha_2 t} \left[\frac{-z}{2\alpha_2 t\beta}\right] \tag{A.8}$$

which ultimately, can be expressed in the form:

$$\theta_n \propto \frac{-z}{(4\alpha_2 t)^{3/2}}\, e^{-z^2/4\alpha_2 t} \tag{A.9}$$

when the appropriate leading constants have been assimilated into the proportionality constant.

An expression of the form of (A.9) is available directly by differentiation of equation (3.14) with $q'(x_0t_0) = \delta(x_0)\,\delta(t_0)$.

REFERENCES

---

1. M. Morse, and H. Feshbach, *Methods of Theoretical Physics* Vol I (McGraw-Hill Book Company, New York, 1953) Chapter 7, p 857.

2. M. Abramowitz, and I.A. Stegun, Ed., *Handbook of Mathematical Functions*, NBS Mathematics Series 55 (National Bureau of Standards, Washington D.C., 1964).

APPENDIX B

BEAM STOP ASSEMBLY

Design, electronic circuit, and computer code (ASYST) to control the beam stop assembly. This allows the excitation source to alternate between the index spot and a sample region.

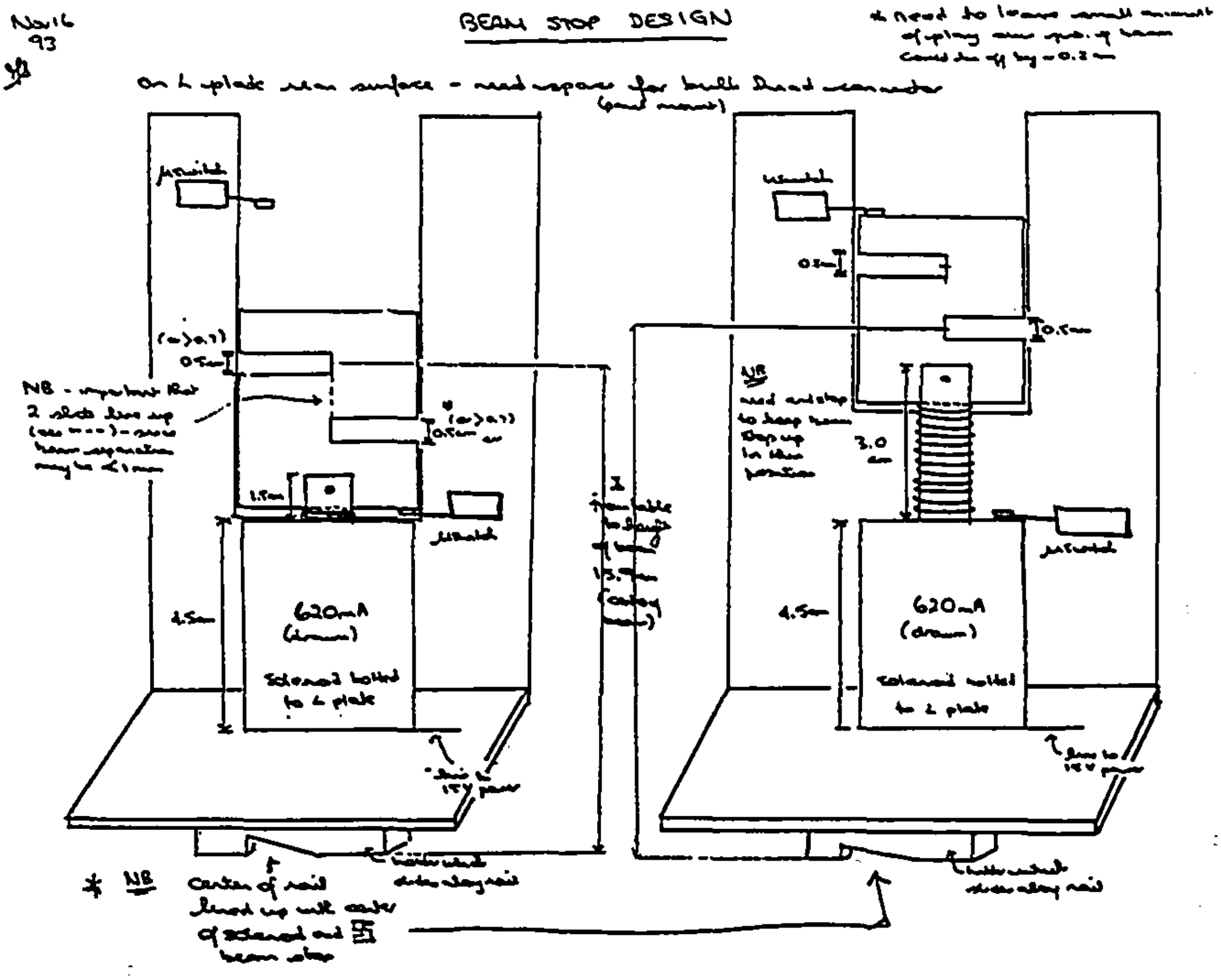

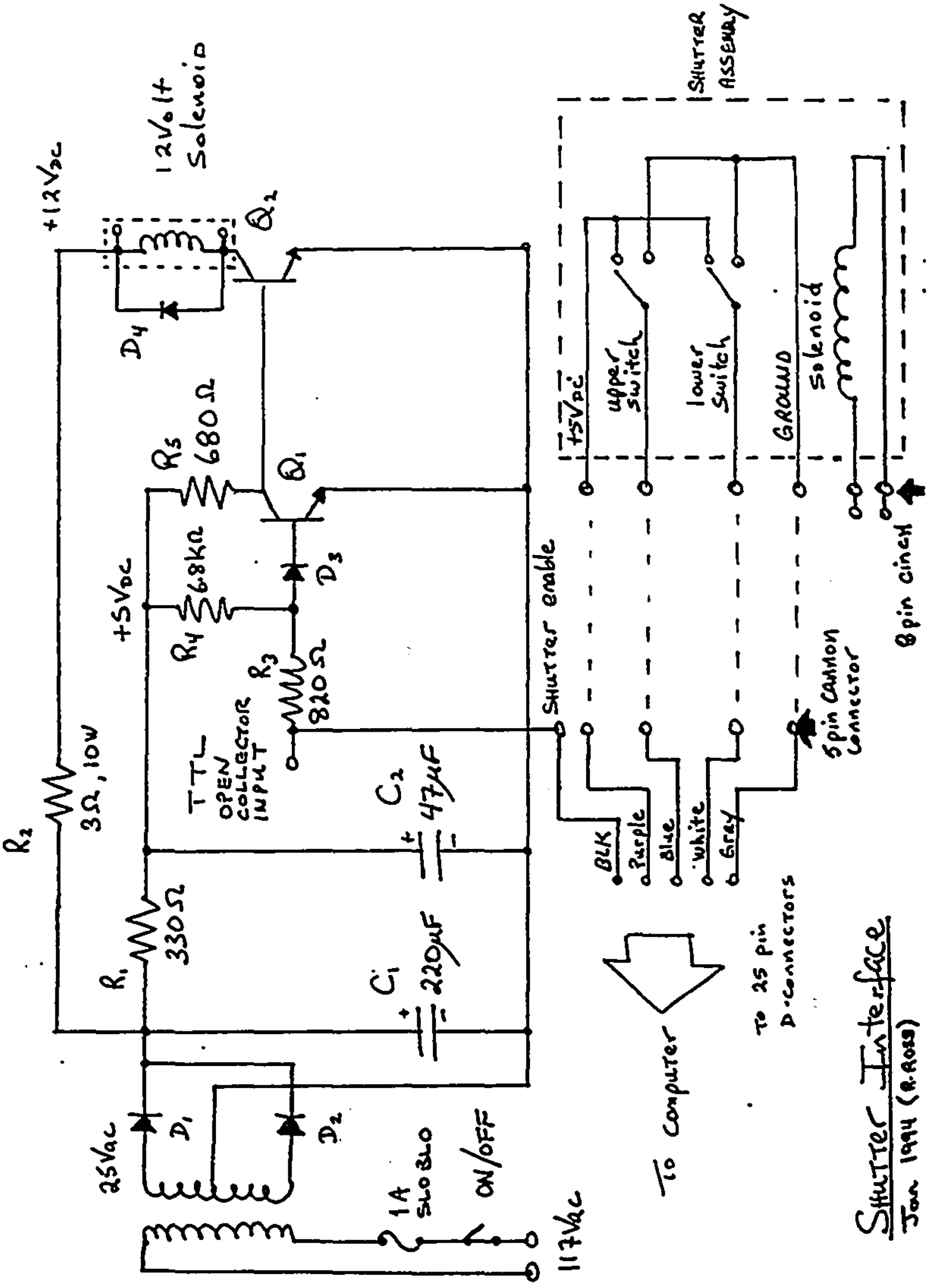

Shutter Interface

Jan 1994 (R. Ross)

```
: MOVE.BEAM.STOP
\ This does the following:
\   (1) sends signal to the solenoid (high or low) to change its position
\         (blocking one beam or the other)
\   (2) receives signal from two microswitches indicating the success of
\         the movement of the beam stop
\   (3) saves a string indicating the region being examined
\
\  the standard base address for LPT1 is 378 HEX, 888 DECIMAL
\  the standard base address for LPT2 is 278 HEX, 632 DECIMAL
      \  ****  N.B. - use line 9 as 5V source for switches ****

\ initialise the pins for ease of reading
128 888 PORT.OUT              \ sets pin 9 HI, 5V supply for switches
4  890 PORT.OUT               \ initialises all pins BA+2 to hi
\ ***** DOWN POSITION : ENERGIZED ******
FLAG 1 =
IF
  15 890 PORT.OUT             \ energized - 0V, send HI to pin 1, inverted LO
                          \ move beam stop to lower position
  " \ index region " REGION ":=

\ Read lower microswitch {read from BA+2 - pin #17)
  890 PORT.IN                 \ is the beam stop in lower position
  VALUE1 :=
  VALUE1 8 #>MASK #>MASK
  AND
  MASK>#  VALUE2 :=
  VALUE2 8 =
  IF
    CR " beam stop in lower position " "TYPE
  THEN
THEN
\ ***** UP POSITION : DE-ENERGIZED ******
FLAG 2 =
IF
  14 890 PORT.OUT             \ de-energized - 5V, send LO to pin 1, inverted HI
                          \ move beam stop to upper position
  " \ sample region " REGION ":=

\ Read upper microswitch {read from BA+2 - pin #14)
  890 PORT.IN                 \ is the beam stop in upper position
  VALUE1 :=
  VALUE1 2 #>MASK #>MASK
  AND
  MASK>#  VALUE2 :=
  VALUE2 2 =
  IF
    CR " beam stop in upper position " "TYPE
  THEN
THEN
;
\ ----------------------------------------------------------------
```

APPENDIX C

```
\ File MTHEORY1.DOC
\ Programme: ASYST
\ Date 25-FEB-91  Updated 10-AUG-94
\ Written: Melodie Schweitzer

\ Programme to express the theoretical interpretation of the mirage
\ effect for a thermally homogeneous optically inhomogenoeus sample,
\ containing multiple layers of varying thickness and absorption
\ coefficients.


\ ***** Define scalar variables and arrays *****

DP.REAL SCALAR K                  \ thermal conductivity of sample
DP.REAL SCALAR K1                 \ thermal conductivity of gas
DP.REAL SCALAR K*                 \ wavenumber (632nm)
DP.REAL SCALAR Z                  \ (z2 - z1) ; distance
DP.REAL SCALAR Z1                 \ position on z axis where mirage
                          \ signal occurs rel. to zero, waist
DP.REAL SCALAR Z2                 \ position on z axis where detector
                          \ aperature is located rel. to zero
DP.REAL SCALAR W                  \ waist size on z axis
DP.REAL SCALAR LAMBDA                \ wavelength of He-Ne laser
DP.REAL SCALAR X                  \ position of beam in detector plane
DP.REAL SCALAR A                  \ offset of He-Ne beam from sample
                          \    on x axis
DP.REAL SCALAR Y                  \ position on y axis
DP.REAL SCALAR ALPHA1                \ thermal diffusivity in gas layer
                          \    (k/rho*Cp)
DP.REAL SCALAR ALPHA2                \ thermal diffusivity in sample layer
                          \    (k/rho*Cp)
DP.REAL SCALAR TR                 \ time resolution parameter
DP.REAL SCALAR EPSILON              \ ratio of thermal diffusivities
DP.REAL SCALAR Wadj                \ adjustment factor for waist size
                          \    as it expands along z axis
DP.REAL SCALAR SCALE
DP.REAL SCALAR VALUE
DP.REAL SCALAR DUMMY1                \ dummy variable
DP.REAL SCALAR DUMMY2                \ dummy variable
DP.REAL SCALAR DUMMY3                \ dummy variable
DP.REAL SCALAR DUMMY4                \ dummy variable

INTEGER SCALAR INDEX               \ index to increment layers (i)
INTEGER SCALAR N                  \ total number layers in sample
INTEGER SCALAR M                  \ total number layers plus one
INTEGER SCALAR JJ                 \ index minus one

DP.COMPLEX SCALAR J                \ imaginary number 0.0 + 1.0i
DP.COMPLEX SCALAR Q                \ cal'd below
```

```
DP.COMPLEX SCALAR QUANTITY           \ cal'd below
DP.COMPLEX SCALAR SIGMA            \ cal'd below
DP.COMPLEX SCALAR PHI            \ cal'd below
DP.COMPLEX SCALAR TMOD             \ cal'd below
DP.COMPLEX SCALAR TERM1            \ cal'd below
DP.COMPLEX SCALAR TERM4            \ cal'd below
DP.COMPLEX SCALAR D1             \ dummy variable
DP.COMPLEX SCALAR D2             \ dummy variable
DP.COMPLEX SCALAR D3             \ dummy variable
DP.COMPLEX SCALAR D4             \ dummy variable
DP.COMPLEX SCALAR S1             \ temp storage
DP.COMPLEX SCALAR S2             \ temp storage
DP.COMPLEX SCALAR S3             \ temp storage
DP.COMPLEX SCALAR S4             \ temp storage
DP.COMPLEX SCALAR S5             \ temp storage
DP.COMPLEX SCALAR S6             \ temp storage
DP.COMPLEX SCALAR S7             \ temp storage

DP.REAL DIM[ 11 ] ARRAY BETA(i)       \ absorption coefficient in ith layer
DP.REAL DIM[ 11 ] ARRAY BETA(i)SQ      \ square of the BETA(i) coefficients
DP.REAL DIM[ 11 ] ARRAY NR(i)        \ non-radiative conversion factor in
                      \    ith layer
DP.REAL DIM[ 11 ] ARRAY I(i-1)       \ intensity of light at input to
                      \    ith layer
DP.REAL DIM[ 11 ] ARRAY L(i)        \ length between layer i and i-1
DP.REAL DIM[ 11 ] ARRAY RHO(i)       \ position of the ith layer relative
                      \    to zero (i.e. quantity is neg. )
DP.REAL DIM[ 11 ] ARRAY RHO(i-1)      \ position of the (i-1)th layer
DP.REAL DIM[ 11 ] ARRAY Topt        \ cal'd below
DP.REAL DIM[ 11 ] ARRAY T(i)        \ cal'd below
DP.REAL DIM[ 11 ] ARRAY T(i-1)       \ cal'd below
DP.REAL DIM[ 11 ] ARRAY DX         \ dummy array
DP.REAL DIM[ 11 ] ARRAY DDX         \ dummy array
DP.REAL DIM[ 11 ] ARRAY DDDX         \ dummy array

DP.REAL DIM[ 512 ] ARRAY INTENSITY.DIFF \ intensity diffraction signal
DP.REAL DIM[ 512 ] ARRAY TIME        \ time base array
DP.REAL DIM[ 512 ] ARRAY ERROR1       \ ERFC term 1
DP.REAL DIM[ 512 ] ARRAY ERROR2       \ ERFC term 2
DP.REAL DIM[ 512 ] ARRAY TERM2       \ cal'd below
DP.REAL DIM[ 512 ] ARRAY TERM3       \ cal'd below
DP.REAL DIM[ 512 ] ARRAY TEMP       \ a temporary storage for a value
DP.REAL DIM[ 512 ] ARRAY PART       \ a temporary storage for a value
DP.REAL DIM[ 512 ] ARRAY PART1       \ a temporary storage for a value
DP.REAL DIM[ 512 ] ARRAY PART2       \ a temporary storage for a value
DP.REAL DIM[ 512 ] ARRAY UNIT.CONV      \ cal'd below
\ DP.REAL DIM[ 512 ] ARRAY INTENSITY
DP.REAL DIM[ 512 ] ARRAY D         \ dummy array
DP.REAL DIM[ 512 ] ARRAY DD         \ dummy array
DP.REAL DIM[ 512 ] ARRAY DDD        \ dummy array
DP.REAL DIM[ 512 ] ARRAY DDDD        \ dummy array
```

```
DP.COMPLEX DIM[ 11 ] ARRAY GAMMA        \ cal'd below
DP.COMPLEX DIM[ 11 ] ARRAY TERM5       \ cal'd below
DP.COMPLEX DIM[ 11 ] ARRAY DDX1        \ dummy array
DP.COMPLEX DIM[ 11 ] ARRAY DDX2        \ dummy array
DP.COMPLEX DIM[ 11 ] ARRAY DDX3        \ dummy array

DP.COMPLEX DIM[ 512 ] ARRAY U         \ electric field vector, diff
DP.COMPLEX DIM[ 512 ] ARRAY UNIT1       \ cal'd below
DP.COMPLEX DIM[ 512 ] ARRAY EQ1        \ part of main equation
DP.COMPLEX DIM[ 512 ] ARRAY EQ2        \ part of main equation
DP.COMPLEX DIM[ 512 ] ARRAY DD1        \ dummy array


\ --------------------------------------------------------------

: INITIALISE

\ ***** Initialise the variables and arrays to zero *****
\ ***** Put the values in scientific notation       *****

NORMAL.DISPLAY
STACK.CLEAR

0 K* := 0 K := 0 K1 :=
0 Z1 := 0 Z2 := 0 Z :=
0 A := 0 X := 0 Y :=
0 W := 0 LAMBDA := 0 ALPHA1 := 0 ALPHA2 :=
0 TR := 0 EPSILON := 0 Wadj :=
0 DUMMY1 := 0 DUMMY2 := 0 DUMMY3 := 0 DUMMY4 :=
0 ERROR1 := 0 ERROR2 :=
0 TERM2 := 0 TERM3 :=
0 TEMP :=  0 INTENSITY.DIFF := 0 UNIT.CONV :=
0 PART := 0 PART1 := 0 PART2 :=
0 BETA(i) := 0 BETA(i)SQ :=
0 INDEX := 0 JJ := 0 N := 0 I(i-1) :=
0 RHO(i) :=  0 RHO(i-1) :=
0 Topt := 0 T(i) := 0 T(i-1) :=
0 TIME := 0 NR(i) := 0 L(i) :=
0 D := 0 DD := 0 DDD := 0 DDDD :=
0 DX := 0 DDX := 0 DDDX :=
0 0 Z=X+IY GAMMA := 0 0 Z=X+IY TERM5 :=
0 0 Z=X+IY TERM1 := 0 0 Z=X+IY TERM4 :=
0 0 Z=X+IY D1 := 0 0 Z=X+IY D2 := 0 0 Z=X+IY D3 :=
0 0 Z=X+IY D4 := 0 0 Z=X+IY EQ1 := 0 0 Z=X+IY EQ2 :=
0 0 Z=X+IY Q := 0 0 Z=X+IY QUANTITY := 0 0 Z=X+IY SIGMA :=
0 0 Z=X+IY PHI := 0 0 Z=X+IY TMOD :=
0 0 Z=X+IY UNIT1 :=
0 0 Z=X+IY U :=
0 0 Z=X+IY DD1 :=  0 0 Z=X+IY DDX1 :=
0 0 Z=X+IY DDX2 := 0 0 Z=X+IY DDX3 :=
```

```
9.94E6 K* :=                    \ wavenumber for 632nm
1.0E-7 Y :=                     \ set value of y

15 5 SCI.FORMAT                    \ set notation for display

0.0 1.0 Z=X+IY
J :=                            \ set J to 0.0+1.0i

;


\ ------------------------------------------------------------

: INPUT.VARIABLES

\ ***** Input values for known quantities *****


\ CR " The following quantities will be used in the theoretical model" "TYPE
\ CR " in order to simulate the experimental system.  " "TYPE
\ CR
\ CR " Please enter the parameters relating to the physical " "TYPE
\ CR " set-up of the instrument.  " "TYPE
\ CR " Enter position of thermal heating on z axis in m :   " "TYPE
\ #INPUT Z1 :=
1.039E-2 Z1 :=

\ CR " Enter position of detector aperature on z axis in m :   " "TYPE
\ #INPUT Z2 :=
10.50E-2 Z2 :=

\ CR " Enter waist size of the He-Ne beam on z axis in m :   " "TYPE
\ #INPUT W :=
\ 4.266E-5 W :=  \ for the air detection medium
8.980E-5 W :=    \ for the water detection medium

\ CR " Enter wavelength of pump beam in m :  " "TYPE
\ #INPUT LAMBDA :=
632.8E-9 LAMBDA :=

\ CR " Enter beam offset position in the detector plane in m :  " "TYPE
\ #INPUT X :=
0.0 X :=

CR CR " Enter He-Ne beam offset from the sample in m : " "TYPE
#INPUT A :=
CR CR
\ CR " Enter thermal diffusivity of medium above sample in m2/s:  " "TYPE
\ CR " For air 22.6E-6;  For water 1.42E-7 ; For oil 0.872E-7 " "TYPE
\ #INPUT ALPHA1 :=
\ 22.6E-6 ALPHA1 :=
```

```
1.42E-7 ALPHA1 :=
\ 0.872E-7 ALPHA1 :=

\ CR " Enter thermal conductivity of medium above sample in W/m-K : " "TYPE
\ CR " For air 26.3E-3;  For water 598.0E-3 ; For oil 145.0E-3  " "TYPE
\ #INPUT K1 :=
\ 26.3E-3 K1 :=
598.0E-3 K1 :=
\ 145.0E-3 K1 :=

\ CR " Enter thermal diffusivity of the sample in m2/s :  " "TYPE
\ CR " For polymer 1.0E-7;  For water 1.42E-7 " "TYPE
\ #INPUT ALPHA2 :=
\ 1.0E-7 ALPHA2 :=
1.42E-7 ALPHA2 :=

\ CR " Enter thermal conductivity of the sample in W/m-K :  " "TYPE
\ CR " For polymer 0.2;  For water 598.0E-3 " "TYPE
\ #INPUT K :=
\ 0.2 K :=
598.0E-3 K :=

CR CR " Please enter the parameters for the sample being examined.  " "TYPE
CR CR " Enter total number of layers in sample : " "TYPE
#INPUT N :=
N 1 + M :=                    \ increment N to account for the
                            \ infinitely thin layer

2 INDEX :=
INDEX
BEGIN
  INDEX
  CR " Sample layer " "TYPE INDEX . " : " "TYPE
  CR " Enter layer thickness in m : " "TYPE
  #INPUT L(i) [ INDEX ] :=
  CR " Enter absorption coefficient : " "TYPE
  #INPUT BETA(i) [ INDEX ] :=
  CR " Enter non-radiative conversion efficiency factor : " "TYPE
  #INPUT NR(i) [ INDEX ] :=

  1 INDEX + INDEX :=
  INDEX M >
UNTIL

CR
CR " Enter the time resolution in s : " "TYPE
#INPUT TR :=

;
```

```
\ ---------------------------------------------------------------

: PREL.CALNS

\ ***** Calculation of Z, Q, QUANTITY, EPSILON, Wadj *****

L(i) [ 2 ]                  \ fill the RHO(i) array
RHO(i) [ 2 ] :=
0 RHO(i-1) [ 2 ] :=

3 INDEX :=
BEGIN
  INDEX 1 - JJ :=
  L(i) [ INDEX ] RHO(i) [ JJ ] +
  RHO(i) [ INDEX ] :=

  RHO(i) [ JJ ]
  RHO(i-1) [ INDEX ] :=

  1 INDEX + INDEX :=
  INDEX M >
UNTIL

0 DX :=                           \ fill intensity array, I(i-1)
1.0 I(i-1) [ 1 ] :=
2 INDEX :=
BEGIN
  INDEX 1 - JJ :=
  BETA(i) [ JJ ] L(i) [ JJ ] *
  DX [ INDEX ] :=
  DX [ INDEX ] DX [ JJ ] +
  DDX [ INDEX ] :=
  DDX [ INDEX ]  -1. * EXP
  I(i-1) [ INDEX ] :=
  1 INDEX + INDEX :=
  INDEX M >
UNTIL

TIME []RAMP                      \ ramp the time
TIME TR *                       \ create proper time scale
TIME :=

Z2 Z1 - Z :=                   \ determination of the distance between
                              \ the mirage signal and detector aperature

ALPHA2 SQRT ALPHA1 SQRT /         \ determination of the value EPSILON
EPSILON :=

LAMBDA Z1 *                      \ determination of the adjustment factor
DUMMY1 :=                        \ for the waist of the He-Ne beam on
W W *                          \ the z axis
```

```
PI *
DUMMY2 :=
DUMMY1 DUMMY2 /
Wadj :=

W W *                      \ determination of the value Q
PI *
DUMMY1 :=
DUMMY1 LAMBDA /
DUMMY3 :=
DUMMY3 J *
D1 :=
Z1 D1 +
Q :=

1. Z /                     \ determination of the value QUANTITY
DUMMY1 :=
1. Q /
D1 :=
DUMMY1 D1 +
SQRT
QUANTITY :=

X Z /                      \ determination of the value of SIGMA
DUMMY1 :=
DUMMY1 QUANTITY /
SIGMA :=

Y Z /                      \ determination of the value of PHI
DUMMY1 :=
DUMMY1 QUANTITY /
PHI :=

;

\ ------------------------------------------------

: OPTIMUM.TIME

\ ***** Fill the time parameter array Topt *****

2 INDEX :=
BEGIN
  BETA(i) [ INDEX ] BETA(i) [ INDEX ] *
  BETA(i)SQ [ INDEX ] :=

  1 INDEX + INDEX :=
  INDEX M >
UNTIL
```

```
2 INDEX :=
BEGIN
  BETA(i)SQ [ INDEX ] ALPHA2 *
  Topt [ INDEX ] :=
  1 INDEX + INDEX :=
  INDEX M >
UNTIL

;


\ ------------------------------------------------------

: FILL.TIME

\ ***** Fill the other time parameter arrays, T(i) and T(i-1) *****

ALPHA2 SQRT                  \ determination of the value of T(i)
DUMMY1 :=
2. DUMMY1 *
DUMMY2 :=
2 INDEX :=
BEGIN
  RHO(i) [ INDEX ]
  DUMMY2
  /
  2. **
  T(i) [ INDEX ] :=
  1 INDEX + INDEX :=
  INDEX M >
UNTIL

2 INDEX :=                  \ determination of the value of T(i-1)
BEGIN
  RHO(i-1) [ INDEX ]
  DUMMY2
  /
  2. **
  T(i-1) [ INDEX ] :=
  1 INDEX + INDEX :=
  INDEX M >
UNTIL

;


\ ------------------------------------------------------

\ DP.REAL SCALAR SQR
\ 1. 2. SQRT / SQR :=
```

```
\ : ERFC

\ ***** Word to determine ERFC for use in ASYST-1 floppy *****

\ 0 SQR NORMAL.DIST
\ -1.0D  * 1.0D  +
\ 2.0D  *

\ ;


\ ------------------------------------------------

: DETN.ERR1

\ ***** Determination of the first error function *****

4. ALPHA1 *
DUMMY1 :=
DUMMY1 TIME *
D :=
D SQRT
DD :=
A DD /
D :=

TIME Topt [ INDEX ] *
DDD :=
DDD SQRT
DD :=

T(i-1) [ INDEX ] TIME /
DDDD :=
DDDD SQRT
DDD :=

DD DDD +
DDDD :=
D DDDD +
D :=

D ERF
DD :=
1. DD -
\  D ERFC
ERROR1 :=

;

\ ------------------------------------------------
```

```
: DETN.ERR2

\ ***** Determination of the second error function *****

4. ALPHA1 *
DUMMY1 :=
DUMMY1 TIME *
D :=
D SQRT
DD :=
A DD /
D :=

TIME Topt [ INDEX ] *
DDD :=
DDD SQRT
DD :=

T(i) [ INDEX ] TIME /
DDDD :=
DDDD SQRT
DDD :=

DD DDD +
DDDD :=
D DDDD +
D :=

D ERF
DD :=
1. DD -
\ D ERFC
ERROR2 :=

;


\ -------------------------------------------------

: PARAMETER2

\ ***** Determination of TERM2 to be used in the main equation *****

EPSILON A *
DUMMY1 :=
DUMMY1 BETA(i) [ INDEX ] *
EXP
DDDX [ INDEX ] :=

ALPHA2 TIME *
DDDD :=
```

```
DDDD BETA(i)SQ [ INDEX ] *
EXP
D :=

DDDX [ INDEX ] D *
DD :=

ALPHA2 SQRT
DUMMY1 :=

BETA(i) [ INDEX ] I(i-1) [ INDEX ] *
NR(i) [ INDEX ] *
DX [ INDEX ] :=

PI DX [ INDEX ] *
4. *
DDDX [ INDEX ] :=

DDDX [ INDEX ] DUMMY1 /
DX [ INDEX ] :=

DX [ INDEX ] DD *
TERM2 :=

;


\ -----------------------------------------------------

: PARAMETER3

\ ***** Determination of TERM3 for use in the main equation *****

BETA(i) [ INDEX ] RHO(i-1) [ INDEX ] *
EXP
DX [ INDEX ] :=
DX [ INDEX ] ERROR1 *
TEMP :=

BETA(i) [ INDEX ] RHO(i) [ INDEX ] *
EXP
DDX [ INDEX ] :=

-1. BETA(i) [ INDEX ] *
L(i) [ INDEX ] *
EXP
DDDX [ INDEX ] :=

DDDX [ INDEX ] DDX [ INDEX ] *
ERROR2 *
DD :=
```

```
TEMP DD -
TERM3 :=

;


\ -----------------------------------------------------------

: PARAMETER4

\ ***** Determination of TERM4 for use in main equation *****

SIGMA SIGMA *
K* *
D2 :=
D2 2. /
D1 :=
0 1 Z=X+IY
D2 :=
D1 D2 *
EXP
TERM4 :=

;


\ -----------------------------------------------------------

: PARAMETERS5

\ ***** Determination of TERM5 to be used in the main equation *****

EPSILON BETA(i) [ INDEX ] *      \ determination of the value GAMMA
DX [ INDEX ] :=
DX [ INDEX ] J *
DDX1 [ INDEX ] :=

DDX1 [ INDEX ] K* /
DDX2 [ INDEX ] :=
DDX2 [ INDEX ] -1. *
DDX3 [ INDEX ] :=

X Z /
DDX3 [ INDEX ] +
DDX1 [ INDEX ] :=

DDX1 [ INDEX ] QUANTITY /
GAMMA [ INDEX ] :=

GAMMA [ INDEX ] GAMMA [ INDEX ] *
K* *
```

```
DDX2 [ INDEX ] :=
DDX2 [ INDEX ] 2. /
DDX1 [ INDEX ] :=
DDX1 [ INDEX ] J *
EXP
TERM5 [ INDEX ] :=
;


\ -----------------------------------------------------

: PARAMETER1

\ ***** Determination of TERM1 to be used in the main equation *****

PHI PHI *
K* *
D2 :=
D2 2. /
D1 :=
J D1 *                          \ the calculation is done from
EXP                             \ back to front and the pieces
S1 :=                           \ multiplied at the end.

Y Y *
K* *
DUMMY2 :=
DUMMY2 J *
D2 :=
D2 -1. *
D3 :=
2. Z *
DUMMY3 :=
D3 DUMMY3 /
D4 :=
D4
ZREAL
EXP
D2 :=
D4
ZIMAG
EXP
D3 :=
D3 J *
D4 :=
D2 D4 +
S2 :=

X X *
K* *
DUMMY2 :=
```

```
DUMMY2 DUMMY3 /
DUMMY1 :=
-1. J *
D2 :=
DUMMY1 D2 *
EXP
S3 :=

-1. J *
PI *
D3 :=
D3 2. /
D2 :=
D2
ZREAL
EXP
D3 :=
D2
ZIMAG
EXP
D4 :=
D4 J *
D4 :=
D3 D4 +
S4 :=

Z K* *
DUMMY1 :=
-1. J *
D2 :=
D2 DUMMY1 *
EXP
D2 :=
J D2 *
D3 :=
D3 Z /
D2 :=
D2 LAMBDA /
S5 :=

Wadj ATAN
-1. *
DUMMY3 :=
Z1 K* *
DUMMY4 :=
DUMMY3 DUMMY4 +
J *
D1 :=
D1 -1. *
EXP
S6 :=
```

```
Wadj Wadj *
DUMMY1 :=
1. DUMMY1 +
SQRT
DUMMY1 :=
W DUMMY1 *
DUMMY3 :=
1. DUMMY3 /
DUMMY1 :=
DUMMY1 VALUE :=

8. PI *
SQRT
DUMMY2 :=
K* QUANTITY *
D2 :=
DUMMY2 D2 /
S7 :=

S7 VALUE *
D1 :=
D1 S6 *
D2 :=
D2 S5 *
D3 :=
D3 S4 *
D1 :=
D1 S3 *
D2 :=
D2 S2 *
D3 :=
D3 S1 *
TERM1 :=

;


\ ---------------------------------------------------------

: PARAMETER.TMOD

\ ***** Determination of the small parameter for delta temperature *****


\ LET DN/DT = -1.0E-5 (for air) AND L = 2.0E-3 (for pump beam heating size)
K* -1.0E-5 *
2.0E-3 *
DUMMY2 :=
DUMMY2 J *
TMOD :=
```

```
;

\ ---------------------------------------------------------------

: PARAMETER.CONVENTIONAL

\ ***** This calculates the conventional mirage model       *****

0 UNIT.CONV :=

2 INDEX :=
BEGIN
  A EPSILON *
  DUMMY1 :=
  BETA(i) [ INDEX ] DUMMY1 * EXP
  DX [ INDEX ] :=

  X EPSILON *
  DUMMY2 :=
  BETA(i) [ INDEX ] DUMMY2 * EXP
  DDX [ INDEX ] :=

  ALPHA2 BETA(i)SQ [ INDEX ] *
  DUMMY1 :=
  TIME DUMMY1 * EXP
  D :=

  ALPHA2 SQRT BETA(i) [ INDEX ] *
  DUMMY2 :=

  DX [ INDEX ] DDX [ INDEX ] *
  DUMMY2 *
  DDDX [ INDEX ] :=
  DDDX [ INDEX ] D *
  PART1 :=

  BETA(i) [ INDEX ] RHO(i-1) [ INDEX ] *
  EXP
  PART1 *
  PART1 :=

  DETN.ERR1
  DETN.ERR2
  ERROR1 ERROR2 -
  TERM3 :=

  TERM3 PART1 *
  PART1 :=

  X A +
```

```
DUMMY1 :=
ALPHA1 SQRT
DUMMY2 :=
DUMMY1 DUMMY2 /
DUMMY1 :=
ALPHA2 SQRT DUMMY2 :=
RHO(i-1) [ INDEX ] DUMMY2 /
DX [ INDEX ] :=
DX [ INDEX ] DUMMY1 +
2. **
-1. *
DDX [ INDEX ] :=
DDX [ INDEX ] 4. /
DDX [ INDEX ] :=
DDX [ INDEX ] TIME /
D :=
D EXP -1. *
DD :=

X A +
DUMMY1 :=
ALPHA1 SQRT
DUMMY2 :=
DUMMY1 DUMMY2 /
DUMMY1 :=
ALPHA2 SQRT
DUMMY2 :=
RHO(i) [ INDEX ] DUMMY2 /
DX [ INDEX ] :=
DX [ INDEX ] DUMMY1 +
2. **
-1. *
DDX [ INDEX ] :=
DDX [ INDEX ] 4. /
DDDX [ INDEX ] :=
DDDX [ INDEX ] TIME /
D :=
D EXP
D :=
L(i) [ INDEX ] BETA(i) [ INDEX ] *
DX [ INDEX ] :=
DX [ INDEX ] -1. * EXP
DX [ INDEX ] :=
D DX [ INDEX ] *
DDD :=

DDD DD +
D :=

1.
PI TIME *
```

```
 SQRT /
 DD :=

 D DD *
 PART2 :=

 PART1 PART2 +
 PART :=

 4. PI *
 NR(i) [ INDEX ] *
 DX [ INDEX ] :=
 BETA(i) [ INDEX ] I(i-1) [ INDEX ] *
 DX [ INDEX ] *
 DDX [ INDEX ] :=
 ALPHA1 SQRT
 DUMMY1 :=
 DDX [ INDEX ] DUMMY1 /
 DX [ INDEX ]

 DX [ INDEX ] PART *
 UNIT.CONV +
 UNIT.CONV :=

 1 INDEX + INDEX :=
 INDEX M >
UNTIL

;


\ ----------------------------------------------------

: PARAMETER.CAL
INITIALISE
INPUT.VARIABLES
PREL.CALNS
OPTIMUM.TIME
FILL.TIME
EQUATION.DIFFRACTION
DETERMINATION.INTENSITY
PARAMETER.CONVENTIONAL
\ INTENSITY.VARIATION
;


\ Words to read and write from/to disk the impulse response acquired
\ from the PHOTOS programme, i.e. the experimental data.

REAL DIM[ 512 ] ARRAY H(T)           \ impulse response array
REAL DIM[ 512 ] ARRAY H1             \ impulse response holding array
```

```
REAL DIM[ 512 ] ARRAY H2          \ impulse response holding array
REAL DIM[ 512 ] ARRAY H3          \ impulse response holding array
REAL DIM[ 512 ] ARRAY H4          \ impulse response holding array
REAL DIM[ 512 ] ARRAY H5          \ impulse response holding array
REAL DIM[ 512 ] ARRAY H6          \ impulse response holding array
REAL DIM[ 512 ] ARRAY H7          \ impulse response holding array

13 STRING FNAME

\ read and write from regular .HTR files (uncommmented)

: READ.DATA
CR " Enter filename (b:7char.ext) :  " "TYPE
"INPUT FNAME ":=
FNAME DEFER> FILE.OPEN
1 SUBFILE H(T) SUB[ 0 , 512 ] FILE>ARRAY
FILE.CLOSE
;

: WRITE.DATA
CR " Enter filename (b:7char.ext) :  " "TYPE
"INPUT FNAME ":=
FNAME DEFER> FILE.OPEN
1 SUBFILE H(T) SUB[ 0 , 512 ] ARRAY>FILE
FILE.CLOSE
;


\ read and write and template for commented .HTR files

\ : H(T).TEMPLATE
\ FILE.TEMPLATE
\ 5 COMMENTS
\ REAL DIM[ 512 ] SUBFILE
\ END
\ ;

\ : WRITE.H(T)
\ REAL.DATE   1 >COMMENT
\ ACTUAL.TIME 2 >COMMENT
\ REGION      3 >COMMENT
\ CONDITIONS  4 >COMMENT
\ ERROR       5 >COMMENT
\ 1 SUBFILE H(T) SUB[ 0 , 512 ] ARRAY>FILE
\ FILE.CLOSE
\ CR " File successfully created: " "TYPE HT.FNAME "TYPE
\ ;

: READ.H(T)
CR " Enter filespec (dir:\8char.htr): " "TYPE
"INPUT FNAME ":=
```

```
FNAME DEFER> FILE.OPEN
CR
1 COMMENT> "TYPE CR
2 COMMENT> "TYPE CR
3 COMMENT> "TYPE CR
4 COMMENT> "TYPE CR
5 COMMENT> "TYPE CR
1 SUBFILE H(T) SUB[ 0 , 512 ] FILE>ARRAY
FILE.CLOSE
;


\ words for processing the H(T) signal into correct form
REAL SCALAR TMEAN
REAL SCALAR EMEAN

WITHOUT.FREQUENCIES

: H2.EM                          \ for inverted signals
H2 -1 *
H2 :=
H2 SUB[ 0 , 128 ] MEAN EMEAN :=
H2 EMEAN - H2 :=
H2 H2 ^MAX [ 512 ] / H2 :=
STACK.CLEAR
;

: H2.EMR                         \ for righted signals
H2 SUB[ 0 , 128 ] MEAN EMEAN :=
H2 EMEAN - H2 :=
H2 H2 ^MAX [ 512 ] / H2 :=
STACK.CLEAR
;

: H3.TM
H1
H3
CONV.APER
SUB[ 0 , 512 ] H3 :=
H3 SUB[ 0 , 128 ] MEAN TMEAN :=
H3 TMEAN - H3 :=
H3 H3 ^MAX [ 512 ] / H3 :=
STACK.CLEAR
;

: H4.EM                          \ for inverted signals
H4 -1 *
H4 :=
H4 SUB[ 0 , 128 ] MEAN EMEAN :=
H4 EMEAN - H4 :=
H4 H4 ^MAX [ 512 ] / H4 :=
```

```
STACK.CLEAR
;

: H4.EMR                        \ for righted signals
H4 SUB[ 0 , 128 ] MEAN EMEAN :=
H4 EMEAN - H4 :=
H4 H4 ^MAX [ 512 ] / H4 :=
STACK.CLEAR
;

: H5.TM
H1
H5
CONV.APER
SUB[ 0 , 512 ] H5 :=
H5 SUB[ 0 , 128 ] MEAN TMEAN :=
H5 TMEAN - H5 :=
H5 H5 ^MAX [ 512 ] / H5 :=
STACK.CLEAR
;

: H6.EM                         \ for inverted signals
H6 -1 *
H6 :=
H6 SUB[ 0 , 128 ] MEAN EMEAN :=
H6 EMEAN - H6 :=
H6 H6 ^MAX [ 512 ] / H6 :=
STACK.CLEAR
;

: H6.EMR                        \ for righted signals
H6 SUB[ 0 , 128 ] MEAN EMEAN :=
H6 EMEAN - H6 :=
H6 H6 ^MAX [ 512 ] / H6 :=
STACK.CLEAR
;

: H7.TM
H1
H7
CONV.APER
SUB[ 0 , 512 ] H7 :=
H7 SUB[ 0 , 128 ] MEAN TMEAN :=
H7 TMEAN - H7 :=
H7 H7 ^MAX [ 512 ] / H7 :=
STACK.CLEAR
;

HORIZONTAL GRID.OFF
VERTICAL   GRID.OFF
```